

Thioether-poly(glycidol) as multifunctional coating system for gold nanoparticles

Dissertation zur Erlangung des
naturwissenschaftlichen Doktorgrades
der Julius-Maximilians-Universität Würzburg



vorgelegt von

Diplom-Chemikerin

Susanne Feineis

aus Würzburg

Würzburg 2018

Eingereicht bei der Fakultät für Chemie und Pharmazie am

Gutachter der schriftlichen Arbeit

1. Gutachter: _____

2. Gutachter: _____

Prüfer des öffentlichen Promotionskolloquiums

1. Prüfer: _____

2. Prüfer: _____

3. Prüfer: _____

Datum des öffentlichen Promotionskolloquiums

Doktorurkunde ausgehändigt am

Die vorliegende Arbeit wurde in der Abteilung für Funktionswerkstoffe der Medizin und Zahnheilkunde, Universität zu Würzburg, Würzburg, Deutschland in der Zeit von Dezember 2012 bis Juli 2017 unter der Leitung von Herrn Prof. Dr. Jürgen Groll angefertigt.

Copyright Remarks

Parts of this thesis have previously been published and adapted with permission from:

F. Rudnitzki, S. Feineis, R. Rahmzadeh, E. Endl, J. Lutz, J. Groll, G. Hüttmann, siRNA release from gold nanoparticles by nanosecond pulsed laser irradiation and analysis of the involved temperature increase, *J. Biophotonics* **2018**, e201700329.

Copyright © 2018 WILEY-VCH Verlag GmbH & Co. KGaA, Weinheim.

S. Feineis, J. Lutz, L. Heffele, K. Albrecht, E. Endl, J. Groll, Thioether–Polyglycidol as Multivalent and Multifunctional Coating System for Gold Nanoparticles, *Adv. Mater.* **2018**, 1704972.

Copyright © 2018 Wiley-VCH Verlag GmbH & Co. KGaA, Weinheim.

B. Baumann, T. Jungst, S. Stichler, S. Feineis, O. Wiltschka, M. Kuhlmann, M. Lindén, J. Groll, Control of Nanoparticle Release Kinetics from 3D Printed Hydrogel Scaffolds, *Angew. Chem. Int. Ed.* **2017**, 56, 4623-4628.

Copyright © 2017 The Authors. Published by Wiley-VCH Verlag GmbH & Co. KGaA, Weinheim.

Content of the thesis

Table of content.....	I
Abbreviations and symbols.....	VI
1 Aim of the thesis	1
2 Background	5
2.1 Colloidal stability	7
2.1.1 Charge stabilisation-DLVO theory	7
2.1.2 Steric stabilisation via polymer adsorption	9
2.1.2.1 Polymer configuration in solution	10
2.1.2.2 Polymer configuration on surfaces	12
2.2 Gold Nanoparticles (AuNPs)	18
2.2.1 Optical properties of AuNPs	18
2.2.2 Surface functionalisation of AuNPs	22
2.2.2.1 Sulfur-gold bonding models-current status	23
2.2.2.2 Experimental studies on the sulfur-gold bond strength for thioethers and thiols	26
2.3 Polymers as AuNP stabiliser	29
2.3.1 Bifunctional poly(ethylene glycol) (PEG)	29
2.3.2 Multifunctional poly(glycidyl ether)	30
3 Results and Discussion	33
3.1 Colloidal stabilisation efficacy of thiol- and thioether-polymers	35
3.1.1 Synthesis of thiol- and thioether-polymers.....	36
3.1.1.1 Monovalent PEG.....	37
3.1.1.2 Multivalent poly(glycidol) (PG).....	40
3.1.2 Synthesis of AuNPs stabilised with thiol- and thioether-polymers.....	45
3.1.2.1 Citrate-AuNPs as basic particles	46
3.1.2.2 Attachment of thiol- and thioether-polymers to citrate-AuNPs.....	49
3.1.2.3 Arrangement of thiol- and thioether-polymers on AuNPs.....	52
3.1.2.3.1 Determination of polymer surface coverages via TGA and XPS.....	52
3.1.2.3.2 Polymeric conformation on AuNPs	57
3.1.3 Colloidal stability of thiol- and thioether-polymer modified AuNPs.....	61
3.1.3.1 Binding kinetics study	61
3.1.3.2 Colloidal stability study	63
3.1.3.2.1 Stability against centrifugation, high temperatures and pH values.....	63

3.1.3.2.2 Stability under physiological conditions.....	66
3.1.3.2.3 Stability against lyophilisation.....	70
3.2 Multifunctionality of thioether-PG for AuNP functionalisation	72
3.2.1 Introduction of charge and hydrophobicity to the AuNP surface.....	73
3.2.1.1 Synthesis of PG bearing amine and carboxylic moieties for AuNP functionalisation ...	74
3.2.1.2 Synthesis of PG with hydrophilic and hydrophobic chains for AuNP functionalisation	81
3.2.2 Introduction of bio-active linkers to the AuNP surface.....	82
3.2.2.1 Synthesis of PG with photo-active diazirine groups.....	83
3.2.2.1.1 Diazirine-initiated binding of biomolecules	86
3.2.2.1.2 Synthesis of peptide functionalised PG.....	87
3.2.2.1.3 Synthesis of streptavidin functionalised PG.....	91
3.2.2.1.4 Streptavidin functionalised AuNPs.....	97
3.2.2.1.4.1 Quantification of streptavidin amount on AuNPs.....	100
3.2.2.1.5 Synthesis of protein G functionalised PG for AuNP coating.....	104
3.2.2.2 Synthesis of PG with biotin groups.....	107
3.3 Applications of multifunctional AuNPs.....	109
3.3.1 Incorporation of charged AuNPs into hyaluronic acid hydrogels ^[154]	110
3.3.2 Complexation of siRNA onto positively charged AuNPs.....	113
3.3.3 Controlled agglomeration of biotin and streptavidin modified AuNPs.....	118
3.3.4 Laser-triggered cell elimination through bio-activated AuNP.....	120
3.3.4.1 P(SET-co-SA ₍₂₎ -co-G).....	122
3.3.4.2 P(SET-co-SA _(x) -co-G) and P(SET-co-PEG-biotin-co-G)	124
4.1 Conclusion	127
4.2 Zusammenfassung.....	131
5 Experimental Section	135
5.1 Materials and Methods	136
5.1.1 Materials.....	136
5.1.2 Methods	138
5.1.2.1 NMR spectroscopy	138
5.1.2.2 SEC.....	138
5.1.2.3 UV-vis absorbance.....	139
5.1.2.4 FT-IR spectroscopy	139
5.1.2.5 RAMAN spectroscopy.....	139
5.1.2.6 Fluorescence spectroscopy	139

5.1.2.7 DLS	139
5.1.2.8 ICP-MS	139
5.1.2.9 TGA	140
5.1.2.10 XPS	140
5.1.2.11 Contact angle based measurements	140
5.1.2.12 SEM	141
5.1.2.13 Laser-triggered cell elimination	141
5.1.2.14 Purification of polymers	141
5.1.2.15 Lyophilisation of polymers	141
5.1.2.16 UV-light triggered reactions	142
5.1.2.17 Characterisation and handling of AuNP@citrate	142
5.1.2.18 Polymer functionalisation of AuNP@citrate	143
5.1.2.19 Ellman assay	143
5.1.2.20 TNBSA assay	143
5.1.2.21 (Micro-)BCA assay	144
5.1.2.22 ELISA	144
5.1.2.23 TEM staining	144
5.2 Polymer Synthesis and AuNP functionalisation	145
5.2.1 EEGE	145
5.2.2 P(AGE _{6/12} -co-EEGE)	146
5.2.3 P(AGE _{6/12} -co-G)	148
5.2.4 P(SH-co-G)	150
5.2.4.1 AuNP@P(SH-co-G)	151
5.2.5 P(SET-co-G)	152
5.2.5.1 AuNP@P(SET-co-G)	153
5.2.6 MeO-PEG-SH	154
5.2.6.1 AuNP@MeO-PEG-SH	154
5.2.7 MeO-PEG-SPentyl	155
5.2.7.1 AuNP@MeO-PEG-SPentyl	155
5.2.8 P(SET-co-COOH-co-G)	156
5.2.8.1 AuNP@P(SET-co-COOH-co-G)	156
5.2.9 P(SET-co-PEG-COOH-co-G)	157
5.2.9.1 AuNP@P(SET-co-PEG-COOH-co-G)	157
5.2.10 P(SET-co-NH ₂ -co-G)	158
5.2.10.1 AuNP@P(SET-co-NH ₂ -co-G)	159

5.2.11 P(SET-co-NH ₂₍₈₎ -co-G)	160
5.2.11.1 AuNP@P(SET-co-NH ₂₍₈₎ -co-G)	161
5.2.12 P(SET-co-NH ₂₍₁₁₎ -co-G)	162
5.2.12.1 AuNP@P(SET-co-NH ₂₍₁₁₎ -co-G)	163
5.2.13 P(SET-co-PEG-NH ₂ -co-G)	164
5.2.13.1 AuNP@P(SET-co-PEG-NH ₂ -co-G)	165
5.2.14 P(SET-co-PEG-OH-co-G).....	166
5.2.14.1 AuNP@P(SET-co-PEG-OH-co-G)	167
5.2.15 P(SET-co-Dodecyl-co-G)	168
5.2.15.1 AuNP@P(SET-co-Dodecyl-co-G)	168
5.2.16 P(SET-co-Diaz-co-G).....	169
5.2.16.1 AuNP@P(SET-co-Diaz-co-G)	170
5.2.17 P(SET-co-Diaz ₍₃₎ -co-G)	171
5.2.17.1 AuNP@P(SET-co-Diaz ₍₃₎ -co-G)	172
5.2.18 P(SET-co-PEG-Diaz-co-G)	173
5.2.19 P(SET-co-peptide-co-G) _{15/3.0}	174
5.2.20 P(SET-co-SA ₍₂₎ -co-G).....	175
5.2.20.1 AuNP@P(SET-co-SA ₍₂₎ -co-G)	176
5.2.21 P(SET-co-PrG-co-G).....	177
5.2.21.1 AuNP@P(SET-co-PrG-co-G)	178
5.2.22 P(SET-co-PEG-biotin-co-G)	179
5.2.22.1 AuNP@P(SET-co-PEG-biotin-co-G).....	180
5.3 Studies and applications of functionalised AuNPs	181
5.3.1 Kinetic study of thiol- and thioether-polymer modified AuNPs.....	181
5.3.2 Stability study of thiol- and thioether-polymer modified AuNPs.....	181
5.3.3 Incorporation of amine- and carboxylic-modified AuNPs into hyaluronic acid hydrogels	181
5.3.4 Complexation of siRNA to amine-modified AuNPs	182
5.3.4.1 AuNP@P(SET-co-NH ₂ -co-G)@siRNA.....	182
5.3.6 Photothermal depletion of mouse cancer B cells via streptavidin-modified AuNPs	183
6 Literature.....	185
Danksagung	195

Abbreviations and symbols

Abbreviations

AFM	atomic force microscopy
AGE	allyl glycidyl ether
Ar	argon
ATR	attenuated total reflection
a.u.	arbitrary unit
Au	Gold
AuNPs	gold nanoparticles
BCA	bicinchoninic acid
BW	bidistilled water
biotin-HRP	biotinylated horseradish peroxidase
C	Carbon
CFPT	critical flocculation point
CaH ₂	calcium hydride
CDCl ₃	deuterated chloroform
cm	centimeter
Cu	Copper
d	day
Da	Dalton
DFT	density functional theory
DLS	dynamic light scattering
DLVO	Derjaguin-Landau-Verwey-Overbeek
DMEM	Dulbecco's Modified Eagle Medium
DMF	N,N-dimethylformamide
DMPA	2,2-dimethoxy-2-phenylacetophenon
DNA	deoxyribonucleic acid
D ₂ O	deuterium oxide
DTNB	5,5'-dithio-bis-(2-nitrobenzoic acid)
DTT	dithiothreitol
EEGE	ethoxyethyl glyciyl ether
ELISA	Enzyme-linked Immunosorbent Assay
et.al.	Et alii (and others)
EtOH	ethanol
EtSH	ethanethiol
eq	equivalent
eV	electron volt
FT-IR	fourier-transform infrared spectroscopy
g	gravitational force
G	glycidol
h	hour

Content of the thesis

H	Hydrogen
HCl	hydrochloric acid
H ₂ O ₂	hydrogen peroxide solution
H ₂ SO ₄	sulfuric acid
HS-PEG-biotin	alpha-mercapto-omega-biotin poly(ethylene glycol)
HS-PEG-COOH	alpha-mercapto-omega-carboxy poly(ethylene glycol)
HS-PEG-NH ₂	alpha-mercapto-omega-amino poly(ethylene glycol)
HS-PEG-OH	alpha-mercapto-omega-hydroxy poly(ethylene glycol)
Hz	hertz
ICP-MS	Inductively coupled mass spectrometry
Irgacure 2959	2-hydroxy-1-[4-(hydroxyethoxy)-phenyl]-2-methyl-1-propanone
KO ^t Bu	potassium tert-butoxide
LED	light emitting diode
M	Molarity
MeO-PEG-SH	alpha-methoxy-omega-mercapto poly(ethylene glycol)
mg	milligram
MgSO ₄	magnesium sulfate
MHz	megahertz
min	minute
mL	millilitre
mmol	millimole
M _n	number-averaged molar mass
mV	millivolt
mW	milliwatt
M _w	weight-averaged molar mass
MW	molecular weight
MWCO	molecular weight cut off
N	Nitrogen
N ₂	nitrogen gas
NaCl	sodium chloride
NaHCO ₃	sodium hydrogen carbonate
NaOH	sodium hydroxide
Nd:YAG	neodymium-doped yttrium aluminium garnet; Nd:Y ₃ Al ₅ O ₁₂
NHS-diazirine	succinimidyl 4,4'-azipentanoate
nm	nanometer
ns	nanoseconds
NMR	nuclear magnetic resonance
O	Oxygen
OD	optical density
PB	phosphate buffer
PBS	phosphate buffered saline
PEG	poly(ethylene glycol)

PG	poly(glycidol)
pH	negative logarithmic value of the hydrogen ion concentration
PrG	recombinant protein G
PMMA	poly(methacrylic acid)
ppb	parts per billion
ppm	parts per million
Pt	Platinum
<i>p</i> TsOH	<i>p</i> -toluene sulfonic acid monohydrate
R	rest
RI	refractive index
RT	room temperature
s	seconds
S	Sulfur
SA	streptavidin
SEC	size exclusion chromatography
SEM	scanning electron microscopy
SDS	sodium dodecyl sulfate
SH	thiol
Si	silicon
siRNA	small interfering ribonucleic acid
SPR	surface plasmon resonance
SR	thioether
SSR	disulfide
STM	scanning tunnelling microscopy
TCEP	tris(2-carboxyethyl)phosphine hydrochloride
TEM	transmission electron microscopy
TGA	thermogravimetric analysis
THF	tetrahydrofuran
TMB	3,3',5,5'-tetramethylbenzidin
TMS	tetramethylsilane
TNBSA	2,4,6-trinitrobenzene sulfonic acid
UV-vis	ultraviolet and visible light
W	Watt
XPS	x-ray photoelectron spectroscopy

Symbols

°	degree
°C	degree Celsius
%	per cent
atom-%	atomic percent
mass-%	weight percent
μL	microlitre
μM	micromolar
μmol	micromole
δ	chemical shift
d	hydrodynamic diameter
Đ	dispersity
ζ	zeta potential
$\tilde{\nu}$	wavenumber
λ	wavelength
R _g	radius of gyration
R _F	Flory radius
σ	polymeric grafting density
e ⁻	electron
ph	phonon
hν	light

1 Aim of the thesis

1 Aim of the thesis

Gold nanoparticles (AuNPs) proved to be extremely helpful tools in biology and medicine, owing to their intrinsic biocompatibility, unique optical properties and ease of surface modification with biological molecules.^[1-2] Moreover, AuNPs can easily be prepared by reduction of gold salts under precise control over size and shape.^[3]

The gold surface exhibits high affinity towards functional groups such as thiols, phosphines and amines and thus a plethora of biomolecules, including drugs,^[4] DNA,^[5] siRNA^[6] and proteins^[7] have been directly coupled to AuNPs. These AuNP-conjugates found a range of applications ranging from *in vitro* biosensing to *in vivo* drug or gene delivery. Here, the strong interaction with light in the visible region can be used to photo-thermally trigger biological release and activity under spatio-temporal control.^[8-9]

However, aforementioned AuNP-conjugates show deficits in colloidal stability when exposed to physiological conditions, which can mainly be attributed to the high sensitivity of electrostatic stabilisation towards ions and proteins.^[10] By introducing polymers to the gold surface, not only the colloidal stability is improved by steric effects but also the circulation time of polymer coated AuNPs *in vivo* increases owing to stealth properties.^[11]

Here, the development of multifunctional polymers featuring both a strong anchor to the gold surface coincident with functional moieties for introducing biological payload still remains a major challenge. Thiol polymers are most widely used for steric stabilisation of AuNPs due to their strong thiol-gold bond which can be considered as quasi-covalent.^[12] On the other hand, thiols possess an oxidative and nucleophilic character, which in particular for multifunctional compounds provokes intra- and inter-polymeric crosslinking^[13] leading to a loss of the stabilisation properties. This problem can only be overcome by applying reductive pre-treatments and by restricting the introduction of electrophilic biological functions.

Chemically-inert thioether-polymers appeared in the last few years as thiol alternative^[14-15] providing the basis for an abundantly multifunctional particle coating system. However, inconsistencies about their colloidal stabilisation efficacy exist within literature. In general, the thioether-gold bond is claimed to be weaker than the thiol analogue.^[16] Yet, most of these studies are *in situ* and consider merely the binding kinetics of thioether compounds, not taking the thermodynamic stability upon polymer coating into account. Thus, these investigations translate a slower as a weaker binding, although longer passivation times for thioether compounds than for thiol analogues were found *per se*.^[16-17] The few studies that examined

the thermodynamic stability of thioether-gold constructs consistently impeded a generalisation of a weaker thioether-gold bond compared to the thiol-gold analogue.^[18-20] Instead, they concluded that the whole molecular structure has to be considered for stabilisation efficacy and found that in dependency on the functionality and structure, thioethers were just as stable as their thiol analogues.^[21-23] In addition, multivalency was concertedly claimed to increase the stabilisation efficacy of thioether-polymers.^[14, 24]

Therefore, the **aim of this thesis** was the development of a multifunctional coating system for AuNPs based on thioether polymers, providing both excellent colloidal stability and unrestricted introduction of functionalities for biological applications. In order to ensure systematics the investigation on the stabilisation efficacy, particularly against biological and physiological conditions was performed with two thioether-polymer systems in comparison to respective thiol analogues, namely commonly used monovalent poly(ethylene glycol) (PEG) and its structural analogue linear poly(glycidol) (PG) bearing multiple statistically distributed thioether or thiol moieties along the backbone. Subsequently, the multi-functionalisability of thioether-PG was examined before exploring the applicability and bioactivity of correspondingly modified particles in diverse studies.

Chapter 2 outlines how polymer characteristics, such as nature and length of polymer chains, as well as the interaction of polymers with the solvent influence the efficacy to stabilise colloids (see **Section 2.1.2**). Besides a detailed introduction of the optical properties of AuNPs in **Section 2.2.1**, the current literature background of the thioether-gold bond strength is given in comparison to the thiol analogue, with regard to theoretical models and experimental results (see **Section 2.2.2**). Moreover, the polymers PEG and PG, which were used throughout this thesis to stabilise and functionalise AuNPs are introduced in **Section 2.3**.

Chapter 3 is divided into three main sections. The first **Section 3.1** covers the synthesis of PEG and PG and its functionalisation with thioether or thiol moieties via thiol-ene click chemistry (see **3.1.1**). The successive modification of varyingly large AuNPs with aforementioned polymers via ligand exchange reaction of citrate-stabilised particles is thoroughly characterised in **Section 3.1.2**, in particular with respect to their polymer coverage. The colloidal stabilisation efficacy of thioether and thiol polymers is examined by exposing the particles to conditions that provoke aggregation, including physiological conditions and freeze-drying (see **3.1.3**).

Secondly, **Section 3.2** focusses on the diverse functionalisability of PG via bimolecular thiol-ene click reaction where additionally to the thioether anchor groups, functional mercaptan compounds are introduced to allyl groups of the PG backbone. In this manner, charged groups and hydrophilic/hydrophobic chains (see **3.2.1**), as well as bio-active moieties, such as diazirine and biotin (see **3.2.2**) are covalently attached to the AuNP surface. Moreover, the introduction of useful biomolecules, including streptavidin and protein G through generic photo-initiated binding of diazirine functionalities is highlighted.

Lastly, **Section 3.3** comprises the applicability of functionalised AuNPs in various fundamental and biological studies. For instance, the mobility of charged AuNPs in three-dimensional charged polymeric constructs is examined (see **3.3.1**) and the utility of positively charged AuNPs as siRNA-complexation scaffolds is demonstrated (see **3.3.2**). At last the activity of streptavidin functionalised AuNPs in laser-triggered cell elimination experiments is thoroughly investigated (see **3.3.3**).

Chapter 4 provides a conclusion of the thesis in English and German language.

Chapter 5 comprises the experimental section providing in-depth information about each performed experiment, including full characterisation of the polymers and correspondingly modified AuNPs.

2 Background

Parts of this chapter have previously been published and adapted with permission from:

F. Rudnitzki, S. Feineis, R. Rahmzadeh, E. Endl, J. Lutz, J. Groll, G. Hüttmann, siRNA release from gold nanoparticles by nanosecond pulsed laser irradiation and analysis of the involved temperature increase, *J. Biophotonics* **2018**, e201700329.

Copyright © 2018 WILEY-VCH Verlag GmbH & Co. KGaA, Weinheim.

2.1 Colloidal stability

Colloidal particles undergo Brownian motion in liquids owing to random collision with themselves and with solvent molecules, resulting in two types of interactions, namely the hydrodynamic (particle-solvent) and the static (particle-particle) force. Thus, the colloidal stability is determined by the interaction between the particles during these collisions. When attraction dominates, the colloids associate in either a reversible (flocculation) or irreversible (coagulation) manner. When repulsion dominates, the colloids remain in a dispersed state. The particle-particle force can more precisely be described by the Derjaguin-Landau-Verwey-Overbeek (DLVO) theory.^[25]

2.1.1 Charge stabilisation-DLVO theory

The DLVO theory assumes two basic interactions: the attractive van-der Waals and the repulsive double-layer interaction.

Attractive van der Waals forces are always present between two similar particles, originating either from permanent dipole-permanent dipole (Keesom) forces or induced dipole (Debye) forces or transitory dipole-transitory dipole (London) forces. While the first two are short range interactions, the London forces appeal in the long range (5-10 nm), emerging as the decisive forces for colloidal stability. The strength of van der Waals forces can be related to the Hamaker constant of the particles, a material constant which can be calculated based on the number densities of the particles. The Hamaker constant is independent of the colloidal geometry.^[26]

In case of ionic stabilisation, double-layer forces arise due to a Coulombic repulsion between the particles, when a layer of ions termed as stationary Stern layer adsorbs onto the surface, being compensated by a second layer of oppositely charged counterions. Here, the counterions are loosely associated to the particle, termed as diffuse layer. The strength of the double-layer force can be determined by zeta potential ζ measurements at the slipping plane and the thickness of this double-layer is directly correlated to the ionic strength of the solvent. For strongly charged particles ($\zeta > +25$ mV; $\zeta < -25$ mV) or particles in low ionic strength solutions ($c_{\text{electrolyte}} = 10^{-3}$ M) the thickness of a double layer is about 5-10 nm, able to compensate the London forces. An increase of the ionic strength ($c_{\text{electrolyte}} > 10^{-1}$ M), however, provokes a decrease of the double-layer thickness to 1 nm, resulting in coagulation. **Figure 1** schematically shows how the DLVO force at surface distances close to zero ($D \sim 0$) features a

2 Background

primary minimum, which results in coagulation. Besides, DLVO interactions display a maximum, whereby its height (energy barrier) and the formation of a secondary minimum depends on the surface charge σ . The high sensitivity towards ionic strength of the solvent hampers the applicability of charge stabilisation tremendously.^[27-30]

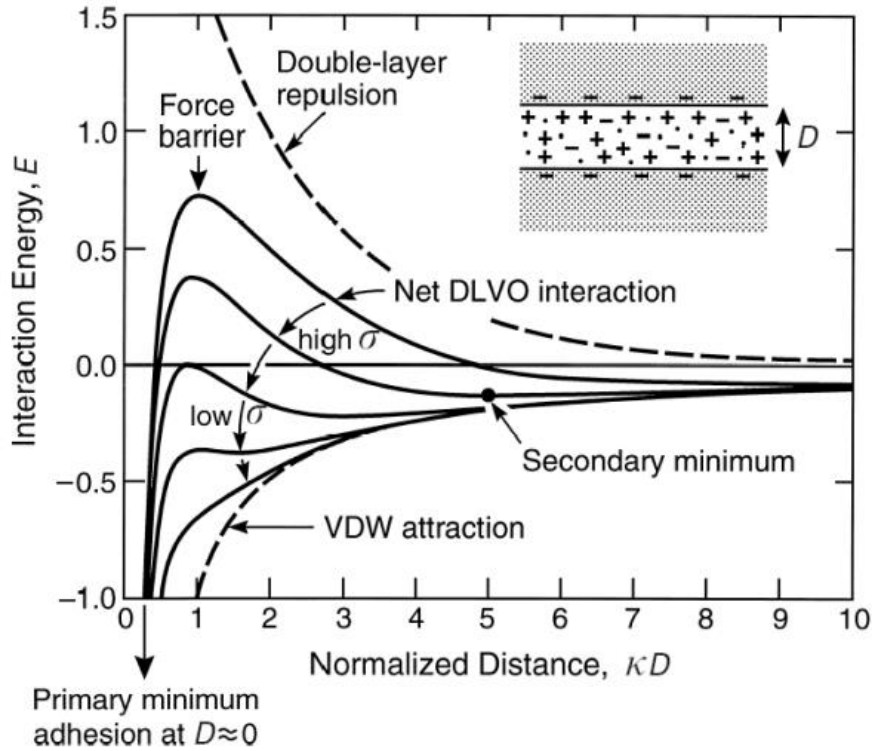


Figure 1: Schematic plot of attractive van der Waals (VDW) forces and repulsive double-layer forces (dashed lines) between two charged surfaces. The net DLVO interaction (solid lines) becomes attractive with decreasing surface charge σ . Reprinted with permission of [31]. Copyright (2011) Elsevier Inc.

A method to overcome the sensitivity of charged systems is the use of polymers that adsorb onto the particle surface. This changes the surface properties in a manner that additional forces between two particles arise (“extended DLVO” forces), including steric forces, as well as Lewis acid-base and hydrophilic/hydrophobic interactions. The next chapter focuses first and foremost on steric forces.^[32]

2.1.2 Steric stabilisation via polymer adsorption

Steric stabilisation is based on the loss of configurational entropy of the adsorbed polymer chains on the particle surface. When two particles approach each other, the adsorbed polymer layers get compressed, limiting the number of possible configurations of the polymer chains. The provoked reduction of entropy renders a particle association unfavourable, producing a net effect of repulsion, which prevents flocculation.^[33]

In contrast to the irreversible coagulation of charge-stabilised particles, the flocculation of sterically stabilised particles can be reversed by e.g. dilution. This difference is due to the fact that sterically stabilised colloidal solutions are thermodynamically stable, whereas charge-stabilised ones are metastable, where the coagulated state represents a lower energy state, which can be reversed only after energy input. The thermodynamic stability of sterically stabilised colloids yields a further advantage, the spontaneous redispersion after drying, including lyophilisation. This provides the preparation of long-term stable colloidal powders that can be liquidised on demand.^[33]

The transition from steric colloidal stability to flocculation occurs abruptly at the critical flocculation point (CFPT). Particle size, nature and molecular weight of the polymer, particle concentration, surface grafting density and the solvent have impact on the CFPT. In general, larger particles with low molecular weight polymers are more prone to flocculation, since van der Waals forces increase with increasing particle size and decreasing particle distance, caused by thin polymer layers. In this case the CFPT correlates with the particle concentration, where dilute solutions are more stable.^[25, 34]

The crucial impact of the surface grafting density and the solvent on the steric colloidal stability will be thoroughly discussed throughout the next chapters. Before describing polymers on colloidal surfaces in more detail (see **Section 2.1.2.2**), firstly the configuration of polymers in solvents will be focussed in **Section 2.1.2.1** in order to introduce basic polymeric properties.

2.1.2.1 Polymer configuration in solution

Polymer configurations in solution are known from the triangle of Haug, as displayed in **Figure 2**. Besides the three extreme types of polymeric conformations, such as the stiff rod, compact globule and random coil (displayed in purple), also the transition conformations ellipsoide, stiff chain and branched coil are shown in grey. The stiff rod (bottom, right) is a linear conformation, which is often accompanied by the formation of a helical structure, as typified by a short DNA double helix and the compact globule (top), where the chain folds back to minimise solvent contact, as found for native proteins. Most synthetic polymers, denatured proteins and DNA, however, correspond to a random coil structure (bottom, left), where the polymer chains adopt many different conformations.

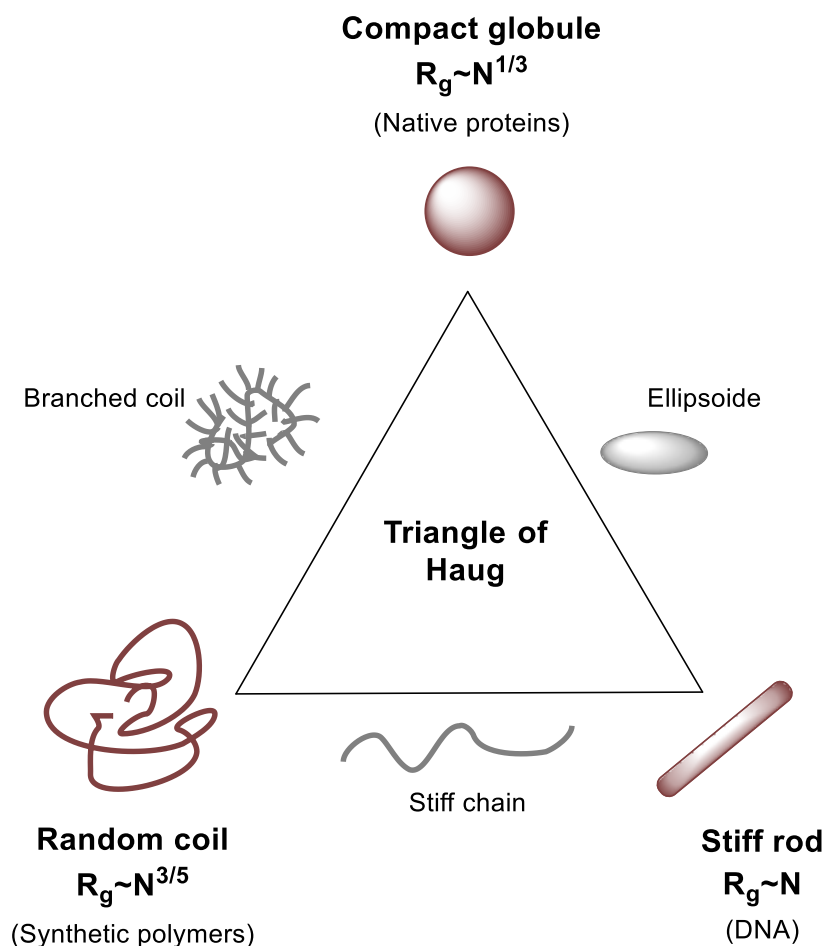


Figure 2: Schematic presentation of Haug's triangle according to [35]. The conformation is determined by the radius of gyration R_g , involving the chain length R or R_F , which is proportional to the number of monomers (N) and the interaction of the polymer with the solvent, considered in the exponent of N .

The average size over all coiled conformations is given by the radius of gyration R_g .^[25]

$$R_g = \frac{R}{\sqrt{6}} \quad \text{Equation 1}$$

$R = \text{end to end distance of polymer}$

R_g is proportional to the end-to-end distance of the polymer R , which is a characteristic length, representing the size of the polymer as described in **Equation 1**. Depending on the theory used for calculation the end-to-end distance is abbreviated with R (freely-jointed-chain model) or R_F (excluded volume model). In the freely-jointed-chain-model the polymer is described as an ideal chain with no limitations in the rotation or bending, according to a random walk. R is the product of the monomer length α and the monomer number N with the exponent $\frac{1}{2}$, corresponding to ideal θ -conditions, where the solvent and temperature disallow the excluded volume model and the polymer behaves ideally, without interference with itself or with other chains (see **Equation 2**).^[25] The excluded volume model considers repulsive monomer interactions, since a region already occupied by a monomer cannot be occupied by another monomer. Hence, the conformational possibilities of a non-ideal chain are reduced, described by a self-avoiding random walk. This results in generally larger values of R_F compared to R in good solvents, corresponding to an extended polymer chain, expressed by the exponent $3/5$. In bad solvents the exponent changes to $1/3$, where the chain conforms to a solid sphere (see **Figure 2** and **Equation 3**). R_F is known as the Flory radius and will be further applied in **Section 2.1.2.2**.^[36]

$$R = \alpha N^{\frac{1}{2}} \quad \text{Equation 2}$$

$$R_F = \alpha N^{\frac{3}{5}} \text{ (good solvent)} \quad \text{Equation 3}$$

$$R_F = \alpha N^{\frac{1}{3}} \text{ (bad solvent)}$$

$\alpha = \text{length of monomer}$

$N = \text{number of monomers}$

2 Background

2.1.2.2 Polymer configuration on surfaces

Polymers may adsorb onto a surface when the interactions between polymer, solvent and surface result in an adsorption energy that is high enough to compensate the loss of configurational entropy related to non-adsorbed polymer chains in solution. Moreover, the release of solvent molecules from the polymer network and the surface apply as entropic driving force for adsorption. Two kinds of adsorption have to be distinguished, the physisorption indicating an adsorption via non-covalent forces and the chemisorption, where the adsorption occurs via a chemical bond.^[32]

Likewise to polymers in solution, the interaction with the solvent is crucial for the conformation on surfaces. In good solvents non-adsorbed parts of the polymer extend out from the surface to maximise polymeric configurations, generating a repulsive steric entropic force with a range determined by R_g . When the distance of two surfaces is $\geq 2R_g$ (10-100 nm), the repulsive polymer-polymer overlap is the decisive force and van der Waals, as well as double-layer forces are negligible. Surface attraction can be induced by changing to a bad solvent, as exemplarily depicted in **Figure 3** for two surfaces with adsorbed polystyrene brushes (left: MW = 60000 Da, $R_g = 7$ nm, right: 150000 Da, $R_g = 11$ nm) in toluene. At 32 °C (good solvent conditions) polystyrene extends out from the surface, resulting in steric repulsion, whereas at 21 °C toluene changes to a bad solvent and attractive forces dominate. An increase of R_g from 7 nm to 11 nm leads to larger separation distances.^[37-38]

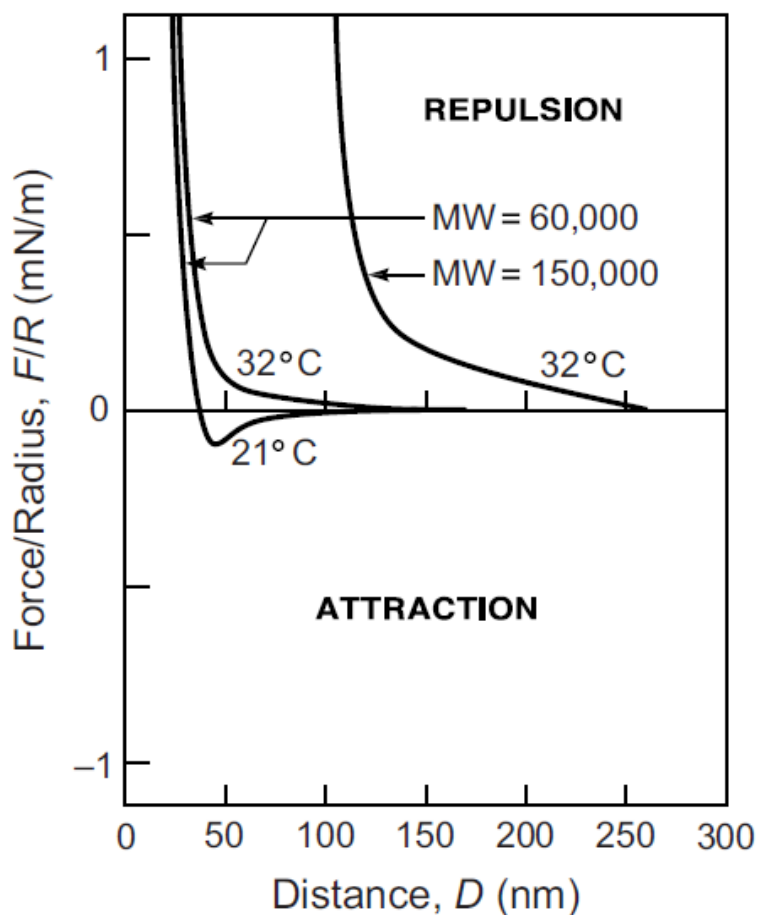


Figure 3: Force-distance profile displaying the dependency of attractive and repulsive forces between two surfaces with adsorbed polystyrene brushes in toluene on the solvent conditions. Reprinted with permission of [39]. Copyright (2011) Elsevier Inc.

As already mentioned in **Section 2.1.2**, besides the solvent also the grafting density (polymer chains per nm^2) determines the repulsive forces between two surfaces. **Figure 4** exemplarily displays that for colloids with a decreasing number of DNA chains per nm^2 (decrease marked by the red arrow) the separation distance of the particles declines owing to less repulsive polymer-polymer overlap.

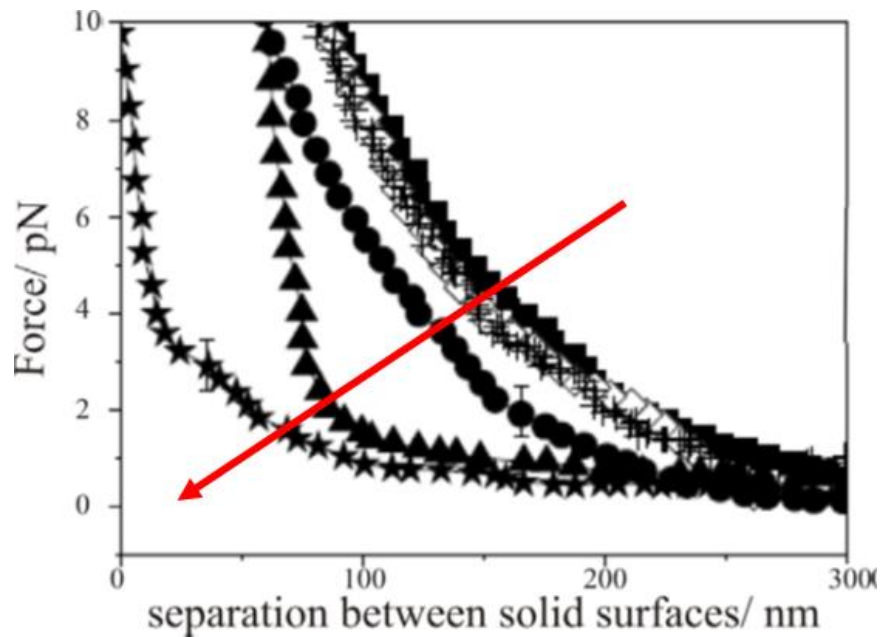


Figure 4: Impact of the grafting density on the repulsive forces between two colloids grafted with DNA. A decrease of DNA chains per nm^2 is highlighted by the red arrow. Reprinted with permission of [40]. Copyright (2007) American Physical Society.

In the following the grafting density and the corresponding polymer conformation on surfaces in good solvents will be further pointed out. As shown in **Figure 5**, two kinds of polymer chains have to be distinguished, polymers with a terminal sequence that features high affinity to the surface, including a grafted chain with only one terminal anchor group or a block copolymer with an adjustable length of the high affinity sequence. On the other hand homopolymers or random copolymers may possess several anchor regions distributed along the chain. In case of the homopolymer it is presumed that each monomer unit displays the same affinity towards the surface. Grafted chains or block polymers arrange either in a brush or in a mushroom regime, depending on the grafting density, whereas homopolymers or random-copolymers feature tails, loops and trains on their surface.

For grafted chains or block-copolymers with small chains the grafting density σ depends solely on the size of the anchor group, whereas for large chains the chain-chain repulsion additionally influences the polymer conformation.^[25]

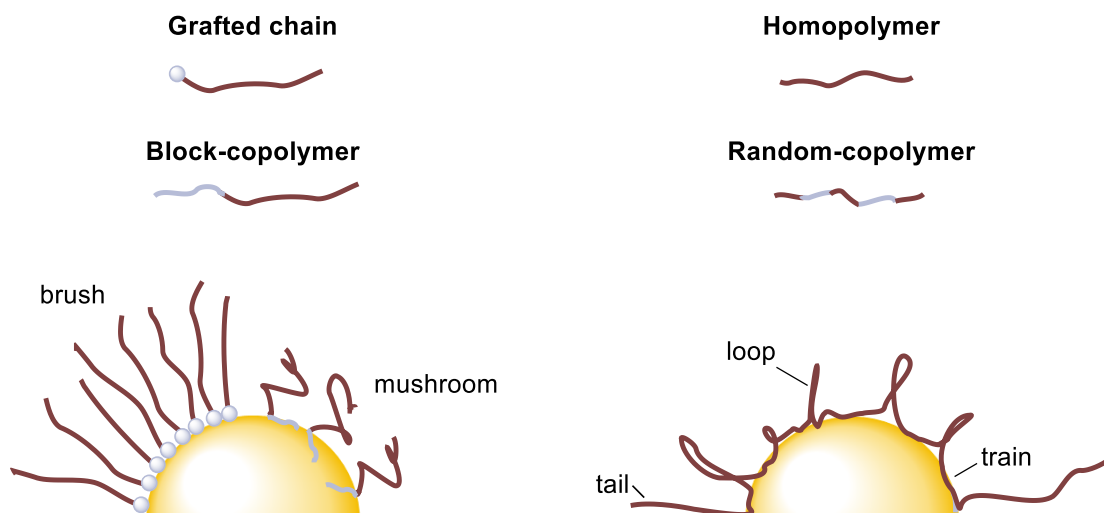


Figure 5: Distinction between polymers with a terminal anchoring sequence (marked in grey), including grafted chains and block-copolymers (left) and polymers with randomly distributed adsorbing regions, such as homopolymers or random-copolymers (right) and their conformations on a particle surface.

Poly(ethylene glycol) (PEG) chains (further described in **Section 2.3.1**) apply as typical example for grafted polymers on surfaces.^[41] Briefly, PEG is a hydrophilic polymer, with water as a good solvent. The PEGylation density is described via R_F of PEG (**Equation 3**) and the distance between the anchor groups of two corresponding PEG chains D_{grafting} and the layer thickness of the PEG coating δ .

D_{grafting} can be obtained by the grafting density σ via **Equation 4**. Latter can be derived from the number of polymers per particle divided by the particle surface area ($4\pi r^2$).^[42-43]

$$D_{\text{grafting}} = 2 \sqrt{\frac{1}{\sigma\pi}}$$

Equation 4

$$\sigma = \text{grafting density} = \frac{\text{Number of polymers per particle}}{4\pi r^2}$$

The calculation of the number of polymers per particle is challenging, since it is based on the polymer to particle ratio in the dry state (see **Equation 5**).^[44-45] One possibility to determine this ratio in weight-% is by gravimetric or spectroscopic measurements, as thoroughly discussed in **Section 3.1.2.3.1**.

Alternatively, the polymer to gold ratio can be visually gauged by staining the dried thickness of the polymer layer via subsequent electron microscopy. However, the determination of the polymer layer width via staining needs to be considered with caution, since the addition of

the staining compound induces morphological changes and might distort values of the layer width.^[46]

$$\text{Polymers per particle} = \frac{\frac{\text{weight}\%_{\text{polymer}}}{\text{weight}\%_{\text{particle}}} \times \rho_{\text{particle}} \times \frac{4}{3}\pi r^3 \times N_A}{M_W} \quad \text{Equation 5}$$

ρ_{particle} = density of particle

r = radius of particle

N_A = avogadro constant

M_W = molecular weight of polymer

For PEGylated particles De Gennes *et al.* suggested a mushroom conformation at low grafting densities, where D_{grafting} is greater than R_F ($D_{\text{grafting}} > R_F$), resulting in thin layers ($\delta \leq R_F$). While higher grafting densities with decreasing D_{grafting} cause an extended brush conformation, due to chain-chain repulsion and excluded volume effects ($D_{\text{grafting}} < R_F$). When the layer thickness exceeds twice the value of R_F ($\delta > 2R_F$), the brush conformation was further defined by Damodaran *et al.* to be a dense brush.^[42, 47-48]

Homopolymers or random-copolymers featuring a coil conformation in a good solvent do not change their conformation dramatically upon adsorption via multiple anchor groups to a surface. Thus, the conformation can be described in terms of two tails (ends of the chain expanding from the surface), a number of trains (sequences of the chain adsorbed to the surface) and a number of loops (sequences of the chain non-adsorbed to the surface, reaching out into the solution), between two trains (see **Figure 5**). Examples for such homopolymers found in literature are poly(vinyl alcohol),^[49-50] poly(vinyl pyrrolidone)^[51] and dextran.^[52] Whereas Khokhlov *et al.* described the tail-train-loop conformation for “truly” random copolymers, with statistically distributed adsorbing segments along the polymer chain.^[53] The thickness of the adsorbed layer is determined by polymer-particle interactions, the density of adsorbed polymer segments and the length of protruding polymer segments, possessing the same magnitude as R_g . Models based on conformational statistics, such as Monte Carlo simulations and self-consistent field methods to determine the composition of trains, loops and tails were described by Fleer *et al.* for the adsorption onto flat surfaces.^[54]

Further facts that have impact on the polymer configuration on particles are the surface curvature and an incomplete surface coverage. For grafted polymers in a brush conformation an increase of the surface curvature resulted in a decrease of the layer thickness, as predicted by “blob” models.^[55] Likewise, polymers with multiple anchor groups that arrange in trains, loops and tails, demonstrated a decrease in the layer thickness with increasing curvature in theoretic and experimental studies.^[32, 56] If the surface features incomplete polymer coverage, an attraction can occur even in good solvents. When a polymer chain has more than one anchor group and extends from one surface to unoccupied parts of another, attractive interactions arise, termed as bridging flocculation. In particular the combination of very small particles and long polymers promote bridging flocculation.^[32]

2 Background

2.2 Gold Nanoparticles (AuNPs)

Colloidal solutions consisting of AuNPs proved to be extremely helpful in nanoscience and nanotechnology, owing to their intrinsic biocompatibility, unique optical properties, ease of surface modification with polymers and biological molecules, accompanied by a high steric colloidal stability.^[3] AuNPs can easily be prepared by citrate reduction of gold salts under precise control over size, where citrate acts as both reducing and stabilisation agent. By changing the gold-to-citrate ratio Frens *et al.* was able to control the particle size of monodisperse spherical AuNPs in the range of 15-150 nm.^[57]

In the next chapter firstly the optical properties of spherical AuNPs will be described, before focussing on the surface modification.

2.2.1 Optical properties of AuNPs

The basis to explain the unique optical properties of AuNPs was provided in 1908 by Mie, who solved Maxwell's equations for the light interaction with a single particle^[58] and completed in the 1960s by introduction of the electron band theory for metals.^[59] The interaction of AuNPs with light is based on a collective, quantised oscillation of the free conduction electrons on the particle, referred to as a quasiparticle termed plasmon. According to the Fermi liquid model plasmons involve a displacement of the (Fermi-)electron cloud from an equilibrium position around positively charged ions of the gold lattice. The resonance frequency of these plasmons is defined by the particle surface and consequently named the surface plasmon resonance (SPR). Depending on the particle diameter (10-100 nm), the SPR of isotropic spherical AuNPs appears around 515-580 nm, giving rise to the characteristic red colour of the particles.^[60]

Figure 6 displays that the red-shift of the SPR for increasing AuNP diameter is accompanied by a broadening of the plasmon band. Generally, the SPR bandwidth of AuNPs is set by the dephasing time of coherent electron oscillation, featuring typical values of 2-50 fs. For small particles (< 25 nm) pure dipolar oscillation dominates the SPR. When the particle size increases (> 60 nm), however, the excitation of multipolar plasmons is triggered, resulting in a broadening of the SPR due to a faster loss of coherence, also referred to as extrinsic size effect.^[59, 61-62]

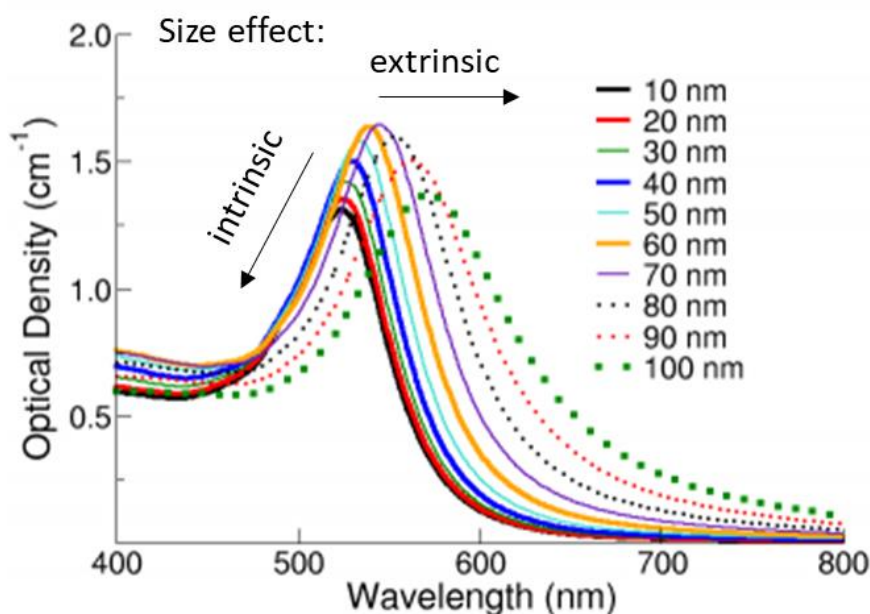


Figure 6: UV-vis absorbance spectra of AuNPs with diameters of 10 nm-100 nm, displaying the extrinsic and intrinsic size effect. Reprinted with permission of reference^[63]. Copyright (2017) Nanocomposix.eu.

On the other hand the intrinsic size effect causes a damping of the SPR when the particle diameter decreases below 30 nm (**Figure 6**). For these AuNPs the particle size corresponds to the conduction electron mean free path, enabling free electron excitation. For AuNPs smaller than 2 nm, the SPR is almost completely quenched and discrete single electron transitions dominate.^[59, 64]

The AuNP size furthermore determines the contributions of scattered and absorbed light. **Figure 7** displays that for particles with sizes smaller than the wavelength of the incoming light ($d < \lambda$) absorption dominates over scattering. For particle sizes around 50 nm the two effects become comparable, whereas above 70 nm scattering exceeds absorption, defining the glance of these AuNPs.^[2]

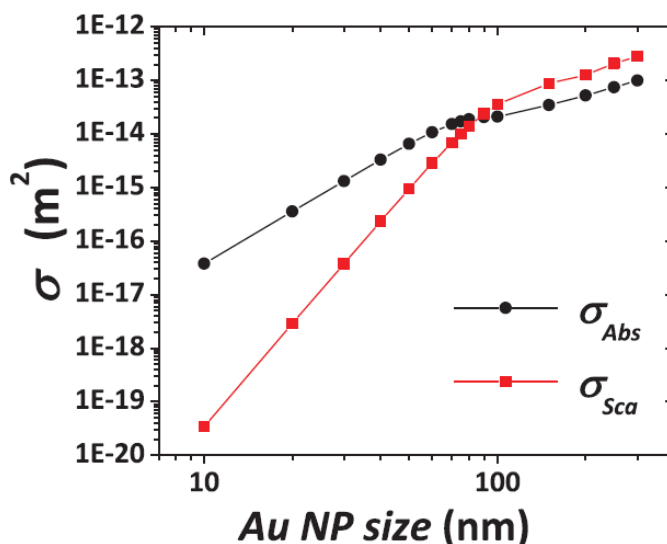


Figure 7: Contribution of absorbed (black) and scattered (red) light in dependence of the AuNP diameter. Reprinted with permission of reference^[2]. Copyright (2017) IOP Publishing Ltd.

Besides, the position of the SPR is influenced by environmental dielectric properties, including solvent or surface modification of the particles, for instance via adsorption of ligands. The ligand shell changes the electron density on the particle surface, provoking a red-shift of the SPR. Interestingly, this red-shift is more pronounced for thiolate ligands, known for their strong binding to the gold surface, than for weakly adsorbed amines (see **Section 2.2.2**). This effect is known as chemical interface damping (see **Figure 8**). Moreover, the introduced ligand electrons open new electron relaxation ways, causing an increased dephasing time and hence broadening of the plasmon band.^[65-66]

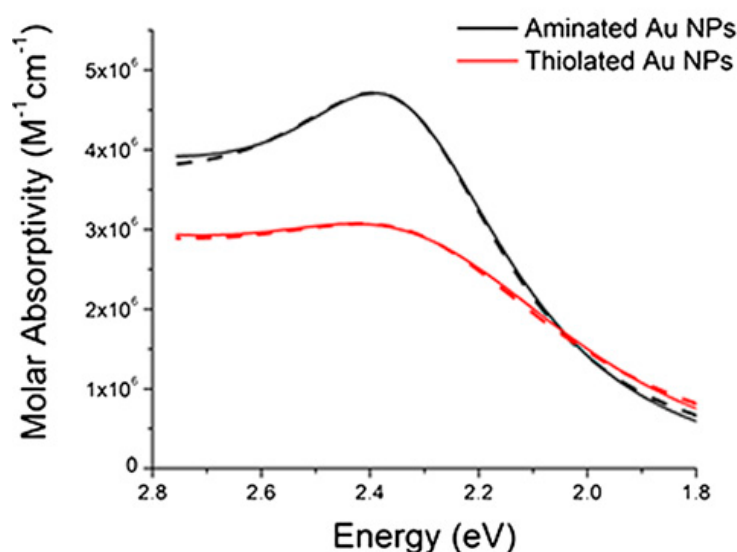


Figure 8: The adsorption of strongly binding thiol ligands (red) onto AuNPs provokes a stronger SPR red-shift, compared to weakly adsorbed amine ligands (black). Adapted with permission of reference^[66].

Depending on the particle distance, plasmons of distinct AuNPs can interact with each other. For the extreme case of aggregation, the electron cloud is delocalised over all adjacent AuNPs with a multitude of plasmon modes, resulting in two bands, one close to the original position and the other red-shifted around 600-700 nm. Both bands are significantly broadened and damped, compared to the single particle SPR.^[2, 67]

The anisotropic distortion of the particle surface such as growth of nanorods causes a splitting of the SPR with a remaining low energy frequency around 520 nm and an arising high energy frequency, which can be tuned in the NIR region of the electromagnetic field.^[68] Yet, the impact of the particle shape on the SPR will not be further amplified, since this thesis exclusively deals with isotropic AuNPs.

The strong SPR absorption in the visible region and its fast relaxation, accompanied by the high photostability and low luminescent of AuNPs, renders the particles into excellent light-to-heat converter. In fact, compared to the strongest absorbing organic chromophores, the absorption cross-section of AuNPs ($d > 2$ nm) is several orders of magnitude larger, enabling 100 % of photothermal conversion. For instance, the absorption cross-section of 40 nm AuNPs was determined to be $\sim 2.9 \cdot 10^{-15} \text{ m}^2$ around 530 nm, whereas the one of indocyanine green is $\sim 1.7 \cdot 10^{-20} \text{ m}^2$ around 800 nm.^[2] In order to describe the mechanism of the photothermal conversion, a detailed investigation on all electronic relaxation processes of AuNPs upon irradiation is given in the following.

Within the irradiation process each AuNP absorbs multiple photons, provoking multiple continuously excited SPRs. As already mentioned in dependence on the particle size, the decay of these excited SPRs involves either photon scattering or absorption, including the formation of non-radiative hot electron-hole pairs. These hot electrons originate from the Fermi-level and thus feature sufficient energy to extend further away from the particle surface than an equilibrium electron. If an electron acceptor, such as a ligand shell is in close proximity, hot electrons can transfer into the electronic states of these adsorbed ligands, referred to as electron-electron coupling (e^-e^- coupling). The e^-e^- coupling displays relaxation times of about 500 fs and provokes ligand dissociation and desorption. This effect is used for the light-triggered spatio-temporal release of drugs,^[9] DNA^[8, 69] and siRNA.^[70-71] Furthermore, hot electrons can transfer their energy to the gold lattice, termed electron-phonon coupling (e^-ph coupling). This process occurs in 1-5 ps, independently of the particle size. Lastly, the e^-ph

2 Background

coupling causes interactions between the gold lattice and the surrounding medium, namely phonon-phonon coupling (ph-ph coupling) with a timescale of 100 ps-ns. All these relaxation processes overlap in time, where the time scale is dependent on the intensity of the incoming light. The higher the intensity of the incoming light, the higher the temperature of the gold lattice and thus the temperature of the surrounding medium. By applying laser pulses temperatures of the surrounding medium can be reached that provoke the formation of vapour bubbles around the particle surface, which rapidly expand until cooling and finally collapse. This effect is termed as cavitation and finds application in tumour cell killing via membrane perforation.^[2, 71-73]

2.2.2 Surface functionalisation of AuNPs

Throughout the synthesis of AuNPs via gold salt reduction, citrate acts as both reducing and stabilising agent. The high sensitivity of the charge stabilisation based on citrate towards coagulation can easily be overcome by ligand exchange reaction with polymers, resulting in steric stabilisation (see **Section 2.1.2**). The adsorption of a polymer layer onto the gold surface lowers the free energy of the interface between the gold surface and the ambient environment. Here, the polymer bears an anchor group that features high affinity towards the surface and the chains assemble in a tight, well-defined manner owing to van der Waals interactions.^[74]

Adsorption of sulfur-compounds on gold surfaces (flat and curved) are by far the best examined, including thiols (RSH), thioethers (RSR) and disulfides (RSSR) as anchor groups (with R as an alkyl or aryl chain), featuring the highest affinity towards the gold surface, besides nitrogen or phosphorus bases.^[75]

The reason for this strong affinity and the corresponding details of the nature of the sulfur-gold interaction are still under current research and are partially controversially discussed, since they are examined by different communities using different techniques and investigating different focus areas. The next chapters aim for an overview of the current literature status. Therefore, firstly the well examined chemisorption of thiols onto gold will be pointed out, before describing the physisorption of thioethers and disulfides,^[76] both with regard to postulated bonding models. Afterwards practical studies comparing the strength of chemisorption to the one of physisorption and its influence on the colloidal stabilisation behaviour will be focussed.

2.2.2.1 Sulfur-gold bonding models-current status

Gold is a noble metal and as such resistant to corrosion and oxidation. This noble character of the gold surface arises due to the electronic configuration of Au ($d^{10} s^1$), where the d orbitals are fully occupied and hence relatively unreactive. The interaction with other atoms arises either from a pair of d electrons or the single s electron, as depicted in **Figure 9**.

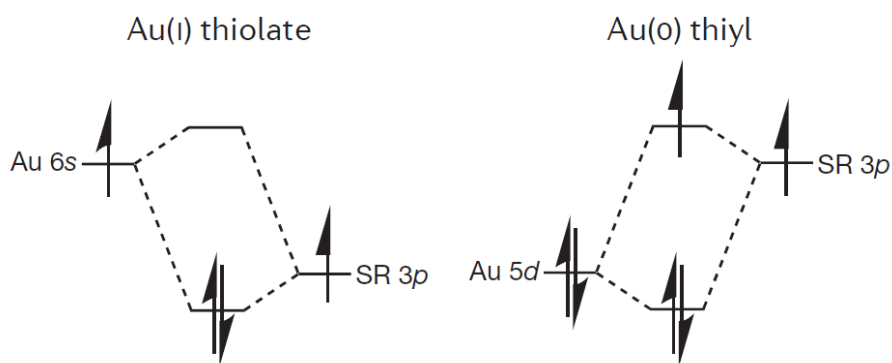


Figure 9: Formation of an Au(I)-thiolate species when Au contributes its s electron, whereas the Au(0)-thiol species results when Au interacts with a pair of d electrons. Reprinted with permission of reference^[77]. Copyright (2017) Nature Publishing Group.

In case of chemisorption the interaction is considered to have ionic character and to base on the p electron of sulfur with an Au s electron, resulting in an Au(I)-thiolate species (**Figure 9**). In fact, the existence of -RS-Au(I)-SR- complexes as polymeric building blocks was verified by total structure determination via single crystal X-ray crystallography of extremely small monodisperse thiolate AuNPs (< 2 nm), termed as nanoclusters (**Figure 10**).^[78] It has explicitly to be mentioned that the chemical and physical properties of nanoclusters differ from those of larger AuNPs, for instance displaying a distinct atomic packing symmetry and lacking the SPR (collective electron excitation), but rather feature discrete single electron transitions (see **Section 2.2.1**).^[79]

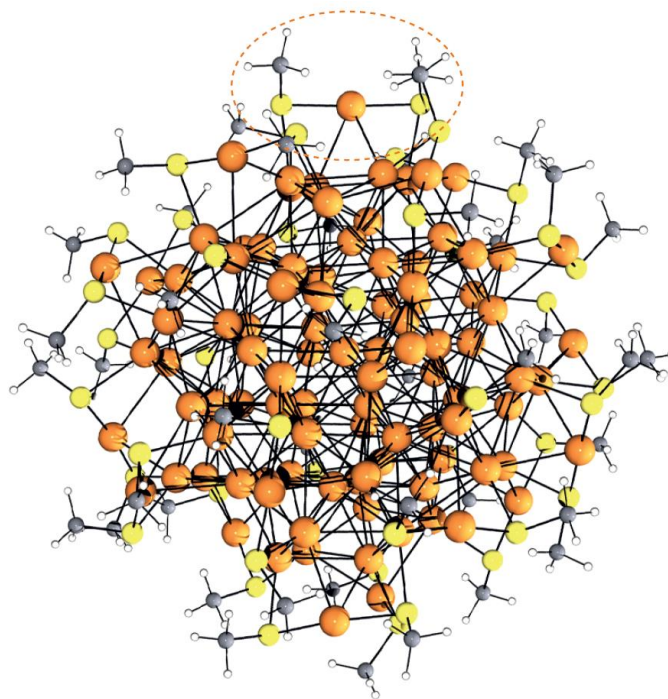


Figure 10: Total structure determination of the nanocluster $Au_{102}(SR)_{44}$ coated with 4-mercaptobenzoic acid, which is replaced with CH_3SH for clarity, featuring 19 $RS-Au-SR$ units (encircled in orange) and two $RS-Au-(RS)-Au-SR$ units. Au atoms are marked orange, sulfur atoms yellow, carbon atoms grey and hydrogen atoms white. Reprinted with permission of reference^[77]. Copyright (2017) Nature Publishing Group.

Within these $-RS-Au(I)-SR-$ units the central Au(I) atom, termed as adatom, is extracted from the gold surface and linearly coordinated by surface-parallel bonds between two thiolates. The sulfur atoms additionally bridge two subjacent Au(0) atoms of the first surface layer (see orange circle in **Figure 10** and **Figure 11A**). The complexation of sulfur with Au atoms of different chemical states Au(0) and Au(I), as well as the bonding to the R-group and the lone-pair orbital create a chiral centre at the sulfur atom, resulting in two positions of the R-group, *cis* and *trans*. The low activation barrier enables facile *cis-trans* isomerisation.^[12, 80]

The finding that the thiolate-gold interaction (40-50 kcal/mol) has a strength comparable to that of the gold-gold bond and consequently is strong enough to extract gold adatoms from the surface was further verified by density functional theory (DFT) computations, photoemission core-level spectroscopy and scanning tunnelling microscopy (STM) and multiple surface-sensitive X-ray spectroscopic techniques. Although most literature^[12, 81] explicitly refers to thiolates from thiols (RSH), thioethers (RSR) and disulfides (RSSR), a chemically correct thiolate can merely be formed by deprotonation of a thiol. By ignoring the chemical difference between the sulfur anchor groups these studies fail to describe the physisorption of thioethers or disulfides, exhibiting a closed-shell configuration.

Consequently, a different model was postulated by Reimers *et al.*, namely the Au(0)-thiyl bonding description, which includes Au(0) and thiyl radicals RS·, featuring different chemical and spectroscopic properties than the Au(I)-thiolate species, as verified by X-ray photoelectron (XPS) and absorption spectroscopy. Here, the p electron of sulfur and two d electrons of Au contribute to the bonding, described as being non-bonding (**Figure 9**). The difference between these two species is the formation of Au–Au s-s bonds (aurophilic effect, **Figure 11B**), which reduce the covalent contributions to Au-S bonds, concluding that the Au(0)-thiyl character is mainly based on strong van der Waals interactions on the order of 23 kcal mol⁻¹ (regarding a net binding energy on surfaces of about 30 kcal mol⁻¹). Turning van der Waals interactions into the critical forces for both physisorption and chemisorption. This allows for a consistent treatment of physisorption (thioethers and disulfides) and chemisorption (thiols) of sulfur compounds to gold.^[77, 82]

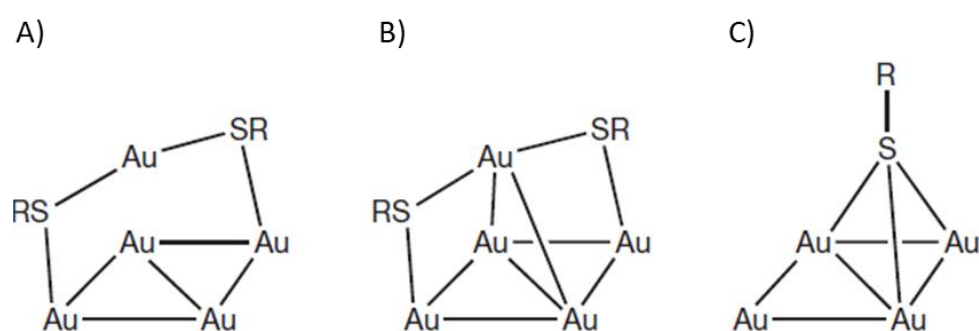


Figure 11: Representation of the 'staple' motifs involving A) RS bonding to Au(I) adatoms (top) and Au(0) (bottom) according to the Au(I)-thiolate species and B) additional Au-Au bonds, which result in the formation of the Au(0)-thiyl species. C) Bonding of RS to Au(0) without adatom extraction. Reprinted with permission of reference^[77]. Copyright (2017) Nature Publishing Group.

Generally, in case of the weaker physisorption the sulfur group binds directly to the gold surface without extracting gold adatoms (**Figure 11C**). For bidentate ligands, however, the physisorption strength corresponds to the one of thiols, thus strong enough to extract adatoms from the surface. Interestingly, for the chemisorption of the four isomers of butanethiol it was found that steric interactions of the R-group decide on the formation of adatoms. Thus, the bulky *tert*-butanethiol binds directly to the gold surface according to **Figure 11C**, since there is no space for the adatom binding mode.^[83-84] **Figure 12** shows that directly bound and adatom motifs can coexist in the same chemisorbed layer of racemic 2-butanethiol on gold. Amplifying that there is no clear separation between the physisorption of thioethers or disulfides and the chemisorption of thiols, instead the whole molecular

composition has to be taken into account in order to make assumptions about the sulfur-gold bond strength.

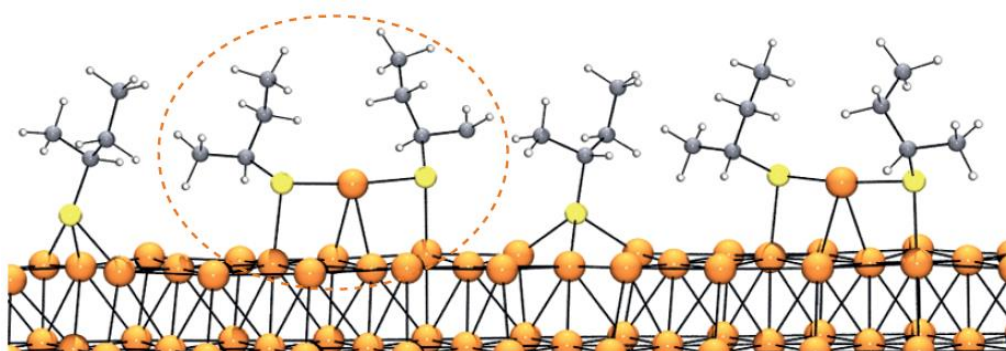


Figure 12: Chemisorbed layer of a racemic mixture of 2-butanethiol on gold, displaying both adatom binding motifs (encircled in orange) and directly bound SR-Au motifs, determined by the available space for the arrangement. Reprinted with permission of reference^[77]. Copyright (2017) Nature Publishing Group.

The complexity of the sulfur-gold interaction is further amplified by the flexibility of the interface, including migration and desorption/readsorption processes.^[80]

2.2.2.2 Experimental studies on the sulfur-gold bond strength for thioethers and thiols

In accordance with results of the postulated bonding models in **Section 2.2.2.1**, a difference between the thioether-gold (physisorption) and thiol-gold (chemisorption) bond strength in experimental studies cannot be generalised. Although most literature refers to a weaker thioether-gold bonding compared to the thiol analogue,^[3] a detailed investigation of these studies as described within this section challenges this assertion. Throughout this chapter firstly the bonding strength of thiol- and thioether-compounds on flat gold surfaces is described, before comparing their efficacy to stabilise AuNPs.

As already mentioned the vast majority of studies within literature claim a weaker thioether-gold bond on surfaces compared to the thiol analogue. In general, a weaker binding of thioether-ligands is attributed to less ordered and thinner films on flat gold surfaces, accompanied with a poor reproducibility, compared to thiol-layers, as determined by ellipsometry, wettability studies, IR spectroscopy, STM and XPS.^[16, 20, 85-86]

Whitesides *et al.*, however, showed that dependent on the analytical technique and molecular composition thioether-ligand layers feature the same characteristics as thiols. For instance, the thickness of symmetric thioether-layers was in the same order as that of the respective thiols, whereas the introduction of a carboxylic moiety provoked thinner films of thioether-ligands.^[19-20] Moreover, for pure thiol-ligands of different chain length it was found that

shorter chains promote less ordered films, additionally emphasising the consideration of the whole molecular composition and precluding the anchor group as only crucial factor to decide on ligand layer characteristics.^[87]

Interestingly, for compounds with multiple anchor groups Reinhoudt *et al.* concluded a more efficient binding of thioether moieties onto gold compared to thiols. Their XPS investigations verified that β -cyclodextrin-layers use on average 4.5 of 7 thioether anchor groups, whereas only 3.5 of 7 thiols attach. Here, it has explicitly to be mentioned that for thioether compounds temperatures around 60 °C were applied in order to obtain highly ordered ligand layers, while for thiols room temperature was sufficient.^[88]

A slower adsorption kinetics of thioether-layers onto flat gold surfaces was consistently found in literature, where thioether compounds after 10 min reach merely 60 % of the surface coverage achieved by corresponding thiols, as confirmed by atomic force microscopy (AFM) and XPS.^[20, 86]

In 2001 Reinhoudt *et al.* used thioether compounds for the first time as AuNP stabiliser.^[21] In accordance to following studies the AuNPs were synthesised via the direct two-phase process according to Brust *et al.*^[89] Within these studies a lower colloidal stability of thioether compounds related to thiols was identified by larger sizes and polydispersity of the *in situ* formed AuNPs, since weak stabiliser provoke a slow passivation of colloids with long nucleation times.^[17]

However, it has to be emphasised that the passivation of *in situ* formed colloids is mainly dominated by the adsorption kinetics and thus appears not as good measure for the thermodynamic bond strength. Based on the fact that thioether compounds feature a significantly slower adsorption kinetics than thiols, conclusions about a generally lower colloidal stabilisation efficacy in case of thioethers are distorted.^[20, 86]

Indeed, corresponding to studies on flat surfaces from Whitesides *et al.*,^[19-20] investigations on thioether compounds with different numbers of anchor groups and functionalities revealed that depending on the functionality, thioethers were just as stable as their thiol analogues.^[21-23] Furthermore, the study from Brust *et al.* extensively demonstrated the impact of the molecular composition of thioether compounds and thiol analogues on the colloidal stability against ionic strength and elevated pH. The group observed that thioethers with longer alkyl

2 Background

end groups and consequently increased hydrophobicity were more efficient than the ones with shorter chains, achieving the same stabilisation efficacy as the respective thiols. **Figure 13** emphasises this high dependency of the AuNP stability on the thioether end group of poly(methacrylic acid) (PMAA) ligands, displaying aggregation of particles coated with dodecanethioether-(DDT)-PMAA (12 carbon atoms) after treatment with 0.8 M NaCl, indicated by the blue colour of the solution. On the other hand particles coated with octadecanethioether-(ODT)-PMAA (18 carbon atoms) remained their stability up to 1.5 M NaCl.^[18] Hence, ODT-PMAA coated particles exhibit colloidal stabilities against ionic strength comparable to that of the corresponding thiol analogue (nonadecanethiol(NDT)-PMAA, 19 carbon atoms). Once more impeding a generalisation of the thioether-gold or thiol-gold bond, rendering the importance to the detailed molecular structure of the anchor group.

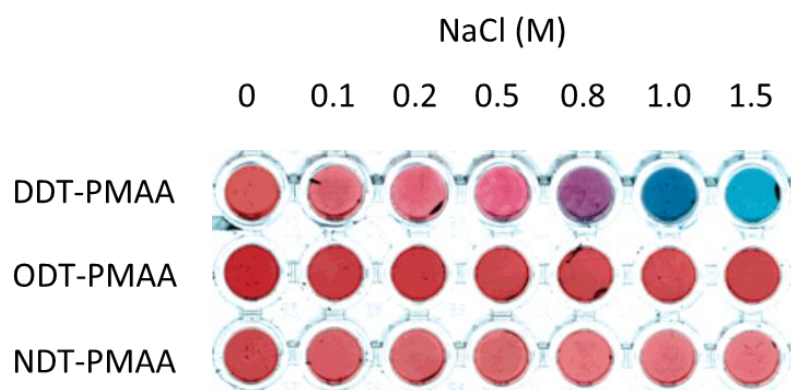


Figure 13: Images of AuNPs coated with two thioether-PMAA bearing different anchor group chain lengths, namely DDT-PMAA (chain with 12 carbons) and ODT-PMAA (chain with 18 carbons) after respective NaCl treatment. Reprinted with permission of reference^[18]. Copyright (2007) American Chemical Society.

The advantage of multivalent thioether ligands, accordingly to studies on flat gold surfaces, was consistently found to improve AuNP stability^[21, 90] pioneering the manifold application of multivalent thioether polymers^[15, 91-92] and dendrimers^[24, 93-95] as AuNP stabiliser.

2.3 Polymers as AuNP stabiliser

A plethora of water-soluble polymers has been used as effective AuNP stabiliser, which can be categorised into two classes: biopolymers, such as polypeptides, nucleic acids and polysaccharides (*e.g.* dextran, chitosan), as well as artificial polymers including poly(vinyl alcohol), poly(ethyleneimine), poly(acrylic acid) and poly(ethylene glycol) (PEG). Latter counts as one of the most commonly applied artificial polymers for AuNP stabilisation and is described in the next chapter in more detail.^[32, 96]

2.3.1 Bifunctional poly(ethylene glycol) (PEG)

PEG is widely synthesised via an anionic ring opening polymerisation of ethylene oxide in polar, aprotic solvents in the presence of nucleophilic alkaline catalysts, first and foremost alkoxides with alkali metal counterions (**Figure 14**). The polymerisation of epoxides is a living process, providing a Poisson distribution of the molecular weight, as well as a straightforward and quantitative functionalisation of the active chain ends.^[97-98] Generally a PEG chain features two functionalisation possibilities, one at the α -position, which can be introduced via a functional initiator containing *e.g.* alkene, alkyne, amine, carboxyl and thiol moieties. During polymerisation most of these functional groups are masked with a cleavable protection group in order to prevent nucleophilic side reactions. The other functionality is located at the chain end and can be inserted by a functional terminating agent. Moreover, the post-polymerisation modification of the hydroxyl moieties of PEG is well established, but is unsuitable for heterofunctional PEGs.^[99-100]

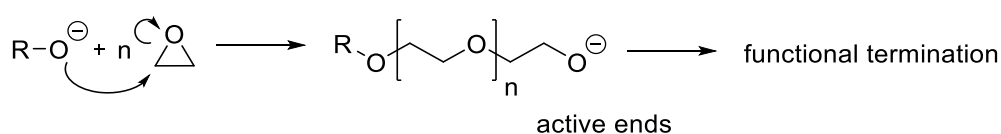


Figure 14: Ring opening polymerisation of ethylene oxide with alkoxides featuring active chain ends owing to a living process.

Thiol-PEG is the most applied polymer for AuNP stabilisation. Besides its high colloidal stabilisation efficacy (see **Section 2.1.2.2**), PEG suppresses non-specific interactions *in vivo*, such as those with blood components owing to its non-ionic character and hydrophilicity. This prolongs the circulation time of AuNPs in the body and thus the time before the particles are recognised as foreign and cleared from the body, known as stealth effect. The study of Gref *et al.* in 1994 provided the basis for the success of PEGylated nanoparticles, where it was

2 Background

shown that less than 30 % of PEGylated (20 kDa) particles were cleared by the liver after 2 h of incubation time, whereas 66 % of uncoated particles were removed after 5 min.^[11, 101]

Therefore, the majority of AuNPs used for drug delivery are coated with a PEG layer in order to increase the probability that drugs or biological payload, such as proteins and antibodies conjugated to the PEG shell reach their target location.^[102] In case of a charged PEG layer biological compounds, first and foremost oligonucleotides, can be complexed to the AuNP surface. Typical examples include the complexation of DNA^[103] and siRNA^[104-105] to amine-PEGylated particles. Furthermore, drugs or biological payload can be covalently coupled to the surface via the terminal functional group at the PEG chain, including hydroxyl,^[4] azide,^[106] maleimide,^[107] carboxyl^[108] and photo-cleavable *o*-nitrobenzyl moieties.^[109]

Yet, the lacking functionalisability along the inert polyether backbone remains a crucial drawback of PEG, limiting the possibility and tunability of biological modifications.

2.3.2 Multifunctional poly(glycidyl ether)

By polymerisation of functional derivatives of ethylene oxide, so called glycidyl ethers, structural analogues of PEG can be synthesised, bearing multiple functional side chains along the linear backbone.

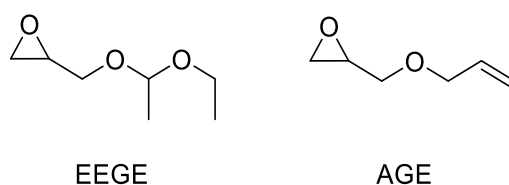


Figure 15: Structural formula of the glycidyl ethers ethoxyethyl glycidyl ether (EEGE) and allyl glycidyl ether (AGE).

Dworak *et al.* described the anionic polymerisation of ethoxyethyl glycidyl ether (EEGE) (see **Figure 15**) with alkali metal based initiators, which can likewise to the PEG polymerisation be considered as living. Successive acidic cleavage of the acetal protection group leads to the formation of hydrophilic and biocompatible linear poly(glycidol) (PG).^[110]

In case of two different glycidyl ethers the structure of the polymer can be adjusted by the manner of copolymerisation, where the functional groups are either statistically distributed along the backbone (random copolymer) or arranged in two consistent blocks (block-copolymer). The random copolymerisation of allyl glycidyl ether (AGE) (see **Figure 15**) with EEGE yields P(AGE-*co*-EEGE).^[111] Successive acidic deprotection leads to the formation of

P(AGE-co-G), featuring hydroxyl and alkene groups as side functions.^[112] While the hydroxyl groups can be further functionalised via Steglich esterification,^[113] in case of alkene groups a large variety of functionalities can be introduced by thiol-ene reaction.^[114]

The free radical addition of thiols onto double bonds triggered by photo-initiators gives rise to stable thioether bonds. Moreover, the reaction exhibits very high yields (> 95 %), high regioselectivity (anti-Markovnikov), orthogonality with other reaction conditions concomitant with a high tolerance towards multiple functionalities, mild aqueous reaction conditions and accessibility to a wide variety of readily available starting compounds. Hence, besides the Huisgen 1,3-dipolar cycloaddition of azides and alkynes^[115-116] the thiol-ene reaction belongs to the most popular click reactions in bio- and polymer chemistry, even if excessive amounts of mercaptan compounds are needed to prevent crosslinking.^[117-119]

Several studies verify the biocompatibility of thiol-ene functionalised AGE-copolymers^[120] and pure PG. For PG additionally a stealth effect was determined, found to be comparable or superior to the one of PEG.^[121-123] Pioneering the way of PG as hydrophilic shell for nanogels^[13, 113] and AuNPs^[15] in drug delivery.^[124]

3 Results and Discussion

Parts of this chapter have previously been published and adapted with permission from:

S. Feineis, J. Lutz, L. Hefele, K. Albrecht, E. Endl, J. Groll, Thioether–Polyglycidol as Multivalent and Multifunctional Coating System for Gold Nanoparticles, *Adv. Mater.* **2018**, 1704972.

Copyright © 2018 WILEY-VCH Verlag GmbH & Co. KGaA, Weinheim.

B. Baumann, T. Jungst, S. Stichler, S. Feineis, O. Wiltschka, M. Kuhlmann, M. Lindén, J. Groll, Control of Nanoparticle Release Kinetics from 3D Printed Hydrogel Scaffolds, *Angew. Chem. Int. Ed.* **2017**, 56, 4623-4628.

Copyright © 2017 The Authors. Published by Wiley-VCH Verlag GmbH & Co. KGaA, Weinheim.

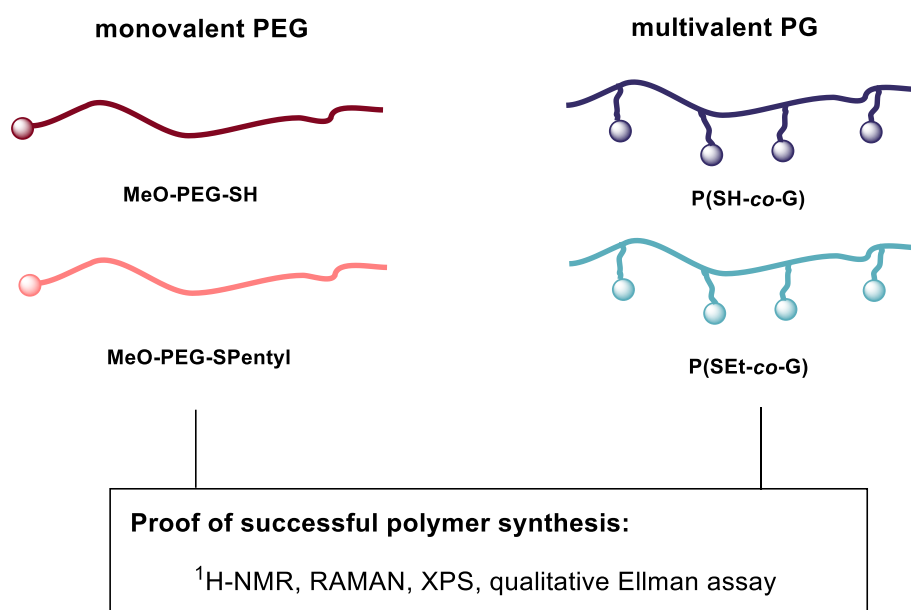
3.1 Colloidal stabilisation efficacy of thiol- and thioether-polymers

In order to systematically investigate the efficacy of thioether-polymers to stabilise AuNPs, two distinct kinds of polymers, based on PEG (6000 Da) and PG (5500 Da) were synthesised. The corresponding thiol-functionalised polymers were used as reference. Linear PEG featured a terminal thioether/thiol moiety, whereas PG carried multiple anchor groups along the polymer backbone. Thiol and thioether functionalities were introduced via a thiol-ene click reaction, where allyl groups react with thiol groups of a mercaptan compound upon UV-light irradiation in the presence of a radical initiator. Throughout this chapter the synthesis of aforementioned polymers was analysed by $^1\text{H-NMR}$, RAMAN and XP spectroscopy (XPS), as well as via reaction with Ellman's reagent. The successive binding of thioether/thiol polymers to varyingly large nanoparticle surfaces was verified by UV-vis absorbance, Dynamic Light Scattering (DLS) and FT-IR spectroscopy. The polymer coverage on AuNPs was determined by Thermogravimetric Analysis (TGA) and XPS measurements. Finally, for investigating the strength of the thioether/thiol-gold linkage, the colloidal stability towards conditions that provoke aggregation, such as centrifugation, high temperatures, pH values, ionic strength and lyophilisation was systematically investigated by UV-vis absorbance spectroscopy.

3.1.1 Synthesis of thiol- and thioether-polymers

In this chapter firstly the synthesis and characterisation of monovalent thiol- and thioether-PEG (marked in dark and light red) is described, followed by the PG analogues (marked in dark and light blue), as depicted in **Scheme 1**.

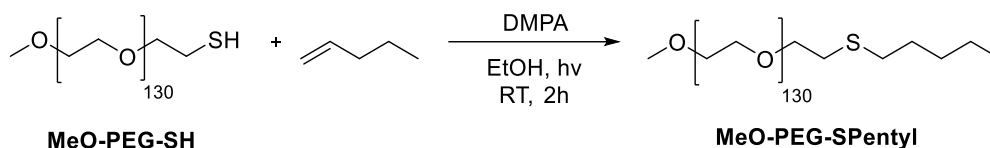
Synthesis of thiol- and thioether-functional polymers:



Scheme 1: Graphical depiction of monovalent and multivalent polymers synthesised and characterised throughout this chapter.

3.1.1.1 Monovalent PEG

Monovalent thiol-PEG, termed as MeO-PEG-SH, was purchased. The characterisation was carried out by direct comparison to its thioether analogue, termed as MeO-PEG-SPentyl. Latter was synthesised via a thiol-ene click reaction^[125] of MeO-PEG-SH and 1-pentene, the shortest non-gaseous alkene chain.



Scheme 2: Synthesis of MeO-PEG-SPentyl via thiol-ene click reaction of MeO-PEG-SH with 4 eq. 1-pentene.

Briefly, 1-pentene was added in 4-fold excess to MeO-PEG-SH in EtOH. After the addition of 2 eq. DMPA as photo-initiator, the solution was irradiated at 365 nm for 2 h at room temperature (RT) (see **Scheme 2**). Subsequently, purification by dialysis was performed and MeO-PEG-SPentyl was obtained as a white solid. Throughout this chapter MeO-PEG-SH was marked in dark red and MeO-PEG-SPentyl in light red.

Figure 16 displays the ¹H-NMR spectra of MeO-PEG-SH (top) and MeO-PEG-SPentyl (bottom). The proton signals at 2.98-2.62 ppm (**5,6**), 1.88-1.20 ppm (**7-9**) and 0.93 ppm (**10**), ascribed to the pentyl chain verified successful synthesis of MeO-PEG-SPentyl. Integration of these ¹H-NMR signals concluded 100 % conversion of thiol to thioether groups.

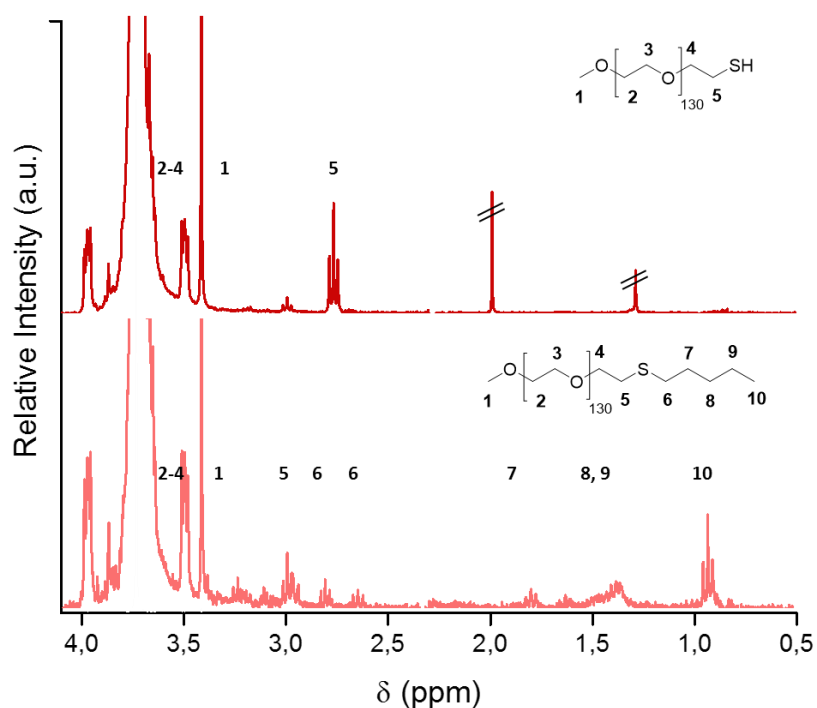


Figure 16: $^1\text{H-NMR}$ spectra of MeO-PEG-SH (top, dark red) and MeO-PEG-SPentyl (bottom, light red), displaying additional proton signals at 2.98-2.62 ppm (5,6), 1.88-1.20 ppm (7-9) and 0.93 ppm (10), ascribed to the pentyl chain of the thioether.

Elemental analysis of MeO-PEG-SH/-SPentyl based on XPS coincided with theoretic values determined by ChemDraw, furthermore confirming successful synthesis. Since a detection of hydrogen is not feasible via XPS, merely the carbon amount is displayed in **Table 1**, whereas theoretic values considered carbon and hydrogen percentages. It was shown that MeO-PEG-SPentyl (66 %) displayed higher mass percentages (mass-%) of carbon than the thiol polymer (63 %), owing to the alkyl chain.

Table 1: Elemental analysis of MeO-PEG-SH/-SPentyl based on XPS in comparison to theoretically expected values.

Mass-%	O	C / C+H	S
<i>MeO-PEG-SH</i> _{theoretic}	36	63	1
<i>MeO-PEG-SH</i> _{XPS}	36	63	1
<i>MeO-PEG-SPentyl</i> _{theoretic}	34	65	1
<i>MeO-PEG-SPentyl</i> _{XPS}	33	66	1

In order to prove the presence or absence of thiol groups within thiol- and thioether-PEG, RAMAN spectroscopy was conducted. The spectra in **Figure 17a**, however, show that a detection of thiol groups around 2550 cm^{-1} and thioether moieties at 650 cm^{-1} (marked yellow) within MeO-PEG-SH and MeO-PEG-SPentyl respectively was challenging, due to the scarce signal intensity of those groups. This was ascribed to the low relative frequency of the thiol or thioether moiety within the high molecular weight polymer. Therefore, qualitative UV-vis absorbance measurements upon reaction of MeO-PEG-SH/-SPentyl with Ellman`s reagent were conducted in order to clearly verify the presence and absence of thiol groups. Here, thiol groups react with DTNB and the resulting chromogenic side product TNB can be detected via UV-vis absorbance spectroscopy at 412 nm . The optical density of a $40\text{ }\mu\text{M}$ MeO-PEG-SH solution was 0.25 a.u. , resulting in a yellow discoloration. Whereas MeO-PEG-SPentyl remained colourless, verifying negligible amounts of thiol groups for the following investigations (see **Figure 17b**).

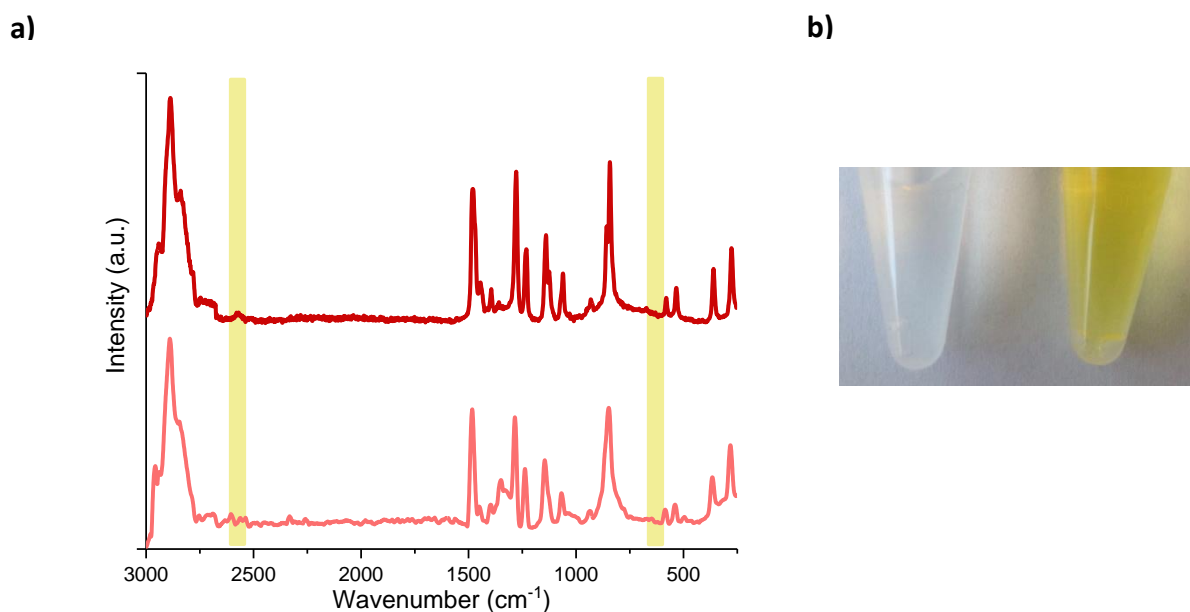
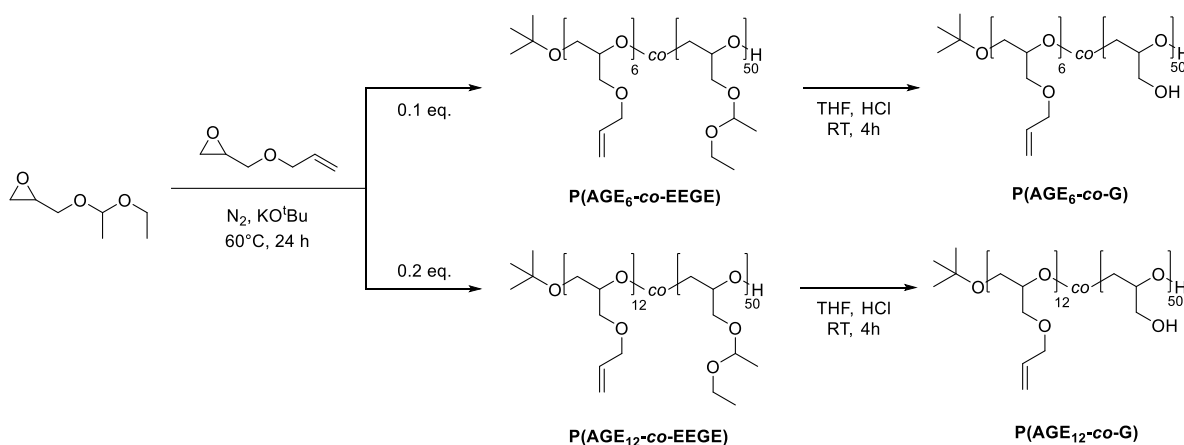


Figure 17: a) RAMAN-spectra of MeO-PEG-SH (dark red, top) and MeO-PEG-SPentyl (light red, bottom) displaying a scarce signal intensity of the thiol- and thioether vibration around 2550 cm^{-1} and 650 cm^{-1} , respectively (marked in yellow). b) Verification of the absence and presence of thiols within MeO-PEG-SPentyl (left) and MeO-PEG-SH (right) by reaction with Ellman`s reagent.

3.1.1.2 Multivalent poly(glycidol) (PG)

Multivalent polymers, bearing various statistically distributed thiol/thioether moieties along the polymer backbone, were synthesised based on allyl-modified PG, termed as P(AGE-co-G).^[111] The allyl groups enabled a thiol/thioether functionalisation via thiol-ene click reaction.^[111-112, 125] Throughout this chapter firstly the polymerisation procedure, and afterwards the modification of P(AGE-co-G) with thiol and thioether moieties was described.

P(AGE-co-G) was obtained via copolymerisation of ethoxy ethyl glyciyl ether (EEGE)^[126] and allyl glyciyl ether (AGE) based on procedures described before.^[127] EEGE was applied as acetal-protected version of glycidol, in order to receive linear polymers. AGE was commercially purchased. Both monomers were dried over CaH₂ for 12 h and fractionally distilled under Ar atmosphere.

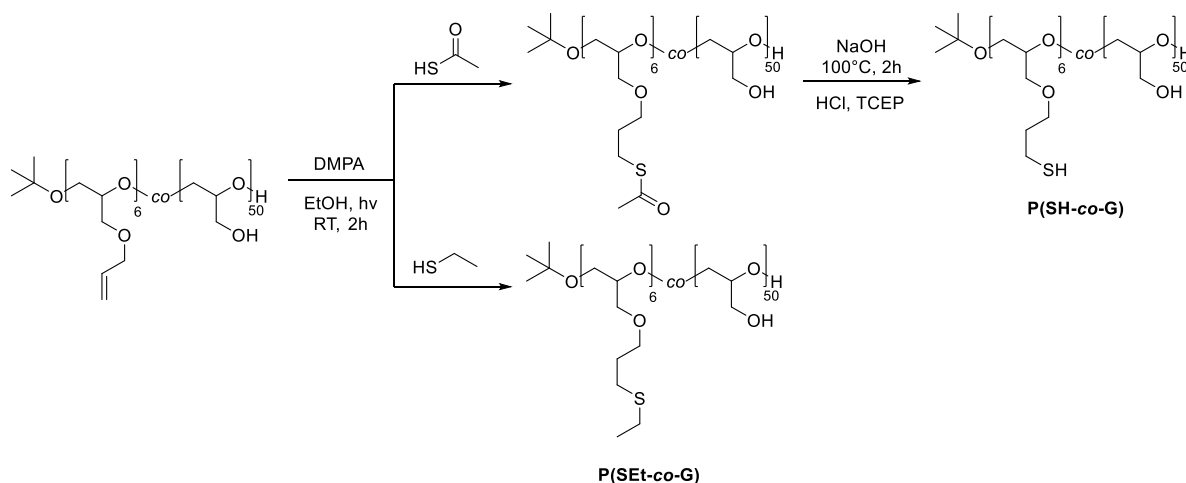


Scheme 3: Synthesis of P(AGE₆-co-EEGE) and P(AGE₁₂-co-EEGE) via copolymerisation of EEGE and AGE in different ratios and successive acidic treatment, yielding P(AGE₆-co-G) and P(AGE₁₂-co-G).

Throughout this thesis two allyl-functionalised PGs were synthesised by varying the EEGE to AGE ratio, termed as P(AGE₆-co-EEGE) and P(AGE₁₂-co-EEGE). Briefly, to EEGE 0.1 eq. or 0.2 eq. AGE were added under N₂ atmosphere. The polymerisations were initiated with KO^tBu and run at 60 °C for 24 h, as shown in **Scheme 3**. By adding EtOH, the polymerisations were stopped and P(AGE₆-co-EEGE) or P(AGE₁₂-co-EEGE) was obtained as a yellow oil. ¹H-NMR spectroscopy and Size Exclusion Chromatography (SEC) verified successful synthesis (see **Section 5.2.2**).

After polymerisation the acetal protection group within EEGE was removed to obtain P(AGE₆-co-G) and P(AGE₁₂-co-G). Therefore, P(AGE₆-co-EEGE) or P(AGE₁₂-co-EEGE) was treated with 37 % HCl for 4 h, as depicted in **Scheme 4**. After neutralisation the polymers were purified by dialysis and received as yellowish oils. Successful synthesis of P(AGE₆-co-G) and P(AGE₁₂-co-G) was confirmed by ¹H-NMR, FT-IR and RAMAN spectroscopy, as well as by SEC (see **Section 5.2.3**).

In order to functionalise PG with thiol and thioether groups, a thiol-ene click reaction of P(AGE₆-co-G) with 7 eq. thioacetic acid and 23 eq. EtSH was performed, yielding P(SH-co-G) and P(SEt-co-G), respectively. The eq. were referenced to the allyl groups within P(AGE₆-co-G). The high excess of EtSH was required due to the volatility of the mercaptan compound.^[128] The UV light triggered reaction and successive purification was performed as described for MeO-PEG-SPentyl. After the reaction of P(AGE₆-co-G) with thioacetic acid, an alkaline deprotection of the thioester and successive reduction with TCEP (16 eq.) was conducted to obtain free thiol groups, as displayed in **Scheme 4**. Throughout this chapter P(SH-co-G) was marked in dark blue and P(SEt-co-G) in light blue.



Scheme 4: Synthesis of P(SH-co-G) and P(SEt-co-G) via thiol-ene click reaction and successive alkaline treatment for the first mentioned.

Synthesis of P(SH-co-G) and P(SEt-co-G) was verified by $^1\text{H-NMR}$ investigations. The spectra of P(SH-co-G) and P(SEt-co-G) in **Figure 18** displayed signals at 2.68-2.64 ppm (**10**) and 1.95-1.90 ppm (**9**), assigned to the methylene protons of the side chain, whereas P(SEt-co-G) featured additional signals at 2.77-2.50 ppm (**11**) and 1.26 ppm (**12**), owing to the ethyl chain of the thioether. $^1\text{H-NMR}$ investigations further determined 5-6 thioether/thiol groups per polymer.

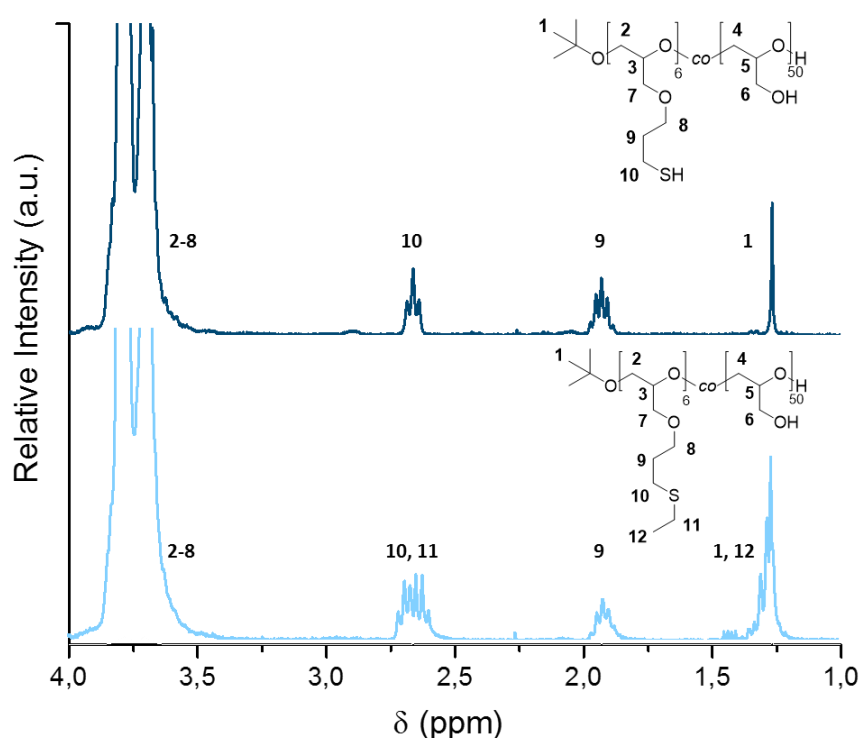


Figure 18: $^1\text{H-NMR}$ spectra of P(SH-co-G) (top, dark blue) and P(SEt-co-G) (bottom, light blue), featuring additional proton signals at 2.77-2.50 ppm (**11**) and 1.26 ppm (**12**), owing to the ethyl chain of the thioether.

Elemental analysis of P(SH-co-G) and P(SEt-co-G) via XPS in **Table 2** confirmed higher carbon percentages in case of P(SEt-co-G), due to the ethyl chain of the thioether. In general, higher deviations from the theoretic values determined by ChemDraw than for MeO-PEG-SH/-SPentyl were ascribed to a broader molecular weight distribution of the initial polymer P(AGE₆-co-G), attributed to the copolymerisation process.

Table 2: Elemental analysis of P(SH-co-G) and P(SEt-co-G) based on XPS in comparison to theoretically expected values.

Mass-%	O	C / C+H	S
$P(\text{SH-co-G})_{\text{theoretic}}$	38	57	4
$P(\text{SH-co-G})_{\text{XPS}}$	32	62	6
$P(\text{SEt-co-G})_{\text{theoretic}}$	37	59	4
$P(\text{SEt-co-G})_{\text{XPS}}$	30	65	5

Due to a higher amount of thiol/thioether groups in case of multivalent PG a determination of these groups via RAMAN spectroscopy was possible, as displayed in **Figure 19a**. The spectra of P(SH-co-G) showed vibrations at 2570 cm^{-1} (marked yellow), which could clearly be attributed to the S-H stretch. Lacking signals around $550\text{-}450 \text{ cm}^{-1}$ on the other hand excluded the oxidative formation of disulfides. The spectra of P(SEt-co-G) featured the C-S stretch of thioethers at 650 cm^{-1} (marked yellow). The presence and absence of thiol units within P(SH-co-G) and P(SEt-co-G) was further confirmed by qualitative UV-vis absorbance measurements based on Ellman's reagent. **Figure 19b** shows that the optical density of a $40 \mu\text{M}$ polymeric solution at 412 nm was 1.16 a.u. for P(SH-co-G) resulting in a yellow discoloration, whereas P(SEt-co-G) remained colourless. A correlation of the absorbance values between MeO-PEG-SH (0.25 a.u.) and P(SH-co-G) (1.16 a.u.) resulted in a ratio of 1:5 and furthermore confirmed the amount of thiol groups within the respective polymers.

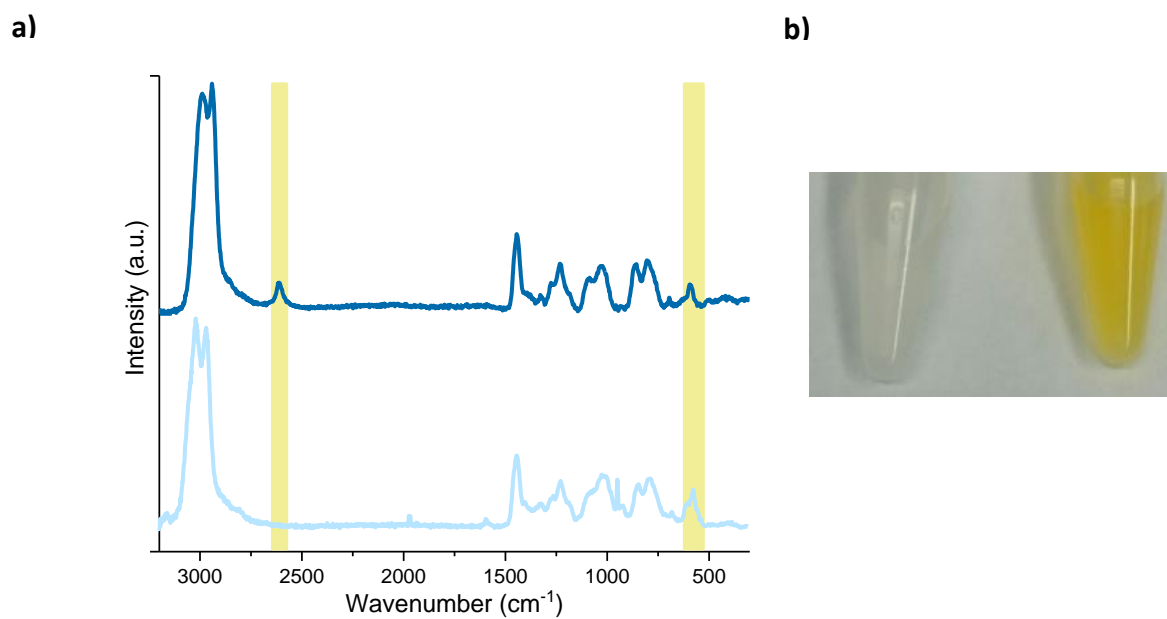
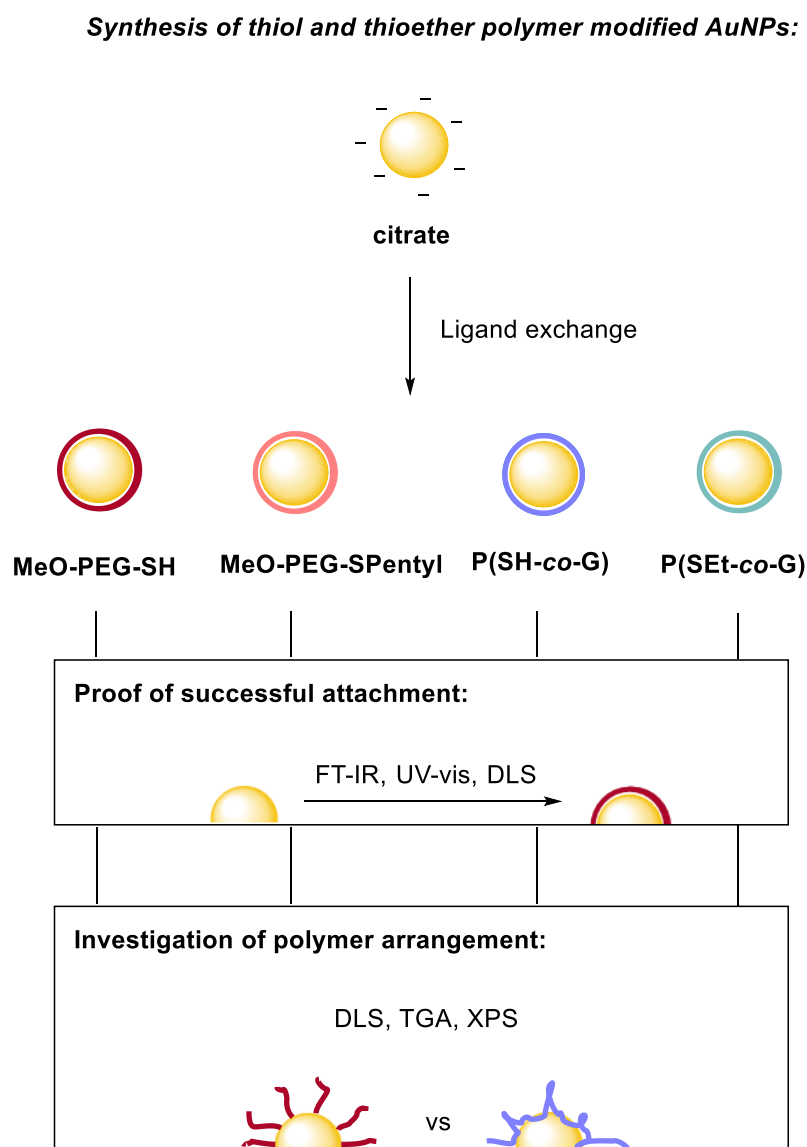


Figure 19: a) RAMAN-spectra of P(SH-co-G) (dark blue, top) and P(SET-co-G) (light blue, bottom), displaying the thiol- and thioether vibration at 2550 cm⁻¹ and 650 cm⁻¹, respectively (both marked yellow). b) Verification of the absence and presence of thiols within P(SET-co-G) (left) and P(SH-co-G) (right) by reaction with Ellman`s reagent.

3.1.2 Synthesis of AuNPs stabilised with thiol- and thioether-polymers

In order to attach thiol and thioether polymers of **Section 3.1.1** to AuNPs, a ligand exchange reaction on citrate stabilised particles was performed. Successful functionalisation of the particles was proven by FT-IR and UV-vis spectroscopy, as well as via DLS. Furthermore, detailed investigations of the arrangement of thiol and thioether polymers on the particle surface via TGA and XPS were performed. Throughout this chapter MeO-PEG-SH was marked in dark red, MeO-PEG-SPentyl in light red, P(SH-co-G) in dark blue and P(SEt-co-G) in light blue, as depicted in **Scheme 5**.



Scheme 5: Functionalisation of AuNPs with thiol and thioether polymers via ligand exchange reaction and the successive characterisation procedure performed throughout this chapter.

3.1.2.1 Citrate-AuNPs as basic particles

The applied citrate-stabilised AuNPs, termed as AuNP@citrate, were purchased. Due to the dependency of the colloidal stability on the curvature of particles,^[45] further investigations in this thesis were carried out with three different particle diameter (15 nm, 30 nm and 50 nm). SEM images of these AuNP@citrate displayed in **Figure 20**, in accordance with specifications of the producer, displayed particles with size deviations of less than 8 %, resulting in diameters with deviations of 15 ± 1.2 nm, 30 ± 2.5 nm and 50 ± 4.0 nm. Furthermore, SEM images revealed 5 % of particles with uneven shapes. In fact, it was found, consistently with literature that AuNP naturally are not perfectly spherical, since they display edges as highlighted in **Figure 20b+c**.

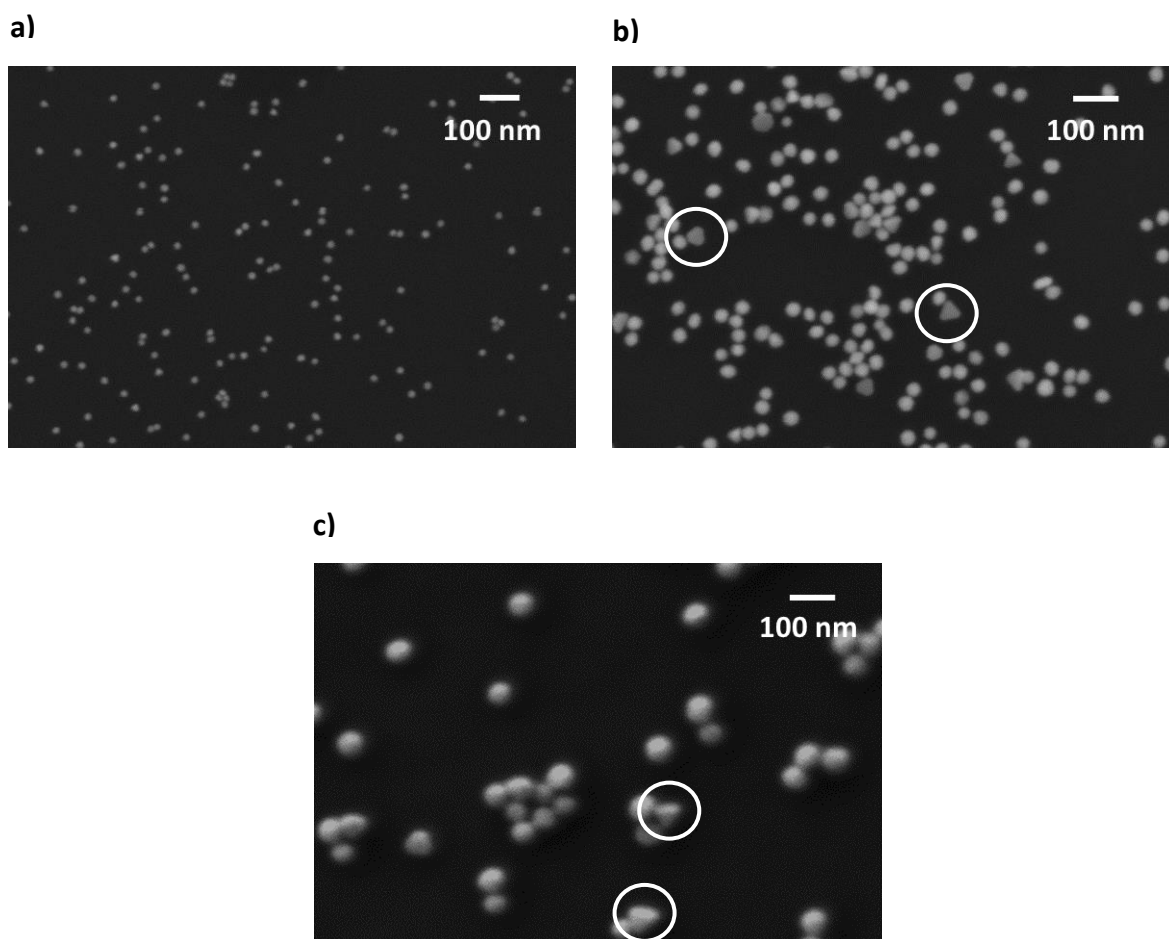


Figure 20: SEM images of a) 15 nm, b) 30 nm and c) 50 nm AuNP@citrate, which were applied throughout this thesis. The white circles highlight AuNPs which are not perfectly spherical.

The different particle sizes were also detectable by UV-vis absorbance spectroscopy, as depicted in **Figure 21**.^[129] An increase of the particle diameter from 15 nm to 30 nm and 50 nm caused a bathochromic surface plasmon resonance (SPR) shift of about 5 nm, resulting in maximal absorbance values of 520 nm, 525 nm and 530 nm, respectively.

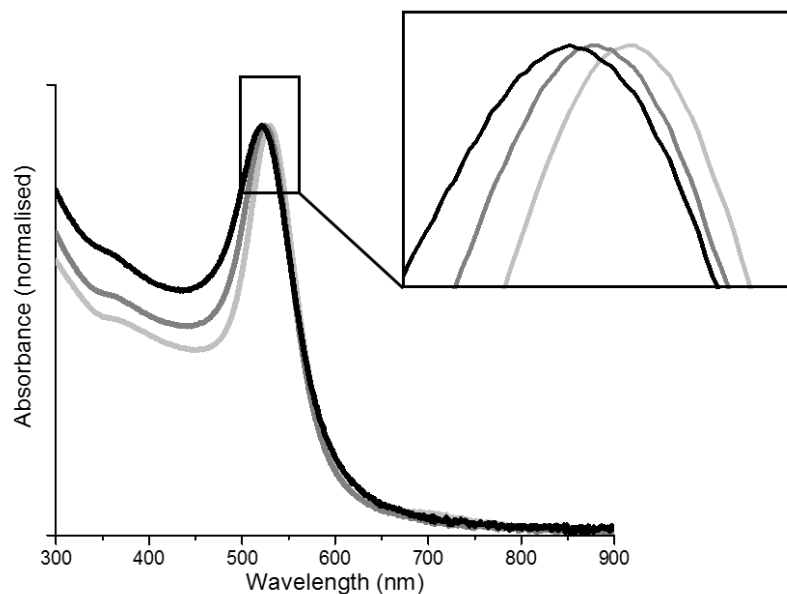


Figure 21: UV-vis absorbance spectra of 15 nm (black, left), 30 nm (dark grey, middle) and 50 nm (light grey, right) AuNP@citrate, displaying a size-dependent SPR red-shift from 520 nm to 525 nm and 530 nm.

The citrate modification of AuNP was verified by FT-IR spectroscopy, featuring the C=O stretch at 1580 cm^{-1} and 1390 cm^{-1} , ascribed to the carboxylate moiety. Thus, the spectra of AuNP@citrate conformed to the one of pure citrate, but additionally displayed the broad O-H stretch at 3420 cm^{-1} , since the particles were dispersed in water (see **Figure 22**).

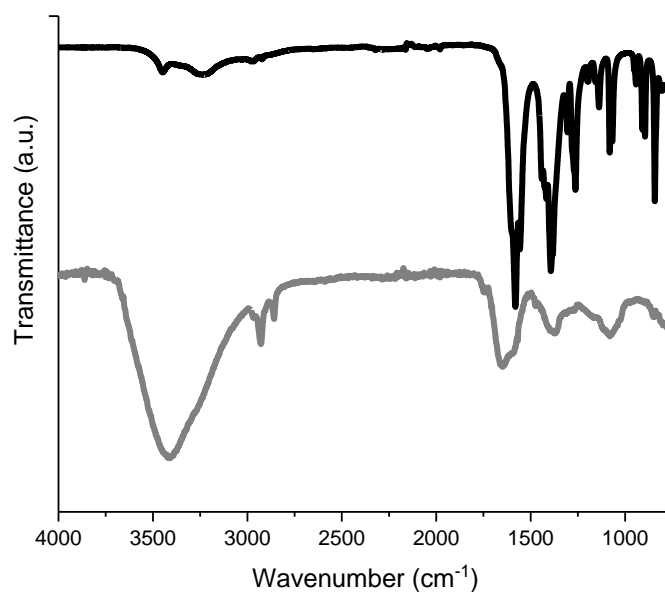


Figure 22: FT-IR spectra of 30 nm AuNP@citrate (grey, bottom), displaying vibrations of pure citrate (black, top) and an additional O-H stretch at 3420 cm⁻¹ owing to the dispersion in water.

The concentration of AuNP@citrate used for further polymer functionalisation was adjusted to $1.60 \cdot 10^{12}$ particles mL⁻¹ for 15 nm particles, $2.70 \cdot 10^{11}$ particles mL⁻¹ for 30 nm particles and $9.40 \cdot 10^{10}$ particles mL⁻¹ for 50 nm particles, as verified by UV-vis absorbance spectroscopy.

3.1.2.2 Attachment of thiol- and thioether-polymers to citrate-AuNPs

The attachment of aforementioned thiol/thioether polymers to the particle surface was carried out via ligand exchange reaction. Therefore, AuNP@citrate (15 nm, 30 nm and 50 nm) were incubated with 350 μM polymeric solution in water at room temperature for 12 h. Unbound polymer was removed by two successive centrifugation- and resuspension-cycles.

Successful binding of thiol/thioether polymers to AuNPs was proven by FT-IR spectroscopy, displaying spectra that correspond to the one of pure polymer, as exemplarily depicted for MeO-PEG-SH/AuNP@MeO-PEG-SH and P(SH-co-G)/AuNP@P(SH-co-G) in **Figure 23**. The spectra of PEG modified AuNPs showed the C-H₂ stretch and bend at 2880 cm^{-1} and 1341 cm^{-1} , as well as the C-O-C stretch at 1100 cm^{-1} , concurrent to the polymer vibrations. The spectrum of the particle suspension additionally displayed the broad O-H stretch at 3500 cm^{-1} of water. PG and the correspondingly coated particles featured vibrations at 3380 cm^{-1} , 2920 cm^{-1} , 2850 cm^{-1} and 1104 cm^{-1} , ascribed to the O-H, C-H and C-H₂ stretch, as well as to the C-O-C stretch.

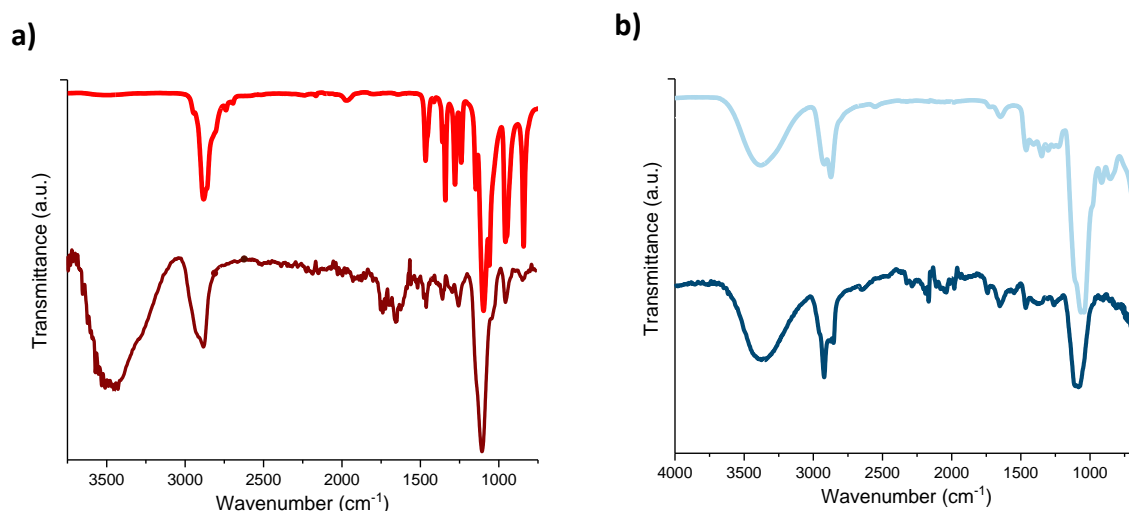


Figure 23: a) FT-IR spectra of MeO-PEG-SH (light red, top) and AuNP@MeO-PEG-SH (dark red, bottom), displaying coinciding signals at 2880 cm^{-1} and 1100 cm^{-1} , ascribed to the methylene and ether vibration. AuNP@MeO-PEG-SH additionally features the O-H stretch, since the particles are suspended in water. b) FT-IR spectra of P(SH-co-G) (light blue, top) and AuNP@P(SH-co-G) (dark blue, bottom), displaying coinciding signals at 3380 cm^{-1} , 2920-2850 cm^{-1} and 1104 cm^{-1} , ascribed to the hydroxyl stretch, methine and methylene stretch, as well as to the ether vibration.

Successful attachment of thiol- and thioether polymers onto the particle surface was further verified by UV-vis absorption and DLS measurements, resulting in a characteristic red-shift of the SPR as depicted in **Figure 24** and an increase of the hydrodynamic diameter d compared to citrate-stabilised particles (see **Table 3**).^[130] The extent of latter was dependent on the polymer coating, decreasing for 15 nm and 30 nm AuNPs in the order MeO-PEG-SH > MeO-PEG-SPentyl and P(SET-co-G) > P(SH-co-G), as thoroughly discussed in the following **Section 3.1.2.3** with regard to the polymer surface coverage and polymer arrangement. For 50 nm this trend, however, was not as obvious probably owing to a naturally occurring broader size distribution of the particles.

Table 3: Values of the hydrodynamic diameter d and the SPR of citrate and thiol/thioether-polymer modified AuNPs measured by DLS and UV-vis spectroscopy.

	<i>citrate</i>	<i>MeO-PEG-SH</i>	<i>MeO-PEG-SPentyl</i>	<i>P(SH-co-G)</i>	<i>P(SET-co-G)</i>
15 nm AuNP					
<i>d (nm)</i>	18 ± 2.0	38 ± 8.0	32 ± 8.0	23 ± 5.0	27 ± 8.0
<i>SPR (nm)</i>	520	526	525	523	524
30 nm AuNP					
<i>d (nm)</i>	28 ± 9.0	48 ± 8.0	41 ± 8.0	38 ± 8.0	42 ± 9.0
<i>SPR (nm)</i>	525	528	527	526	527
50 nm AuNP					
<i>d (nm)</i>	49 ± 12	64 ± 12	59 ± 14	60 ± 15	53 ± 14
<i>SPR (nm)</i>	530	533	533	531	533

Transmission electron microscopy (TEM) staining with *e.g.* phosphotungstic acid is another technique to visualise and gauge the polymer layer on AuNPs, where due to interactions with the polar phosphotungstic acid the contrast of the polymer layer is enhanced. While staining of PEGylated AuNPs is well known in literature^[46, 131] and was successfully performed with AuNP@MeO-PEG-SH and AuNP@MeO-PEG-SPentyl (see **Section 5.1.2.23**), a method to distinctly stain the PG layer still needs to be found. However, the determination of the polymer layer width via TEM staining needs to be considered with caution, since the addition of the

staining compound induces morphological changes and might distort values of the layer width.^[46]

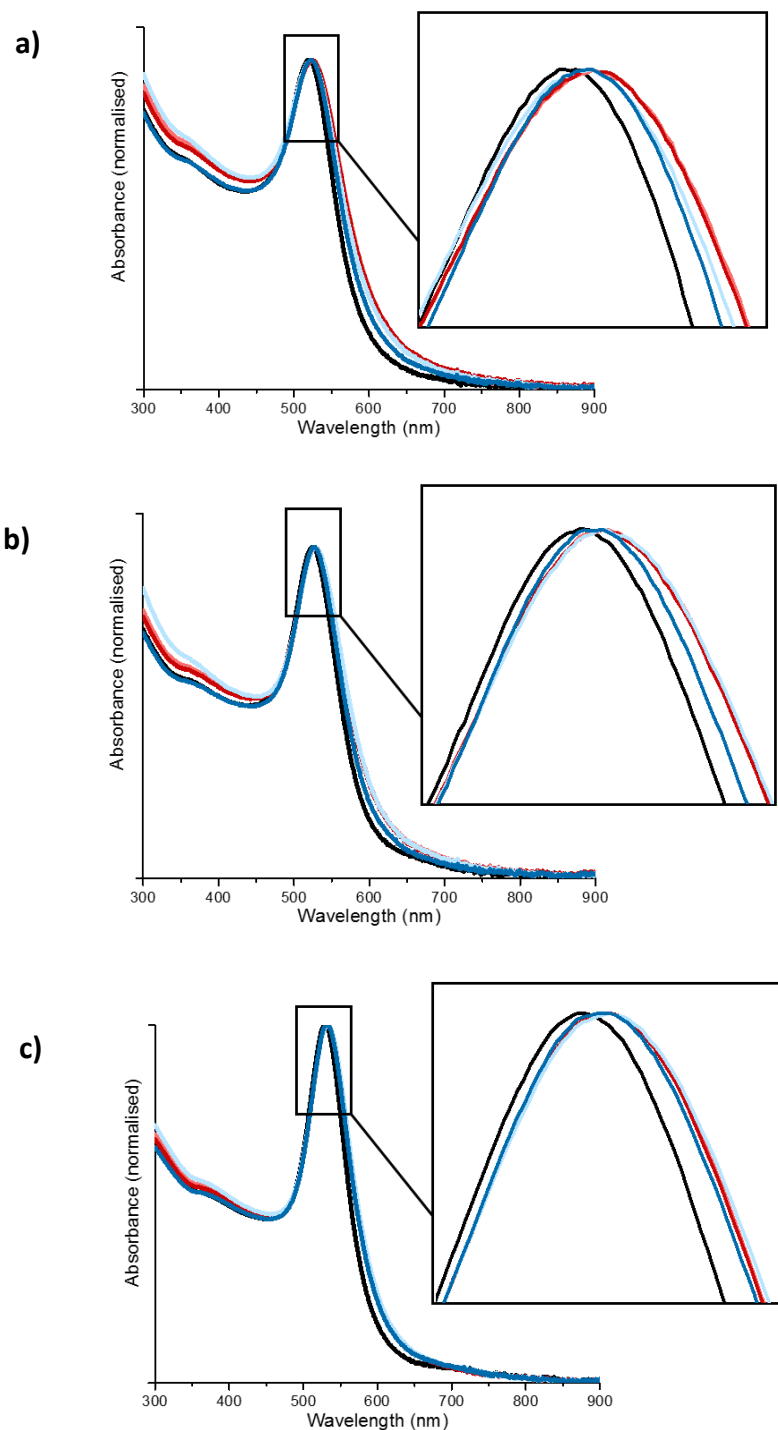


Figure 24: UV-vis spectra of a) 15 nm, b) 30 nm and c) 50 nm AuNP coated with citrate (black), MeO-PEG-SH (dark red), MeO-PEG-SPentyl (light red), P(SH-co-G) (dark blue) and P(SET-co-G) (light blue), displaying a polymer dependent SPR red-shift.

3.1.2.3 Arrangement of thiol- and thioether-polymers on AuNPs

3.1.2.3.1 Determination of polymer surface coverages via TGA and XPS

In order to determine the polymer surface coverage and thus the polymeric arrangement (see **Section 3.1.2.3.2**) on the particles, TGA and XPS investigations with 30 nm thiol- and thioether polymer coated AuNPs were conducted. Both features are critical when designing nanoparticles for biological applications, since they are claimed to affect the colloidal stability. Liu *et al.* showed that the stability of 10 nm AuNPs in salt solution correlated directly with the polymeric coverage density. Here, coverage densities lower than 50 polymers per particle caused aggregation of AuNPs in 1 M NaCl.^[132] Furthermore, a strong dependency between circulation time and polymer coverage was found in biodistribution studies for PEG modified nanocapsules. Particles with higher polymeric grafting densities displayed longer blood circulation times and reduced clearance by liver, spleen and kidney.^[133]

The polymer surface coverage (number of polymers per particle) was derived from the polymer to gold ($[\text{polymer}] / [\text{Au}]$) ratio in mass percent, which was determined via TGA and XPS. The two distinct experimental procedures and subsequent calculations are described in the following, starting with the TGA procedure.

TG analysis is widely used for the determination of the polymer number on nanoparticles.^[44, 134-135] Therefore, a dried AuNP@polymer sample is exposed to increasing temperatures (under a constant heating rate) and the polymeric weight loss is measured. Here, the distinct thermal decomposition of organic and inorganic substances is used to determine the $[\text{polymer}] / [\text{Au}]$ ratio in mass-% and concomitantly the surface coverage. The weight loss spectra of thiol/thioether-polymer coated AuNPs are depicted in **Figure 25a**, displaying a polymer dependent $[\text{polymer}] / [\text{Au}]$ ratio, decreasing in the order $\text{P}(\text{SEt-co-G}) \geq \text{MeO-PEG-SH} > \text{MeO-PEG-SPentyl} > \text{P}(\text{SH-co-G})$ (see **Table 4**). The first deviation of these curves (see **Figure 25b**) emphasised that the weight loss between 320 °C and 460 °C was ascribed to PEG attached to the gold surface, whereas for bound PG the region between 215 °C and 320 °C was considered. The weight loss below 320 °C (PEG) or 215 °C (PG) was attributed to loose polymer and not taken into account for calculations.^[45]

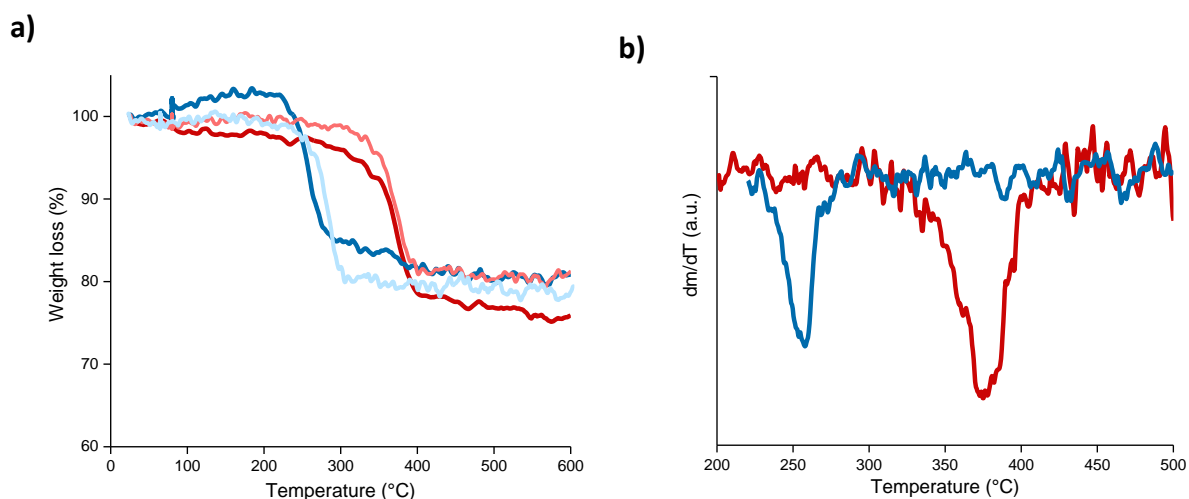


Figure 25: a) Weight loss spectra of 30 nm AuNP coated with MeO-PEG-SH (dark red), MeO-PEG-SPentyl (light red), P(SH-co-G) (dark blue) and P(SET-co-G) (light blue), displaying a polymer dependent $[\text{polymer}] / [\text{Au}]$ ratio. b) First deviation of the weight loss spectra of 30 nm AuNP coated with MeO-PEG-SH (red) and P(SH-co-G) (blue), emphasising the temperature region of 215-320 °C for PG and 320-460 °C for PEG, which was taken into account for the $[\text{polymer}] / [\text{Au}]$ ratio.

Next, XPS was applied to determine the $[\text{polymer}] / [\text{Au}]$ ratio. Since hydrogen is not detectable by XPS merely the carbon mass-% [C] was applied as polymer ratio for further investigations. Here, the elemental composition of a dried AuNP@polymer sample, immobilised on a silicon wafer was detected. By irradiation of the sample with a beam of x-rays, the kinetic energy and number of electrons that escape from the material can be ascertained. By relating the signal area of Au 4f (79.0 eV) to the one of C 1s (280 eV) the $[\text{C}] / [\text{Au}]$ ratio was determined as atomic-%. By multiplication of atom-% with the atomic weight, mass-% were defined, which were used for further calculations. The $[\text{C}] / [\text{Au}]$ ratio was found to decrease in the order MeO-PEG-SH > P(SET-co-G) > MeO-PEG-SPentyl (see **Table 4**). The $[\text{C}] / [\text{Au}]$ ratio of 30 nm AuNP@P(SH-co-G) deviated from the ones of the other particles in a magnitude that rendered a consideration unreasonable. The reason for this deviation remained unclear.

The $[\text{polymer}] / [\text{Au}]$ and $[\text{C}] / [\text{Au}]$ ratios in mass-% obtained by TGA and XPS respectively are presented in **Table 4**. The percentage terms of [Au] within both methods were in good accordance, whereas the slightly smaller polymeric amounts in case of XPS compared to TGA measurements were explained by the distinct detection methods. While in case of TGA the whole polymeric mass [polymer] was considered, for XPS analysis merely the carbon [C] amount was taken into account, lacking the contribution of other elements within the polymers, such as sulfur and hydrogen.

Table 4: [polymer] / [Au] and [C] / [Au] ratios in mass-% of 30 nm thiol- and thioether polymer coated AuNPs, obtained by TGA and XPS investigations.

Mass-%	MeO-PEG-SH	MeO-PEG-SPentyl	P(SH-co-G)	P(SET-co-G)
[polymer] / [Au] _{TGA}	[17.7] / [77.0]	[17.2] / [80.7]	[15.5] / [84.5]	[18.8] / [76.1]
[C] / [Au] _{XPS}	[16.3] / [75.6]	[14.6] / [78.6]	[20.6] / [62.7]*	[14.6.] / [75.6]

*high deviation: not taken into account.

Based on the [polymer] / [Au] and [C] / [Au] ratio in mass-% the number of polymers per AuNP were calculated for thiol- and thioether polymer coated particles via **Equation 5** (see **Table 5**).^[44-45] Firstly, the number of polymers in the total sample was derived via division of [polymer] or [C] by the molecular weight of the polymer M_W and multiplication with Avogadro constant N_A . The number of polymers in the total sample was normalised to the number of polymers per particle, via division of the number of particles in the sample. Latter was derived from [Au] divided by the particle mass, which corresponded to the product of the density of Au ρ_{Au} and the volume of a single particle ($4/3\pi r^3$). The surface area and volume calculations assume spherically shaped particles.

$$\text{Polymers per AuNP}_{TGA/XPS} = \frac{\frac{\text{mass}\%_{\text{polymer}}}{\text{mass}\%_{\text{AuNP}}} \times \rho_{Au} \times \frac{4}{3}\pi r^3 \times N_A}{M_W} \quad \text{Equation 5}$$

$$\rho_{Au} = \text{density of Au (1.96 gcm}^{-3}\text{)}$$

$$r = \text{radius of AuNP}$$

$$N_A = \text{avogadro constant}$$

$$M_W = \text{molecular weight of polymer}$$

It has explicitly to be mentioned that the numbers of thiol- and thioether polymers per 30 nm AuNP in **Table 5**, determined via **Equation 5** are based on the [polymer] / [Au]_{TGA} and [C] / [Au]_{XPS} ratio in mass-% as individual measured values. Yet, despite of the different measurement techniques, the ratios were in acceptable accordance, justifying further interpretations of the polymer surface coverage on the particles. Moreover, the calculation of **Equation 5** includes assumptions, such as assertion of the exact polymeric molecular weight and a particle volume, calculated for perfectly monodisperse and spherical 30 nm particles, although **Section 3.1.2.1** displayed particles with edges. Hence, standard deviations were not

considered as reasonable and not taken into account. The rounded values in **Table 5** should be considered with caution. In fact, the trend of a polymer dependent decrease of the polymer surface coverage on 30 nm AuNP should rather be pointed out, as thoroughly discussed in the following.

Table 5: Number of polymers per 30 nm AuNP, based on TGA and XPS results determined via Equation 1.

	<i>MeO-PEG-SH</i>	<i>MeO-PEG-SPentyl</i>	<i>P(SH-co-G)</i>	<i>P(SEt-co-G)</i>
TGA	6400	5900	5600	7200
XPS	6000	5200	-	5900
Mean value_{TGA/XPS}	6200	5600	5600	6600

Owing to the different structure of PEG and PG and concomitant distinct arrangement on the particle surface, which is abundantly characterised in the next **Section 3.1.2.3.2**, a comparison of the polymer numbers within the two polymer systems was not reasonable, hence merely the difference between MeO-PEG-SH and MeO-PEG-SPentyl or P(SH-co-G) and P(SEt-co-G) is discussed hereafter.

Table 5 reveals that the number of polymer chains per particle was noticeably higher for the MeO-PEG-SH coating compared to MeO-PEG-SPentyl, coinciding with generally increased hydrodynamic diameter d and SPR of all AuNP sizes in case of the thiol-PEG modification (see **Table 3**). This difference in the polymer coverage was ascribed to the size difference of the anchor groups, where thioether moieties ($-S-C_5H_{11}$, 103 g mol^{-1}) most probably demanded more space on the particle surface than thiol units ($-S-H$, 33 g mol^{-1}) and consequently resulted in lower numbers of polymer chains on the particle.

On the other hand, regarding the PG coating, the polymer coverage, hydrodynamic diameter and SPR of 15 nm and 30 nm AuNPs was consistently higher for P(SEt-co-G) than for P(SH-co-G). Since the size difference between thioether moieties ($-S-C_2H_5$, 61 g mol^{-1}) and thiol units ($-S-H$, 33 g mol^{-1}) was less important for PG, higher numbers of polymers regarding P(SEt-co-G) were not attributed to the structure of the anchor group. Instead, it was hypothesised that the binding strength between thioether groups and the gold surface is larger than that of thiols ($-SR > -SH$) causing increased polymer coverages. While the impact of the single anchor group within the high molecular weight PEG probably was less crucial for the grafting behaviour, for

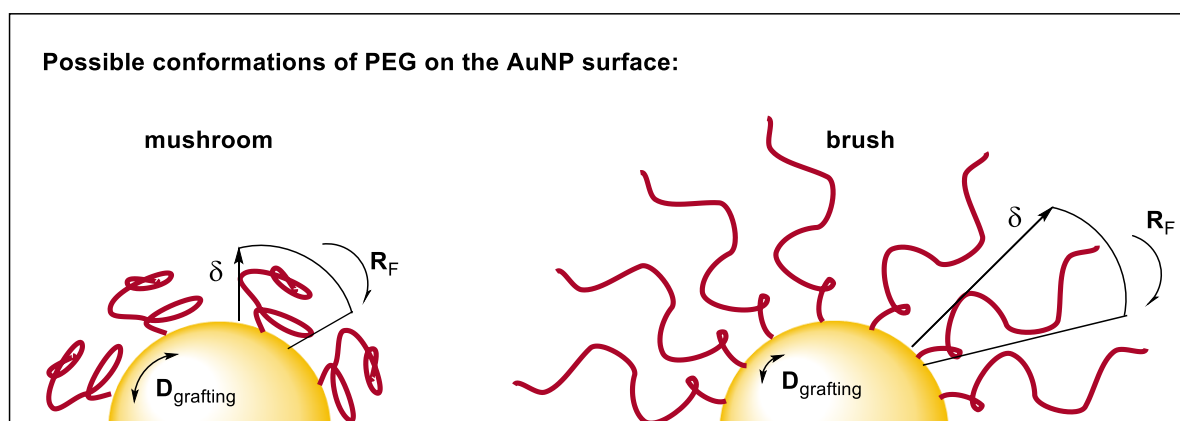
3 Results and Discussion

PG featuring multiple thiol/thioether moieties the affinity of the anchor group towards the gold surface could gain influence on the polymer coverage. This hypothesis was reassumed in **Section 3.1.3** regarding a higher colloidal stability of thioether polymer coated AuNPs in comparison to their thiol analogues.

3.1.2.3.2 Polymeric conformation on AuNPs

Throughout this section firstly the conformation of MeO-PEG-SH and MeO-PEG-SPentyl on the particle surface of a 30 nm AuNP was determined based on the polymer number (see **Table 5**), before suggesting possible conformations for the structurally more complex P(SH-co-G) and P(SET-co-G).

In literature two main conformations of end-grafted PEG on nanoparticles are described. As depicted in **Scheme 6** for low grafting densities a coiled conformation of PEG is assumed, leading to a mushroom regime. Whereas for high surface coverages an extended conformation of the PEG chain, corresponding to a brush regime, is ascribed (see **Section 2.1.2.2**).^[42]



Scheme 6: Depiction of the mushroom and brush conformation of PEG chains on the particle surface.

The relationship between mushroom and brush regime can more precisely be explained by introduction of the Flory radius R_F of PEG, which is given by **Equation 3** (see **Section 2.1.2.1**). Here α is the length of one monomer unit and n corresponds to the number of monomer units within the PEG chain. The factor $3/5$ assumes a conformation of PEG in a good solvent (e.g. water), where it takes up more space than in a bad solvent (hexane).^[43] The value of R_F for MeO-PEG-SH and MeO-PEG-SPentyl used in this study corresponded to 6.7 nm.

$$R_F = \alpha n^{\frac{3}{5}}$$

Equation 3

α = length of monomer (3.5 Å for PEG)

n = number of monomers (136 for PEG 6000)

The crucial factor that determines mushroom or brush conformation is the relation between R_F and the effective distance between two grafted PEG chains D_{grafting} , containing the grafting density σ . Latter refers to polymer chains per nm^2 , which can be derived from the number of polymers per particle (see **Table 5**) divided by the particle surface area ($4\pi r^2$), as displayed in **Equation 4**.^[42-43]

$$D_{\text{grafting}} = 2 \sqrt{\frac{1}{\sigma\pi}}$$

Equation 4

$$\sigma = \text{grafting density} = \frac{\text{Number of polymers per particle}}{4\pi r^2}$$

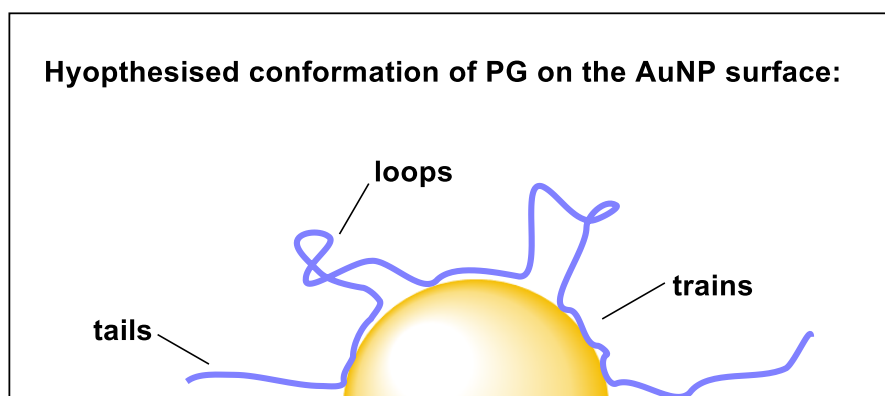
Values of the grafting density σ and D_{grafting} of 30 nm AuNPs coated with MeO-PEG-SH and MeO-PEG-SPentyl are depicted in **Table 6**. Damodaran *et al.* reported that a mushroom regime becomes brush-like when D_{grafting} on the surface nears R_F . Thus, if $D_{\text{grafting}} > R_F$ PEG chains acquire a mushroom conformation on the particle surface, where a chain occupies roughly a sphere with a radius comparable to R_F . $D_{\text{grafting}} < R_F$ is regarded as the onset of the brush regime (see **Scheme 6**).^[42] The values in **Table 6** verified that PEG chains within 30 nm AuNP@MeO-PEG-SH and AuNP@MeO-PEG-SPentyl definitely featured an extended conformation, corresponding to a brush regime.

Table 6: Determination of a brush conformation for MeO-PEG-SH and MeO-PEG-SPentyl on 30 nm AuNP.

	σ (polymer chains per nm^2)	D_{grafting} (nm)
MeO-PEG-SH_{TGA}	2.3	0.74
MeO-PEG-SH_{XPS}	2.1	0.78
MeO-PEG-SPentyl_{TGA}	2.1	0.78
MeO-PEG-SPentyl_{XPS}	1.8	0.84
Conformation		$D_{\text{grafting}} < R_F$ (6.7 nm) \rightarrow brush

It is generally accepted that approximately three PEG chains per nm² can be seen as a realistic value for the grafting density σ of PEG (2000-5000 Da) on AuNPs (2-30 nm).^[134-136] However, in literature discussed values based on TGA investigations range from 1-15 polymer chains per nm². Unrealistically high values of σ were explained by high percentages of polymer chains that are adsorbed to other chains and not chemically anchored to the particle surface.^[137] These inconsistencies within literature were ascribed to different measurement procedures, which result in inconsistent decomposition of the sample at a regarded temperature.^[134] Likewise, not all groups worked with micro-TG analysis, which is mandatory for a correct mass detection. Furthermore, assumptions were made for calculating σ (**Equation 4** and **Equation 5**), such as assertion of the exact polymeric molecular weight and a particle volume or surface area, calculated for perfectly spherically shaped 30 nm particles. Although SEM measurements displayed AuNPs with edged, as already discussed in **Section 3.1.2.1**. Thus, due to inconsistencies mentioned before, values of σ for 30 nm AuNP@MeO-PEG-SH and AuNP@MeO-PEG-SPentyl were not further compared to values within literature.

So far calculations known from literature were applied to determine the arrangement of PEG brushes on 30 nm AuNPs, which have been established for linear and end-grafted polymer chains. The following section concerns conformations of the structurally more complex PG. Due to statistically distributed anchor groups along the backbone an exact prediction of the PG conformation on the particle surface was extremely difficult and theoretical models for their prediction are lacking. Based on investigations of nanoparticles coated with multivalent homopolymers, such as poly(vinyl alcohol)^[49-50], poly(vinyl pyrrolidone)^[51] and dextran,^[52] as well as with help of one study about copolymers^[53] it was suggested that P(SH-co-G) and P(SET-co-G) adopted a conformation on the surface that is characterised by varyingly large tails, loops and trains, where tails are non-adsorbed ends of the polymer, loops are non-adsorbed polymer segments between trains, which are considered as the adsorbed segments, as depicted in **Scheme 7**.^[138-139]



Scheme 7: Hypothesised conformation of PG on the particle surface, provoked by statistically distributed anchor groups along the backbone.

It has to be mentioned that these studies refer to linear homopolymers and “truly random”^[53] copolymers with statistically distributed anchor groups, where each section of the polymer has the same affinity to adsorb to the particle surface. Thus, the polymeric arrangement can be predicted via conformational statistics, determining the contribution and extend of tails, loops and trains.^[50] However, the exact calculation of the arrangement of P(SH-co-G) and P(SET-co-G) on 30 nm AuNPs is based on the specific surface adsorption of the monomer units and on the different binding kinetics of thiols and thioethers. A theoretical model for this situation remains to be developed.

Yet, the existence of long protruding loops and tails could be excluded, since such extending segments could reach other particles and adsorb thereon, provoking a bridging of the particles termed as bridging flocculation,^[140] which was not found for AuNP@P(SH-co-G) and AuNP@P(SET-co-G). Since aforementioned bridging requires unoccupied regions on the particle surface, where polymer tails and loops from other particles can adsorb to furthermore, a dense particle coating of thiol- and thioether-PG was concluded.^[50]

At the beginning of this chapter it was claimed that the polymer coverage on AuNPs is directly correlated with the colloidal stability.^[132-133] To which extent this applied to thiol- and thioether-polymer coated particles of this thesis, was examined in a stability study throughout the next **Section 3.1.3**. Therefore, the particles were exposed to conditions that provoke aggregation, such as centrifugation, high temperatures, pH, ionic strength and lyophilisation. First and foremost, however, the study investigated and compared the strength of the thiol/thioether-gold interaction.

3.1.3 Colloidal stability of thiol- and thioether-polymer modified AuNPs

Before investigating the thermodynamic colloidal stability upon polymer coating, firstly a study on the binding kinetics of thiol/thioether polymers to the particle surface was carried out.

3.1.3.1 Binding kinetics study

The binding kinetics of thiol- and thioether-polymers towards the particle surface was investigated by recording a time evolution of UV-vis absorbance spectra of 30 nm AuNPs. The time points of absorbance measurements ranged from 5 min to 12 h upon polymer addition. The polymeric incubation was stopped by centrifugation. An incubation of 12 h conformed to the standard procedure followed in this thesis. **Figure 26** shows that an incubation time of 5 min was sufficient to ensure steric stabilisation, except for P(SEt-co-G). Here, an incubation time shorter than 2 h caused a broadening of the SPR in the range of 600-700 nm, due to aggregation of the particles. The need for a longer passivation time regarding P(SEt-co-G) in comparison to P(SH-co-G) coincided with precedent studies, comparing the thiol/thioether binding kinetics. These studies were based on the direct two-phase synthesis reported by Brust *et al.*,^[89] where a slower thioether-passivation of AuNP resulted in longer nucleation processes and increased polydispersity of the obtained gold cores.^[17] In case of MeO-PEG-SH/-SPentyl featuring completely passivated AuNPs after 5 min incubation, the influence of the anchor group on the passivation time was suggested to be masked by interactions among the extended PEG brushes, ensuring sufficient colloidal stability.^[141]

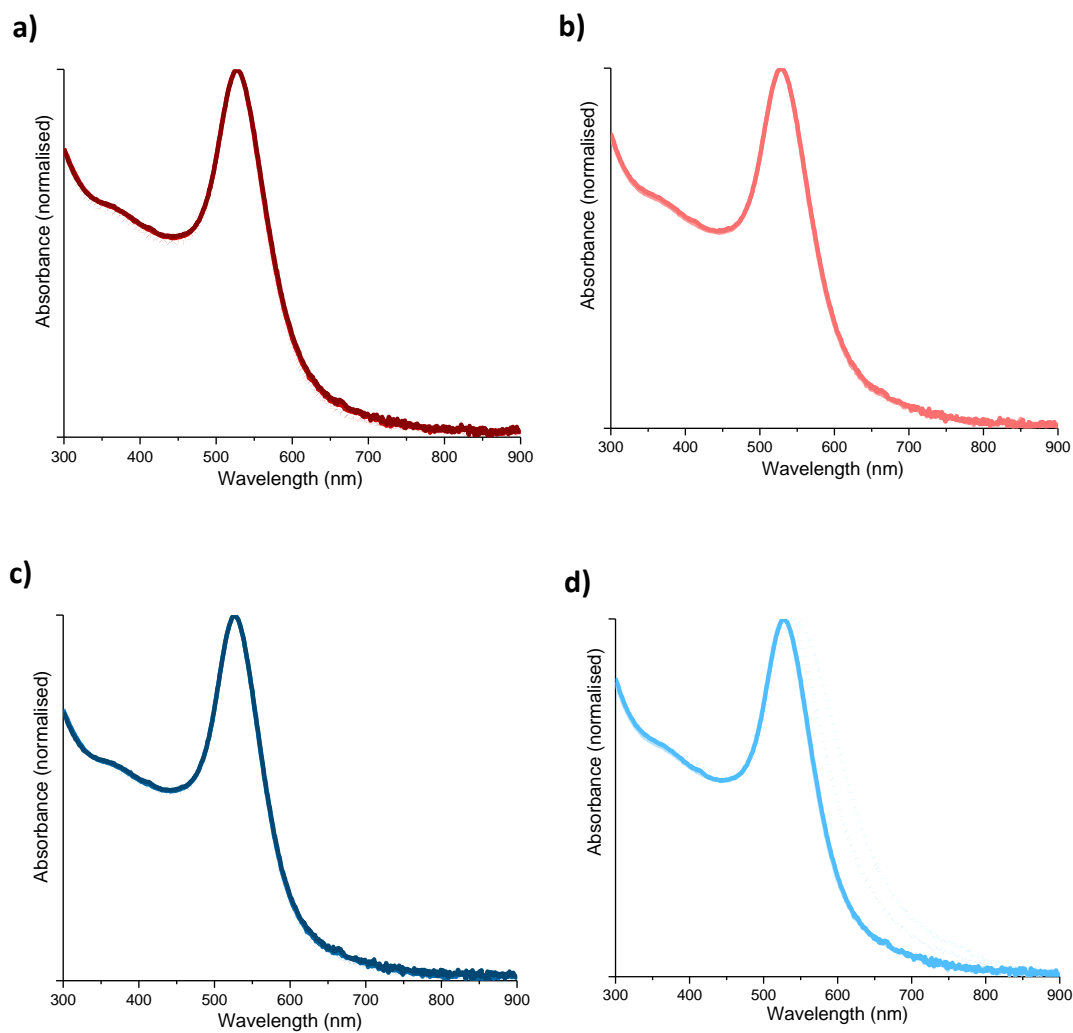


Figure 26: UV-vis absorbance spectra of 30 nm AuNPs after 5 min (light colour, dashed), 30 min (dark colour, dashed), 2 h (light colour, solid), 6 h (medium colour, solid) and 12 h (dark colour, solid) incubation time with a) MeO-PEG-SH (dark red), b) MeO-PEG-SPentyl (light red), c) P(SH-co-G) (dark blue) and d) P(SET-co-G) (light blue). For d) P(SET-co-G) an incubation time shorter than 2 h caused a broadening of the SPR in the range of 600-700 nm, due to aggregation of the particles.

3.1.3.2 Colloidal stability study

Understanding the factors that influence the colloidal stability is mandatory for the development of safe and effective nano-therapeutics, since aggregation of AuNPs influences the *in vitro* cellular response owing to an increased size and altered diffusion velocity. Hence, a lacking colloidal stability renders results of biodistribution, pharmacokinetics and toxicity unpredictable and impedes reproducibility.^[142] In order to prove the colloidal stability of varyingly large thiol- and thioether-polymer coated AuNPs, the particles were exposed to conditions that provoke aggregation, such as centrifugation, high temperatures, different pH values, physiological environments and lyophilisation.^[143-144]

3.1.3.2.1 Stability against centrifugation, high temperatures and pH values

In order to investigate the influence of centrifugation, high temperatures and pH on the aggregation behaviour, 15 nm, 30 nm and 50 nm AuNPs modified with thiol and thioether polymers were exposed to five successive centrifugation-(22000 x g) and resuspension-cycles in water, heated to 80 °C for 12 h and suspended in phosphate buffer (5 mM) of a broad pH range (5.4, 7.4, 9.4). The colloidal stability before and after the respective treatment was systematically investigated by recording UV-vis absorbance spectra.

As depicted for 15 nm, 30 nm and 50 nm AuNPs modified with thiol- and thioether-polymers in **Figure 27-29**, it was shown that temperatures up to 80 °C (exclusively shown for 30 nm AuNPs), centrifugation, as well as acidic and alkaline pH had no impact on the colloidal stability, independent of particle size and coating.

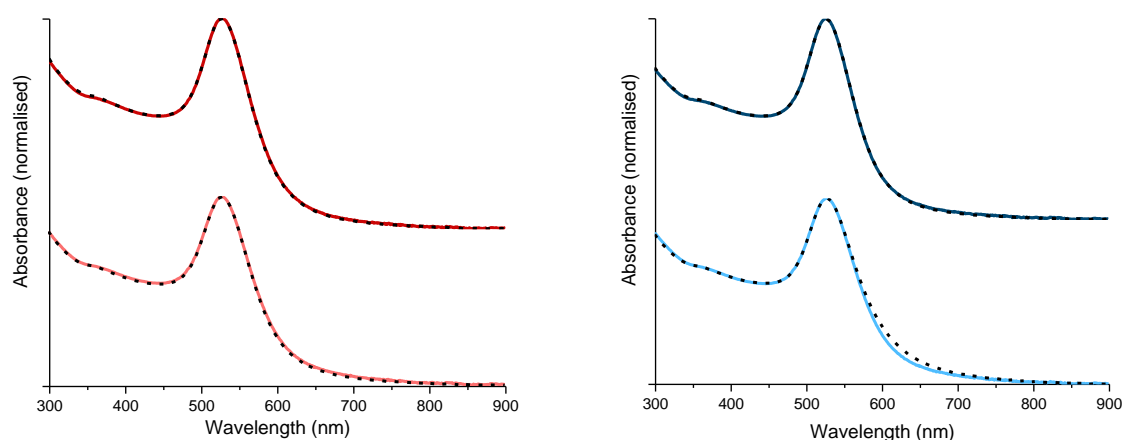


Figure 27: UV-vis absorbance spectra of 30 nm AuNPs modified with MeO-PEG-SH (top, dark red), MeO-PEG-SPentyl (bottom, light red), P(SH-co-G) (top, dark blue) and P(SET-co-G) (bottom, light blue), before (solid line) and after (black, dashed line) treatment at 80 °C for 12 h, displaying no changes of the optical properties.

3 Results and Discussion

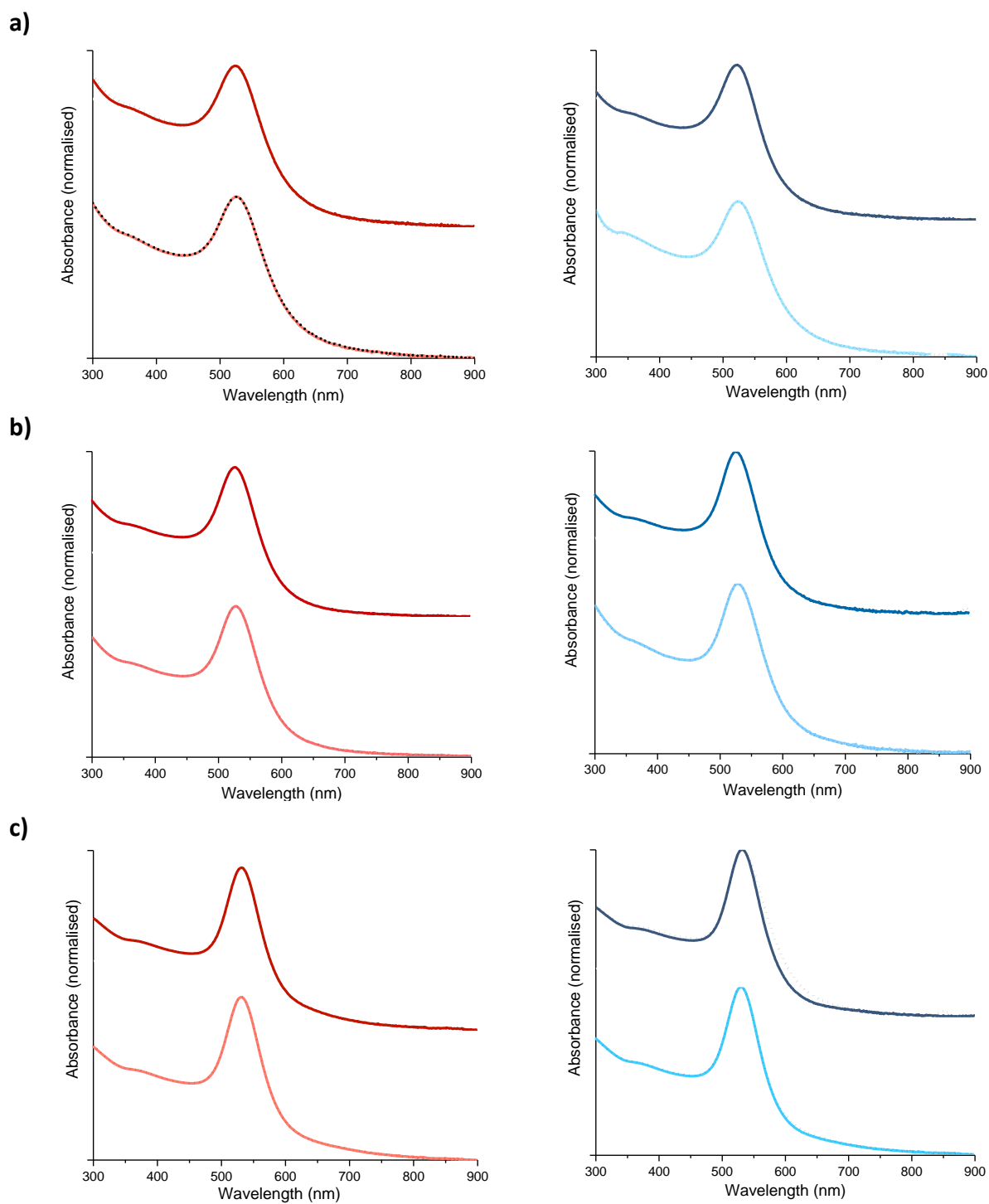


Figure 28: UV-vis absorbance spectra of a) 15 nm, b) 30 nm and c) 50 nm AuNPs modified with MeO-PEG-SH (top, dark red), MeO-PEG-SPentyl (bottom, light red), P(SH-co-G) (top, dark blue) and P(SET-co-G) (bottom, light blue), before (solid line) and after (black, dashed line) five centrifugation and resuspension cycles, displaying no changes of the optical properties.

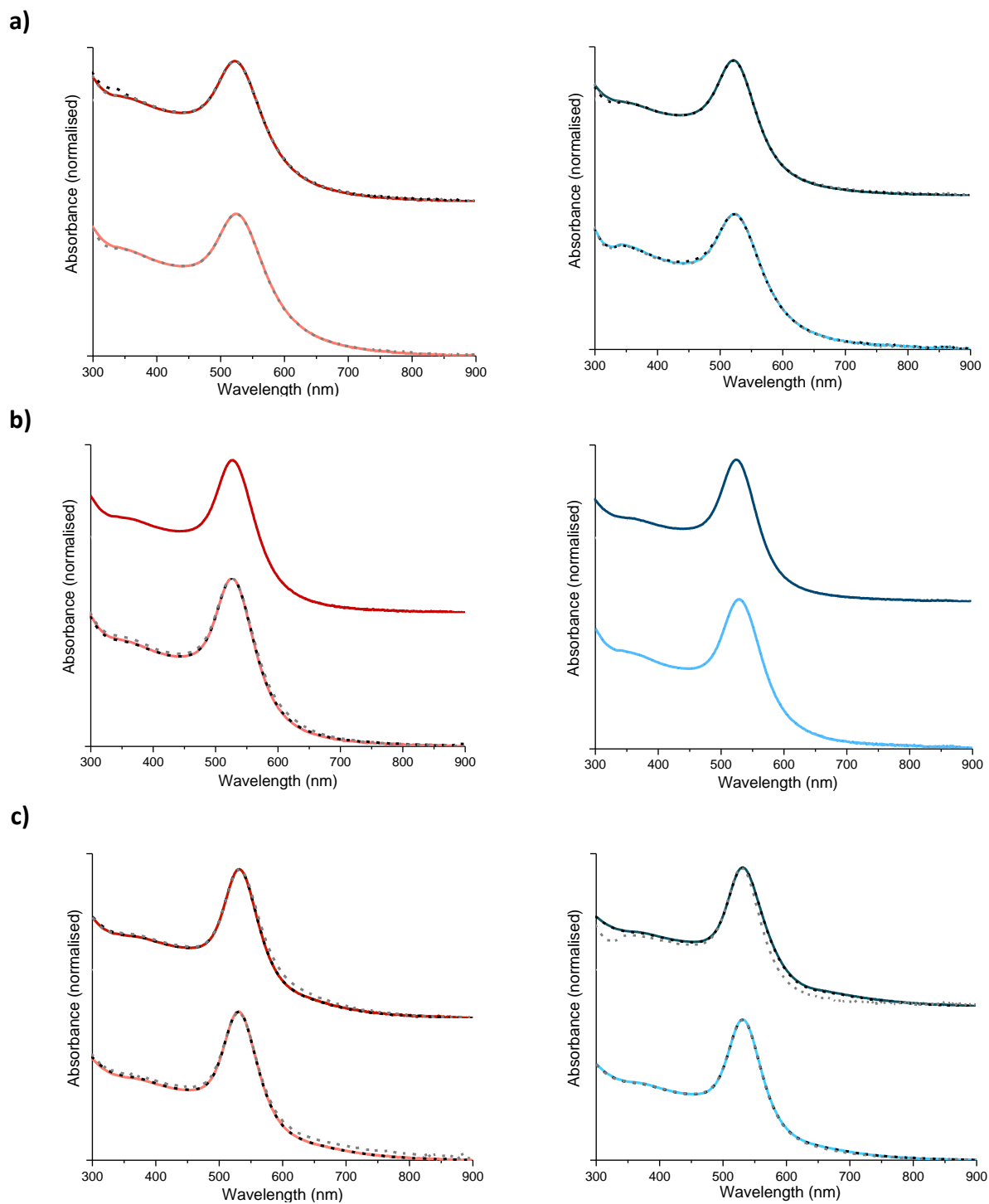


Figure 29: UV-vis absorbance spectra of a) 15 nm, b) 30 nm and c) 50 nm AuNPs modified with MeO-PEG-SH (top, dark red), MeO-PEG-SPentyl (bottom, light red), P(SH-co-G) (top, dark blue) and P(SEt-co-G) (bottom, light blue), after treatment at pH 5.4 (solid line), 7.4 (black, dashed line) and 9.4 (grey, dashed line) for 12 h, displaying no changes of the optical properties.

3.1.3.2.2 Stability under physiological conditions

Particularly the dispersion of AuNPs in fluids that mimic physiological conditions, including increased ionic strength and the presence of a wide range of bio-macromolecules, provokes colloidal instability. If the polymer is not properly anchored to the particle surface ions and first and foremost proteins can adsorb onto the particle and cause aggregation. In the following firstly the colloidal stability against a salt solution and afterwards against cell culture medium (CCM) was investigated. For clarity the colloidal stability in percentage terms was introduced. Therefore, the absorbance values at 530 nm before and after the respective treatment were correlated, since a decreased absorbance at this value was attributed to a particle loss owing to aggregation.

The influence of ions on the colloidal stability was investigated by incubating 15 nm, 30 nm and 50 nm AuNPs modified with thiol and thioether polymers in 1 x PBS (0.1 M NaCl) for 12 h. After successive centrifugation the particles were once more suspended in PBS and UV-vis absorbance measurements were performed.

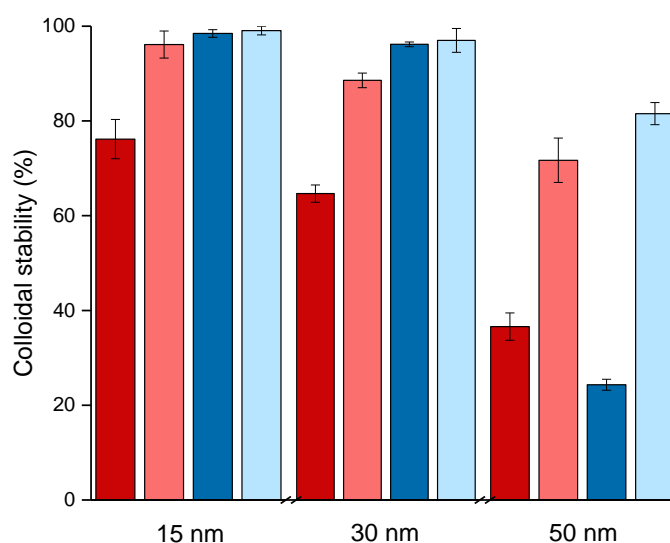


Figure 30: Colloidal stability of 15 nm (left), 30 nm (middle) and 50 nm (right) AuNP modified with MeO-PEG-SH (dark red), MeO-PEG-SPentyl (light red), P(SH-co-G) (dark blue) and P(SET-co-G) (light blue) after treatment with PBS.

Figure 30 shows that suspension of AuNPs in PBS caused a size and polymer coating dependent impairment of the colloidal stability. For 15 nm and 30 nm AuNPs the polymer coating had a lower impact on the stabilisation against ions, resulting in good stabilities of all thiol/thioether-polymer coated AuNPs (90 %-99 %), with the exception of AuNP@MeO-PEG-SH (77 %). Interestingly, **Table 5** indicates that 30 nm AuNP@MeO-PEG-SH possessed higher

polymer coverages than AuNP@MeO-PEG-SPentyl. Proving that although the density of MeO-PEG-SPentyl on AuNPs was lower than that of the thiol analogue, AuNP@MeO-PEG-SPentyl ensured a better stabilisation against ions, indicating a stronger adsorption.

In case of 50 nm AuNPs the anchor group-gold interaction gained even more influence on the colloidal stability. Here, additionally to AuNP@MeO-PEG-SH also AuNP@P(SH-co-G) displayed significant aggregation upon PBS treatment, whereas the thioether analogues featured good colloidal stability (72 %-82 %). The generally higher sensitivity of larger particles towards aggregation conforms to findings in literature.^[34] Corresponding UV-vis spectra of 50 nm AuNPs are displayed in **Figure 31**.

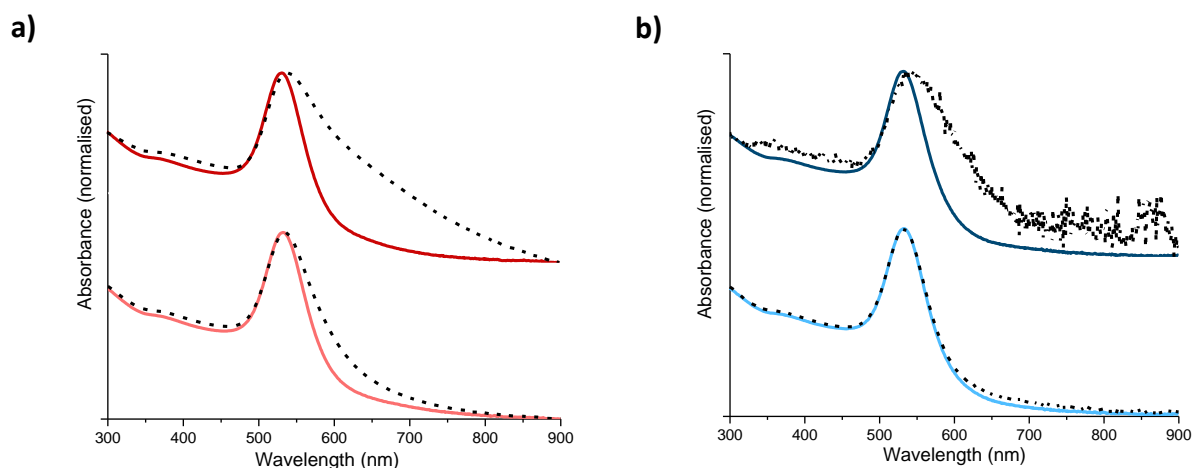


Figure 31: UV-vis absorbance spectra of 50 nm AuNP modified with a) MeO-PEG-SH (top, dark red) and MeO-PEG-SPentyl (bottom, light red), as well as b) P(SH-co-G) (top, dark blue) and P(SET-co-G) (bottom, light blue), before (solid line) and after (black, dashed line) suspension in PBS, displaying a minor impairment of the colloidal stability for MeO-PEG-SPentyl and no impact on the colloidal stability for P(SET-co-G).

Moreover, the impact of proteins in the presence of ions on the colloidal stability was investigated by treatment of AuNPs with CCM. The procedure conformed to the study in PBS. Briefly, 15 nm, 30 nm and 50 nm AuNPs modified with thiol and thioether polymers were incubated with CCM for 12 h. After centrifugation the particles were once more suspended in CCM and UV-vis absorbance measurements were performed.

In accordance with precedent studies on ionic strength (PBS), it was found that the impact of the polymer coating on the stability of 15 nm against CCM was rather low, resulting in a slightly improved stabilisation of the PG coating (97 %-98 %) compared to PEG (80 %-84 %), as displayed in **Figure 32**.

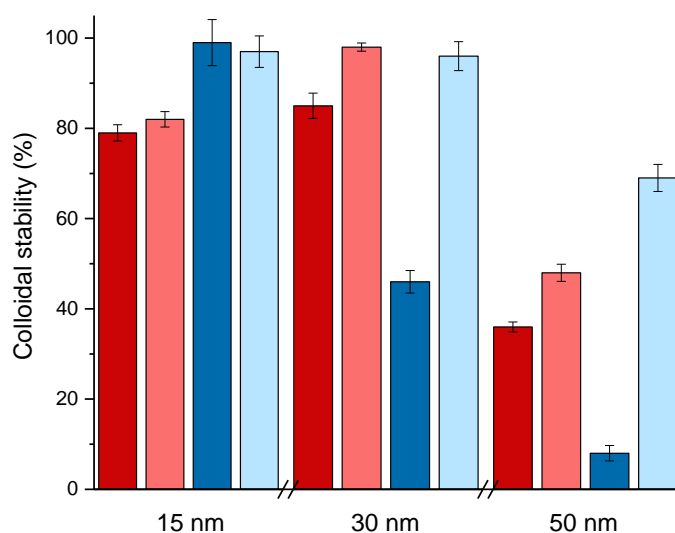
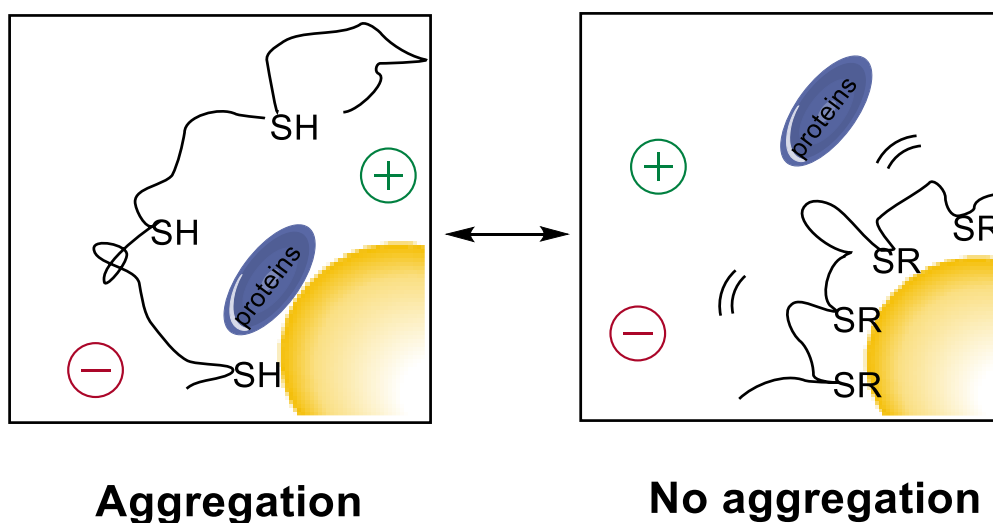


Figure 32: Colloidal stability of 15 nm (left), 30 nm (middle) and 50 nm (right) AuNPs modified with MeO-PEG-SH (dark red), MeO-PEG-SPentyl (light red), P(SH-co-G) (dark blue) and P(SET-co-G) (light blue) after treatment with CCM.

Figure 32 further shows that for 30 nm and 50 nm thiol/thioether-polymer coated AuNPs a clear dependency of the colloidal stability on the polymer coating was detectable. P(SH-co-G) featured by far worst colloidal stabilisation, with barely half of the colloidal stability related to the other polymer coatings. **Table 5** reveals that 30 nm AuNP@P(SH-co-G) possessed the lowest polymer coverage of all 30 nm polymer modified AuNPs. Hence, for 30 nm AuNP@P(SH-co-G) the low number of polymers per particle correlated with a low stability against CCM. For the other polymer coatings no such dependency was found, displaying consistently good particle recoveries in the range of 85 %-98 %, although there were crucial differences in the coverage density (**Table 5**).

Instead, a direct correlation between the anchor group and the stabilisation efficacy was determined. In accordance with previous stability studies in PBS, also against CCM a thioether-gold linkage ensured better stability than the corresponding thiol linkage. In fact, 30 nm AuNP@MeO-PEG-SPentyl (96 %) displayed a better stabilisation against ions and proteins than the thiol analogue (85 %), despite lower polymer coverages.

Moreover, the hypothesis given at the end of **Section 3.1.2.3.1** that a more stable thioether-gold interaction can be reassumed with regard to the distinct structures of PEG and PG. In case of PEG the influence of the single anchor group most probably was less crucial for the particle stabilisation, since the extended PEG brushes additionally featured stability. On the contrary, in **Section 3.1.2.3.2** a rather flat arrangement of PG in loops, tails and trains was suggested, as depicted in **Scheme 8**. Here, by a higher number of thiol/thioether moieties accompanied by a minor polymeric steric stabilisation, the PG coating featured an increased dependency of the colloidal stability on the anchoring groups and thus results in higher amount of aggregated particles for 50 nm AuNP@P(SH-co-G) than 50 nm AuNP@P(SEt-co-G).



Scheme 8: Depiction of AuNPs modified with P(SH-co-G) (left) and P(SEt-co-G) (right), featuring a rather flat polymeric layer with loops, tails and trains with minor steric stabilisation. Thus the dependency of the colloidal stability against ions and proteins on the anchor groups increases, resulting in a higher sensitivity towards aggregation in case of thiols (left) compared to thioethers (right).

3.1.3.2.3 Stability against lyophilisation

Furthermore, the effect of freeze-drying on the colloidal stability of thiol/thioether-polymer coated AuNPs was studied. This method is extremely helpful for practical handling, in particular when developing nano-therapeutics, since the conversion of a solution into a powder provides the facility of long-term storage and thus enables the clinical use of nanoparticles.^[145]

The impact of lyophilisation on the colloidal stability was investigated by freezing 15 nm, 30 nm and 50 nm AuNPs modified with thiol and thioether polymers and by successively removing the ice under reduced pressure. After lyophilisation, the dried pellets of thiol/thioether-polymer coated AuNPs were suspended in water and UV-vis absorbance measurements were carried out.

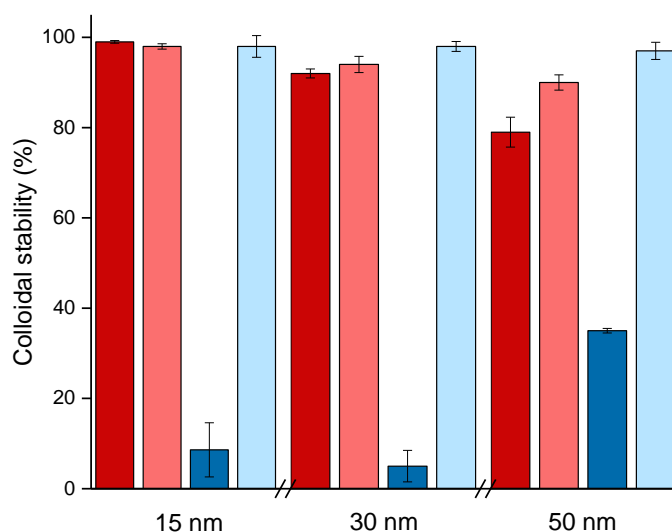


Figure 33: Colloidal stability of 15 nm (left), 30 nm (middle) and 50 nm (right) AuNPs modified with MeO-PEG-SH (dark red), MeO-PEG-SPentyl (light red), P(SH-co-G) (dark blue) and P(SET-co-G) (light blue) after lyophilisation.

Figure 33 shows that the influence of the lyophilisation process was highly dependent on the polymer coating, whereas particle size played a negligible role. For all particle sizes, a P(SH-co-G) coating resulted in tremendous aggregation with stability values ranging from 5 %-30 %, while all other polymer coatings displayed good particle recoveries (80 %-99 %).

As already mentioned, 30 nm AuNP@P(SH-co-G) possessed the lowest polymer coverage of all 30 nm AuNPs (see **Table 5**) correlating with the lowest stability against lyophilisation. However, accordingly to previous studies in PBS and CCM, no such dependency on the number of polymers per particle was found for 30 nm AuNP@MeO-PEG-SH (92 %) and AuNP@MeO-PEG-SPentyl (94 %), displaying comparable colloidal stability.

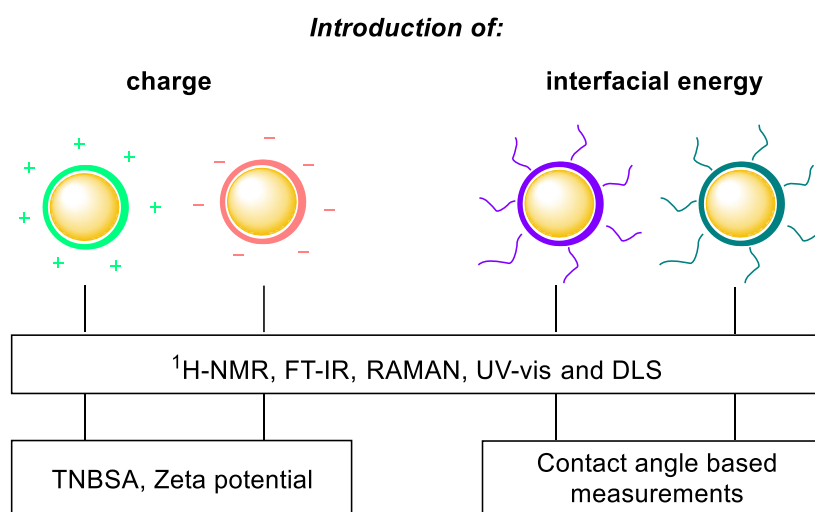
In accordance with previous studies in PBS and CCM this verified the anchor group-gold interaction as decisive factor for particle stabilisation. Consistent with the study in CCM in case of PEG where the extended polymer brushes additionally featured stability, the influence of the anchor group on the colloidal stability against freeze-drying was less crucial. Resulting in good stabilities of AuNP@MeO-PEG-SH and AuNP@MeO-PEG-SPentyl for all sizes (80 %-99 %). Regarding PG, however, the dependency of the colloidal stability on these anchoring groups increased tremendously. The lower steric stabilisation concurrent with a higher number of thiol/thioether moieties, lead to a huge difference in particle stability between thioether- and thiol-PG coating for all sizes (55 %-89 %).

3.2 Multifunctionality of thioether-PG for AuNP functionalisation

It was shown in the last **Section 3.1.3.2** that due to the stable thioether-gold interaction, P(SET-*co*-G) ensured excellent colloidal stability towards conditions that provoke aggregation, such as centrifugation, high temperatures, pH, ionic strength and lyophilisation. An additional outstanding feature of thioether-PG is the possibility to introduce chemical functionality. The non-nucleophilic and non-oxidative character of thioether moieties allowed the introduction of a broad variety of functional groups to the polymer backbone, without causing intra- or inter-polymeric crosslinking. In order to equip PG with functionalities, a bimolecular thiol-ene click reaction was performed throughout this **Section 3.2**, where additionally to EtSH a functional mercaptan compound was introduced to P(AGE-*co*-G). In this manner a library of multifunctional PG for AuNP coating was generated, featuring functionalities, such as charged moieties and hydrophilic/hydrophobic chains, as well as bio-active linker, consisting of diazirine or biotin units. Within this chapter first the polymer- and then the corresponding particle-synthesis was described and analysed.

3.2.1 Introduction of charge and hydrophobicity to the AuNP surface

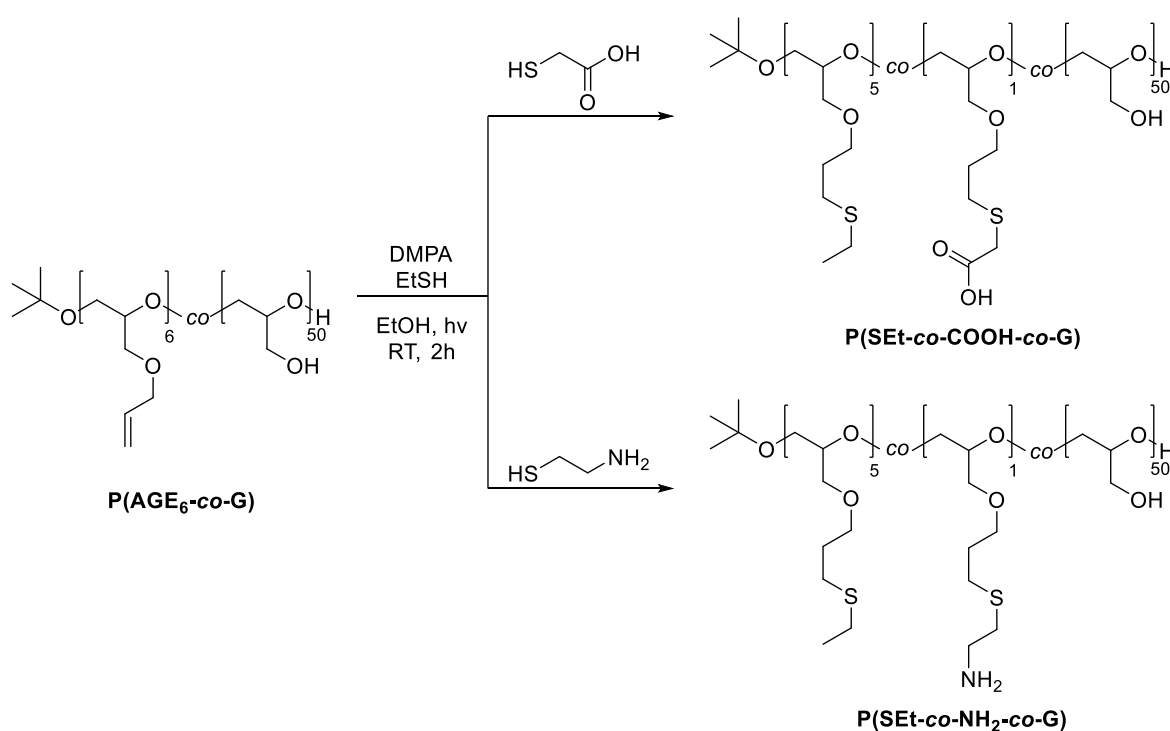
In this section the synthesis of PG with charged moieties and hydrophilic/hydrophobic chains was performed and confirmed by $^1\text{H-NMR}$, FT-IR and RAMAN spectroscopy, as well as via TNBSA assay and contact angle based measurements. The successive binding of these functional polymers to the nanoparticle surface was verified by FT-IR, UV-vis spectroscopy and DLS investigations, including size and zeta potential measurements. Throughout this section positive charge was marked in green, negative charge in red, hydrophilicity in purple and hydrophobicity in cyan, as depicted in **Scheme 9**.



Scheme 9: Depiction of AuNPs bearing distinct charge (marked green and red) and hydrophobicity (marked purple and cyan) accompanied by an overview of the characterisation methods performed in this section, verifying successful functionalisation.

3.2.1.1 Synthesis of PG bearing amine and carboxylic moieties for AuNP functionalisation

In order to functionalise PG with positively and negatively charged groups, a bimolecular thiol-ene click reaction of P(AGE₆-co-G) with 10 eq. EtSH and 2 eq. cysteamine or 1.2 eq. thioglycolic acid was performed. After the addition of 0.6 eq. photo-initiator the solution was stirred at room temperature under UV-irradiation for 2 h and purified by dialysis, yielding P(SET-co-NH₂-co-G) and P(SET-co-COOH-co-G) as a light yellow oil (see **Scheme 10**). The molar equivalents were referenced to the allyl groups within P(AGE₆-co-G).



Scheme 10: Synthesis of P(SET-co-COOH-co-G) and P(SET-co-NH₂-co-G) via bimolecular thiol-ene click reaction with P(AGE₆-co-G), EtSH and thioglycolic acid or cysteamine.

The signal in the ¹H-NMR spectra displayed in **Figure 34** at 3.25 ppm (**18**), appearing as a triplet for P(SET-co-NH₂-co-G) and as a singlet for P(SET-co-COOH-co-G) revealed that one amine or carboxylic moiety per polymer backbone was introduced. In case of P(SET-co-NH₂-co-G), the amine amount per polymer was further verified by reaction with TNBSA (see **Table 7**), where the resulting chromogenic derivative was quantified via UV-vis spectroscopy at 335 nm.

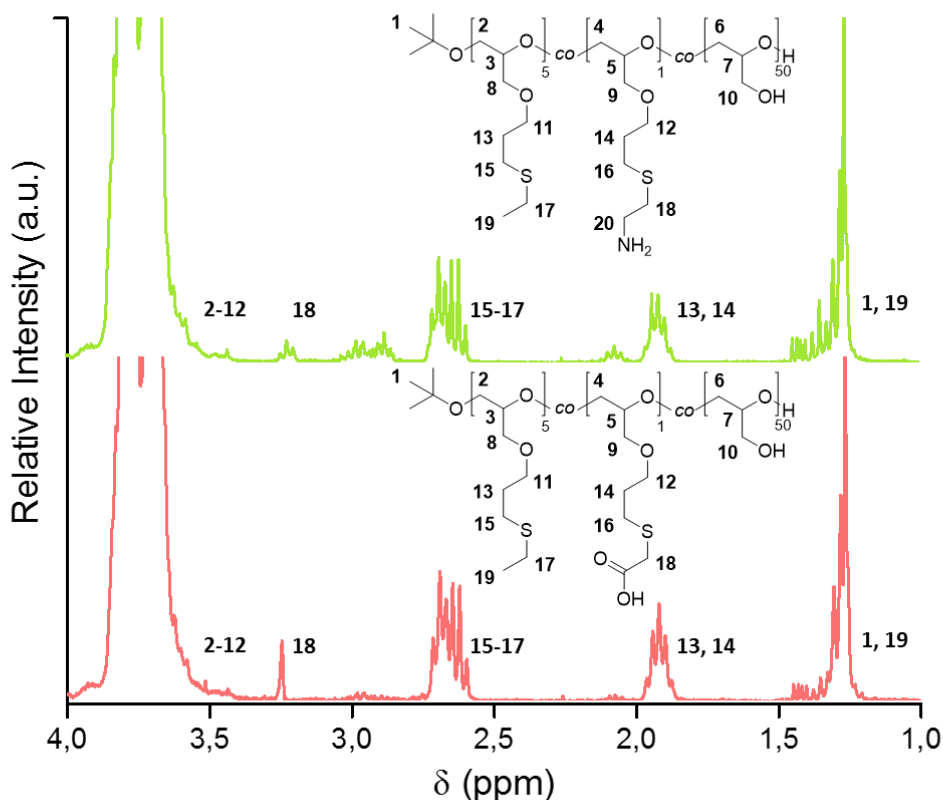


Figure 34: $^1\text{H-NMR}$ spectra of $P(\text{SEt-co-NH}_2\text{-co-G})$ (top, green) and $P(\text{SEt-co-COOH-co-G})$ (bottom, red), differing in the proton signal around 3.25 ppm (18), appearing as a triplet adjacent to the amine moiety and as a singlet next to the carboxylic unit.

The Introduction of amine and carboxyl functions was further proven by FT-IR- and RAMAN-spectroscopy. The spectra of $P(\text{SEt-co-NH}_2\text{-co-G})$ in **Figure 35a** shows vibrations at 3500-3100 cm^{-1} (overlapping with the broad O-H stretch) and 1600 cm^{-1} , ascribed to the asymmetric and symmetric NH_2 stretch and NH_2 scissors vibrations. On the other hand, the vibration at 1730 cm^{-1} in the spectra of $P(\text{SEt-co-COOH-co-G})$ arose due to the COOH stretch, as depicted in **Figure 35b**.

The successful coating of 30 nm AuNPs with the described polymers was proven by UV-vis absorbance, FT-IR and DLS measurements (see **Section 5.2.8** and **5.2.10**). The introduction of positive and negative charge to the particle surface owing to the functionalisation with $P(\text{SEt-co-NH}_2\text{-co-G})$ and $P(\text{SEt-co-COOH-co-G})$ respectively was verified by zeta-potential investigations, as depicted in **Figure 35c**.

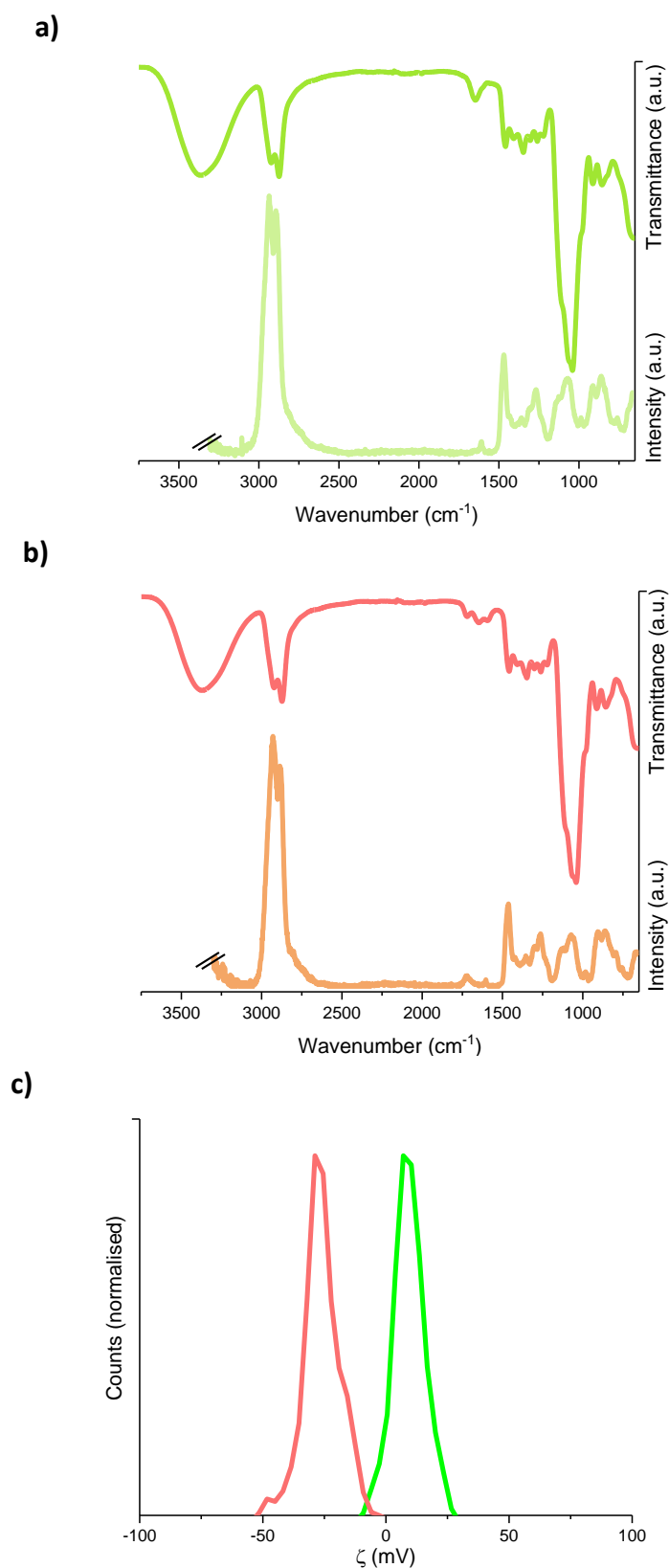


Figure 35: FT-IR (top) and RAMAN spectra (bottom) of a) P(SET-co-NH₂-co-G), displaying amine vibrations at 1600 cm⁻¹ and b) P(SET-co-COOH-co-G), displaying carboxylic vibrations at 1730 cm⁻¹. c) Zeta potential of AuNP@P(SET-co-NH₂-co-G) (green) and AuNP@P(SET-co-COOH-co-G) (red), verifying the introduction of positive (+7 mV) and negative (-29 mV) charge to the surface of 30 nm particles.

Moreover, thiol-ene click-reactions of P(AGE₁₂-co-G) with EtSH and cysteamine hydrochloride were performed, in order to increase the number of amine groups and consequently the positive charge of the polymer. Eight (P(SEt-co-NH₂₍₈₎-co-G)) or eleven (P(SEt-co-NH₂₍₁₁₎-co-G)) amine moieties per polymer were adjusted, as investigated by ¹H-NMR spectroscopy and TNBSA-assay (see **Table 7**).

Table 7: Determination of amine moieties within PG via ¹H-NMR spectroscopy and TNBSA-assay.

Amine-Polymer	Number of amine moieties	
	¹ H-NMR spectroscopy	TNBSA-assay
P(SEt-co-NH₂-co-G)	0.8	1.0
P(SEt-co-NH₂₍₈₎-co-G)	7.5	8.0
P(SEt-co-NH₂₍₁₁₎-co-G)	10.5	10.5

An increase of primary amine groups within the aforementioned amine-PG was further confirmed by FT-IR-spectroscopy. The spectra depicted in **Figure 36a** featured an intensity growth of the vibrations at 3500-3100 cm⁻¹ (asymmetric and symmetric NH₂ stretch) and 1600 cm⁻¹ (NH₂ scissors) for P(SEt-co-NH₂₍₈₎-co-G) and P(SEt-co-NH₂₍₁₁₎-co-G) related to P(SEt-co-NH₂-co-G). With increasing amine content the interaction of the polymers with the SEC column material became attractive, thus P(SEt-co-NH₂₍₈₎-co-G) and P(SEt-co-NH₂₍₁₁₎-co-G) remained longer on the column than P(SEt-co-NH₂-co-G), resulting in a broadening of the band concomitant with increased retention volumes, as displayed in **Figure 36b**. Moreover, **Figure 36c** verified that upon binding of the polymers with increasing amine amount to 15 nm AuNPs, the zeta potential ζ of the particles shifted to more positive values (ζ=7.0 mV-33 mV).

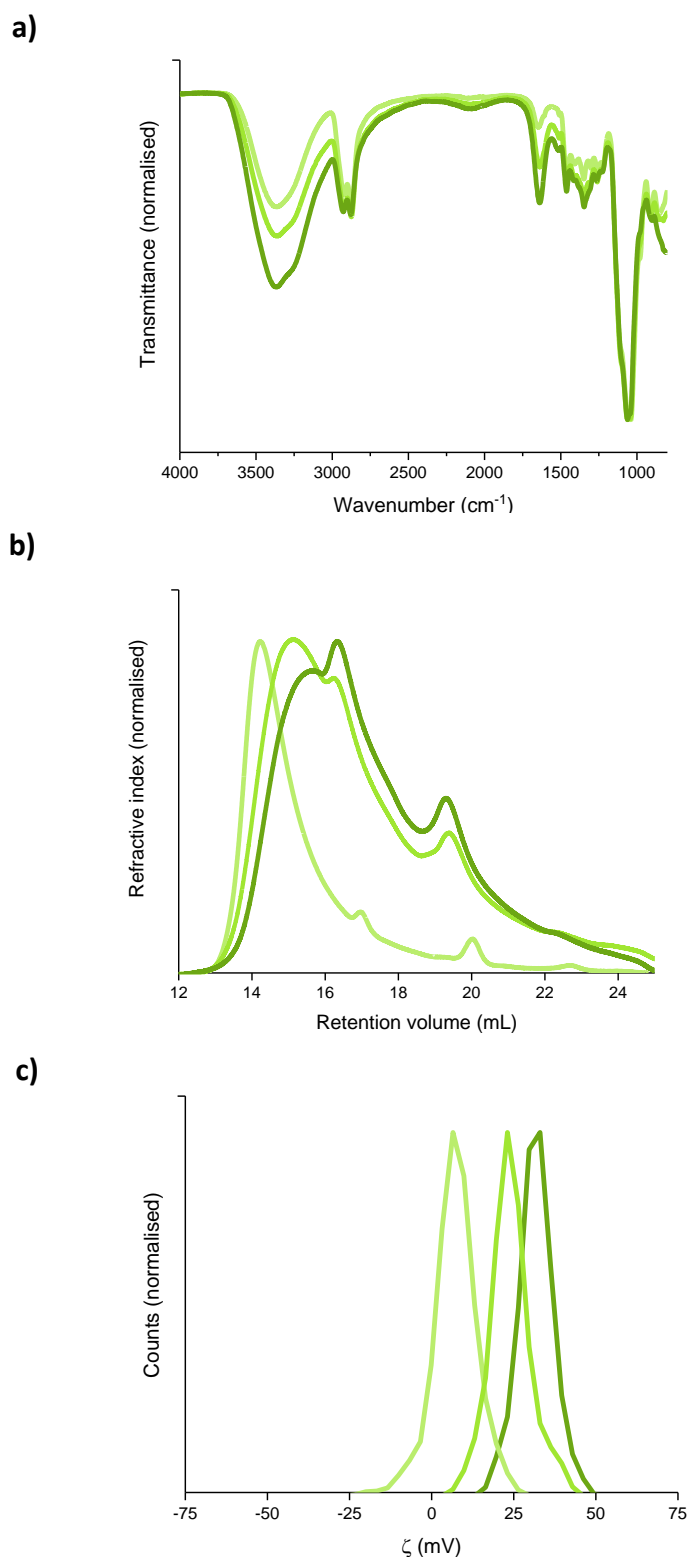
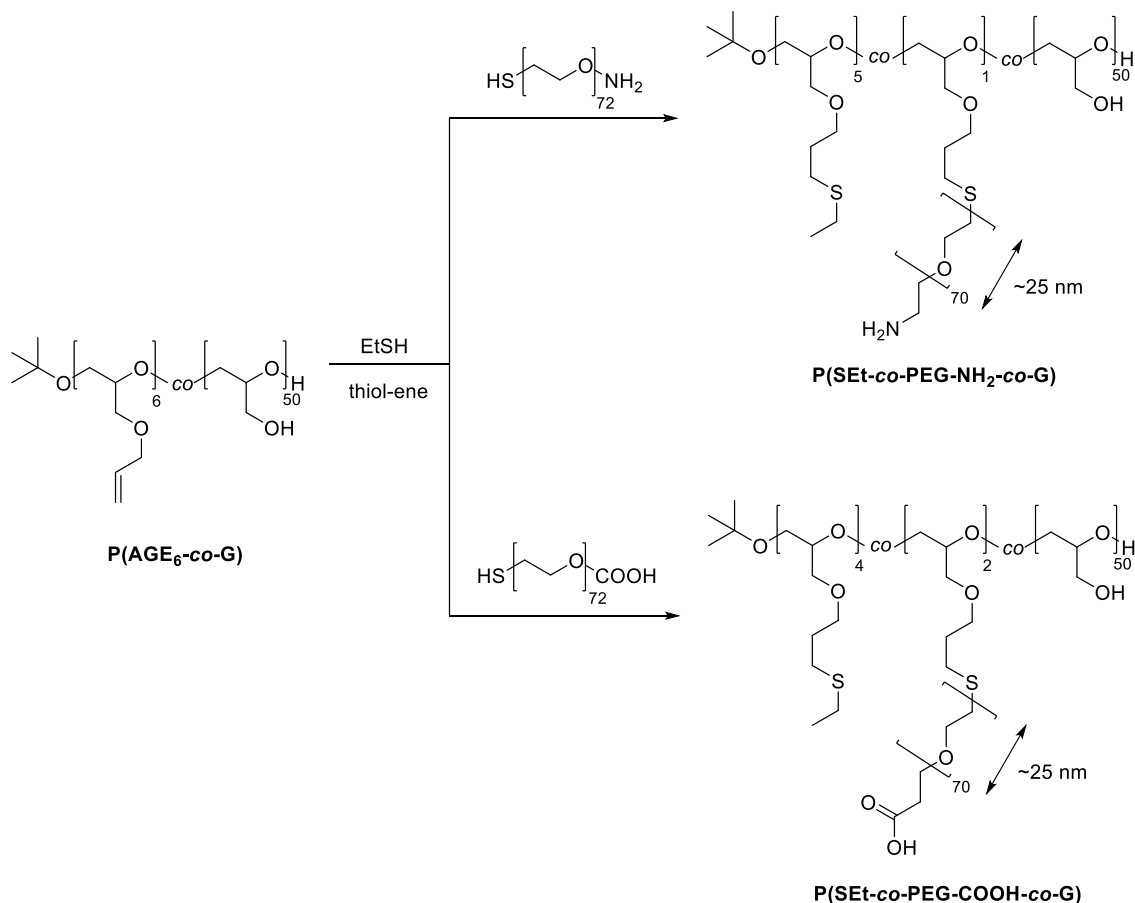


Figure 36: a) FT-IR spectra of *P(SET-co-NH₂-co-G)* (top), *P(SET-co-NH₂₍₈₎-co-G)* (middle) and *P(SET-co-NH₂₍₁₁₎-co-G)* (bottom), featuring increased signal intensities of the amine vibrations at 3500-3100 cm⁻¹ and 1600 cm⁻¹ in the prescribed order. b) SEC elugram of *P(SET-co-NH₂-co-G)* (left), *P(SET-co-NH₂₍₈₎-co-G)* (middle) and *P(SET-co-NH₂₍₁₁₎-co-G)* (right), featuring a band broadening for the latter accompanied by increased retention volumes due to interactions with the column material. c) Zeta potential of 15 nm AuNP modified with *P(SET-co-NH₂-co-G)* (left), *P(SET-co-NH₂₍₈₎-co-G)* (middle) and *P(SET-co-NH₂₍₁₁₎-co-G)* (right), displaying increasingly positive values from +7.0 mV to +23 mV and +33 mV.

In order to introduce a PEG linker (approximate length of 25 nm), keeping the charged groups at distance from the particle surface, P(SET-co-PEG-NH₂-co-G) and P(SET-co-PEG-COOH-co-G) was synthesised. Therefore, a thiol-ene click reaction of P(AGE₆-co-G) with 21 eq. EtSH and 0.2 eq. HS-PEG-NH₂ or HS-PEG-COOH in a mixture of DMF and water was carried out, according to procedures described before (see **Scheme 11**).



Scheme 11: Synthesis of P(SET-co-PEG-NH₂-co-G) and P(SET-co-PEG-COOH-co-G) via bimolecular thiol-ene click reaction with P(AGE₆-co-G), EtSH and HS-PEG-NH₂ or HS-PEG-COOH.

Successful synthesis of P(SET-co-PEG-NH₂-co-G) and P(SET-co-PEG-COOH-co-G) was proven by ¹H-NMR and FT-IR spectroscopy, revealing that one PEG-NH₂ chain and two PEG-COOH chains were introduced to the polymer backbone (see **Section 5.2.9** and **5.2.13**).

P(SET-co-PEG-NH₂-co-G) and P(SET-co-PEG-COOH-co-G) were attached to 15 nm AuNPs, as verified by FT-IR, UV-vis absorbance spectroscopy and DLS measurements (see **Section 5.2.9** and **5.2.13**). The introduction of positive and negative charge to the particle surface was confirmed by zeta-potential investigations, as depicted in **Figure 37**. The relatively low positive value of +2 mV of P(SET-co-PEG-NH₂-co-G) can be attributed to the *per se* negative zeta potential of PEG^[146] and PG (see **Section 3.2.1.2** and **5.2.14**).

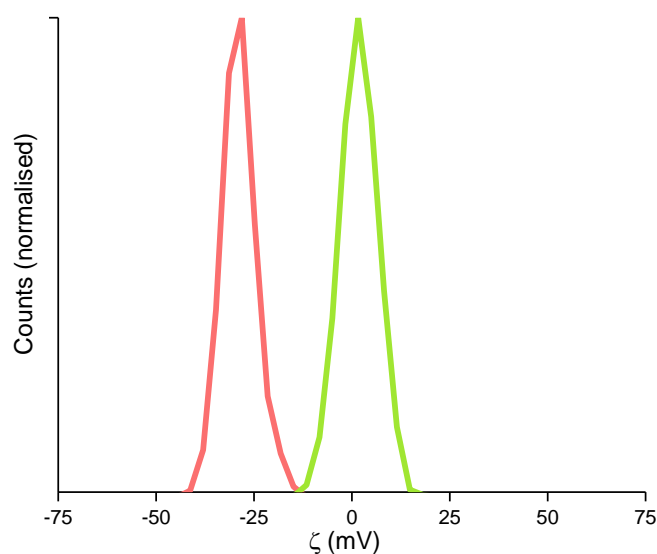
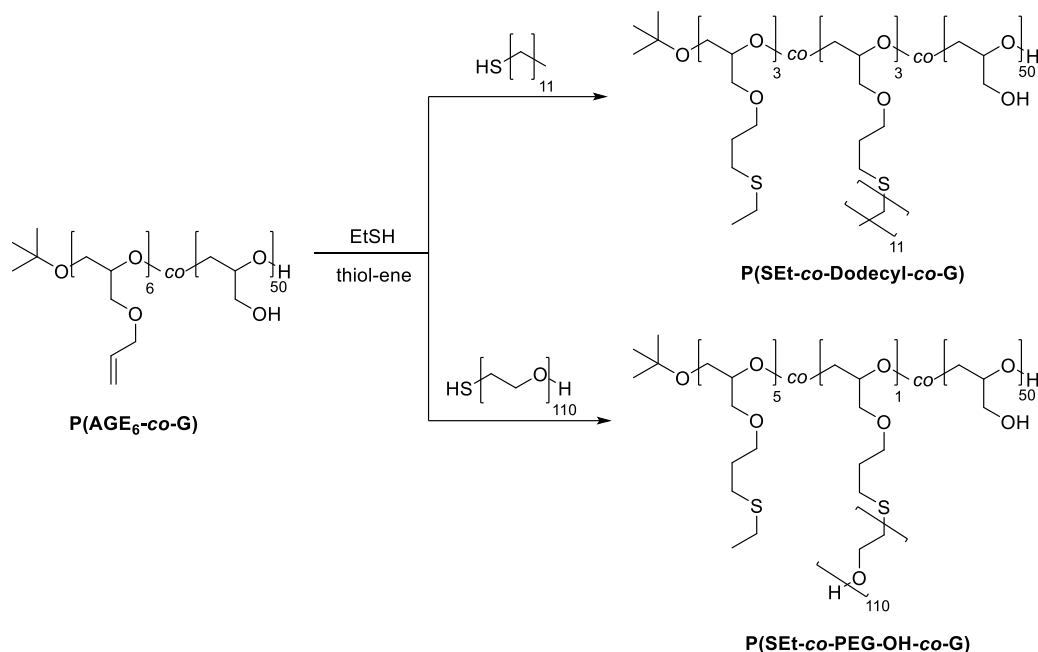


Figure 37: Zeta potential of AuNP@P(SET-co-PEG-NH₂-co-G) (green) and AuNP@P(SET-co-PEG-COOH-co-G) (red), verifying the introduction of positive (+2 mV) and negative (-28 mV) charge to the surface of 15 nm particles.

3.2.1.2 Synthesis of PG with hydrophilic and hydrophobic chains for AuNP functionalisation

In order to introduce hydrophobicity and hydrophilicity, 1-dodecanethiol and HS-PEG-OH were introduced to the backbone of P(AGE₆-co-G) via a thiol-ene click reaction, according to procedures described before (see **Scheme 12**).



Scheme 12: Synthesis of P(SET-co-Dodecyl-co-G) and P(SET-co-PEG-OH-co-G) via bimolecular thiol-ene click reaction with P(AGE₆-co-G), EtSH and 1-dodecanethiol or HS-PEG-OH.

Successful synthesis of P(SET-co-PEG-OH-co-G) and P(SET-co-Dodecyl-co-G) and successive functionalisation of 15 nm AuNPs was proven by ¹H-NMR, FT-IR and UV-vis spectroscopy, as well as via DLS (see **Section 5.2.14** and **5.2.15**). ¹H-NMR investigations revealed that one PEG-OH and three dodecyl chains were introduced to PG. Contact angle based measurements, where the polymers were coated on a substrate and the interaction with a water droplet was observed (see **Figure 38**), verified an increased hydrophobicity in case of **b)** P(SET-co-Dodecyl-co-G) (27 °), compared to **a)** P(SET-co-PEG-OH-co-G) (9 °).

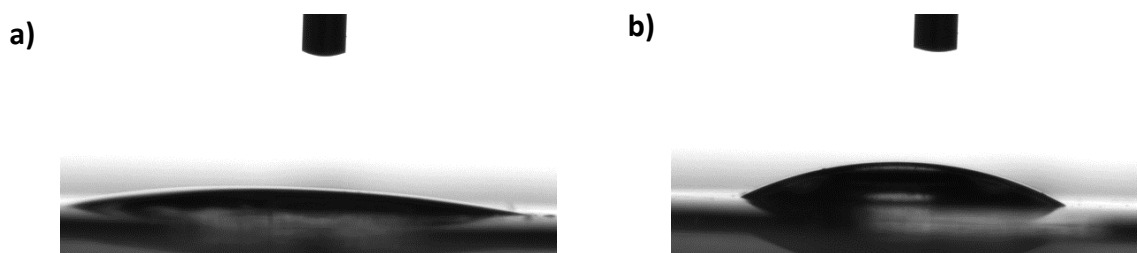
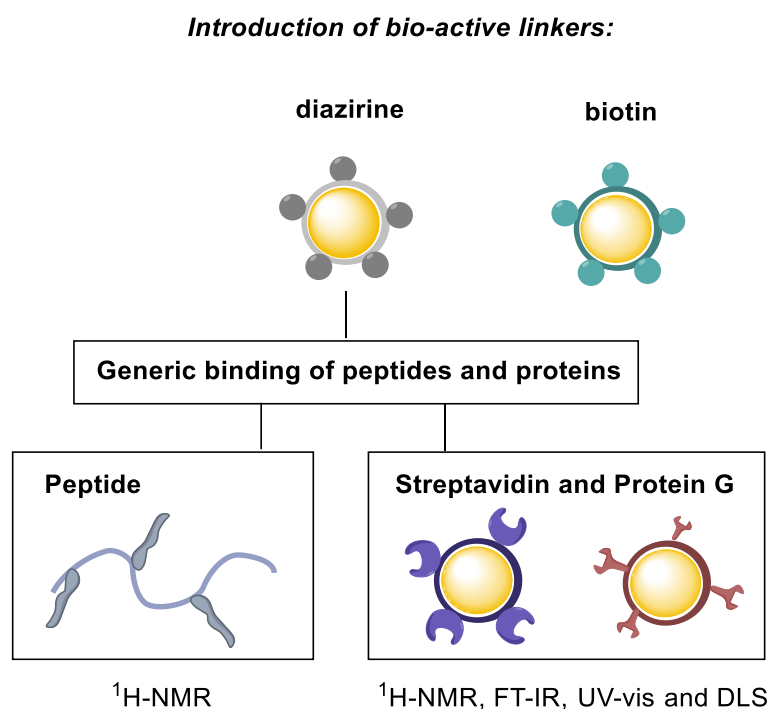


Figure 38: Contact angle based measurements of **a)** P(SET-co-PEG-OH-co-G), displaying an average contact angle of 9 ° and **b)** P(SET-co-Dodecyl-co-G) with an average contact angle of 27 °.

3.2.2 Introduction of bio-active linkers to the AuNP surface

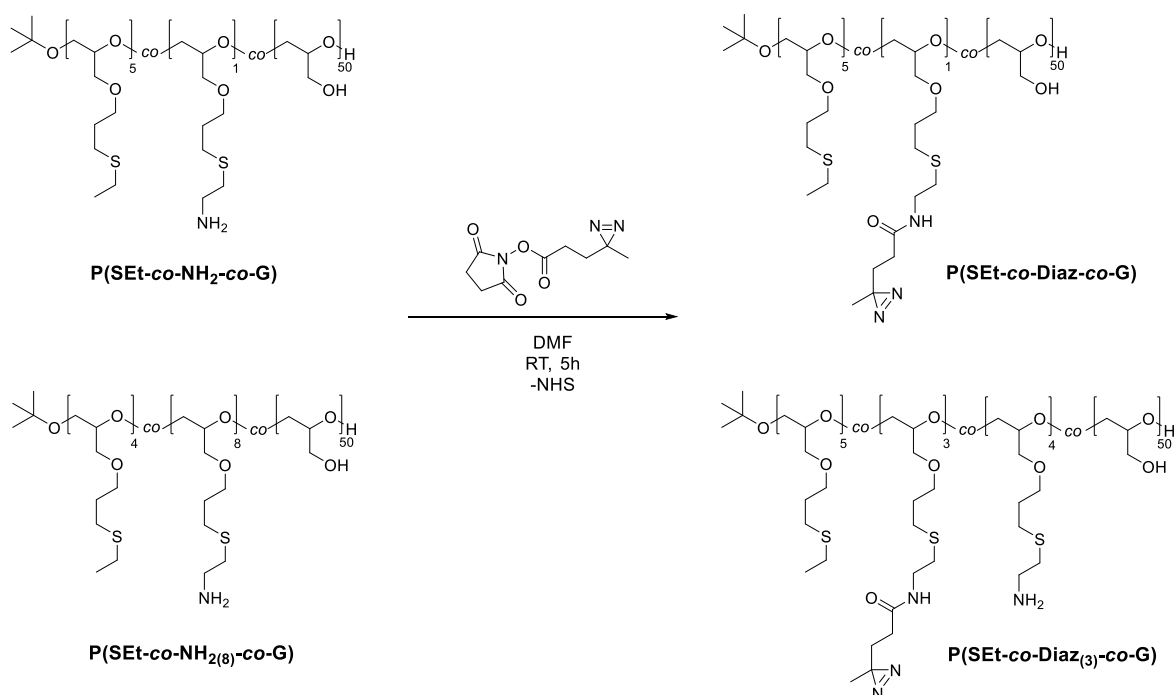
In this Section the synthesis of PG with bio-active linkers, bearing diazirine or biotin moieties and successive AuNP functionalisation was carried out. The generic binding of diazirine groups was proven by reaction with distinct biomolecules, including peptides and proteins. While the functionalisation of PG with a peptide was applied as model reaction for $^1\text{H-NMR}$ spectroscopic characterisation, upon introduction of useful proteins such as streptavidin and protein G to PG successive particle functionalisation was conducted and thoroughly verified by $^1\text{H-NMR}$, FT-IR and UV-vis absorbance spectroscopy and DLS, as depicted in **Scheme 13**.



Scheme 13: Depiction of AuNPs bearing bio-active linker, namely diazirine and biotin. While the binding of a peptide to diazirine modified PG was used for detailed polymeric $^1\text{H-NMR}$ investigations, protein binding, including streptavidin and protein G was also characterised with regard to the particle functionalisation.

3.2.2.1 Synthesis of PG with photo-active diazirine groups

The introduction of diazirine moieties to the polymer backbone provides the facility of a photo-initiated binding of biomolecules. Based on P(SET-co-NH₂-co-G) and P(SET-co-NH₂(₈)-co-G) two diazirine functionalised polymers were synthesised, termed as P(SET-co-Diaz-co-G) and P(SET-co-Diaz(₃)-co-G), respectively. The designation is clarified in the following. In both cases the diazirine linker was introduced via straightforward active-ester reaction with NHS-diazirine (1.7-fold or 1.0-fold excess regarding the amine groups) at room temperature for 5 h as depicted in **Scheme 14**.



Scheme 14: Synthesis of P(SET-co-Diaz-co-G) and P(SET-co-Diaz(₃)-co-G) via active-ester reaction of P(AGE₆-co-G) with NHS-diazirine.

Two-dimensional 600 MHz ¹H- and ¹³C-NMR investigations (see **Section 5.2.16**) proved successful synthesis of P(SET-co-Diaz-co-G), whereas 300 MHz ¹H-NMR studies verified the formation of P(SET-co-Diaz(₃)-co-G). Latter spectrum is depicted in **Figure 39** featuring signals at 3.44 ppm (**27**), 2.23 ppm (**29**), 1.80-1.66 ppm (**30**) and 1.10 ppm (**31**), ascribed to the diazirine linker. Despite of excessive amounts of NHS-diazirine, both diazirine-functionalised polymers displayed proton signals of unconverted amine groups at 3.26 ppm (**28**) and 2.90 ppm (**25**), as exemplarily depicted for P(SET-co-Diaz(₃)-co-G) in **Figure 39**.

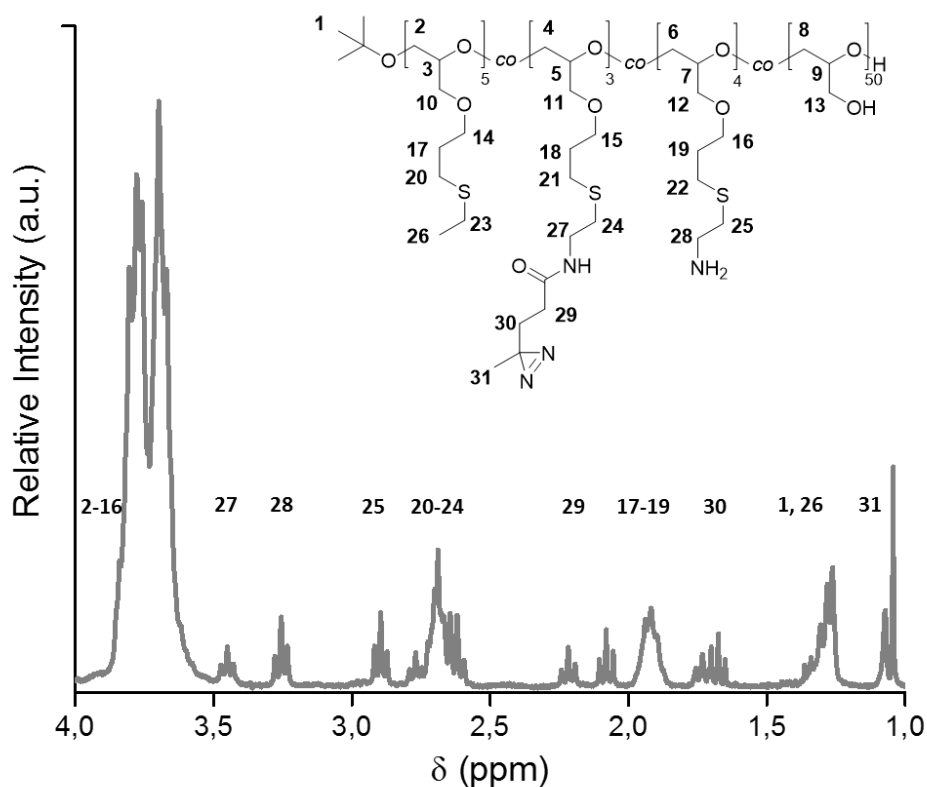


Figure 39: $^1\text{H-NMR}$ spectrum of $P(\text{SEt-co-Diaz}_{(3)}\text{-co-G})$ displaying proton signals at 3.44 ppm (27), 2.23 ppm (29), 1.80-1.66 ppm (30) and 1.10 ppm (31) ascribed to the diazine linker and at 3.26 ppm (28) and 2.90 ppm (25) corresponding to residual amine groups.

Integration of the $^1\text{H-NMR}$ signals revealed that $P(\text{SEt-co-Diaz-co-G})/P(\text{SEt-co-Diaz}_{(3)}\text{-co-G})$ carried approximately one/three diazine and 0.2/4 amine groups, as summarised in **Table 8**. Since the amount of residual amine groups within $P(\text{SEt-co-Diaz-co-G})$ was negligible small it was not taken into account in the structural formula. The impact of these residual amine groups on the following experiments could not be clarified in this chapter, but is reassumed in **Section 3.2.2.1.4**.

Table 8: Functional composition of diazine-modified PG, displaying the amount of thioether-, amine- and diazine-moieties.

	SEt	NH ₂	Diaz
$P(\text{SEt-co-Diaz-co-G})$	4.8	0.2	1.0
$P(\text{SEt-co-Diaz}_{(3)}\text{-co-G})$	5.0	4.0	3.0

A successful synthesis of P(SET-co-Diaz-co-G) and P(SET-co-Diaz₍₃₎-co-G) was further verified by UV-vis (see **Figure 40a**) and FT-IR spectroscopy (see **Figure 40b**), displaying a maximal absorbance peak at 360 nm, ascribed to the diazirine unit and a C=O stretch (1650 cm⁻¹, amide I) and N-H bend (1550 cm⁻¹, amide II) vibration corresponding to the diazirine linker, respectively. Both signal intensities increased in case of P(SET-co-Diaz₍₃₎-co-G) owing to a higher amount of diazirine moieties.

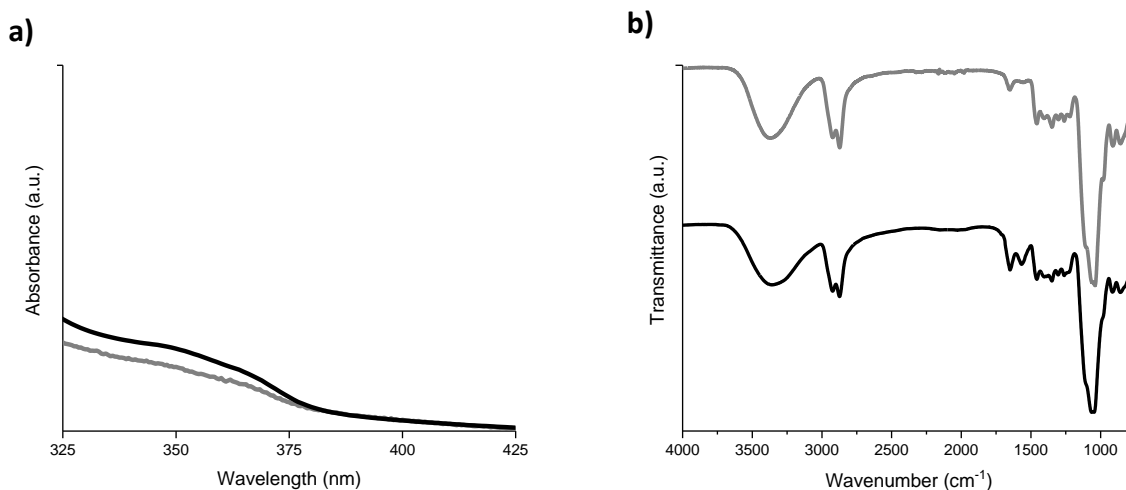


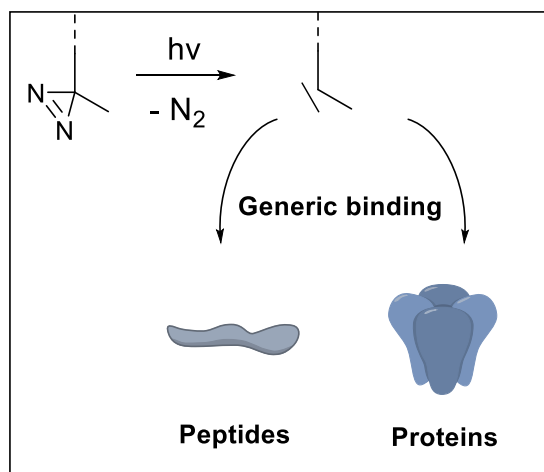
Figure 40: a) UV-vis absorbance spectra of P(SET-co-Diaz-co-G) (grey) and P(SET-co-Diaz₍₃₎-co-G) (black), displaying a maxima at 360 nm ascribed to the diazirine moiety. b) FT-IR spectra of P(SET-co-Diaz-co-G) (grey) and P(SET-co-Diaz₍₃₎-co-G) (black), featuring the amide I and amide II vibration at 1650 cm⁻¹ and 1550 cm⁻¹.

In order to introduce a PEG linker, keeping the diazirine group at distance from the particle surface, P(SET-co-PEG-Diaz-co-G) was synthesised based on P(SET-co-PEG-NH₂-co-G). Likewise to P(SET-co-Diaz₍₃₎-co-G) according to ¹H-NMR spectroscopy merely half of the amine groups within P(SET-co-PEG-NH₂-co-G) were converted, resulting in a diazirine functionalisation of every second polymer. UV-vis absorbance and FT-IR investigations additionally confirmed successful synthesis of P(SET-co-PEG-Diaz-co-G) (see **Section 5.2.18**).

The coating of AuNPs with diazirine-functionalised PG was verified in **Section 3.2.2.1.3** by comparison with the respective bio-functionalised consecutive products.

3.2.2.1.1 Diazirine-initiated binding of biomolecules

Upon UV-light irradiation diazirine moieties decompose under the release of N_2 into highly reactive carbenes that readily form a covalent bond with biomolecules through C–C, C–H, and X–H (X=heteroatom) insertions, as depicted in **Scheme 15**.^[147-148] Due to the non-specific nature of carbenes neither modifications of the biomolecules, nor further additives are needed enabling a generic bio-functionalisation.^[149]

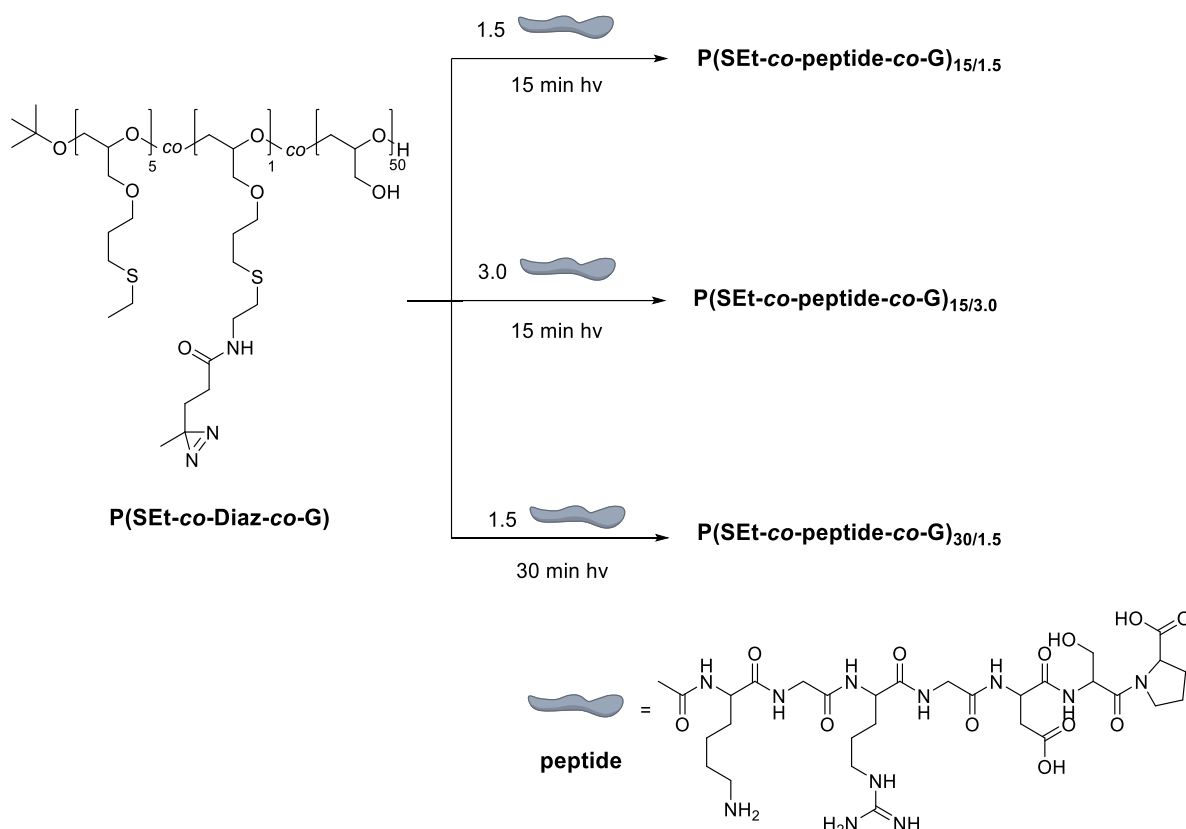


Scheme 15: Depiction of the photo-triggered conversion of diazirines into reactive carbenes, enabling a generic binding of biomolecules.

In the following **Section 3.2.2.1.2** firstly a model reaction of P(SEt-co-Diaz-co-G) with a small molecular weight peptide (757 g/mol) was carried out, providing detailed investigations by ¹H-NMR spectroscopy. Secondly, the linkage of large proteins such as streptavidin (60 kDa) and protein G (22 kDa) to P(SEt-co-Diaz-co-G) or P(SEt-co-Diaz₍₃₎-co-G) was examined in **Section 3.2.2.1.3**.

3.2.2.1.2 Synthesis of peptide functionalised PG

In order to investigate appropriate irradiation conditions and concentration ratios for photo-triggered diazirine functionalisation, P(SET-co-Diaz-co-G) was irradiated at 365 nm for 15 min (1.5- or 3.0-fold excess) or 30 min (1.5-fold excess) with peptide AKGRGDSP in water, referred to as P(SET-co-peptide-co-G)_{15/1.5}, P(SET-co-peptide-co-G)_{15/3.0} and P(SET-co-peptide-co-G)_{30/1.5}, as summarised in **Scheme 16**. Throughout this section the impact of residual amine groups (0.2) within P(SET-co-Diaz-co-G) was suggested to be negligible, but is reassumed in **Section 3.2.2.1.4**.



Scheme 16: Investigation of distinct irradiation durations and concentration ratios for the photo-triggered binding of peptide AKGRGDSP to P(SET-co-Diaz-co-G). The structural formula of the peptide is depicted.

Further conditions, such as solvent volume, distance to the radiation source and purification by dialysis remained unchanged. It has to be noted that the irradiation in an open reaction vessel turned out to be mandatory, since the absorption of the flask reduced the intensity of the incoming light, hampering the activation of diazirines.

The $^1\text{H-NMR}$ signals in **Figure 41** at 4.42-4.17 ppm, 2.02 ppm and 1.52-1.39 ppm (marked with blue beam) attributed to peptide protons verified successful synthesis of $\text{P}(\text{SEt-co-peptide-co-G})_{15/3.0}$ (bottom, black) and $\text{P}(\text{SEt-co-peptide-co-G})_{30/1.5}$ (middle, blue). The spectra of $\text{P}(\text{SEt-co-peptide-co-G})_{15/1.5}$ (top, grey), however, lacked these signals concluding that a 1.5-fold excess of peptide under an irradiation time of 15 min was not sufficient to trigger a binding via diazirines.

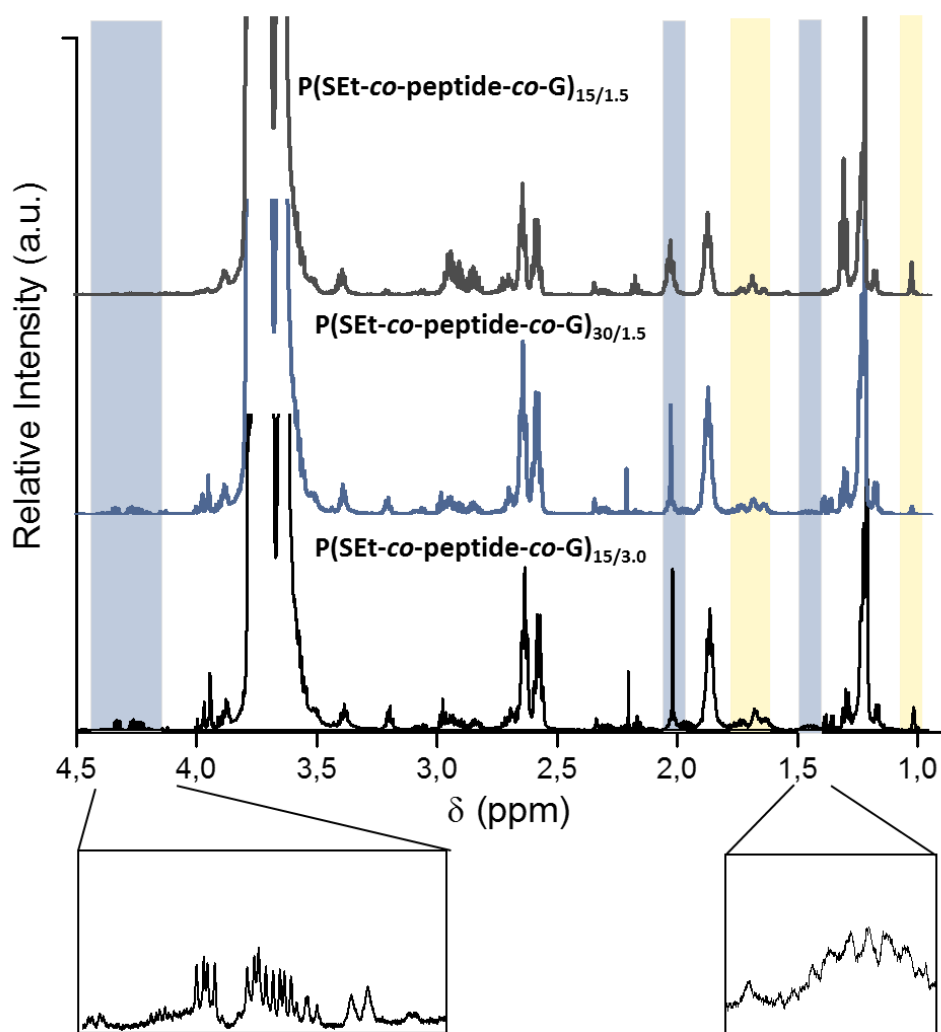


Figure 41: $^1\text{H-NMR}$ spectra of $\text{P}(\text{SEt-co-peptide-co-G})_{15/1.5}$ (top, grey), $\text{P}(\text{SEt-co-peptide-co-G})_{30/1.5}$ (middle, blue) and $\text{P}(\text{SEt-co-peptide-co-G})_{15/3.0}$ (bottom, black), displaying proton signals of residual diazirine moieties (marked with yellow beam). For $\text{P}(\text{SEt-co-peptide-co-G})_{30/1.5}$ (middle, blue) and $\text{P}(\text{SEt-co-peptide-co-G})_{15/3.0}$ (bottom, black) signals ascribed to peptide protons (marked with blue beam) were detectable, which are magnified below the spectra, verifying successful peptide binding via diazirine groups.

$^1\text{H-NMR}$ integration of the peptide-ascribed signals at 4.42-4.17 ppm, 2.02 ppm and 1.52-1.39 ppm (marked with blue beam in **Figure 41**) within $\text{P}(\text{SEt-co-peptide-co-G})_{15/3.0}$ (bottom) and $\text{P}(\text{SEt-co-peptide-co-G})_{30/1.5}$ (middle) determined a peptide functionalisation of every 1.5th (67 %) and 2nd (50 %) polymer, respectively. The presence of a triplet at 1.68 ppm and singlet

at 1.01 ppm (marked with yellow beam in **Figure 41**) belonging to the methylene and methyl group next to the diazirine unit additionally showed that not every polymer was functionalised with a peptide and that unconverted diazirine units remained. For clarity, **Figure 42** demonstrates a comparison of the $^1\text{H-NMR}$ spectra of $\text{P}(\text{SEt-co-peptide-co-G})_{30/1.5}$ (top, blue) and $\text{P}(\text{SEt-co-Diaz-co-G})$ (bottom, black). The reduced intensity of the signals at 1.68 ppm (**a**) and at 1.01 ppm (**b**) in case of $\text{P}(\text{SEt-co-peptide-co-G})_{30/1.5}$ nonetheless indicated peptide introduction, since latter changed the environment of the protons adjacent to the former diazirine unit. Provoking a shift and splitting of the former methylene triplet (**a**) to a multiplet at 1.79-1.56 ppm (**a'**) and of the methyl singlet (**b**) to most probably a multiplet at 1.19-1.13 ppm (**b'**). For protons **b'**, an exact assignment to the respective signals was challenging owing to an overlap with signals of the initiating ^tBu -group.

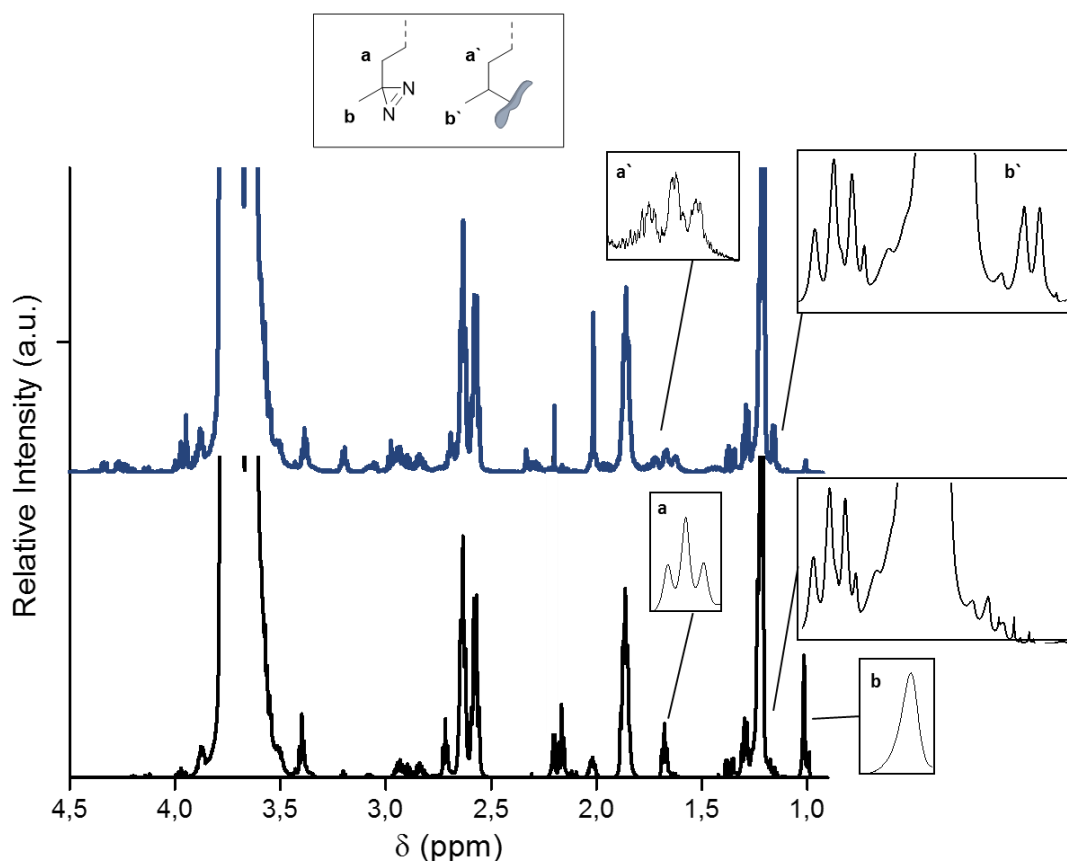


Figure 42: $^1\text{H-NMR}$ spectra of $\text{P}(\text{SEt-co-peptide-co-G})_{30/1.5}$ (top, blue) featuring decreased intensity of protons adjacent to the diazirine group (**a+b**) and displaying the presence of protons adjacent to the peptide (**a'+b'**), indicating successful introduction of the peptide. In contrast, $\text{P}(\text{SEt-co-Diaz-co-G})$ (bottom, black) merely displayed protons **a+b**.

The signal intensities of the methylene group at 1.68 ppm (**a**) and methyl group at 1.01 ppm (**b**) within $\text{P}(\text{SEt-co-peptide-co-G})_{15/3.0}$ and $\text{P}(\text{SEt-co-peptide-co-G})_{30/1.5}$ concluded residual diazirine functionalisation of every 3th (33%) and 5th (20%) polymer, respectively.

Table 9 summarises that for $P(\text{SEt-co-peptide-co-G})_{15/3.0}$ the combination of the diazirine (33 %) and peptide (67 %) functionalised polymers equalled 100 %, indicating no other products. In contrast, for $P(\text{SEt-co-peptide-co-G})_{30/1.5}$ 30 % of products remained that neither carried a peptide, nor a diazirine unit. This residual product most probably consisted of intermolecular linked polymers, termed as $P(\text{SEt-co-Diaz-co-G})\text{-}P(\text{SEt-co-Diaz-co-G})$, as a 1.5-fold excess did not guarantee peptide saturation of diazirine moieties (see **Figure 42**).

Table 9: Polymer composition within peptide-modified PG, including peptide-, diazirine- and polymer-polymer functions.

<i>Polymer</i>	<i>Functionalisation (%)</i>		
	<i>Peptide</i>	<i>Diazirine</i>	<i>Polymer-Polymer</i>
<i>$P(\text{SEt-co-peptide-co-G})_{15/1.5}$</i>	-	25	75
<i>$P(\text{SEt-co-peptide-co-G})_{15/3.0}$</i>	67	33	-
<i>$P(\text{SEt-co-peptide-co-G})_{30/1.5}$</i>	50	20	30

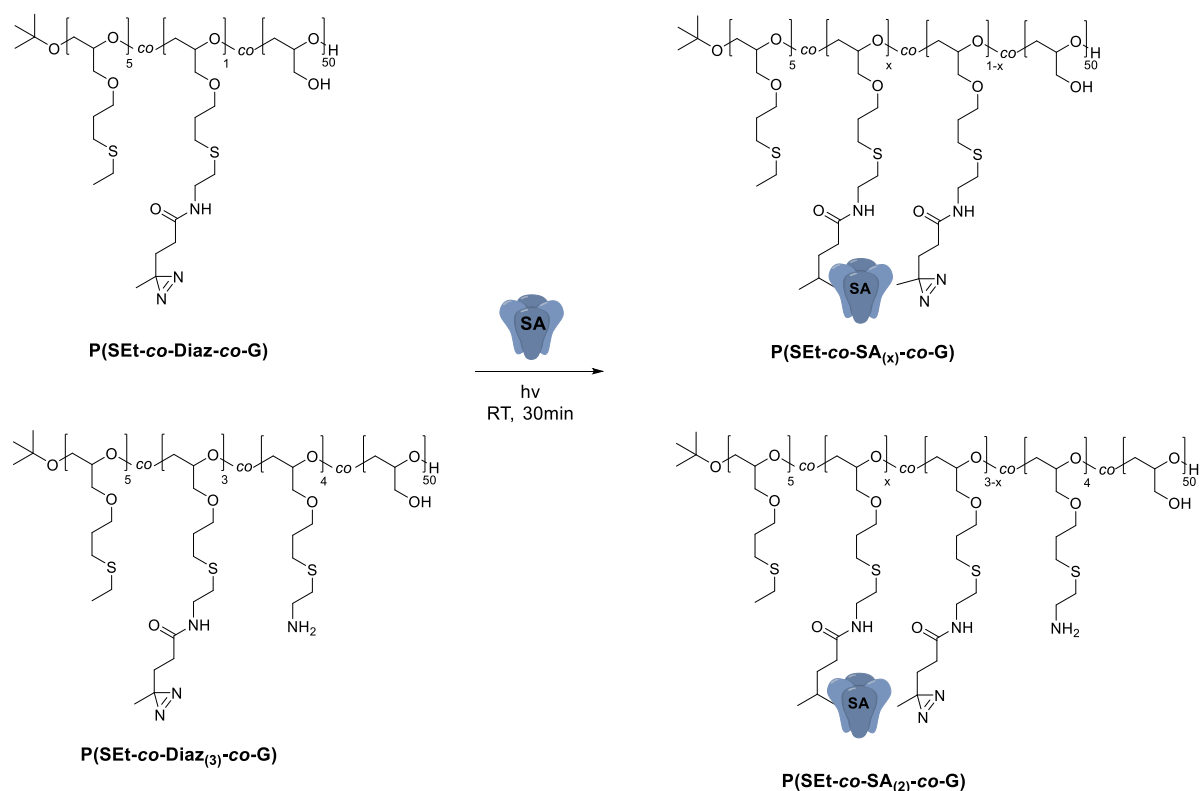
Investigations of $P(\text{SEt-co-peptide-co-G})_{15/1.5}$, where no peptide (or at least no via $^1\text{H-NMR}$ investigations detectable amount of peptide) was bound to PG, additionally confirmed this conclusion. $^1\text{H-NMR}$ studies determined a reduced signal intensity of the methylene group at 1.68 ppm (**a**) and methyl group at 1.01 ppm (**b**), corresponding to 25% unconverted diazirine groups. Since no peptide was linked, merely the reaction of the polymer with itself was reasonable, resulting in 75% $P(\text{SEt-co-Diaz-co-G})\text{-}P(\text{SEt-co-Diaz-co-G})$.

Most probably, a peptide-excess higher than 3.0 under an irradiation time of 30 min could increase the amount of bound peptide, but was not further investigated throughout this chapter.

3.2.2.1.3 Synthesis of streptavidin functionalised PG

The introduction of streptavidin (SA) to PG enables successive functionalisation with any biotinylated compound. The conjugation of SA and biotin ($K_d \sim 10^{-14}$ mol/L)^[150] is one of the strongest non-covalent interaction in nature and proved to be extremely valuable in bio-applications, including affinity chromatography, immunoassays and western blotting.

The functionalisation of P(SET-co-Diaz-co-G) and P(SET-co-Diaz₍₃₎-co-G) with SA was conducted according to procedures that proved to be successful in the previous **Section 3.2.2.1.2**, and was termed as P(SET-co-SA_(x)-co-G) and P(SET-co-SA₍₂₎-co-G) respectively. It has explicitly to be mentioned that the designation (x) and (2) does not refer to the SA amount in the polymers, but on the protein amount on 30 nm AuNPs upon functionalisation with P(SET-co-SA_(x)-co-G) and P(SET-co-SA₍₂₎-co-G), which is clarified in **Section 3.2.2.1.4.1**. Yet, for reasons of consistency the designations were introduced at this point. Briefly, the polymers were irradiated at 365 nm for 30 min with SA in water and purified by dialysis, as depicted in **Scheme 17**.



Scheme 17: Synthesis of P(SET-co-SA_(x)-co-G) and P(SET-co-SA₍₂₎-co-G) via photo-triggered binding of P(SET-co-Diaz-co-G) and P(SET-co-Diaz₍₃₎-co-G) to SA.

The characterisation of P(SET-co-SA_(x)-co-G) and P(SET-co-SA₍₂₎-co-G) via ¹H-NMR spectroscopy turned out to be more challenging than that of P(SET-co-peptide-co-G) described in the previous **Section 3.2.2.1.2**. Due to the high molecular weight and complex structure of streptavidin an exact assignment of ¹H-NMR signals to the respective protein protons was not feasible, rendering the correlation to polymer protons and thus the determination of the functionalisation degree impossible.

Figure 43 proved that in particular ¹H-NMR investigations of P(SET-co-SA_(x)-co-G) (top, blue) were challenging owing to the scarce intensity of SA reference signals suggesting very small percentages of bio-functionalised polymer. For clarity **Figure 43** additionally displays the spectrum of P(SET-co-Diaz-co-G) (bottom, black).

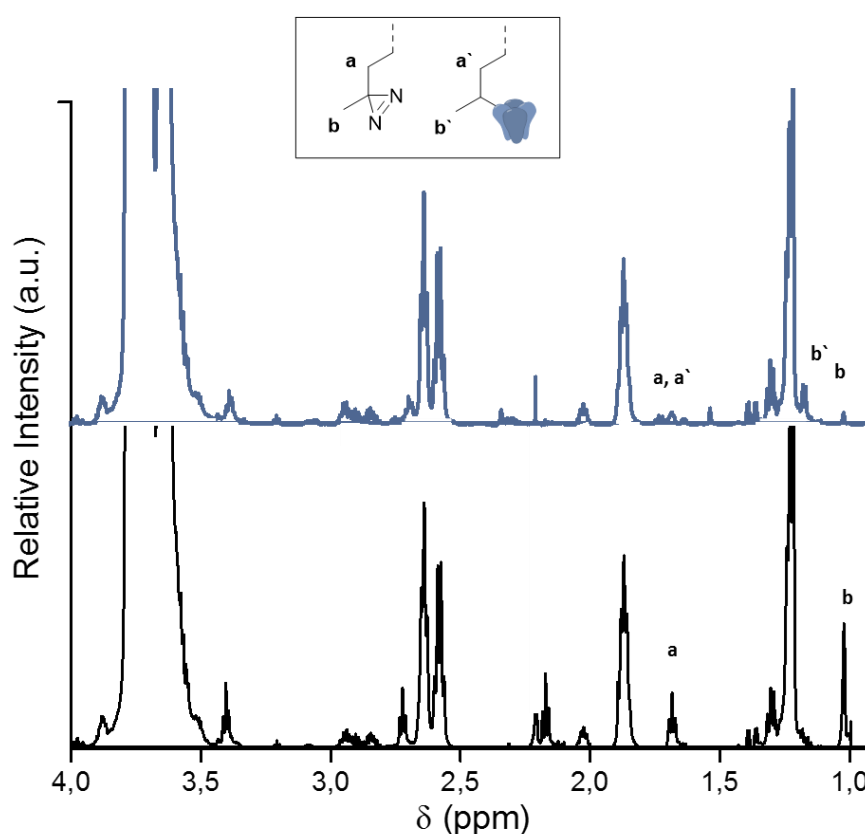


Figure 43: ¹H-NMR spectra of P(SET-co-SA_(x)-co-G) (top, blue), featuring decreased signal intensity of protons adjacent to the diazirine group (a+b) and most probably next to streptavidin (a'+b'), in comparison to P(SET-co-Diaz-co-G) (bottom, black), merely displaying protons a+b.

However, based on ¹H-NMR information gained by P(SET-co-peptide-co-G) (see **Section 3.2.2.1.2**), it was shown that the reduced intensity of the triplet at 1.68 ppm (**a**) and singlet at 1.01 ppm (**b**), belonging to the methylene and methyl group next to the diazirine unit could indicate a successful reaction. Here, SA binding changed the environment of the

protons adjacent to the former diazirine unit, provoking a shift and splitting of the former methylene triplet to a multiplet at 1.79-1.56 ppm (**a`**) and of the methyl singlet to most probably a multiplet at 1.19-1.13 ppm (**b`**). As already mentioned in **Section 3.2.2.1.2**, an exact assignment of protons **b`** to the respective signals was not possible owing to an overlap with signals of the ^tBu group.

The reduced signal intensity of the methyl group at 1.01 ppm (**b**) within P(SEt-co-SA_(x)-co-G) concluded unconverted diazirine groups in every 4th (29 %) polymer. The other percentage most probably consisted of a mixture of P(SEt-co-SA_(x)-co-G) and P(SEt-co-Diaz-co-G)-P(SEt-co-Diaz-co-G), as concluded for P(SEt-co-peptide-co-G) in **Section 3.2.2.1.2**. The composition of this mixture and concomitantly the successful synthesis of P(SEt-co-SA_(x)-co-G), however, could not be clarified by ¹H-NMR investigations within this thesis. Therefore, characterisation methods upon particle functionalisation providing a higher sensitivity towards SA were applied, including laser-triggered cell experiments (see **Section 3.3.4**).

In contrast, P(SEt-co-SA₍₂₎-co-G) featured detectable amounts of SA for ¹H-NMR spectroscopic investigations (see **Figure 44**). The appearance of SA reference signals at 3.29-3.03 ppm, 1.49-1.35 ppm and 0.99-0.54 ppm (marked with blue beam) confirmed successful introduction of the protein. Integration of the methyl signal corresponding to unconverted diazirine groups at 1.01 ppm (marked with yellow beam) was error-prone due to an overlap with SA signals, but concluded residual diazirine functionalisation of every 3th (33 %) polymer. Nonetheless, a correlation of polymer to SA signals and thus a quantification of SA within P(SEt-co-SA₍₂₎-co-G) was not possible, due to the complex structure of the protein. Once more, it has to be mentioned that the designation (2) in P(SEt-co-SA₍₂₎-co-G) did not refer to the amount of SA functionalities within the polymer and is clarified in **Section 3.2.2.1.4.1**. These ¹H-NMR investigations raised to question if all of the detected SA in the spectra of P(SEt-co-SA₍₂₎-co-G) was covalently linked or if in fact amounts of adsorbed protein contributed to the signal intensities at 3.29-3.13 ppm, 1.49-1.35 ppm and 0.99-0.54 ppm (marked with blue beam in **Figure 44**), which is clarified in the following **Section 3.2.2.1.4**.

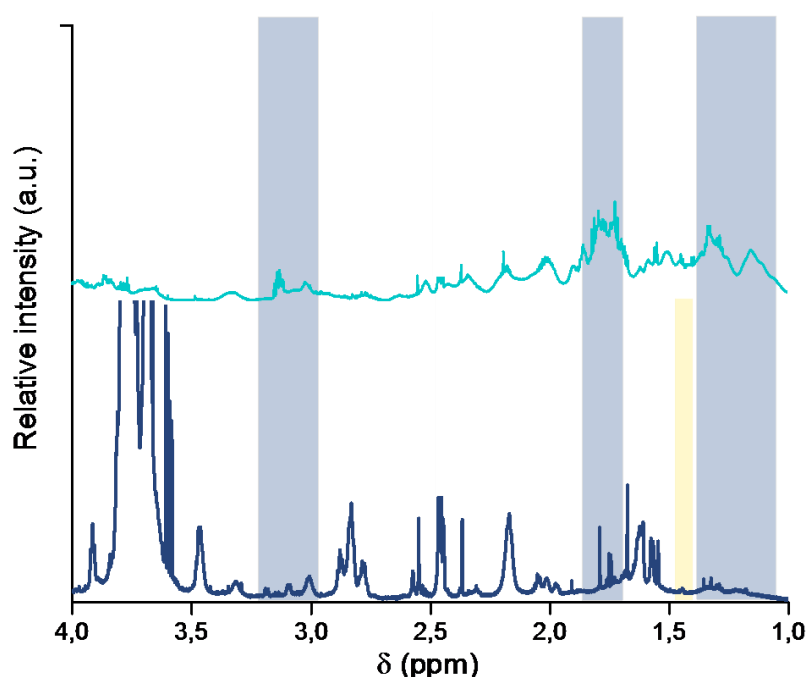


Figure 44: $^1\text{H-NMR}$ spectra of $\text{P}(\text{SEt-co-SA}_{(2)}\text{-co-G})$ (bottom, dark blue), featuring reference signals of streptavidin (top, light blue), additionally marked with blue beam. The methyl signal of residual diazirine moieties is marked with a yellow beam.

A qualitative proof of SA within $\text{P}(\text{SEt-co-SA}_{(2)}\text{-co-G})$ was moreover demonstrated by UV-vis absorbance investigations in **Figure 45a**, displaying an absorbance peak around 280 nm, caused by the $\pi\text{-}\pi^*$ absorption of aromatic amino acids within SA. Further, the absence of the diazirine absorption around 360 nm confirmed successful conversion of these moieties. The FT-IR spectra of $\text{P}(\text{SEt-co-SA}_{(x)}\text{-co-G})$ and $\text{P}(\text{SEt-co-SA}_{(2)}\text{-co-G})$ in **Figure 45b** featured an intensity increase of the amide vibrations at 1650 cm^{-1} (C=O stretch) and 1550 cm^{-1} (N-H bend) relative to the respective diazirine compounds (see **Figure 40a**), which was higher for $\text{P}(\text{SEt-co-SA}_{(2)}\text{-co-G})$ owing to larger amounts of SA. Moreover, the SEC elugram of $\text{P}(\text{SEt-co-SA}_{(2)}\text{-co-G})$ in **Figure 45c** corresponded to the one of pure SA, confirming functionalisation of the polymer with SA.

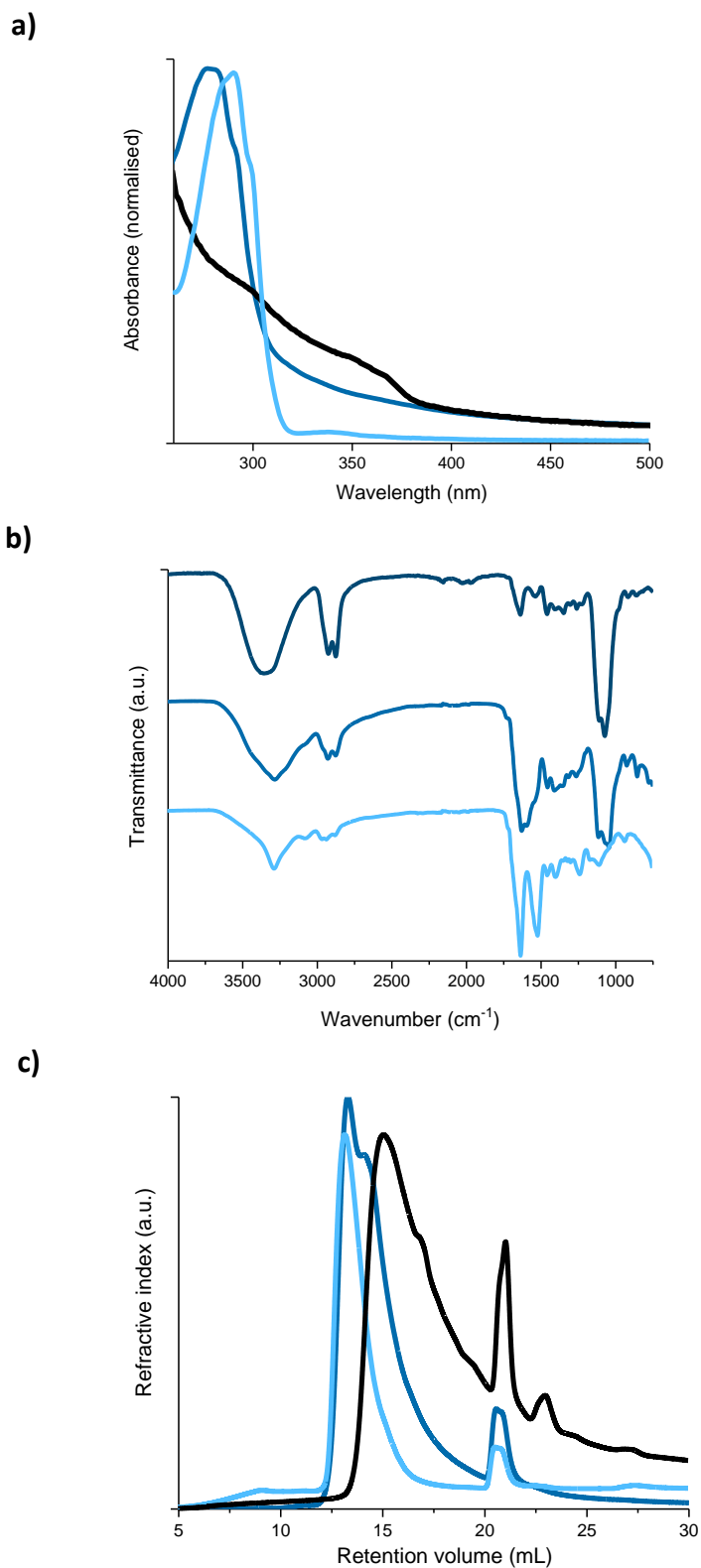


Figure 45: a) UV-vis absorbance spectra of $P(\text{SEt-co-Diaz}_{(3)\text{-co-G}}$ (black) and $P(\text{SEt-co-SA}_{(2)\text{-co-G}}$ (dark blue), lacking the diazirine absorbance at 360 nm and corresponding to the one of pure SA (light blue). b) FT-IR spectra of $P(\text{SEt-co-SA}_{(x)\text{-co-G}}$ (dark blue, top) and $P(\text{SEt-co-SA}_{(2)\text{-co-G}}$ (medium blue, middle), displaying an increase of the amide vibrations at 1650-1550 cm^{-1} ascribed to SA (light blue, bottom). c) SEC elugramm of $P(\text{SEt-co-Diaz}_{(3)\text{-co-G}}$ (black) and $P(\text{SEt-co-SA}_{(2)\text{-co-G}}$ (dark blue), with the latter corresponding to the one of pure SA (light blue).

3 Results and Discussion

It was shown that regarding P(SEt-co-SA_(x)-co-G) merely FT-IR spectroscopy clearly proved successful functionalisation with SA. In case of P(SEt-co-SA₍₂₎-co-G), ¹H-NMR, UV-vis and FT-IR spectra displayed signals corresponding to SA, confirming a successful linkage between SA and PG. Whether this linkage, however, was covalent or based on strong adsorption could not be clarified. Therefore, alternative methods to verify the covalent character between SA and PG on the basis of particle characterisation were performed. Besides the standard characterisation, including UV-vis absorbance and DLS investigations, an ELISA and laser-triggered cell experiments were carried out in **Section 3.2.2.1.4.1** and **3.3.4**.

3.2.2.1.4 Streptavidin functionalised AuNPs

Functionalisation of 30 nm AuNPs with P(SET-co-SA_(x)-co-G) and (SET-co-SA₍₂₎-co-G) was performed via ligand exchange reaction on AuNP@citrate as described before. Besides the straightforward characterisation of SA-modified AuNPs, including UV-vis absorbance and DLS investigations a further advantage of particle functionalisation with high molecular weight proteins appears in its purification via centrifugation. Here, in addition to pre-purification of P(SET-co-SA_(x)-co-G) and (SET-co-SA₍₂₎-co-G) via dialysis, upon coating of 30 nm AuNPs high mechanical forces (22000 x g) were applied in order to supplementary remove unbound or adsorbed SA.

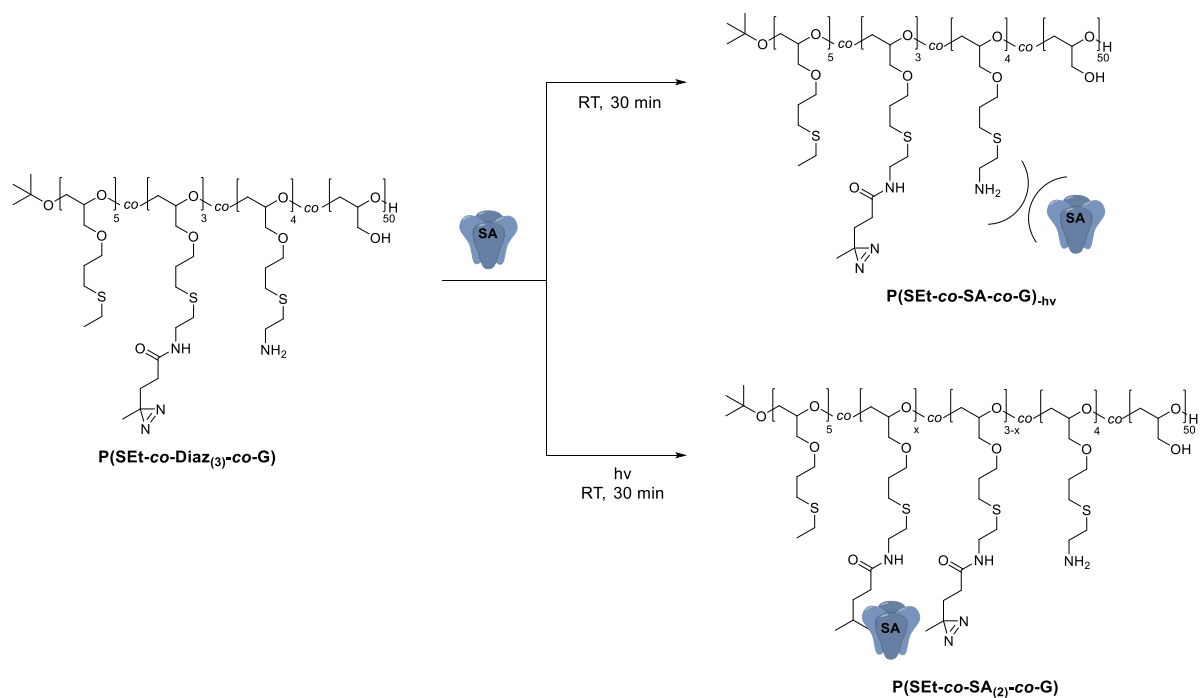
Successful functionalisation of 30 nm AuNPs with SA-modified PG was shown in direct comparison to the respective diazirine precursors via UV-vis absorbance and DLS investigations in **Table 10**. Due to the high molecular weight of SA, the SPR of 30 nm AuNP@P(SET-co-SA_(x)-co-G) (530 nm) and AuNP@P(SET-co-SA₍₂₎-co-G) (532 nm) exhibited a stronger bathochromic shift compared to diazirine-modified AuNPs (529 nm). Regarding the hydrodynamic diameter this resulted in an increase from 34 ± 09 nm to 43 ± 10 and 53 ± 13 nm respectively.

Table 10: SPR and hydrodynamic diameter *d* values of diazirine- and SA-modified AuNPs.

<i>Type of particle</i>	<i>Characterisation method</i>	
	<i>SPR (nm)</i>	<i>d (nm)</i>
AuNP@P(SET-co-Diaz₍₃₎-co-G)	529	34 ± 09
AuNP@P(SET-co-SA_(x)-co-G)	530	43 ± 10
AuNP@P(SET-co-SA₍₂₎-co-G)	532	53 ± 13
AuNP@P(SET-co-SA-co-G)_{-hv}	529	37 ± 08

As mentioned before, diazirine-functionalised polymers, in particular P(SET-co-Diaz₍₃₎-co-G), contained non-negligible amounts of residual amine moieties that were not converted to photoactive diazirine groups. Within this section possible interactions of these residual amine groups towards SA were investigated. These experiments further clarified the binding situation (covalent vs. adsorption) between diazirine moieties and SA, which was broached in

Section 3.2.2.1.3. In order to determine the influence of residual amine groups, the reaction of P(SET-co-Diaz₍₃₎-co-G) and SA was carried out under the exclusion of light, termed as P(SET-co-SA-co-G)_{-hv}. All other conditions, such as incubation time and purification remained unchanged. In this manner it was ensured that the diazirine moieties did not contribute to the SA binding as depicted in **Scheme 18**.



Scheme 18: Investigation of the impact of residual amine moieties within P(SET-co-Diaz₍₃₎-co-G) on the SA binding by performing the reaction without (top) and with (bottom) light.

Characterisation of 30 nm AuNPs functionalised with P(SET-co-SA-co-G)_{-hv} via UV-vis absorbance and DLS measurements was performed. The lacking red-shift of the SPR and the missing increase of the hydrodynamic diameter in comparison to 30 nm AuNP@P(SET-co-SA₍₂₎-co-G) indicated neither a covalent binding, nor a strong adsorption of SA to the particle surface (see **Figure 46** and **Table 10**).

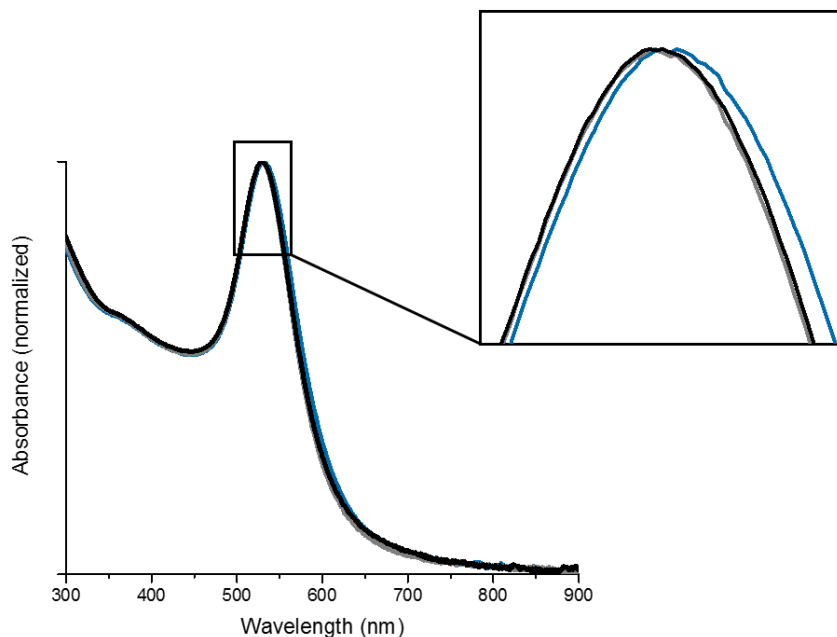


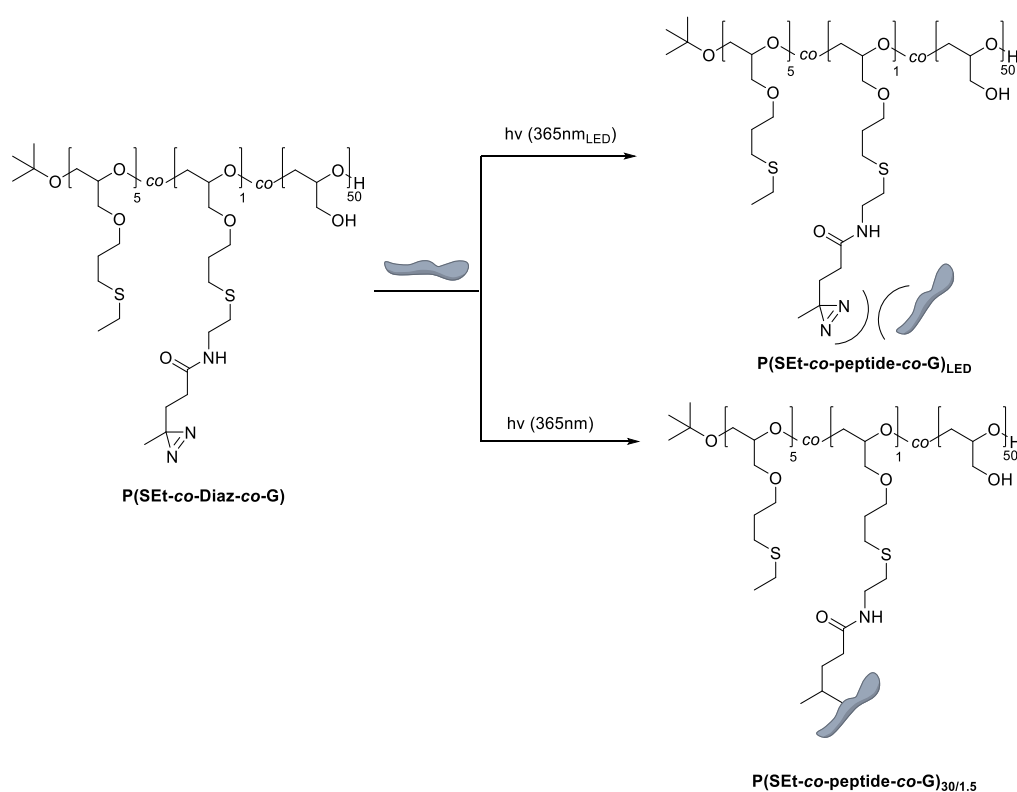
Figure 46: UV-vis absorbance spectra of 30 nm AuNP@P(SET-co-Diaz₍₃₎-co-G) (black), AuNP@P(SET-co-SA-co-G)-_{hv} (grey) and AuNP@P(SET-co-SA₍₂₎-co-G) (blue), where only latter particles featured a SPR red-shift owing to the binding of SA.

Hence, it was shown that the residual amine groups did not influence or conducive the binding between P(SET-co-Diaz₍₃₎-co-G) and SA in any way. Moreover, these experiments confirmed that the linkage of diazirine moieties to SA or biomolecules in general exhibited a covalent character and adsorption was negligible. Latter was additionally verified in laser-triggered cell experiments in **Section 3.3.4**, featuring a more sensitive detection towards traces of SA.

3.2.2.1.4.1 Quantification of streptavidin amount on AuNPs

In the next step a quantification of SA on 30 nm AuNPs was conducted, associated with the clarification of the designations (x) in AuNP@P(SET-co-SA_(x)-co-G) and (2) in AuNP@P(SET-co-SA₍₂₎-co-G). Several methods to quantify the SA amount on the particle surface were carried out.

First trials consisted of fluorescence intensity measurements. Therefore fluorescently labelled SA was released from the AuNP surface by incubating the samples in a solution of DTT for 20 h. The fluorescence in the supernatant was measured after centrifugation. The negative control consisted of a measurement of an untreated sample after centrifugation. It was shown that there was no detectable fluorescence in the supernatant after DTT substitution for two distinctly labelled SA conjugates, namely Cy5- or AlexaFluor647-SA. It was ascertained that the treatment with DTT and the irradiation at 365 nm had no impact on the fluorescence of both dyes. However, for the reaction with labelled-SA monochromatic LED light at 365 nm (365 nm_{LED}) was mandatory, since the light source (320 nm-390 nm) prior used in this chapter resulted in a bleaching of both dyes.



Scheme 19: Investigation of the impact of distinct light sources on the photo-triggered binding of peptide AKGRGDSP to P(SET-co-Diaz-co-G).

In order to investigate the influence of LED light on the diazirine activation, a model reaction with peptide AKGRGDSP, introduced in **Section 3.2.2.1.2** was performed, since the low molecular weight peptide enabled detailed investigations of the binding conditions based on $^1\text{H-NMR}$ spectroscopy. As depicted in **Scheme 19** P(SET-co-Diaz-co-G) was irradiated at 365 nm_{LED} (top) for 30 min with peptide AKGRGDSP according to procedures of **Section 3.2.2.1.2** (bottom). The $^1\text{H-NMR}$ spectra of P(SET-co-peptide-co-G)_{LED} in **Figure 47** clearly lacked the peptide-ascribed signals at 4.42-4.17 ppm and 2.02 ppm (marked with blue beam), which appeared within P(SET-co-peptide-co-G)_{30/1.5}. Furthermore, it was shown that merely 50% of the former diazirine moieties (marked with yellow beam) within P(SET-co-peptide-co-G)_{LED} were converted, whereas P(SET-co-peptide-co-G)_{30/1.5} featured 70-80% conversion. Thus an irradiation at 365 nm_{LED} was not appropriate for diazirine functionalisation and did not result in a peptide linkage.

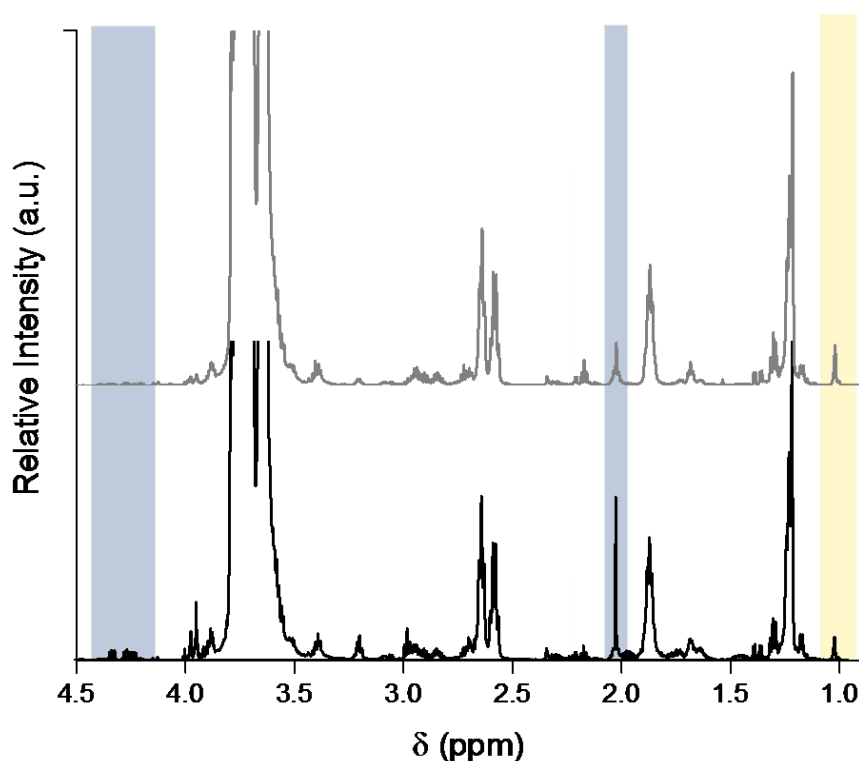


Figure 47: $^1\text{H-NMR}$ spectra of P(SET-co-peptide-co-G)_{LED} (top, grey), lacking the peptide-ascribed signals at 4.42-4.17 ppm and 2.02 ppm (marked blue), which appeared within P(SET-co-peptide-co-G)_{30/1.5} (bottom, black). The methyl signal adjacent to the diazirine moiety is marked yellow.

On the basis of this experiment it could be concluded that most probably neither the reaction of labelled-SA with P(SET-co-Diaz-co-G) at 365 nm_{LED} succeeded, explaining why the detection via fluorescence intensity measurements was not possible.

3 Results and Discussion

Next trials to quantify the SA amount on 30 nm AuNP were based on the (micro)-bichinchonic acid (BCA) assay, where protein-induced reduction of Cu^{+2} to Cu^{+1} in alkaline medium and successive colorimetric detection of Cu^{+1} via BCA (absorbance at 562 nm) was conducted. A concentration series of BSA was used as calibration.

Here, a direct quantification of bound SA by substitution with DTT, as performed before, was not possible due to incompatibility of DTT with the assay. Instead, the initial amount of added SA, as well as unbound SA in the negative controls (supernatant after first and second centrifugation-step) were measured and relation of latter was supposed to predict the SA amount on the particle. However, unrealistically high amounts of SA of about 300 μg per $4 \cdot 10^{11}$ particles, resulting in 7800 SA molecules per AuNP, were detected, which were not taken into consideration.

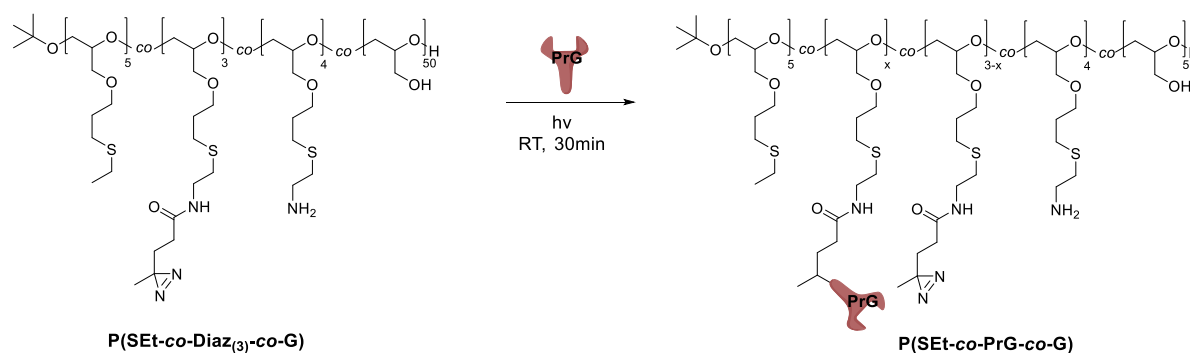
Finally, an ELISA was carried out in order to quantify the SA amount on 30 nm AuNPs. In addition to quantitative investigations, this assay examined the intactness of SA by verifiable interaction with biotin. Therefore, the SA-modified particles were incubated with biotinylated horseradish peroxidase (Biotin-HAP). After washing procedures, 3,3',5,5'-Tetramethylbenzidin (TMB) was added as colorimetric substance, which upon oxidation by HAP and successive addition of sulfuric acid was detected via absorbance measurements at 450 nm. A concentration series of equally treated SA, immobilised on a well plate, was used as calibration. The amount of SA on AuNP@P(SEt-co-SA_(x)-co-G) was below the detection limit, resulting in an unknown amount of SA coincident with the designation SA_(x). Whereas absorbance measurements of AuNP@P(SEt-co-SA₍₂₎-co-G) concluded realistic and reproducible amounts of approximately 80 ng SA per $4.4 \cdot 10^{11}$ particles, resulting in two SA molecules per AuNP, clarifying the designation SA₍₂₎. Regarding a SA size of about 5 nm (contact area 25 nm²), the attachment of two SA molecules on a 30 nm particle seemed reasonable.^[151-152] Though, it has to be considered that the determination via ELISA is error-prone, since SA on a three-dimensional AuNP was compared to SA fixed onto a two-dimensional well plate, offering distinct binding opportunities for Biotin-HAP. Furthermore, there was no proof of the concentration series, where the added amount of SA could be validated as ultimately bound SA on the well plate.

As already mentioned at the beginning of this chapter, SA-functionalised AuNPs feature a broad spectrum of bio-applications, owing to the straightforward conjugation with

biotinylated compounds, such as antibodies. Prior biotin-modification of such antibodies, however, is mandatory, limiting the spectrum of bio-conjugation partner. Via functionalisation of AuNPs with protein G no pre-treatment of the biomolecule is needed, since protein G features high affinity to almost all classes of antibodies, in particular mammalian IgGs.^[153]

3.2.2.1.5 Synthesis of protein G functionalised PG for AuNP coating

The introduction of protein G (PrG) to PG provides the facility of a generic binding of antibodies, due to its high affinity to most mammalian IgGs. PrG functionalised PG, namely P(SET-co-PrG-co-G) was synthesised according to procedures of **Section 3.2.2.1.3**. Briefly, P(SET-co-Diaz₍₃₎-co-G) and PrG were dissolved in PBS at pH 7.0, where PrG features the highest binding affinity, irradiated at 360 nm for 30 min and purified by dialysis (see **Scheme 20**). Here, a recombinant PrG was used, which contrary to the native protein, lacks the albumin and cell surface binding domains, in order to reduce nonspecific binding.^[153]



Scheme 20: Synthesis of P(SET-co-PrG-co-G) via photo-triggered binding of P(SET-co-Diaz₍₃₎-co-G) to protein G.

According to ¹H-NMR spectroscopic investigations of P(SET-co-SA₍₂₎-co-G) discussed in **Section 3.2.2.1.3**, the spectrum of P(SET-co-PrG-co-G) (bottom, dark brown) in **Figure 48** displays signals ascribed to the protein (top, light brown) at 3.11-2.79 ppm, 1.55-1.31 ppm and 1.07-0.66 ppm (marked yellow), confirming successful introduction of PrG. However, due to the complex structure of PrG and signal overlapping a correlation of polymer to protein signals and thus a quantification of PrG within P(SET-co-PrG-co-G) was not possible.

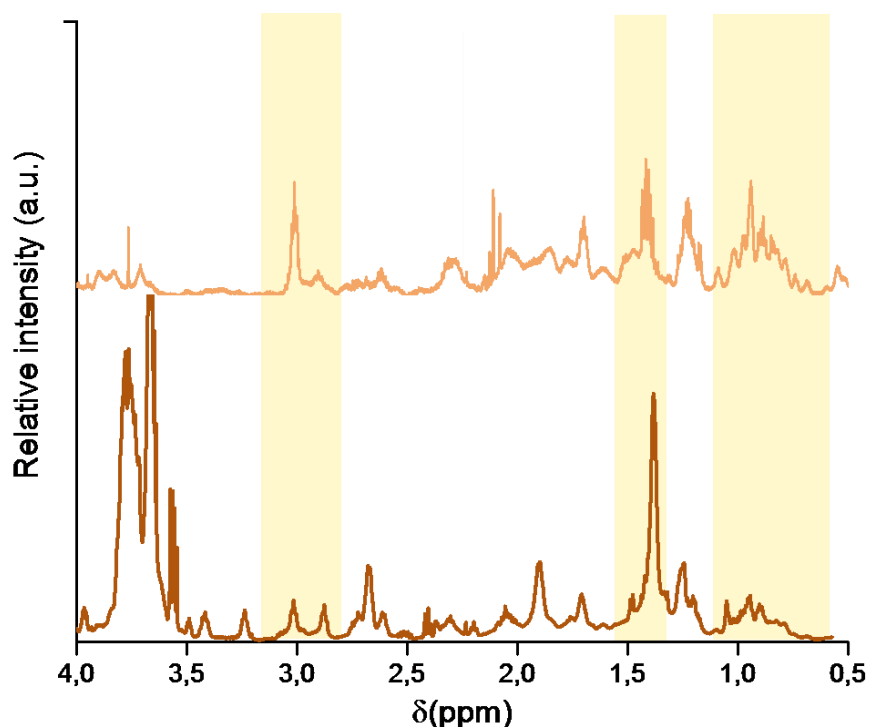
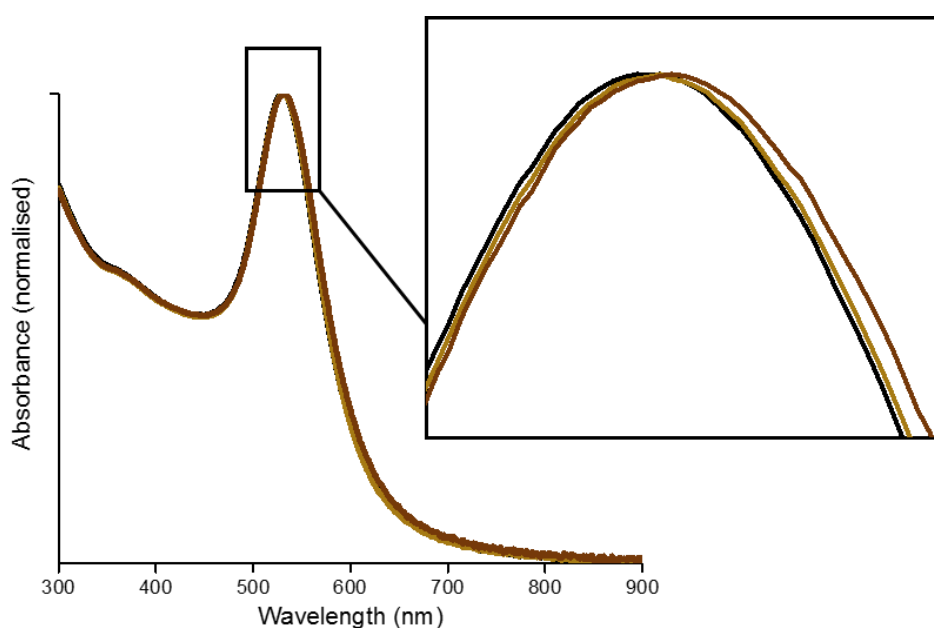


Figure 48: $^1\text{H-NMR}$ spectra of $\text{P}(\text{SEt-co-PrG-co-G})$ (bottom, dark brown), featuring reference signals of protein G (top, light brown), additionally marked yellow.

Successful functionalisation of 30 nm AuNPs with $\text{P}(\text{SEt-co-PrG-co-G})$ and successive antibody coupling was proven by UV-vis absorbance and DLS measurements. Therefore, $\text{AuNP@P}(\text{SEt-co-PrG-co-G})$ were incubated with antibody JAM-C in PBS (pH 7.0) at 4 °C for 30 min. Unbound antibody was removed via centrifugation. **Table 11** and **Figure 49** verified that the SPR of 30 nm $\text{AuNP@P}(\text{SEt-co-PrG-co-G})$ (531 nm) and $\text{AuNP@P}(\text{SEt-co-PrG-co-G})@$ antibody (532 nm) exhibited stronger bathochromic shifts compared to diazirine-modified AuNPs (529 nm). Regarding the hydrodynamic diameter d this resulted in an increase from 34 ± 09 nm to 48 ± 06 nm for PrG-modified AuNPs and 83 ± 19 nm for antibody-modified AuNPs (see **Table 11**).

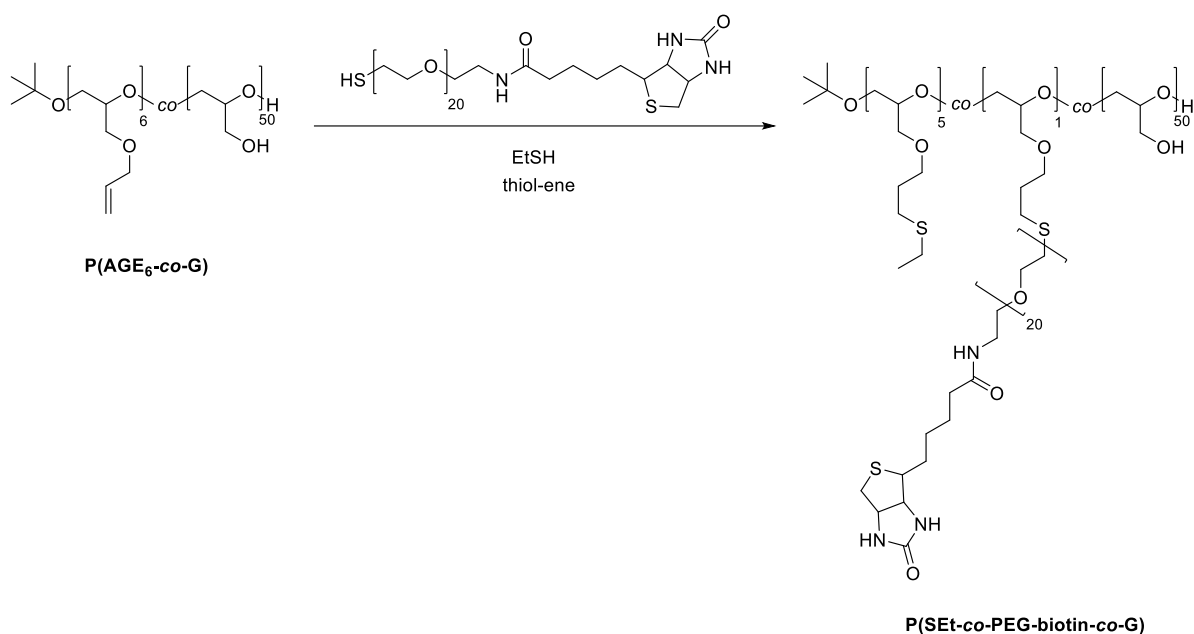
Table 11: SPR and hydrodynamic diameter d values of PrG modified 30 nm AuNPs and successive antibody coupling.

Type of particle	Characterisation	
	SPR (nm)	d (nm)
AuNP@P(SET-co-Diaz₍₃₎-co-G)	529	34 ± 09
AuNP@P(SET-co-PrG-co-G)	531	48 ± 06
AuNP@P(SET-co-PrG-co-G)@antibody	532	83 ± 19

**Figure 49: UV-vis absorbance spectra of 30 nm AuNP@P(SET-co-Diaz₍₃₎-co-G) (black), AuNP@P(SET-co-PrG-co-G) (light brown) and P(SET-co-PrG-co-G)@antibody (dark brown), featuring a bathochromic SPR red-shift of the same specified order.**

3.2.2.2 Synthesis of PG with biotin groups

Biotin-functionalised PG, namely P(SET-co-PEG-biotin-co-G), was synthesised via a thiol-ene click reaction as antagonist to SA modified PG of **Section 3.2.2.1.3**. Briefly, to P(AGE₆-co-G) 21 eq. EtSH and 0.1 eq. HS-PEG-biotin were added and dissolved in a mixture of DMF and water as depicted in **Scheme 21**. After the addition of 0.6 eq. photo-initiator the solution was stirred at room temperature under UV-irradiation for 2 h and purified by dialysis. The eq. were referenced to the allyl groups within P(AGE₆-co-G).



Scheme 21: Synthesis of P(SET-co-PEG-biotin-co-G) via bimolecular thiol-ene click reaction of P(AGE₆-co-G) with EtSH and HS-PEG-biotin.

¹H-NMR spectroscopy verified successful synthesis of P(SET-co-PEG-biotin-co-G) and determined a biotin functionalisation of every second polymer (see **Section 5.2.22**). The FT-IR-spectra of P(SET-co-PEG-biotin-co-G) (marked dark green) in **Figure 50** featured characteristic vibrations of HS-PEG-biotin (marked light green) at 1700-1640 cm⁻¹, attributed to the C=O stretch of the uric acid unit.

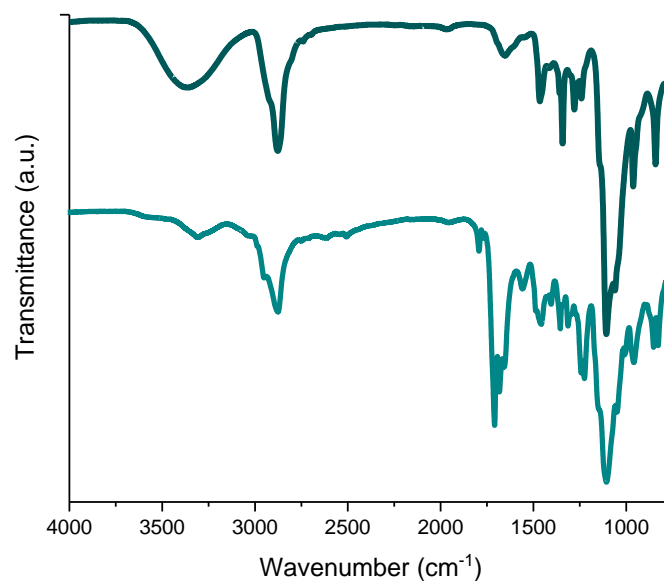


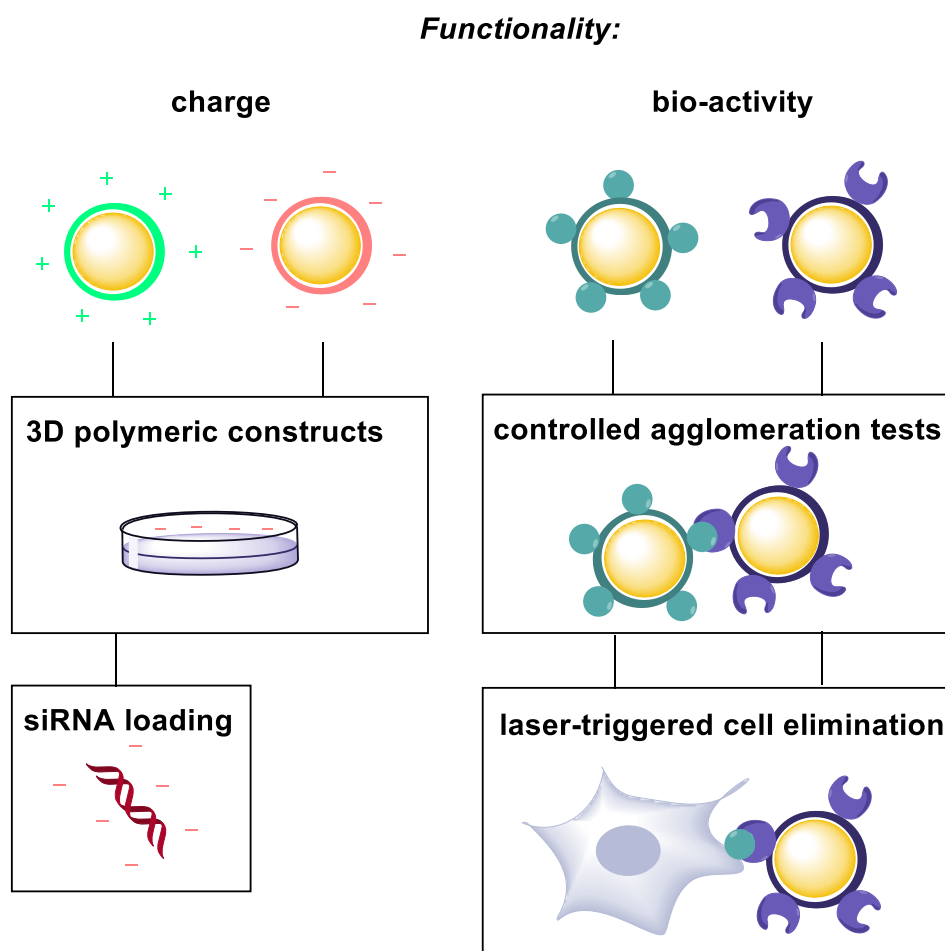
Figure 50: FT-IR spectra of P(SET-co-PEG-biotin-co-G) (dark green, top), displaying signals at 1700-1640 cm^{-1} ascribed to the HS-PEG-biotin linker (light green, bottom).

Successful binding of P(SET-co-PEG-biotin-co-G) to the surface of 30 nm AuNPs was verified by UV-vis absorbance and DLS measurements (see **Section 5.2.22**), as well as by controlled agglomeration tests and laser-triggered cell depletion experiments, conducted in the following **Section 3.3**.

3.3 Applications of multifunctional AuNPs

Throughout this chapter useful applications of functionalised AuNPs introduced in **Section 3.2** were exemplified, additionally verifying successful introduction of the functions onto the particle surface.

Firstly, the impact of AuNPs with distinct charge on three-dimensional polymeric constructs and on the siRNA-loading efficiency was investigated. Moreover, the successful synthesis of SA- and biotin-modified AuNPs was proven in controlled agglomeration tests and laser-triggered cell elimination experiments, as depicted in **Scheme 22**.

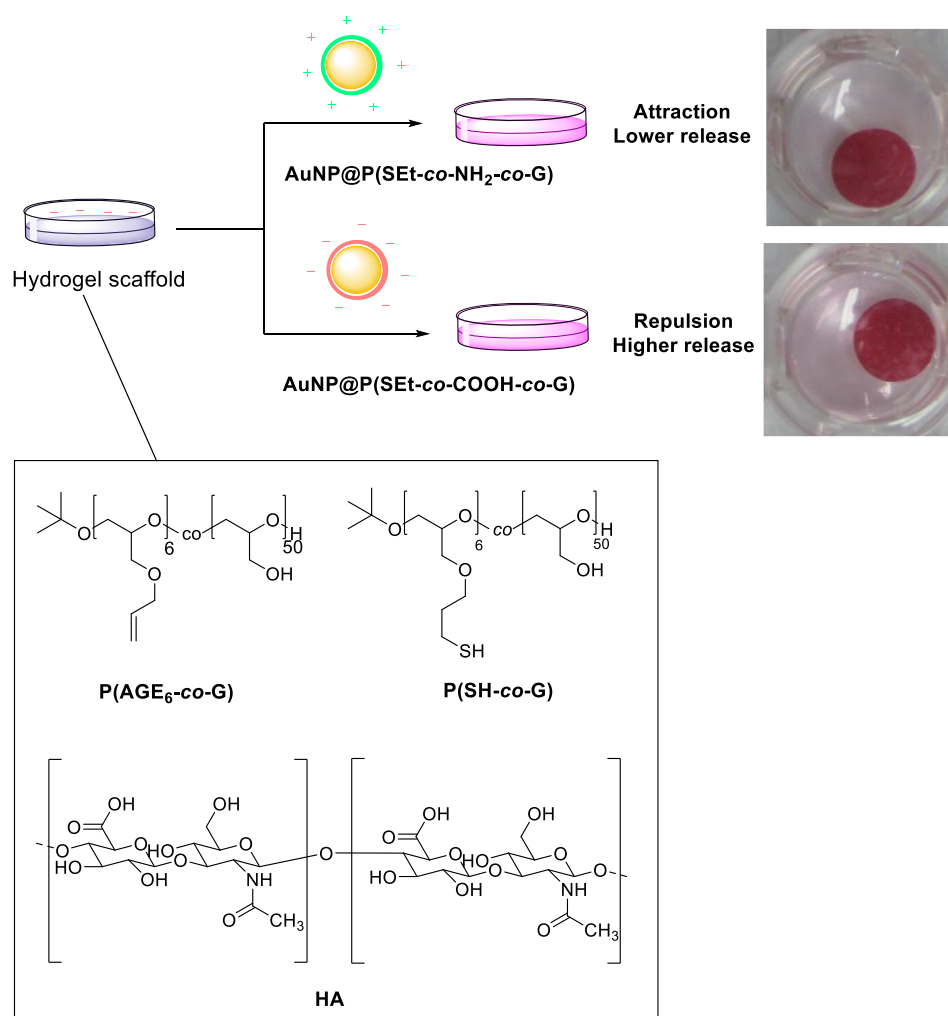


Scheme 22: Depiction of the applicability of functionalised AuNPs introduced in Section 3.2 in diverse studies as described throughout this chapter.

3.3.1 Incorporation of charged AuNPs into hyaluronic acid hydrogels^[154]

The content of this Section is part of a publication.^[154]

In this section the mobility of charged AuNPs within three-dimensional hydrogel scaffolds was examined. Hydrogels are crosslinked polymeric networks, possessing high water contents that when cell-laden function as extracellular matrix analogues. They are widely applied as wound dressings, since they can absorb wound exudates and additionally protect the wound from infections.^[155] By incorporating nanoparticles functionalised with drugs into the scaffolds, for instance an anti-inflammatory activity could be triggered at the wound upon nanoparticulate release. The interplay of nanoparticles and hydrogels, however, is largely unexplored. Therefore, basic investigations of distinctly charged AuNPs of **Section 3.2.1** on the release from negatively charged hydrogels were carried out throughout this section, where positive charge was consistently marked in green and negative charge in red.



Scheme 23: Depiction of the experimental setup concerning the incorporation of 30 nm AuNP@P(SET-co-NH₂-co-G) and 30 nm AuNP@P(SET-co-COOH-co-G) into hyaluronic acid hydrogel scaffolds.

In detail, 30 nm AuNP@P(SET-co-NH₂-co-G) and 30 nm AuNP@P(SET-co-COOH-co-G) were incorporated into hydrogels, where thiol-ene crosslinked P(AGE₆-co-G) and P(SH-co-G) served as matrix and negatively charged hyaluronic acid (HA) as bulking agent, as depicted in **Scheme 23**. The constructs were separately stored in PBS in order to investigate the release kinetics of the contrarily charged AuNPs. Inductively Coupled Plasma-Mass Spectroscopy (ICP-MS) displayed in **Figure 51a** and UV-vis absorbance spectroscopy (see **Figure 51b**) of the PBS supernatant after 1 d, 5 d and 9 d revealed that negatively charged AuNP@P(SET-co-COOH-co-G) were released in higher amounts than positively charged particles at all time points.

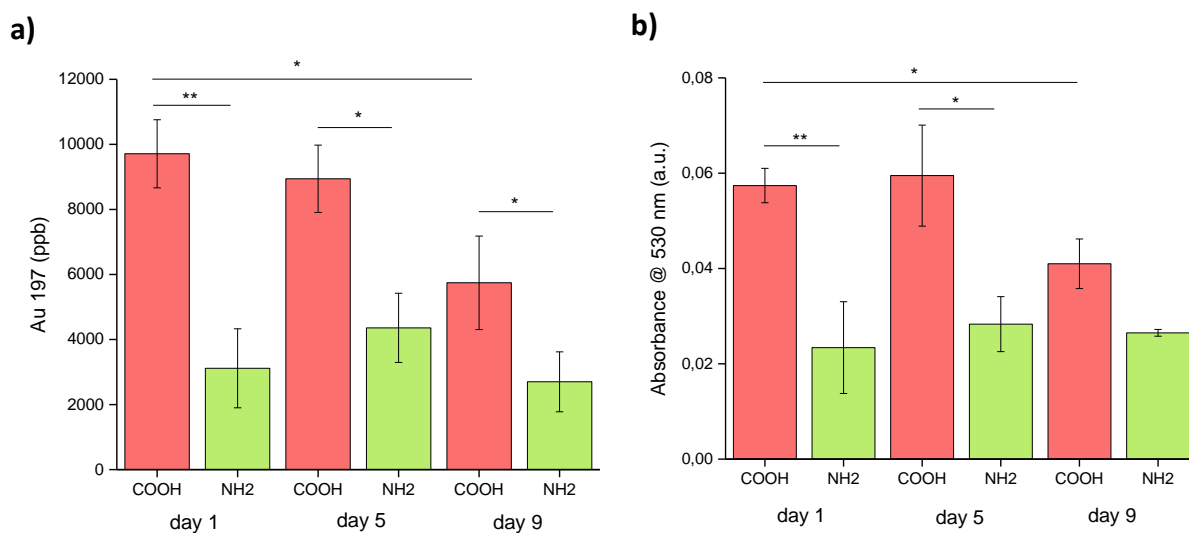


Figure 51: Amount of released 30 nm AuNP@P(SET-co-NH₂-co-G) (green) and 30 nm AuNP@P(SET-co-COOH-co-G) (red) in the supernatant after 1-9 d, determined by a) ICP-MS and b) UV-vis spectroscopy.

This effect was explained by electrostatic interactions of the negatively charged HA with the amine and carboxylic functionalised nanoparticles. While the amount of negatively charged AuNPs decreased within d 1-d 9, positively charged AuNPs were released without significant rate change over time, as highlighted in **Table 12** displaying the percentage amounts of released particles in relation to the initially added particle concentration. This could be due to a lower amount of AuNPs left in the construct, as the supernatant was changed at each time point, resulting in a lower diffusion gradient between hydrogel and supernatant.

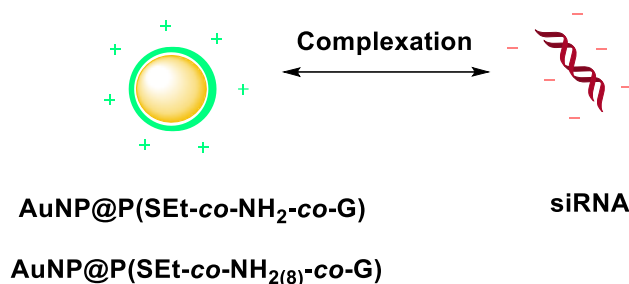
3 Results and Discussion

Table 12: Released amount of 30 nm AuNP@P(SET-co-NH₂-co-G) and 30 nm AuNP@P(SET-co-COOH-co-G) from three-dimensional hyaluronic acid constructs in percentage terms.

	AuNP@P(SET-co-COOH-co-G) (%)	AuNP@P(SET-co-NH₂-co-G) (%)
day 1	7.6 ± 0.2	2.3 ± 0.9
day 5	6.6 ± 0.8	3.2 ± 0.8
day 9	4.2 ± 1.0	1.9 ± 0.7

3.3.2 Complexation of siRNA onto positively charged AuNPs

The modification of AuNP surfaces with positively charged polymers provides the facility of siRNA binding via electrostatic interaction. These noncovalent AuNP@siRNA conjugates are an attractive alternative to covalent systems based on the direct attachment of thiolated siRNA to AuNPs, as the polymer layer ensures steric stabilisation against ionic strength and moreover, the use of unmodified oligonucleotides is possible.



Scheme 24: Depiction of the complexation of siRNA to positively charged AuNPs through modification with amine-PG.

It was shown that a number of parameters are important for successful complexation of siRNA to positively charged AuNPs, including surface charge coverage, ionic strength of the surrounding medium and the AuNP to siRNA ratio. Latter is also termed N/P ratio and describes the ratio between amine groups on the particle surface and phosphate groups of the siRNA. The N/P ratios were calculated via **Equation 6**.

$$\frac{N}{P} = \frac{n(\text{amine}) \times N_{\text{amine groups}}}{n(\text{siRNA}) \times N_{\text{phosphate groups}}} \quad \text{Equation 6}$$

$$n(\text{amine}) = \text{Polymeric amount of substance}$$

$$n(\text{siRNA}) = \text{siRNA amount of substance}$$

$$N_{\text{amine groups}} = \text{number of amine moieties per polymer}$$

$$N_{\text{phosphate groups}} = \text{number of phosphate moieties per siRNA}$$

3 Results and Discussion

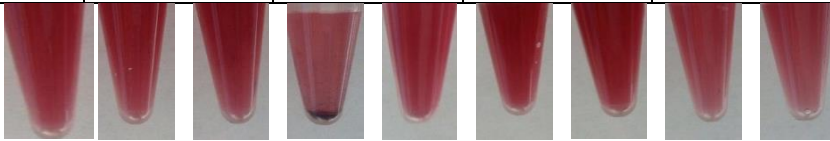
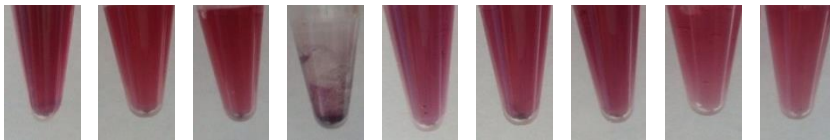
In the following the siRNA complexation on 15 nm AuNPs with two distinct amine amounts, namely AuNP@P(SEt-co-NH₂-co-G) ($\zeta = +07$ mV) and AuNP@P(SEt-co-NH₂₍₈₎-co-G) ($\zeta = +23$ mV) was examined (see **Scheme 24**). The amine moieties per polymer ($N_{\text{amine groups}}$) were determined by averaging the values of TNBSA-assay and ¹H-NMR spectroscopy (see **Table 7** in **Section 3.2.1**). The applied siRNA consisted of 20/21 nucleotides, resulting in 41 phosphate groups ($N_{\text{phosphate groups}}$). n_{amine} and n_{siRNA} corresponded to the respective amount of substance that were investigated within this section. Latter and the corresponding N/P ratio were summarised in **Table 13**.

Table 13: Overview of n_{amine} , $N_{\text{amine groups}}$, n_{siRNA} and $N_{\text{phosphate groups}}$ values and corresponding N/P ratios calculated via Equation 6 of the two positively charged AuNPs.

	$n(\text{amine})$ (nmol)	$N_{\text{amine groups}}$	$n(\text{siRNA})$ (pmol)	$N_{\text{phosphate groups}}$	N/P ratio
AuNP@P(SEt-co-NH₂-co-G)	510	0.9	650	41	20
	510	0.9	260	41	50
AuNP@P(SEt-co-NH₂₍₈₎-co-G)	3724	7.8	1850	41	50
	3724	7.8	900	41	100

Before studying the siRNA complexation behaviour, firstly the colloidal stability of initial amine modified AuNPs in different ionic strength solutions and at different pH values was investigated including bidistilled water, phosphate buffer (5 mM and 10 mM; pH 6.5, 7.0, 7.5) and PBS (5 mM and 10 mM; pH 7.4). The images of correspondingly suspended particles in **Table 14** show that bidistilled water (BW) and phosphate buffer (5 mM; pH 6.5) (PB), ensured best colloidal stability for both amine modified AuNPs, since no changes in the optical properties were observable. Therefore, in the following the impact of BW and PB featuring different ionic strengths on the siRNA complexation behaviour was investigated.

Table 14: Images of 15 nm AuNP@P(SET-co-NH₂-co-G) and 15 nm AuNP@P(SET-co-NH₂₍₈₎-co-G) indicating good (no discolouration) or bad (discolouration and bleaching) colloidal stability in bidistilled water (BW), phosphate buffer (PB) (pH 7.5, 7.0, 6.5; 10 mM, 5 mM) and PBS (pH 7.4, 10 mM, 5 mM).

	BW			PB				PBS	
pH	-	7.5		7.0		6.5		7.4	
C (mM)	-	10	5	10	5	10	5	10	5
P(SET-co-NH₂-co-G)									
P(SET-co-NH₂₍₈₎-co-G)									

A qualitative proof of successful siRNA complexation onto both amine modified AuNPs in BW and PB was proven by a red-shift of the SPR, a change to negative zeta-potentials and an increase of the hydrodynamic diameter related to amine functionalised AuNP, as determined by UV-vis absorbance and DLS measurements, respectively (see **Table 15** and **Figure 52a**). The FT-IR spectrum of AuNP@P(SET-co-NH₂-co-G)@siRNA in **Figure 52b** exhibited typical aliphatic and aromatic vibrations of the C-H stretch between 3100-2800 cm⁻¹, C=N, C=C, and C=O double bond stretching frequencies of the planar bases at 1650 cm⁻¹ and phosphate vibrations at 1140 cm⁻¹, additionally confirming successful complexation of siRNA to the amine modified nanoparticle surface.^[156]

Table 15: Zeta potential ζ and hydrodynamic diameter d values of both amine- and siRNA-functionalised AuNPs in BW.

	ζ (mV)	d (nm)
AuNP@P(SET-co-NH₂-co-G)	+07 ± 04	36 ± 09
AuNP@P(SET-co-NH₂-co-G)@siRNA	-11 ± 05	49 ± 10
AuNP@P(SET-co-NH₂₍₈₎-co-G)	+23 ± 08	39 ± 08
AuNP@P(SET-co-NH₂₍₈₎-co-G)@siRNA	-19 ± 08	57 ± 11

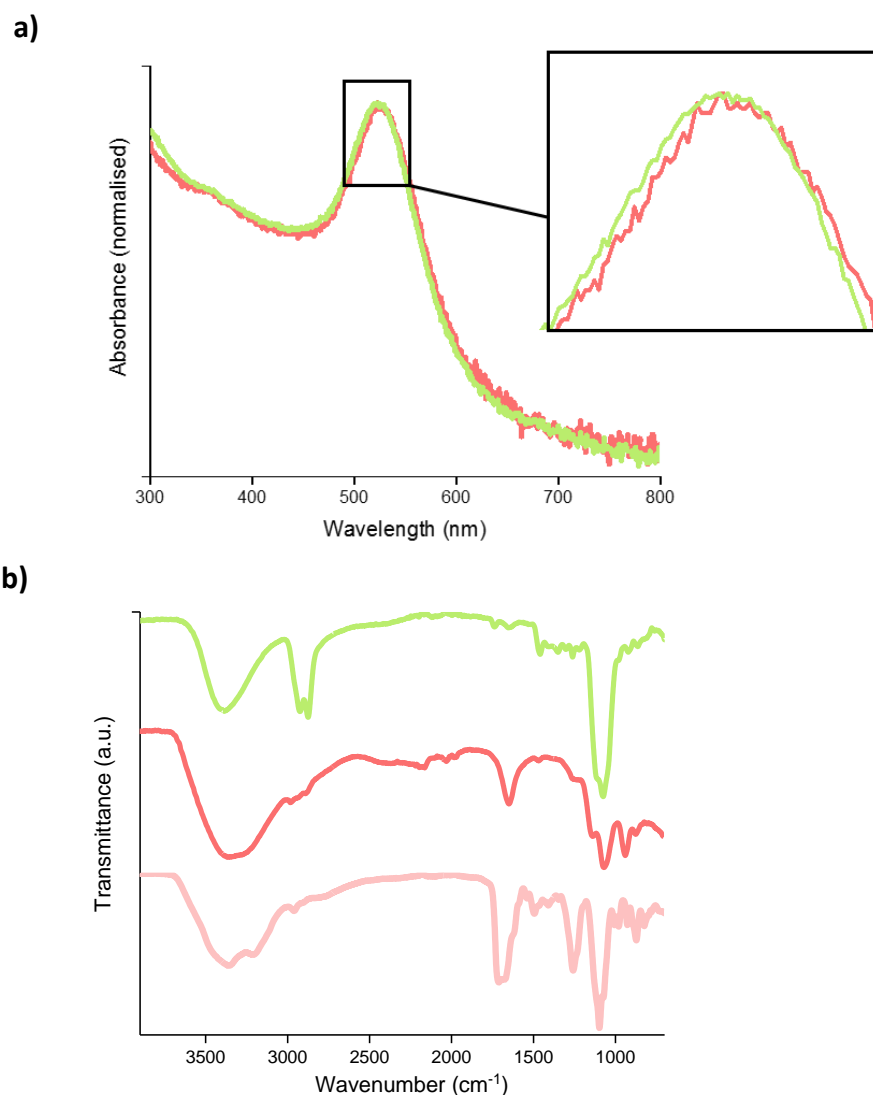


Figure 52: a) UV-vis spectra of 15 nm AuNP@P(SET-co-NH₂-co-G) (green) and 15 nm AuNP@P(SET-co-NH₂-co-G)@siRNA (red), displaying a SPR red-shift upon siRNA complexation. b) FT-IR spectra of 15 nm AuNP@P(SET-co-NH₂-co-G) (top, green) and 15 nm AuNP@P(SET-co-NH₂-co-G)@siRNA (middle, red) conforming to the one of pure siRNA (bottom, light red).

The amount of complexed siRNA was determined via fluorescence intensity measurements. Therefore, Cy5-labelled siRNA was released from the AuNP surface by incubating the samples in a solution of DTT for 20 h. The resulting fluorescence in the supernatant was measured after centrifugation. Values of the fluorescence intensity displayed in **Figure 53** corresponded to the integrated fluorescence of all samples (left ordinate). The siRNA payload (right ordinate) was quantified by plotting the integrated fluorescence against a siRNA concentration series. **Figure 53** furthermore reveals the negative control (marked grey), which consisted of a fluorescence measurement of an untreated sample after centrifugation and was relatively low for all samples, indicating a strong complexation of siRNA.

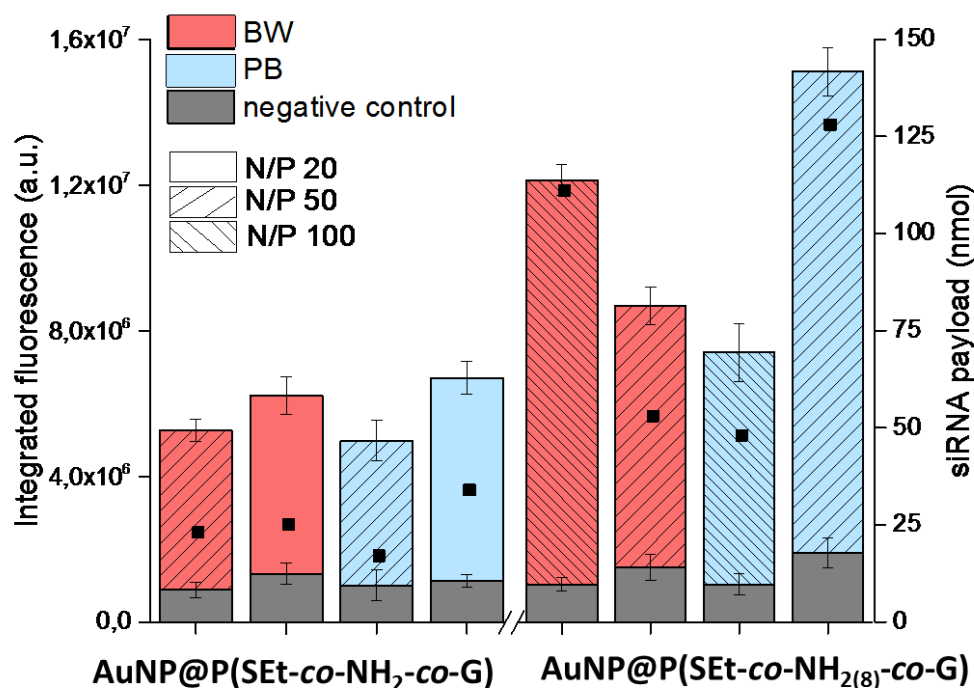
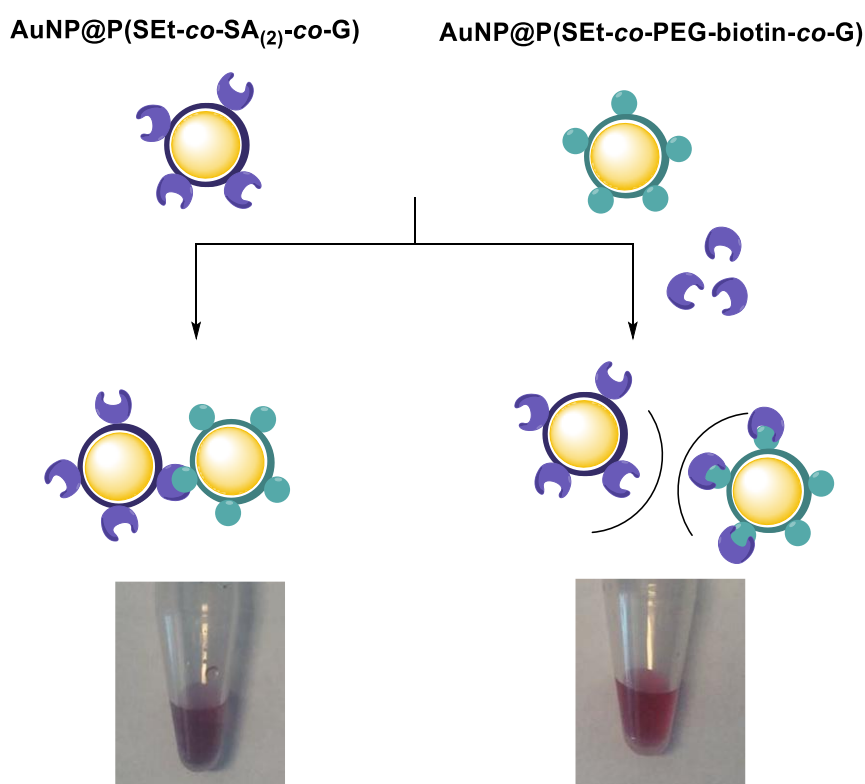


Figure 53: Amount of complexed siRNA on 15 nm AuNP@P(SET-co-NH₂-co-G) (left) and 15 nm AuNP@P(SET-co-NH₂₍₈₎-co-G) (right) in bidistilled water (BW, red) and phosphate buffer (pH 6.5, 5 mM) (PB, blue) with varying N/P ratios (20: blank, 50: broadly dashed, 100: tightly dashed), determined by fluorescence intensity measurements. The respective negative controls are depicted in grey.

Fluorescence intensity studies showed that merely in case of AuNP@P(SET-co-NH₂₍₈₎-co-G) ($\zeta = +23$ mV) the siRNA cargo could distinctly be increased by varying the N/P ratio or the ionic strength of the surrounding medium. For AuNP@P(SET-co-NH₂-co-G)@siRNA most probably the saturation value was already reached with the addition of 260 pmol (N/P: 50) and a higher siRNA net payload than 34 nmol could not be obtained. In case of AuNP@P(SET-co-NH₂₍₈₎-co-G) in BW (marked red) an increase of n_{siRNA} from 900 pmol (N/P: 100) to 1850 pmol (N/P: 50) caused a decrease of the net siRNA cargo from 111 nmol to 48 nmol, whereas in PB (marked blue) it resulted in an increase of the siRNA payload from 53 nmol to 128 nmol. Here, most probably the repulsive forces between the negatively charged siRNA duplexes were compensated by the higher ionic strength of PB and hence more siRNA could be complexed to positive AuNPs. Moreover, it was found that the conformation of amine functionalised polymer on the particle surface changes with the presence of salt. While in low ionic strength medium or water the polymer is adsorbed rather flat at the surface, a sufficient amount of salt probably results in an extension of polymeric loops and tails.^[157] In addition to a better repulsive force compensation in PB compared to BW, also an expanded positively charged polymer surface could promote a higher siRNA loading capacity.

3.3.3 Controlled agglomeration of biotin and streptavidin modified AuNPs

Throughout this section the strong biotin-SA conjugation^[150] was used to provoke reversible agglomeration. Briefly, 30 nm P(SET-co-SA₍₂₎-co-G) and 30 nm P(SET-co-PEG-biotin-co-G) were combined in a ratio of 1:4 and immediate agglomeration was observed by a blue colouration of the colloidal solution (see **Scheme 25**) concomitant with an absorbance peak at 600-700 nm in the UV-vis spectrum (see **Figure 54**). After the addition of excessive amounts of loose SA (8 nmol) the biotin groups within 30 nm P(SET-co-PEG-biotin-co-G) were saturated and the agglomeration with SA-modified AuNPs was reversed, resulting in dispersed particles, which was indicated by regaining of the red colouration (see **Scheme 25** and **Figure 54**).^[158]



Scheme 25: Reversible agglomeration of 30 nm AuNP@P(SET-co-SA₍₂₎-co-G) and 30 nm AuNP@P(SET-co-PEG-biotin-co-G) triggered by the addition of SA.

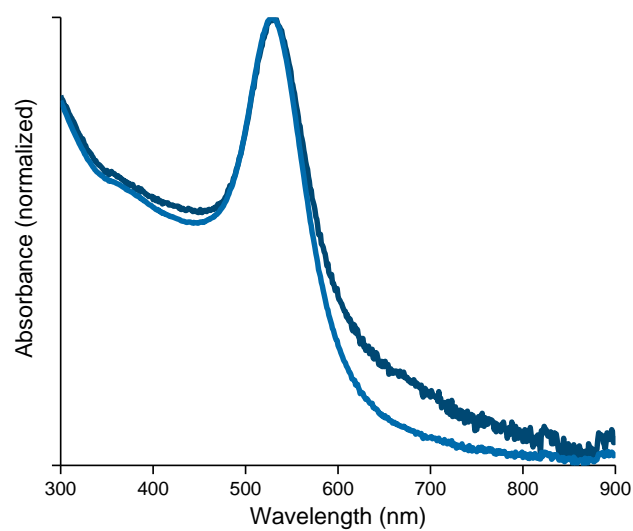


Figure 54: UV-vis absorbance spectra of 30 nm AuNP@P(SET-co-SA₍₂₎-co-G) and 30 nm AuNP@P(SET-co-PEG-biotin-co-G) combined in ratio 1:4 before (dark blue) and after (light blue) the addition of excessive amounts of SA.

3.3.4 Laser-triggered cell elimination through bio-activated AuNP

AuNPs strongly absorb light at their SPR and efficiently convert it to heat, which is then transferred to the surrounding environment (see **Section 2.2.1**). This photo-thermal conversion proved to be versatile in diverse biological applications, such as controllable gene release,^[69, 159] drug delivery,^[160-161] biological imaging^[162] and selective cancer depletion. For the latter AuNPs are functionalised with antibodies that specifically attach to the cancer cell surface. Upon irradiation with laser pulses the fluid around the particles vaporises, rapidly expands and finally collapses. This effect, termed as nanobubble, has enough energy to destroy cellular structures and provoke cell depletion.^[73, 163]

Within this chapter the photo-thermal conversion efficiency of varyingly large bio-activated AuNPs, including P(SET-co-PEG-biotin-co-G) and P(SET-co-SA_(x)/2-co-G), in cell elimination studies was investigated. These experiments provided a sensitive method to verify successful synthesis and biological viability of SA-modified AuNPs, which turned out to be challenging via standard characterisation procedures described throughout **Section 3.2.2.1**. Therefore, cell surfaces were functionalised with the corresponding biotin or streptavidin antibodies. The strong streptavidin-biotin conjugation enabled the formation of stable AuNP-cell conjugates as depicted in **Figure 55** and **Scheme 26**. After irradiation with laser pulses at 532 nm live and dead cells were quantified by flow cytometry analyses (FACS) via Hoechst33258 and CalceinGreen staining.

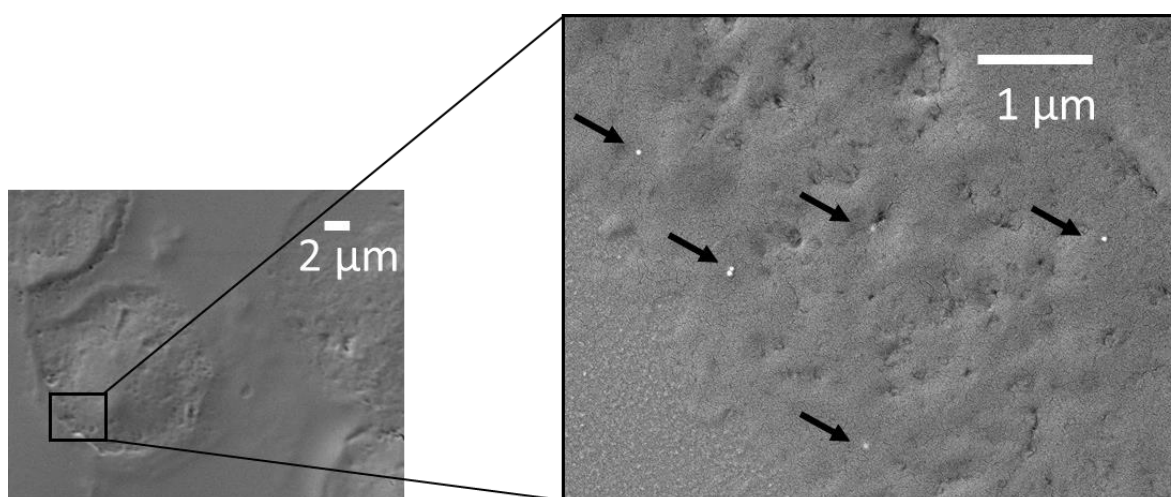
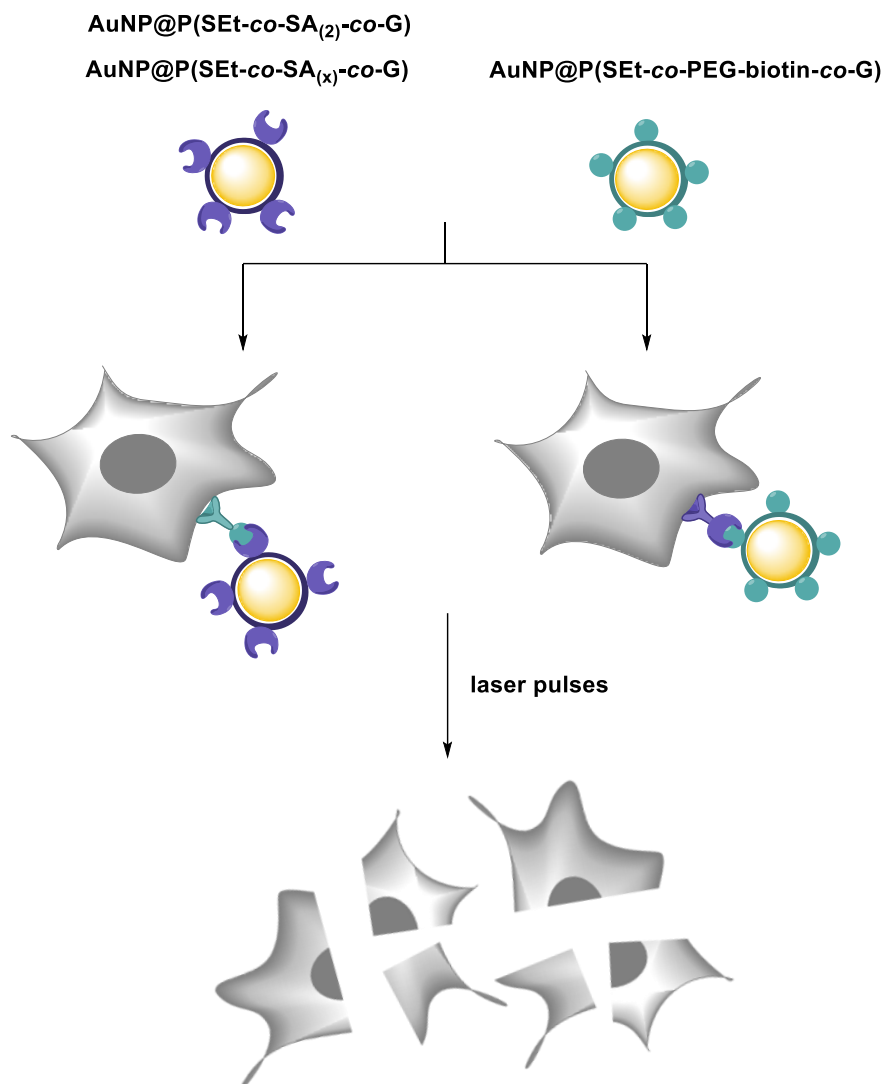


Figure 55: SEM image of 30 nm AuNP@P(SET-co-SA₍₂₎-co-G) attached to the mouse B cell membrane via a biotinylated antibody.



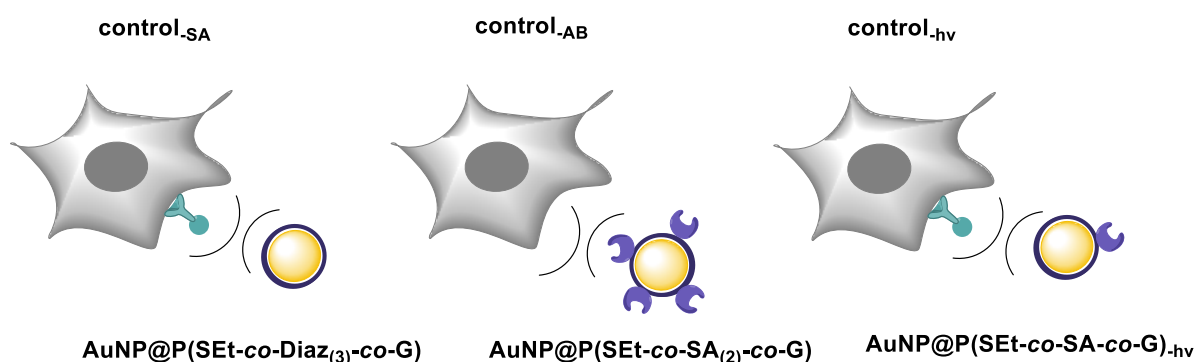
Scheme 26: Elimination of streptavidin- (blue, left) and biotin- (green, right) modified AuNP-cell conjugates triggered by laser irradiation.

Firstly, cell elimination experiments with 30 nm $\text{AuNP@P(SET-co-SA}_{(2)}\text{-co-G)}$ were carried out, in particular to ascertain the covalent linkage between polymer and SA, which was concluded in **Section 3.2.2.1.4** based on UV-vis absorbance and DLS results. The cell depletion experiments were performed according to approaches, developed by a project partner (LH). Further experiments of this section with $\text{AuNP@P(SET-co-PEG-biotin-co-G)}$ and $\text{AuNP@P(SET-co-SA}_{(x)}\text{-co-G)}$ were conducted by the project partner (LH) itself and should be regarded as a proof of principle for the successful introduction of the bio-active group onto the particle surface.

3.3.4.1 $P(\text{SEt-co-SA}_{(2)}\text{-co-G})$

Briefly, for cell depletion experiments with 30 nm $\text{AuNP@P}(\text{SEt-co-SA}_{(2)}\text{-co-G})$ mouse B cells were incubated with a biotinylated CD45R antibody. Afterwards approximately 6000 AuNPs per cell were added. The concentration of cells and particles was determined by FACS and UV-vis absorbance, respectively.

In order to prove the selectivity of the SA-biotin conjugation corresponding investigations with unfunctionalised 30 nm $\text{AuNP@P}(\text{SEt-co-Diaz}_{(3)}\text{-co-G})$ and 30 nm $\text{AuNP@P}(\text{SEt-co-SA}_{(2)}\text{-co-G})$, where no antibody was added to the cells were carried out, termed as $\text{control}_{\text{SA}}$ and $\text{control}_{\text{AB}}$ (see **Scheme 27**). As a further control, namely $\text{control}_{\text{hv}}$, 30 nm $\text{AuNP@P}(\text{SEt-co-SA-co-G})_{\text{hv}}$ were added to cells in equivalent amounts. $\text{P}(\text{SEt-co-SA-co-G})_{\text{hv}}$ was introduced in **Section 3.2.2.1.4** referring to the reaction of $\text{P}(\text{SEt-co-Diaz}_{(3)}\text{-co-G})$ with SA under the exclusion of light, to investigate possible binding contributions of residual amine groups within the diazine modified polymer.



Scheme 27: Depiction of controls conducted within laser-triggered cell experiments, in order to exclude unspecific binding of AuNPs to the cell membrane.

It was shown in **Figure 56** that 30 nm $\text{AuNP@P}(\text{SEt-co-SA}_{(2)}\text{-co-G})$ featured effective cell elimination of about 88 %, whereas $\text{control}_{\text{SA}}$ and $\text{control}_{\text{AB}}$ resulted in negligible values of 2-3 %. The excellent cell viability of $\text{control}_{\text{SA}}$ and $\text{control}_{\text{AB}}$ after laser irradiation indicated no unspecific binding of respective AuNPs to the cell membrane, verifying that the AuNP-cell conjugates are exclusively linked via the SA-biotin conjugation. $\text{control}_{\text{hv}}$ displayed minor cell elimination of about 15 %, which could be provoked by small amounts of SA adsorbed on the surface of $\text{AuNP@P}(\text{SEt-co-SA-co-G})_{\text{hv}}$. In contrast, UV-vis absorbance and DLS investigations of $\text{AuNP@P}(\text{SEt-co-SA-co-G})_{\text{hv}}$ in **Section 3.2.2.1.4** detected no SA on the surface, due to the lacking SPR red-shift and increase of the hydrodynamic diameter compared to $\text{AuNP@P}(\text{SEt-co-SA}_{(2)}\text{-co-G})$. Relating cell depletion results to those obtained by UV-vis absorbance and DLS

in **Section 3.2.2.1.4** it could be concluded that first-mentioned investigations were more sensitive towards traces of SA. However, since cell elimination of AuNP@P(SEt-co-SA-co-G)_{-hv} was marginal with values of about 15 %, negligible traces of SA on AuNP were concluded.

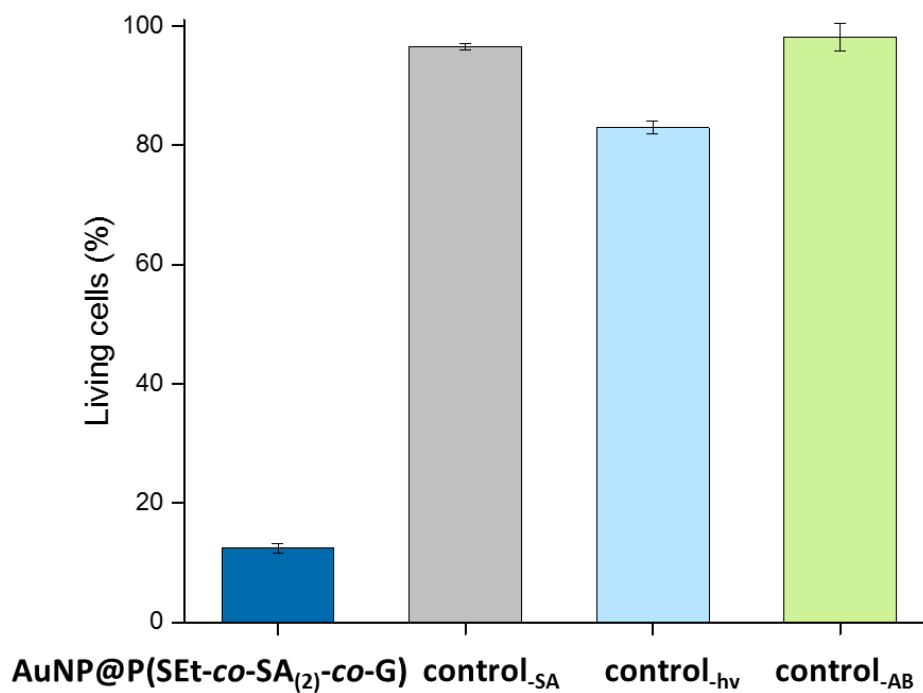


Figure 56: Percentage of live mouse B cells after laser irradiation and treatment with (from left to right) 30 nm AuNP@P(SEt-co-SA₍₂₎-co-G), control-SA, control-hv and control-AB.

3.3.4.2 *P(SEt-co-SA_(x)-co-G)* and *P(SEt-co-PEG-biotin-co-G)*

Although following cell elimination experiments with AuNP@P(SEt-co-SA_(x)-co-G) and AuNP@P(SEt-co-PEG-biotin-co-G) were carried out accordingly to the one of AuNP@P(SEt-co-SA₍₂₎-co-G) in **Section 3.3.4.1** a direct comparison was not possible since a project partner (LH) conducted the work. Furthermore, merely single measurements were performed, impeding significant assertions. Nonetheless, within these single measurements different particle diameter and concentrations were investigated, justifying the incorporation of these results into this thesis. However, it has explicitly to be mentioned that the results should be regarded as a proof of principle for a successful synthesis of the bio-activated particles.

Table 16: Percentage of living mouse B cells after treatment with 30 nm AuNP@P(SEt-co-SA_(x)-co-G) and AuNP@P(SEt-co-PEG-biotin-co-G) and successive laser irradiation.

<i>Living cells (%) in dependency of</i>			
<i>Particle-size (nm)</i>	<i>Particle-number (per cell)</i>	<i>Polymer coating</i>	
		<i>P(SEt-co-SA_(x)-co-G)</i>	<i>P(SEt-co-PEG-biotin-co-G)</i>
15	12000	66.3	
	6000	90.3	0.92
	3000	91.1	1.73
30	6000	0.01	0.03
	3000	0.45	0.15
	1500	2.13	0.20
50	1500	0.01	0.02
	750	0.44	-

Table 16 shows that 15 nm (12000, 6000, 3000 AuNPs per cell), 30 nm (6000, 3000, 1500 AuNPs per cell) and 50 nm (1500, 750 AuNPs per cell) bio-activated particles (if available) caused efficient cell elimination of about 100 %-87 %, confirming successful introduction of the bio-active moiety to the surface. With the exception of 15 nm AuNP@P(SEt-co-SA_(x)-co-G) featuring high cell viabilities of 66 %-91 %. This could be related to the small surface of 15 nm

particles that converted insufficient heat to the cell membrane, associated with a generally higher required number of 15 nm AuNP@P(SET-co-SA_(x)-co-G) per cell. On the other hand, the excellent cell elimination of 15 nm AuNP@P(SET-co-PEG-biotin-co-G) (98-99 %) contradicted this explanation and excluded the small particle surface as only reason for a failed photo-thermal conversion. Instead, the functionalisation degree on the particle surface was considered, where the arrangement of high molecular weight SA (53 kDa) on the particle surface appeared more challenging than that of small biotin moieties (244 g mol⁻¹). With respect to ELISA results in **Section 3.2.2.1.4.1**, where the amount of SA on 30 nm AuNP@P(SET-co-SA_(x)-co-G) was below the detection limit, it seemed likely that the SA amount on 15 nm particles was even lower, most probably featuring crucial parts of unfunctionalised particles that could not attach to the cell surface. Thus, low cell elimination was attributed to a lower functionalisation degree of 15 nm AuNP@P(SET-co-SA_(x)-co-G) compared to 15 nm AuNP@P(SET-co-PEG-biotin-co-G).

4.1 Conclusion

4.1 Conclusion

The *aim of this thesis* was the development of a multifunctional coating system for AuNPs based on thioether polymers, providing both excellent colloidal stability and a variable possibility to introduce functionalities for biological applications.

First, two thioether-polymer systems were synthesised within **Section 3.1.1** as a systematic investigation into colloidal stabilisation efficacy. Besides commonly used monovalent poly(ethylene glycol) (PEG-SR), its structural analogue linear poly(glycidol) (PG-SR) bearing multiple statistically distributed thioether moieties along the backbone was synthesised. Additionally, respective thiol analogues (PEG-SH and PG-SH) were produced and applied as reference. A successful polymer synthesis was confirmed by SEC, ¹H-NMR and XP spectroscopy. The absence or presence of thiols was verified by RAMAN spectroscopy and Ellman assay.

Successive modification of varyingly large AuNPs with aforementioned thiol- and thioether-polymers was performed in **Section 3.1.2** via ligand exchange reaction on citrate stabilised AuNPs. Successful polymer attachment on the particles was thoroughly proven by UV-vis, FT-IR spectroscopy and DLS. Investigations based on TGA and XPS revealed a polymer dependant surface coverage, which decreased in the order PEG-SH > PG-SR ≥ PEG-SR > PG-SH. In detail, for thiol- and thioether-PEG a brush regime on 30 nm AuNPs was determined with lower grafting densities in case of PEG-SR ascribed to the bulkier thioether anchor group demanding more space on the surface than the thiol analogue. On the other hand for PG a conformation with trains, loops and tails was suggested, where PG-SR featured higher polymer coverages, which were hypothesised to base on a higher affinity of multiple thioether groups within PG-SR towards the gold surface compared to thiol moieties.

Regarding the kinetics of particle coating, a longer passivation time of PG-SR compared to the thiol analogue was found for 30 nm AuNPs, whereas thiol- and thioether-PEG featured similar passivation kinetics (see **Section 3.1.3**). The minor influence of the anchor group within PEG on the binding kinetics was attributed to dominating steric interactions between the PEG chains. However, contrary to studies in literature, the slower binding of PG-SR was not ascribed to a weaker thioether-gold interaction. In fact, an increased stabilisation efficacy of both thioether-polymers against biological and physiological conditions, as well as against freeze-drying compared to thiol analogues was determined in a systematic study with varyingly large AuNPs. The superiority of thioether-polymers regarding colloidal stability was

particularly noticeable throughout the freeze-drying process, which in case of thiol-polymers most probably provoked oxidative polymeric crosslinking and thus loss of the stabilisation properties. Interestingly, the colloidal stability of AuNPs was independent of the polymer coverage, once more emphasising the anchor group as decisive factor for the stabilisation efficacy. Yet, in contrast to studies in literature^[14, 24] the multivalency of PG-SR did not distinctly increase the colloidal stability against ions and proteins related to PEG-SR.

Based on the excellent colloidal stabilisation efficacy and multi-functionalisation of thioether-PG, throughout **Section 3.2** a plethora of functional groups was introduced to the AuNP surface. Firstly, the successful synthesis of PG-SR bearing charged groups and hydrophilic/hydrophobic chains (see **3.2.1**), as well as bio-active moieties such as diazirine and biotin (see **3.2.2**) was verified by ¹H-NMR, FT-IR, RAMAN, UV-vis spectroscopy and via contact angle based measurements. Successive functionalisation of AuNPs with aforementioned polymers was proven by FT-IR, UV-vis spectroscopy and DLS, including size and zeta potential measurements of the particles. Moreover, the generic and covalent binding of diazirine-modified PG-SR with biomolecules including peptides and proteins was thoroughly demonstrated. Here, the binding of a small molecular weight peptide allowed for detailed polymeric investigation via ¹H-NMR spectroscopy, whereas the successful introduction of complex proteins, first and foremost streptavidin was demonstrated and quantified upon particle attachment.

Lastly, in **Section 3.3**, diverse applicability and bioactivity of aforementioned modified particles in various studies was displayed, once more verifying the introduction of functionalities. On the one hand the electrostatic interaction of charged AuNPs with hydrogels based on hyaluronic acid was applied to tune the release kinetics of particles from three-dimensional scaffolds as determined by ICP-MS and UV-vis spectroscopy (see **3.3.1**). In case of AuNPs functionalised with drugs this provides the facility of a charge controlled delivery and release of therapeutics to the wound centre, where the hydrogel is introduced.

On the other hand in **Section 3.3.2**, the strong complexation of siRNA onto two positively charged AuNPs was proven by FT-IR, UV-vis spectroscopy, DLS and fluorescence intensity measurements. The amount of siRNA payload was tuneable by varying the surface charge, ionic strength of the surrounding medium and the N/P ratio. However, the efficacy of siRNA functionalised AuNPs to knockdown the target gene remains to be verified *in vitro*.

4.1 Conclusion

Furthermore, the necessity of an additional polymer layer, ensuring protection against RNase has to be investigated.

Moreover, the biological activity and selectivity of the biotin-streptavidin conjugation was verified with respectively functionalised particles in controlled agglomeration test via UV-vis spectroscopy (see **3.3.3**) and in laser-triggered cell elimination experiments (see **3.3.4**). In the latter, streptavidin-functionalised AuNPs resulted in excellent depletion of biotinylated cells as determined via FACS, whereas unfunctionalised control particles failed, excluding unspecific binding of these particles to the cell surface.

Since all particle coatings consist of an identical PG backbone and merely differ in an adjustable number of functional side chains *in future* manifold systematic investigations on sensitive *in vitro* effects, including cytotoxicity, cellular uptake and manipulation could be provided.

4.2 Zusammenfassung

Ziel der Arbeit war die Entwicklung eines multifunktionalen Beschichtungssystems für Gold Nanopartikel (AuNP) basierend auf Thioether-Polymeren, das sowohl eine hervorragende kolloidale Stabilität aufweist, als auch eine variable Einbringung von Funktionalitäten für biologische Anwendungen ermöglicht.

Um eine Systematik der Untersuchung von kolloidaler Stabilisierungseffizienz zu gewährleisten, wurden zwei Thioether-Polymersysteme in **Sektion 3.1.1** synthetisiert. Diese basierten auf dem gebräuchlichen monovalenten Polyethylenglykol (PEG-SR) und dessen Struktur analog Polyglycidol (PG-SR), das mehrere statistisch verteilte Thioethergruppen an seinem Rückgrat trägt. Zusätzlich wurden entsprechende Thiol-Polymere hergestellt (PEG-SH and PG-SH) und als Referenz eingesetzt. Die erfolgreiche Synthese der Polymere wurde per SEC, $^1\text{H-NMR}$ und XP Spektroskopie nachgewiesen. Das Vorhandensein von Thiolgruppen wurde per RAMAN Spektroskopie und über Ellman Assay verifiziert.

Die anschließende Modifikation von unterschiedlich großen AuNP mit zuvor erwähnten Thiol- und Thioether-Polymeren wurde in **Sektion 3.1.2** über eine Liganden-Austausch-Reaktion auf Citrat-stabilisierten AuNP durchgeführt. Eine erfolgreiche Anbindung der Polymere an die Partikeloberfläche wurde durch UV-vis, FT-IR Spektroskopie und DLS bestätigt. TGA- und XPS-Untersuchungen zeigten eine Polymer-abhängige Oberflächenbelegung auf, welche in der Reihenfolge PEG-SH > PG-SR \geq PEG-SR > PG-SH abnahm. Des Weiteren wurde für Thiol- und Thioether-PEG eine „Bürsten“-Anordnung der Polymerketten auf 30 nm AuNP berechnet. Die geringere Propfdichte im Falle von PEG-SR wurde auf die räumlich anspruchsvollere Thioether-Verankerungsgruppe zurückgeführt, die mehr Platz auf der Partikeloberfläche in Anspruch nimmt als die Thiolgruppe. Zum anderen wurde für PG eine Anordnung auf der Partikeloberfläche angenommen, in der verschieden lange Kettensegmente zwischen den Ankergruppen von der Partikeloberfläche abstehen, wobei PG-SR eine höhere Oberflächenbelegung aufwies. Diese wurde durch die Hypothese einer stärkeren Affinität von mehreren Thioethergruppen zur Goldoberfläche als von entsprechenden Thiolgruppen erklärt.

Innerhalb von **Sektion 3.1.3** wurde in Übereinstimmung mit der Literatur^[16-17] eine längere Passivierungszeit von PG-SR im Vergleich zu dem Thiol-Analog für 30 nm AuNP gefunden, wohingegen Thiol- und Thioether-PEG ähnliche Passivierungskinetiken aufwiesen. Der geringe Einfluss der Verankerungsgruppe auf die Bindungskinetik innerhalb von PEG wurde durch die

dominierende sterische Wechselwirkung der PEG-Ketten erklärt. Im Gegensatz zu den Studien in der Literatur, wurde die langsamere Bindung von PG-SR an die Goldoberfläche jedoch nicht einer schwächeren Thioether-Gold Wechselwirkung zugeschrieben. Genau genommen, wurde sogar für beide Thioether-Polymere eine höhere Stabilisierungseffizienz, insbesondere gegen biologische und physiologische Bedingungen, als auch gegen Gefriertrocknung im Vergleich zu entsprechenden Thiol-Analogen in einer systematischen Studie mit unterschiedlich großen AuNP festgestellt. Die Überlegenheit von Thioether-Polymeren hinsichtlich der kolloidalen Stabilität war insbesondere innerhalb des Gefriertrocknungsprozesses erkennbar. Dieser führte im Falle von Thiol-Polymeren höchstwahrscheinlich zu einer oxidativen Vernetzung der Polymere und deshalb zu einem Verlust der Stabilisierungseigenschaften. Interessanterweise war in dieser Studie kein Zusammenhang zwischen der kolloidalen Stabilität und der Polymer-Oberflächenbedeckung erkennbar, was nochmals die Verankerungsgruppe als ausschlaggebenden Faktor für die Stabilisierungseffizienz betont. Im Gegensatz zu Studien in der Literatur wurde jedoch keine eindeutige Steigerung der kolloidalen Stabilität gegen Ionen und Proteinen durch die Multivalenz von PG-SR im Vergleich zu PEG-SR nachgewiesen.

Basierend auf der exzellenten kolloidalen Stabilisierungseffizienz und der multifunktionalisierbarkeit von Thioether-PG, wurde wie in **Sektion 3.2** beschrieben, eine Vielzahl an funktionellen Gruppen auf die AuNP Oberfläche eingebracht. Per $^1\text{H-NMR}$, FT-IR, RAMAN, UV-vis Spektroskopie und über Kontaktwinkel-basierte Messungen wurde zunächst die erfolgreiche Synthese von PG-SR mit geladenen Gruppen und hydrophilen/hydrophoben Ketten (siehe **3.2.1**) und anschließend von PG-SR funktionalisiert mit bioaktiven Einheiten wie Diazirin und Biotin (siehe **3.2.2**) bestätigt. Anschließende Anbindung von eben erwähnten Polymeren an AuNP wurde mittels FT-IR, UV-vis Spektroskopie und Partikelgrößen- und Zeta-Potentialmessung per DLS nachgewiesen. Des Weiteren wurde die generische und kovalente Bindung zwischen Diazirin-modifiziertem PG-SR und Biomolekülen, wie Peptiden und Proteinen ausführlich aufgezeigt. Hierbei ließ die Bindung des Peptides mit kleinem Molekulargewicht detaillierte Untersuchungen mittels $^1\text{H-NMR}$ Spektroskopie zu, während die erfolgreiche Einbringung von komplexeren Proteinen, vor allem Streptavidin nach Anbindung des Polymers an die Partikeloberfläche veranschaulicht und quantifiziert wurde.

Zuletzt, wurde in **Sektion 3.3** die vielfältige Anwendungsmöglichkeit und Bioaktivität der zuvor erwähnten modifizierten Partikel in diversen Studien dargestellt, wodurch nochmals die erfolgreiche Einbringung der Funktionalitäten verifiziert wurde. Zum einen wurde hierbei die elektrostatische Wechselwirkung zwischen geladenen AuNP und Hydrogelen, die auf Hyaluronsäure basierten genutzt, um die Freisetzungskinetik der Partikel aus den dreidimensionalen Gerüsten zu steuern, wie mittels ICP-MS und UV-vis Spektroskopie nachgewiesen wurde (siehe **3.3.1**). Im Falle von wirkstofftragenden AuNP, könnte auf diese Weise eine ladungskontrollierte Zufuhr und Freisetzung der Therapeutika an das Entzündungszentrum, wo zuvor das Hydrogel eingebracht wurden, ermöglicht werden.

Zum anderen wurde in **Sektion 3.3.2** die starke Komplexierung von siRNA an zwei unterschiedlich stark positiv geladene AuNP mittels FT-IR, UV-vis Spektroskopie, DLS und Fluoreszenzintensitätsmessungen nachgewiesen. Die Menge an komplexierter siRNA konnte über Variation der Oberflächenladung, der Ionenstärke des umgebenden Mediums und des N/P Verhältnisses eingestellt werden. Die Reduktionseffizienz der siRNA-funktionalisierten AuNP bezüglich des Zielgenes muss jedoch erst noch *in vitro* nachgewiesen werden. Des Weiteren sollte die Notwendigkeit einer zusätzlichen abschließenden Polymerschicht untersucht werden, die einen Schutz vor RNasen gewährleisten könnte.

Zudem wurde die biologische Aktivität und Selektivität der Biotin-Streptavidin Konjugation mittels entsprechend funktionalisierter AuNP in kontrollierten Agglomerationstests mittels UV-vis Spektroskopie (siehe **3.3.3**) und in ausführlichen Laser-induzierten Zelleliminationsstudien (siehe **3.3.4**) nachgewiesen. In letzteren Studien riefen Streptavidin-funktionalisierte AuNP exzellente Depletion von biotinylierten-Zellen hervor, wie mittels FACS nachgewiesen wurde, wohingegen unfunktionalisierte Kontrollpartikel versagten, was eine unspezifische Bindung dieser Partikel an die Zelloberfläche ausschloss.

Da alle Partikelbeschichtungen aus einem identischen PG Rückgrat bestehen und sich lediglich in einer einstellbaren Anzahl an funktionellen Seitenketten unterscheiden, könnte **in Zukunft** eine Vielzahl an systematischen Untersuchungen über empfindliche *in vitro* Effekte durchgeführt werden, diese beinhalten beispielsweise die Zytotoxizität, die zelluläre Aufnahme und anschließende Manipulation.

5 Experimental Section

5 Experimental Section

5.1 Materials and Methods

5.1.1 Materials

Ethoxyethyl glycidyl ether (EEGE) was synthesized according to Fitton *et al.*^[126] Allyl glycidyl ether (AGE) ($\geq 99\%$, Sigma-Aldrich, St. Louis, MO, USA) and EEGE were purified via drying over calcium hydride (CaH_2) (92% , ABCR, Karlsruhe, Germany) for 12 h and distilled under reduced pressure and under argon (Ar) atmosphere. The purified monomers were stored under nitrogen (N_2) atmosphere before use. All polymerisations were conducted in a glovebox under nitrogen (N_2) atmosphere. The following chemicals were used as received. 2,2-dimethoxy-2-phenylacetophenon (DMPA) (99%), ethyl vinyl ether (99% , KOH stabilised), glycidol (96%), *p*-toluene sulfonic acid monohydrate (*p*TsOH) ($>98.5\%$), anhydrous N,N-dimethylformamide (DMF) ($>99.8\%$), potassium tert-butoxide (KO^tBu) (1 M in THF), tris(2-carboxyethyl)phosphine hydrochloride (TCEP) ($\geq 98\%$), ethanethiol (EtSH) ($\geq 97\%$), cysteamine hydrochloride ($\geq 98\%$), dithiothreitol (DTT) ($>99\%$), thioacetic acid (96%), thioglycolic acid ($\geq 99\%$), 1-dodecanethiol ($\geq 98\%$), 1-pentene ($\geq 98.5\%$), alpha-methoxy-omega-mercapto poly(ethylene glycol) (MeO-PEG-SH), streptavidin from *streptomyces avidinii* (SA) ($\geq 13\text{ units/mg protein}$), tetramethylsilane (TMS) as analytical standard for NMR spectroscopy, sodium dodecyl sulfate (SDS) (98%) and sodium hydroxide (NaOH) ($>98\%$) were purchased from Sigma-Aldrich (St. Louis, MO, USA). Deuterium oxide (D_2O), deuterated chloroform (CDCl_3) (Deutero GmbH, Kastellaun, Germany), diethylether (Staub Co., Nürnberg, Germany), ethanol (EtOH) (99% , TH Geyer, Renningen, Germany), hydrochloric acid (HCl) (37%), sulfuric acid (H_2SO_4) (99.9%), hydrogen peroxide solution (H_2O_2) (30%), sodium hydrogen carbonate (NaHCO_3), magnesium sulfate (MgSO_4) (Merck, Darmstadt, Germany), 2-hydroxy-1-[4-(hydroxyethoxy)-phenyl]-2-methyl-1-propanone (Irgacure 2959) (BASF, Ludwigshafen, Germany), alpha-mercapto-omega-amino poly(ethylene glycol) (HS-PEG-NH₂), alpha-mercapto-omega-carboxy poly(ethylene glycol) (HS-PEG-COOH) (Iris Biotech, Marktredwitz, Germany), alpha-mercapto-omega-hydroxy poly(ethylene glycol) (HS-PEG-OH), alpha-mercapto-omega-biotin poly(ethylene glycol) (HS-PEG-biotin) (Nanocs, New York, NY, USA), gold nanoparticles (AuNPs) (BBI, Cardiff, UK), CD45R (B220) antibody (Miltenyi Biotech, Bergisch Gladbach, Germany), recombinant protein G (PrG), 2,4,6-trinitrobenzene sulfonic acid (TNBSA), 5,5'-dithio-bis-(2-nitrobenzoic acid) (DTNB), bicinchoninic acid (BCA) protein assay kit, Cell Trace Calcein Green, Hoechst 33342, biotinylated horseradish peroxidase (biotin-HRP), Dulbecco's Modified Eagle Medium (DMEM) and succinimidyl 4,4'-azipentanoate (NHS-diazirine) (Thermo

Fisher Scientific, Waltham, MA, USA), 3,3',5,5'-Tetramethylbenzidin (TMB) (AppliChem, Darmstadt, Germany) were used as received. Phosphate buffered saline (PBS, pH 7.4) was made by diluting sodium chloride (NaCl) (8.00 g, 136 mmol), potassium dihydrogen phosphate (KH_2PO_4) (0.20 g, 1.47 mmol), sodium phosphate dibasic dodecahydrate ($\text{Na}_2\text{HPO}_4 \cdot 12\text{H}_2\text{O}$) (2.80 g, 7.82 mmol) and potassium chloride (KCl) (0.20 g, 2.68 mmol) in 1 L deionised water and phosphate buffer (PB, pH 7.5) was prepared by mixing 39 mL 0.2 M sodium dihydrogen phosphate (NaH_2PO_4) stock solution with 61 mL 0.2 M sodium hydrogen diphosphate dodecahydrate ($\text{Na}_2\text{HPO}_4 \cdot 12\text{H}_2\text{O}$) solution and diluting in deionised water to a total volume of 200 mL (all salts from Merck, Darmstadt, Germany).

5 Experimental Section

5.1.2 Methods

5.1.2.1 NMR spectroscopy

NMR spectra were recorded on a Bruker Fourier 300 at 300 MHz with 128 scans and on a Bruker Fourier 600 at 600 MHz with up to 4096 scans (Billerica, MA, USA). Deuterated chloroform (CDCl_3) and deuterium oxide (D_2O) with TMS as internal reference were applied. Signal multiplicities were abbreviated with s (singlet), d (doublet), tr (triplet), m (multiplet).

5.1.2.2 SEC

SEC measurements were performed on a Viscotek SECmax (Malvern Instruments, Malvern, UK) with water (including 0.1 M NaNO_3 and 0.02 % NaN_3) as solvent and on an OmniSEC Resolve (Malvern Instruments, Malvern, UK) with DMF (including 1 g/L LiBr) as solvent. In the water system a flow rate of 0.7 mL/min was applied, whereas for the DMF system a flow rate of 1.0 mL/ was adjusted. The water system further consists of a column oven at 35 °C and a refractive index (RI) detector (Viscotek VE3580). Viscotek A2000 and A3000 columns (length: 300 mm, width: 8 mm, polymethylmethacrylate (PMMA) with a pore diameter of 6 μm and 8 μm) were used. PEG standards were used for calibration. The DMF system contains a column oven at 45 °C and a RI detector. The column (A2000 and A3000) material is styrene-divinyl benzene (styrene-DVB) (length: 300 mm, width: 8 mm, pore diameter of 6 μm). PMMA standards were used for calibration. For sample preparation approximately 5 mg of the samples were dissolved in 1 ml of the corresponding eluent and filtered (cellulose or PTFE, 0.2 μm pore size).

The functionalities of the polymers can provoke attractive interactions with the column material, which may result in prolonged retention times and thus in a broad dispersity, falsifying values of M_w , M_N and \bar{D} . Therefore, thorough SEC characterisation of non-functionalised P(AGE_{6/12}-CO-EEGE) and P(AGE_{6/12}-CO-G) is given in **Section 5.2.2** and **5.2.3**, in order to verify polymers with small \bar{D} and realistic values of M_w and M_N .

5.1.2.3 UV-vis absorbance

UV-vis absorbance scans in the range from 250 nm to 900 nm were performed on a Genesys 10S Bio spectrophotometer (Thermo Fisher Scientific, Waltham, MA, USA) at room temperature in UV-transparent plastic cuvettes. Samples were prepared by diluting the colloidal solutions 1:10.

5.1.2.4 FT-IR spectroscopy

FT-IR spectroscopy was carried out with a NICOLET iS 10 spectrometer (Thermo Fisher Scientific, Waltham, MA, USA) carrying an ATR unit by using the software OMNIC 8.2 (Thermo Fisher Scientific, Waltham, MA, USA).

5.1.2.5 RAMAN spectroscopy

RAMAN measurements were performed with a DXR RAMAN Microscope (Thermo Fisher Scientific; Waltham, MA, USA) with a special resolution of 540 nm, a confocal depth resolution of 1.7 μm , with laser class 1 and an excitation laser of 780 nm.

5.1.2.6 Fluorescence spectroscopy

Fluorescence measurements were performed with a SQ-2000-4 fluorescence spectrometer (Photon Technology International, Edison, NJ, USA) with a xenon lamp (75 W) and photomultiplier (R928P) in a 1 cm quartz cuvette.

5.1.2.7 DLS

DLS measurements, including the determination of the hydrodynamic diameter and the zeta potential were performed with a Zetasizer Nano ZSP in the backscatter mode at 173° in bidistilled water. Samples for DLS measurements were prepared by diluting the colloidal solutions 1:10.

5.1.2.8 ICP-MS

The particle concentration was determined via ICP-MS (Varian, Darmstadt, Germany). AuNPs were dissolved with aqua regia ($\text{HCl}:\text{HNO}_3 / 3:1$), afterwards gold ions were measured against standard solutions (100 ppb, 1000 ppb and 10000 ppb).

5.1.2.9 TGA

TGA experiments were carried out by NETZSCH GmbH Headquarters with a micro-TG 209 F1 Libra (NETZSCH, Selb, Germany). The samples were pre-dried in a compartment dryer at 80 °C till all water was evaporated. Afterwards the samples were heated from 25 °C to 80 °C (N₂) in the thermo-microbalance and kept at that temperature, in order to prove that water is completely removed. The samples were further heated with a heating rate of 10 °C/min till 550 °C under N₂ atmosphere, before the atmosphere was switched to air and the temperature was raised to 900 °C. The weight loss between 320 °C and 460 °C was ascribed to PEG attached to the gold surface, whereas for bound PG the region between 215 °C and 320 °C was considered. The weight loss below 320 °C (PEG) or 215 °C (PG) was attributed to loose polymer and not taken into account for calculations.^[43]

5.1.2.10 XPS

XPS measurements were carried out by the DWI Aachen in an Ultra Axis™ spectrometer (Kratos Analytical, Manchester, UK). The samples were irradiated with monoenergetic Al K α 1,2 radiation (1486.6 eV) and the spectra were taken at a power of 144 W (12 kV x 12 mA). The aliphatic carbon (C-C, C-H) at a binding energy of 285 eV (C 1s photoline) was used to determine the charging. The spectral resolution, i.e. the Full Width of Half Maximum (FWHM) of the ester-carbon from PET, was better than 0.68 eV for the elemental spectra. The elemental concentration is given in atom-%. This method can detect all elements except hydrogen and helium. Thus, the determination of the composition does not consider both these elements. The information depth is about 10 nm nanometers for polymers. For the calculation of atom-% the percentages of each elemental RAW area were determined. Therefore, the RAW area was corrected via division by the RSF factor, where all areas equalled 100 %. By multiplication of atom-% with the atomic weight mass-% were defined. The samples were prepared by coating all polymers and correspondingly modified 30 nm AuNPs onto Si wafer.

5.1.2.11 Contact angle based measurements

Water droplets (3 μ L) were placed onto glass sides coated with the respective polymer, images were taken after 5 s of the deposition and the left and right contact angles were measured successively (Contact Angle System OCA, DataPhysics Instruments GmbH, Filderstadt, Germany).

5.1.2.12 SEM

SEM (Carl Zeiss Microscopy, Göttingen, Germany) images of AuNP were recorded by dropping the colloidal solutions on a silica wafer, which was fixed with conductive silver to SEM stubs. After the evaporation of water AuNP were measured with secondary electron detector. For the depiction of AuNP@P(SET-co-SA-co-G) attached to mouse B cells, the AuNP-cell conjugates were spin coated onto glass-slides. After applying a 4 nm Pt layer, the conjugates were measured with secondary electron detector.

5.1.2.13 Laser-triggered cell elimination

Laser irradiation of AuNP-cell-conjugates was performed at the IMMEI Bonn with a DIVA II Nd:YAG laser (Soliton Laser- und Messtechnik GmbH, Gilching, Germany) emitting a wavelength of 532 nm (frequency doubled Nd:YAG) with a pulse duration of 11 ns and a repetition rate of 20 Hz. AuNP-cells-conjugates were placed in a quartz well plate and observed under an inverted microscope. With the help of an adjustable stage the samples were moved through the laser beam with a defined scan profile in x- and y-direction under an irradiation with 1.25 J cm^{-2} (125 mW), ensuring a consistent energy exposure on cells. The percentage of eliminated cells was quantified by fluorescence-activated cell sorting on a MACSQuant-10 (Miltenyi Biotech GmbH, Bergisch Gladbach, Germany) after Calcein Green and Hoechst 33342 staining

5.1.2.14 Purification of polymers

For purification all polymers were dialysed against deionised water for 3 d (4 x water exchange/d) (Biotech Cellulose Ester dialysis membrane, MW cut-off 1000, 3500, 14000, 50000 Da, spectrumlabs.com, Rancho Dominguez, CA, USA). Depending on the solubility of the reagents a dialysis against a mixture of deionised water and DMF or EtOH for 2 d was conducted prior to that.

5.1.2.15 Lyophilisation of polymers

In order to remove water of the polymeric solutions freeze-drying was applied (Alpha 1-2 LD, Christ, Osterode am Harz, Germany).

5.1.2.16 UV-light triggered reactions

Thiol-ene click reactions were either conducted in EtOH with DMPA as photo-initiator under LED UV-irradiation for 2 h at a distance of 2 cm (365 nm_{LED}, 2 x 11 W, Polymerschmiede, Aachen, Germany) or in a mixture of DMF and deionised water with Irgacure I2959 under UV irradiation for 2 h at a distance of 2 cm (365 nm, 4 W, Hartenstein, Würzburg, Germany). Crosslinking of hydrogels was initiated with UV-light for 10 s at a distance of 5 cm (365 nm, 200 W, 5 x 2 s pulses, bluepoint 4, hönle, Gräfeling, Germany). Diazirines were activated with UV-light irradiation (365 nm, UV handlamp, Hartenstein, Würzburg, Germany) for 20 min.

5.1.2.17 Characterisation and handling of AuNP@citrate

The characterisation of initial AuNP@citrate was performed via DLS and UV-vis absorbance measurements, as displayed in **Table 17**.

DLS, UV-vis (Water):

Table 17: *d*, ζ and SPR of 15 nm, 30 nm and 50 nm AuNP@citrate, determined by DLS and UV-vis absorbance measurements.

<i>AuNP@citrate</i>	15 nm	30 nm	50 nm
<i>d (nm)</i>	18 ± 02	28 ± 09	49 ± 12
<i>ζ (mV)</i>	-29 ± 07	-34 ± 12	-36 ± 08
<i>SPR (nm)</i>	520	525	530

The particle concentration of AuNP@citrate was adjusted by concentrating the colloidal solutions via centrifugation (22000 x g, 30 min, 4 °C) (Mega Star 1.6R, Thermo Fisher Scientific, Waltham, MA, USA) and successive suspension in 800 μL bidistilled water and determined by UV-vis absorbance spectroscopy, as shown in **Table 18**.

UV-vis (Water):**Table 18: Initial and adjusted particle concentration of AuNP@citrate, as determined by UV-vis absorbance spectroscopy.**

Concentration	15 nm	30 nm	50 nm
<i>Initial concentration (particles per mL)</i>	$1.4 \cdot 10^{12}$	$2.0 \cdot 10^{11}$	$4.5 \cdot 10^{10}$
<i>and OD</i>	(OD: 1)	(OD: 1)	(OD: 1)
<i>Adjusted concentration ((particles per mL) and OD</i>	$1.6 \cdot 10^{12}$	$2.7 \cdot 10^{11}$	$9.4 \cdot 10^{10}$
	(OD: 1.04)	(OD: 1.47)	(OD: 2.24)

5.1.2.18 Polymer functionalisation of AuNP@citrate

All successive reactions with AuNPs were conducted in bidistilled water. AuNP@citrate were functionalised with polymers via ligand exchange reaction. Therefore, 900 μ L of AuNP@citrate with adjusted particle concentration (see **Table 18**) were combined with 200 μ L (800 nmol) of a polymeric solution. After incubation at room temperature for 12 h the colloidal solutions were purified by two successive centrifugation- (22000 x g, 30 min, 4°C) and resuspension-cycles in bidistilled water in order to remove unbound polymers.

5.1.2.19 Ellman assay

Thiol groups of the polymer were qualitatively determined by reaction with DTNB and successive UV-vis measurements of the chromogenic side product 2-nitro-5-thiobenzoic acid (TNB) at 412 nm. Therefore, polymers (2 mg in 50 μ L) were dissolved in 900 μ L 0.8 M sodium phosphate buffer (pH 7.0). After the addition of DTNB (4 mg in 50 μ L) absorbance measurements of the solutions at 412 nm were performed.

5.1.2.20 TNBSA assay

The number of primary amine moieties per polymer was quantitatively determined by reaction with TNBSA, resulting in a chromogenic derivative, which can be measured via UV-vis spectroscopy at 335 nm. Ethanolamine was used as a calibration. Briefly, P(SEt-co-NH₂-co-G) was dissolved in 0.1 M NaHCO₃ (pH 8.5) to yield concentrations of 2-100 μ g/mL. To 500 μ L of the polymeric solution, 250 μ L of 0.01% TNBSA solution in NaHCO₃ were added and the mixture was incubated at 37 °C for 2 h. After the addition of 250 μ L 10 % SDS and 125 μ L 1 N HCl, the absorbance of the solutions at 335 nm was measured.

5.1.2.21 (Micro-)BCA assay

The amount of SA on 30 nm AuNP was determined via protein-induced reduction of Cu^{+2} to Cu^{+1} in alkaline medium and successive colorimetric detection of Cu^{+1} via BCA. Therefore 25 μL of the initial SA concentration and 25 μL of the 1st and 2nd supernatant upon centrifugation of AuNP@P(SEt-co-SA-co-G) were treated with 200 μL working reagent, respectively. This working reagent contained a mixture of BCA in alkaline buffer and cupric sulfate (commercially available). After incubation at 37 °C for 30 min the absorbance of the solutions at 562 nm was measured. BSA was used as a calibration. All measurements were performed in triplicate.

5.1.2.22 ELISA

An ELISA was carried out in order to quantify the SA amount on 30 nm AuNP. 50 μL AuNP@P(SEt-co-SA-co-G) were suspended in 150 μL PBS and treated with 20 μL (2.5 mg in 1 mL) biotin-HRP. After incubation at room temperature for 30 min, the particles were purified by two successive centrifugation- and resuspension-steps. Afterwards 100 μL of a mixture of 50 μL 1% TMB in DMSO with 4950 μL citrate buffer and 2 μL 30 % H_2O_2 were added and the solutions were kept at room temperature for 1 h under the exclusion of light. After the addition of 100 μL 0.1 M H_2SO_4 the absorbance of the solutions at 450 nm was measured. A concentration series of SA immobilised onto a maxisorp well plate (Nunc, Thermo Fisher Scientific, Waltham, MA, USA) was used as calibration. Therefore SA was incubated at 4 °C for 24 h on the wells and unbound SA was removed by extensive washing with PBS. Further treatment of immobilised SA corresponded to that of AuNP@P(SEt-co-SA-co-G). All measurements were performed in triplicate.

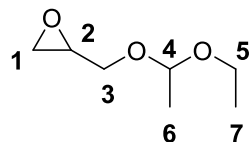
5.1.2.23 TEM staining

Transmission electron microscopy (TEM) staining of PEGylated AuNPs was performed with a Zeiss Libra 120 TEM with an accelerating voltage of 120 kV. Samples were prepared by putting 30 μL of AuNP@MeO-PEG-SH or AuNP@MeO-PEG-SPentyl on a carbon coated copper TEM grid. After evaporation of water, staining was carried out by adding 9 μL of a 2 wt% phosphotungstic acid solution in water. The samples were dried at room temperature. Staining of the poly(glycidol) layer within AuNP@P(SH-co-G) and AuNP@P(SEt-co-G) via this method was not possible.

5.2 Polymer Synthesis and AuNP functionalisation

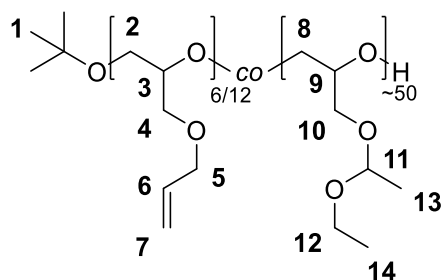
Throughout this section firstly the polymer syntheses are described, followed by (if existing) characterisation of correspondingly functionalised particles.

5.2.1 EEGE



EEGE was synthesised according to literature^[126]. Glycidol (71 mL, 1.07 mol) was combined with ethyl vinyl ether (425 mL, 4.39 mol) and cooled to 0 °C. *p*TsOH (2.00 g, 10.8 mmol) was slowly added, to keep the solution temperature under 20 °C. After stirring for 3 h at room temperature, the mixture was washed with saturated NaHCO₃ solution (3 x 30 mL). The organic phase was dried with MgSO₄ and the ether was removed under vacuum. After pre-drying with CaH₂ for 12 h and subsequent distillation under Ar atmosphere, EEGE was obtained as a colourless liquid.

¹H-NMR (300 MHz, CDCl₃): δ = 4.73-4.70 (m, 1 H, **4**), 3.80-3.35 (m, 4 H, **3+5**), 3.12-3.09 (m, 1 H, **2**), 2.78-2.74 (m, 1 H, **1**), 2.62-2.55 (m, 1 H, **1**), 1.30-1.26 (m, 3 H, **6**), 1.19–1.14 (m, 3 H, **7**) ppm.

5.2.2 P(AGE_{6/12}-co-EEGE)

The copolymerisation of EEGE and AGE was conducted referring to literature^[112]. Throughout this thesis two allyl functionalised PG were synthesised by varying the EEGE/AGE ratio, termed as P(AGE₆-co-EEGE) and P(AGE₁₂-co-EEGE). The respective amount of substances are displayed in **Table 19**. EEGE and AGE were mixed under N₂ atmosphere. KO^tBu was added and the mixture was stirred at 60 °C for 24 h. The polymerisation was stopped by adding 1 mL EtOH. The solvent was removed under reduced pressure and the product was received as a yellow oil.

Table 19: Amount of substances of EEGE, AGE and KO^tBu for polymerisation of P(AGE₆-co-EEGE) and P(AGE₁₂-co-EEGE).

<i>Designation</i>	<i>EEGE</i>	<i>AGE</i>	<i>KO^tBu</i>
<i>P(AGE₆-co-EEGE)</i>	<i>16 mL, 108 mmol</i>	<i>1.5 mL, 12.6 mmol</i>	<i>2 mL, 2.00 mmol</i>
<i>P(AGE₁₂-co-EEGE)</i>	<i>16 mL, 108 mmol</i>	<i>3.0 mL, 25.2 mmol</i>	<i>2 mL, 2.00 mmol</i>

¹H-NMR (300 MHz, CDCl₃): δ = 5.97-5.76 (m, 6 H/12 H, **6**), 5.32-5.06 (m, 12 H/24 H, **7**), 4.78-4.60 (m, 49 H/46 H, **11**), 4.01-3.92 (m, 12 H/24 H, **5**), 3.80-3.31 (m, 415 H/421 H, **2-4, 8-10, 12**), 1.33-1.09 (m, 311 H/297 H, **1, 13, 14**) ppm.

SEC (RI, DMF): (see **Section 5.1.2.2**)

Table 20: Distribution, M_w , M_n and \mathcal{D} of $P(\text{AGE}_6\text{-co-EEGE})$ and $P(\text{AGE}_{12}\text{-co-EEGE})$ in DMF, determined by SEC.

<i>Designation</i>	<i>Distribution</i>	M_w	M_n	\mathcal{D}
$P(\text{AGE}_6\text{-co-EEGE})$	bimodal	6300	5100	1.2
$P(\text{AGE}_{12}\text{-co-EEGE})$	bimodal	6800	5200	1.3

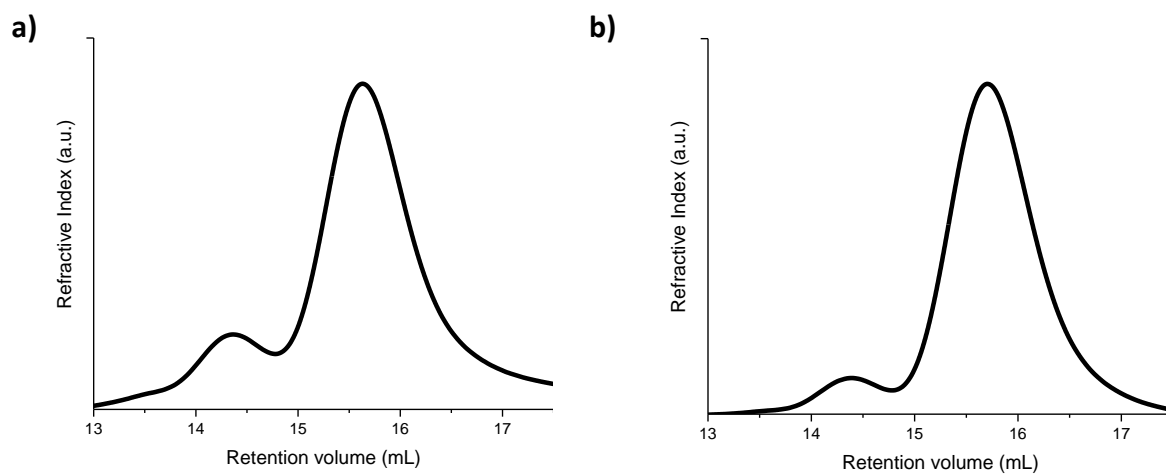
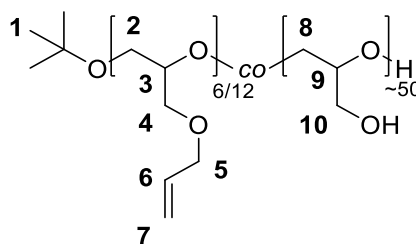


Figure 57: SEC elugram of a) $P(\text{AGE}_6\text{-co-EEGE})$ and b) $P(\text{AGE}_{12}\text{-co-EEGE})$ in DMF, displaying a bimodal distribution.

5.2.3 P(AGE_{6/12}-CO-G)

The acetal protection group of P(AGE₆-co-EEGE) and P(AGE₁₂-co-EEGE) was removed under acidic conditions in order to obtain P(AGE₆-co-G) and P(AGE₁₂-co-G).^[112] Therefore, the polymers were dissolved in THF. After the slow addition of 37 % HCl, the solution was left standing for 4 h. The respective amount of substances are displayed in **Table 21**. Subsequently, THF was decanted, the polymers were dissolved in 200 mL deionised water and neutralised with NaOH. Dialysis (MW cut-off 3500 Da) against deionised water was performed for 3 d and the polymers were freeze-dried and received as a highly viscous yellowish oil.

Table 21: Amount of substances of THF and HCl for the synthesis of P(AGE₆-co-G) and P(AGE₁₂-co-G).

<i>Designation</i>	<i>THF</i>	<i>HCl</i>
<i>P(AGE₆-co-G)</i>	600 mL	16 mL
<i>P(AGE₁₂-co-G)</i>	800 mL	22 mL

¹H-NMR (300 MHz, D₂O): δ = 6.05-5.83 (m, 6 H/12 H, **6**), 5.41-5.19 (m, 12 H/24 H, **7**), 4.14-4.00 (m, 12 H/24 H, **5**), 3.93-3.33 (m, 258 H/300 H, **2-4**, **8-10**), 1.48-1.15 (m, 9 H, **1**) ppm.

Throughout this thesis two batches of P(AGE₆-co-EEGE) and one of P(AGE₁₂-co-EEGE) were synthesised. **Table 22** shows deviations of the monomer repeating units within the batches.

Table 22: Deviation of the ratio between AGE and EEGE within different batches of P(AGE₆-co-G) and the final ratio of P(AGE₆-co-G) and P(AGE₁₂-co-G) used for calculations.

<i>Designation</i>	<i>Ratio of protons</i>	<i>Ratio of AGE:G</i>	<i>Final ratio used for calculations</i>
	6:2-4		
<i>P(AGE₆-co-G) (1)</i>	5.5:245	5.5:44	5.5:50
<i>P(AGE₆-co-G) (2)</i>	5.5:258	5.5:46	5.5:50
<i>P(AGE₁₂-co-G) (1)</i>	12:30	12:48	12:50

SEC (RI, DMF, Water): (see **Section 5.1.2.2**)

Table 23: Distribution, M_w , M_n and \bar{D} of $P(AGE_6\text{-co-G})$ and $P(AGE_{12}\text{-co-G})$ in DMF and water, determined by SEC.

<i>Designation</i>	<i>Distribution</i>	M_w	M_n	\bar{D}
$P(AGE_6\text{-co-G})$				
DMF	<i>monomodal with high molecular weight shoulder</i>	6700	5400	1.2
Water	<i>monomodal with high molecular weight shoulder</i>	3300	2400	1.4
$P(AGE_{12}\text{-co-G})$				
DMF	<i>monomodal with low molecular weight tailing</i>	7000	5600	1.2
Water	<i>monomodal with low molecular weight tailing</i>	2200	1400	1.4

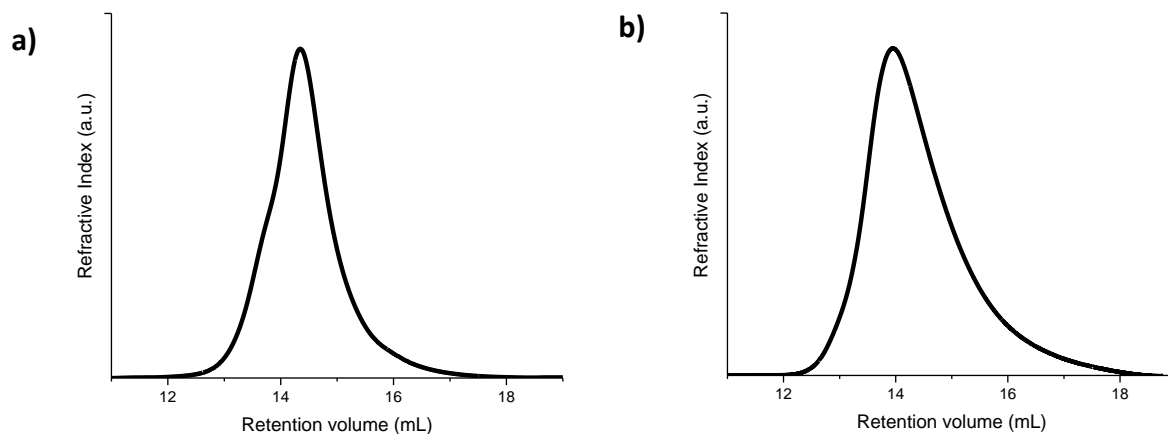
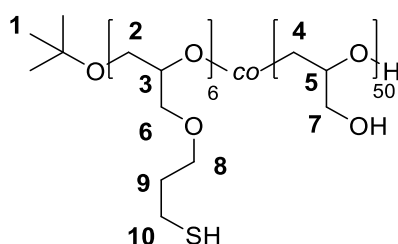


Figure 58: SEC elugram of a) $P(AGE_6\text{-co-G})$ and b) $P(AGE_{12}\text{-co-G})$ in water, displaying a monomodal distribution.

FT-IR (ATR): $\tilde{\nu} = 3370$ (-OH), 2920-2870 (-CH, -CH₂), 1650 (-C=C-), 1040 (-C-O-C-) cm⁻¹.

RAMAN: $\tilde{\nu} = 2940\text{-}2880$ (-CH, -CH₂), 1644 (-C=C-), 1466 (-CH₂-) cm⁻¹.

5.2.4 P(SH-co-G)



P(SH-co-G) was synthesised according to literature^[112]. P(AGE₆-co-G) (1.45 g, 290 μ mol) was dissolved in 200 mL EtOH and the mixture was degassed for 45 min with Ar. After the addition of DMPA (450 mg, 1.75 mmol) and thioacetic acid (876 μ L, 12.3 mmol), the solution was stirred at room temperature under UV irradiation for 2 h. EtOH was removed under vacuum and the polymer was dissolved in 70 mL EtOH and precipitated in 700 mL cold diethylether. After the removal of diethylether under reduced pressure, the polymer was dissolved in 70 mL deionised water with NaOH (7.00 g, 175 mmol). The reaction mixture was refluxed for 2.5 h. Further, the reaction mixture was cooled to room temperature and neutralised with HCl. Afterwards TCEP (1.00 g, 3.90 mmol) was added and the solution was stirred for at room temperature for 12 h. After dialysis against degassed deionised water (2 h Ar flow/2 L water) for 3 d, the polymer was freeze-dried and received as a light yellow oil.

¹H-NMR (300 MHz, D₂O): δ = 3.80-3.67 (m, 285 H, **2-8**), 2.68-2.64 (m, 11 H, **10**), 1.95-1.90 (m, 11 H, **9**), 1.26 (s, 7 H, **1**) ppm.

XPS (mass-%): 32 % O, 62 % C, 6 % S. Calc.: 38 % O, 57 % C, 4 % S.

RAMAN: $\tilde{\nu}$ = 2900-2850 (-CH, -CH₂), 2570 (-S-H), 1460 (-C-O-C-) cm⁻¹.

Ellman assay (OD, 412 nm, 40 μ M): 1.16 a.u.

SEC (RI, Water): M_w: 2700 Da, M_n: 1300 Da, \bar{D} : 2.06.

5.2.4.1 AuNP@P(SH-co-G)

TGA (30 nm AuNP, mass-%): 16 % organic, 84 % inorganic.

FT-IR (ATR): $\tilde{\nu}$ = 3375 (-OH), 2925-2800 (-CH, -CH₂), 1062 (-C-O-C-) cm⁻¹.

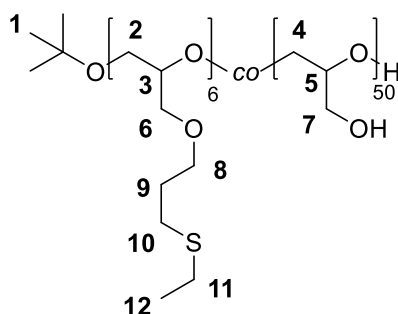
DLS, UV-vis (Water):

Table 24: *d*, ζ and SPR of 15 nm, 30 nm and 50 nm AuNP@P(SH-co-G), determined by DLS and UV-vis absorbance measurements.

AuNP@P(SH-co-G)	15 nm	30 nm	50 nm
<i>d</i> (nm)	23 ± 05	38 ± 08	60 ± 15
ζ (mV)	-19 ± 06	-22 ± 10	-25 ± 08
SPR (nm)	523	526	531

5 Experimental Section

5.2.5 P(SET-co-G)



P(AGE₆-co-G) (700 mg, 146 μ mol) was dissolved in 35 mL EtOH and the mixture was degassed for 30 min with Ar. DMPA (128 mg, 499 μ mol) and EtSH (1.50 mL, 20.2 mmol) were added to the solution and stirred at room temperature under UV irradiation for 2 h. EtOH was removed under reduced pressure and the polymer was dissolved in 60 mL deionised water and dialysed (MW cut-off 3500 Da) against a mixture of deionised water and EtOH (100:1) for 2 d and against pure deionised water for 2 d. Subsequently the polymer was freeze-dried and received as a light yellow oil.

¹H-NMR (300 MHz, D₂O): δ = 3.90-3.39 (m, 285 H, **2-8**), 2.77-2.50 (m, 20 H, **10, 11**), 1.99-1.80 (m, 10 H, **9**), 1.48-1.17 (m, 28 H, **1, 12**) ppm.

XPS (mass-%): 30 % O, 65 % C, 5 % S. Calc.: 37 % O, 59 % C, 4 % S.

RAMAN: $\tilde{\nu}$ = 2900-2850 (-CH, -CH₂), 1460 (-C-O-C-), 650 (-C-S-C-) cm⁻¹.

SEC (RI, Water): M_w: 1800 Da, M_n: 900 Da, Đ: 1.97.

5.2.5.1 AuNP@P(SEt-co-G)

XPS (30 nm AuNP, mass-%): 7 % O, 14 % C, 3 % S, 76 % Au. 15 % organic, 76 % inorganic.

TGA (30 nm AuNP, mass-%): 19 % organic, 76 % inorganic.

FT-IR (ATR): $\tilde{\nu}$ = 2920-2850 (-CH, -CH₂), 1104 (-CH, -CH₂), 1100 (-C-O-C-) cm⁻¹.

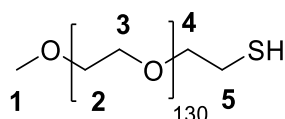
DLS, UV-vis (Water):

Table 25: *d*, ζ and SPR of 15 nm, 30 nm and 50 nm AuNP@P(SEt-co-G), determined by DLS and UV-vis absorbance measurements.

AuNP@P(SEt-co-G)	15 nm	30 nm	50 nm
<i>d</i> (nm)	<i>27 ± 08</i>	<i>42 ± 09</i>	<i>53 ± 14</i>
ζ (mV)	<i>-05 ± 03</i>	<i>-21 ± 07</i>	<i>-08 ± 02</i>
SPR (nm)	524	527	533

5 Experimental Section

5.2.6 MeO-PEG-SH



Commercially purchased. Molecular weight of 6000 Da, as defined by the manufacturer.

¹H-NMR (300 MHz, D₂O): δ = 3.90-3.50 (m, 520 H, backbone-H **2-4**), 3.40 (s, 3 H, **1**), 2.78 (tr, 2 H, **5**) ppm.

XPS (mass-%): 36 % O, 63 % C, 1 % S. Calc.: 36 % O, 63 % C, 1 % S.

Ellman assay (OD, 412 nm, 40 μ M): 0.25 a.u.

SEC (RI, Water): M_w: 2000 Da, M_n: 1800 Da, \bar{D} : 1.08.

5.2.6.1 AuNP@MeO-PEG-SH

XPS (30 nm AuNP, mass-%): 8 % O, 16 % C, 0 % S, 76 % Au. 16 % organic, 76 % inorganic.

TGA (30 nm AuNP, mass-%): 18 % organic, 77 % inorganic.

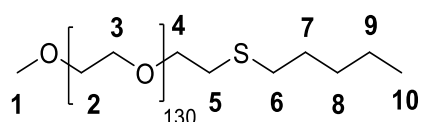
FT-IR (ATR): $\tilde{\nu}$ = 2880 (-CH₂), 1341 (-CH₂), 1100 (-C-O-C-) cm⁻¹.

DLS, UV-vis (Water):

Table 26: *d*, ζ and SPR of 15 nm, 30 nm and 50 nm AuNP@MeO-PEG-SH, determined by DLS and UV-vis absorbance measurements.

AuNP@MeO-PEG-SH	15 nm	30 nm	50 nm
<i>d</i> (nm)	38 ± 06	48 ± 08	64 ± 12
ζ (mV)	-10 ± 07	-29 ± 10	-27 ± 07
SPR (nm)	526	528	533

5.2.7 MeO-PEG-SPentyl



MeO-PEG-SH (150 mg, 25.0 μmol) was dissolved in 8 mL EtOH and the mixture was degassed for 30 min with Ar. DMPA (13.0 mg, 50.7 μmol) and 1-pentene (100 μL , 89.7 μmol) were added to the solution and stirred at room temperature under UV irradiation for 2 h. EtOH was removed under vacuum, the polymer was dissolved in 20 mL deionised water and dialysed (MW cut-off 3500 Da) against a mixture of deionised water and EtOH (100:1) for 2 d and against deionised water for 3 d. Afterwards the polymer was freeze-dried and received as a white powder.

$^1\text{H-NMR}$ (300 MHz, D_2O): δ = 3.90-3.50 (m, 520 H, backbone-H **2-4**), 3.40 (s, 3 H, **1**), 3.03-2.92 (m, 2 H, **5**), 2.88-2.72 (m, 2 H, **6**), 1.88-1.20 (m, 6 H, **7-9**), 0.93 (tr, 3 H, **10**) ppm.

XPS (mass-%): 33 % O, 66 % C, 1 % S. Calc.: 34 % O, 65 % C, 1 % S.

SEC (RI, Water): M_w : 2000 Da, M_n : 1800 Da, D : 1.09.

5.2.7.1 AuNP@MeO-PEG-SPentyl

XPS (30 nm AuNP, mass-%): 6 % O, 14 % C, 1 % S, 79 % Au. 15 % organic, 79 % inorganic.

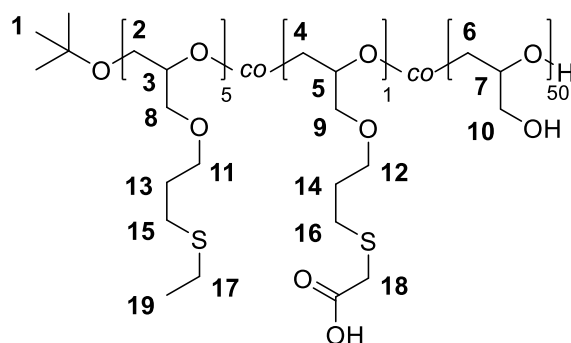
TGA (30 nm AuNP, mass-%): 17 % organic, 81 % inorganic.

DLS, UV-vis (Water):

Table 27: *d*, ζ and SPR of 15 nm, 30 nm and 50 nm AuNP@MeO-PEG-SPentyl, determined by DLS and UV-vis absorbance measurements.

AuNP@MeO-PEG-SPentyl	15 nm	30 nm	50 nm
<i>d</i> (nm)	32 ± 08	41 ± 08	59 ± 14
ζ (mV)	-15 ± 03	-21 ± 07	-23 ± 05
SPR (nm)	526	527	533

5.2.8 P(SEt-co-COOH-co-G)



P(AGE₆-co-G) (700 mg, 146 μ mol) was dissolved in 35 mL EtOH and the mixture was degassed for 30 min with Ar. Subsequently DMPA (128 mg, 499 μ mol), EtSH (600 μ L, 8.08 mmol) and thioglycolic acid (70.0 mL, 1.01 mmol) were added and the solution was stirred at room temperature under UV irradiation for 2 h. Afterwards EtOH was removed under reduced pressure and the polymer was dissolved in 80 mL deionised water and dialysed (MW cut-off 3500 Da) against a mixture of deionised water and EtOH (100:1) for 2 d and against deionised water for 2 d. After freeze-drying the polymer was obtained as a light yellow oil.

¹H-NMR (300 MHz, D₂O): δ = 3.90-3.39 (m, 285 H, **2-12**), 3.25 (s, 2 H, **18**), 2.77-2.55 (m, 20 H, **15-17**), 2.00-1.85 (m, 10 H, **13, 14**), 1.49-1.17 (m, 25 H, **1, 19**) ppm.

FT-IR (ATR): $\tilde{\nu}$ = 3500-3100 (-O-H), 2900-2850 (-CH, -CH₂), 1730 (-COOH), 1460 (-C-O-C-) cm⁻¹.

SEC (RI, Water): M_w: 7200 Da, M_n: 3900 Da, Đ: 1.85.

5.2.8.1 AuNP@P(SEt-co-COOH-co-G)

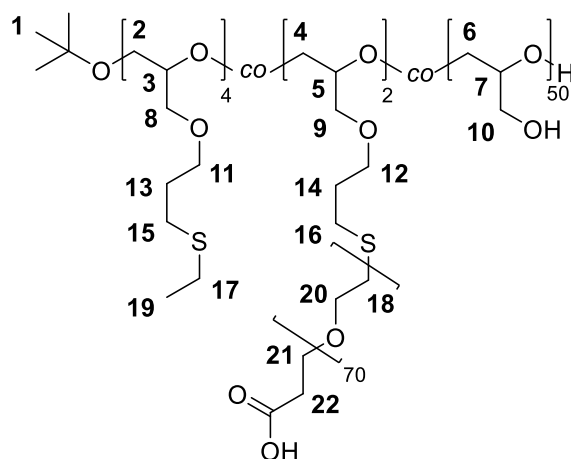
FT-IR (ATR): $\tilde{\nu}$ = 3500-3100 (-O-H), 2900-2850 (-CH, -CH₂), 1730 (-COOH), 1460 (-C-O-C-) cm⁻¹.

DLS, UV-vis (Water):

Table 28: d, ζ and SPR of 30 nm AuNP@P(SEt-co-COOH-co-G).

AuNP@P(SEt-co-COOH-co-G)	30 nm
d (nm)	37 ± 08
ζ (mV)	-23 ± 05
SPR (nm)	528

5.2.9 P(SEt-co-PEG-COOH-co-G)



P(AGE₆-co-G) (100 mg, 20.9 μmol) was dissolved in a mixture of 10 mL DMF and 10 mL deionised water and degassed for 20 min. After the addition of Irgacure (32.0 mg, 143 μmol), EtSH (200 μL, 2.69 mmol) and HS-PEG-COOH (70 mg, 22.8 μmol), the solution was stirred at room temperature under UV irradiation for 2 h. Subsequently the solvents were removed under reduced pressure and the polymer was dissolved in 40 mL deionised water and dialysed (MW cut-off 3500 Da) against a mixture of deionised water and DMF (100:1) for 3 d and against deionised water for 3 d. The polymer was freeze-dried and obtained as a white solid.

¹H-NMR (600 MHz, D₂O): δ = 4.05-3.52 (m, 845 H, **2-12**, **18**, **20**, **21**), 3.41 (t, 5 H, **22**), 3.00-2.65 (m, 18 H, **15-17**), 2.21-2.01 (m, 10 H, **13**, **14**), 1.47-1.23 (m, 19 H, **1**, **19**) ppm.

FT-IR (ATR): $\tilde{\nu}$ = 3500-3100 (-O-H), 2900-2850 (-CH, -CH₂), 1730 (-COOH), 1460 (-C-O-C-) cm⁻¹.

SEC (RI, Water): M_w: 8600 Da, M_n: 4700 Da, Đ: 1.83.

5.2.9.1 AuNP@P(SEt-co-PEG-COOH-co-G)

FT-IR (ATR): $\tilde{\nu}$ = 3500-3100 (-O-H), 2900-2850 (-CH, -CH₂), 1730 (-COOH), 1460 (-C-O-C-) cm⁻¹.

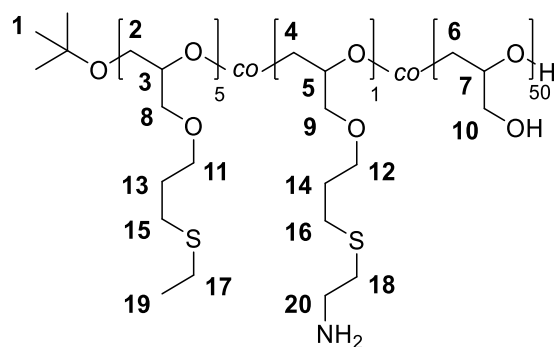
DLS, UV-vis (Water):

Table 29: d, ζ and SPR of 15 nm AuNP@P(SEt-co-PEG-COOH-co-G).

AuNP@P(SEt-co-PEG-COOH-co-G)	15 nm
d (nm)	31 ± 05
ζ (mV)	-27 ± 06
SPR (nm)	523

5 Experimental Section

5.2.10 P(SET-*co*-NH₂-*co*-G)



P(AGE₆-*co*-G) (350 mg, 70.0 μmol) was dissolved in a mixture of 15 mL deionised water and 15 mL DMF. After degassing for 30 min with Ar, Irgacure (58.0 mg, 259 μmol), EtSH (300 μL , 4.04 mmol) and cysteamine hydrochloride (100 mg, 880 μmol) were added. The solution was stirred at room temperature under UV irradiation for 2 h. The solvent was removed under vacuum. The polymer was dissolved in 40 mL deionised water and dialysed (MW cut-off 3500 Da) against a mixture of deionised water and DMF (100:1) for 2 d and against deionised water for 3 d. The polymer was freeze-dried and obtained as a light yellow oil.

¹H-NMR (300 MHz, D₂O): δ = 4.08-3.42 (m, 285 H, **2-12**), 3.25 (t, 2 H, **20**), 3.05-2.80 (m, 2 H, **18**), 2.75-2.52 (m, 19 H, **15-17**), 1.99-1.81 (m, 10 H, **13, 14**), 1.44-1.16 (m, 21 H, **1, 19**) ppm.

FT-IR (ATR): $\tilde{\nu}$ = 3500-3100 (-O-H, -NH₂), 2900-2850 (-CH, -CH₂), 1600 (-NH₂), 1460 (-C-O-C-) cm⁻¹.

TNBSA assay (OD: 335 nm, 60-100 μM): 0.16-0.25 a.u.

SEC (RI, Water): M_w: 1900 Da, M_n: 1200 Da, \bar{D} : 1.68.

5.2.10.1 AuNP@P(SEt-co-NH₂-co-G)

FT-IR (ATR): $\tilde{\nu}$ = 3500-3100 (-O-H, -NH₂), 2900-2850 (-CH, -CH₂), 1600 (-NH₂), 1460 (-C-O-C-) cm⁻¹.

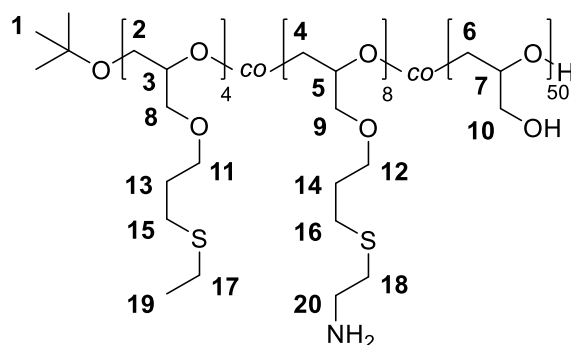
DLS, UV-vis (Water):

Table 30: *d*, ζ and SPR of 15 nm and 30 nm AuNP@P(SEt-co-NH₂-co-G).

AuNP@P(SEt-co-NH₂-co-G)	15 nm	30 nm
<i>d</i> (nm)	31 ± 07	100 ± 20
ζ (mV)	$+07 \pm 04$	$+10 \pm 05$
SPR (nm)	524	529

5 Experimental Section

5.2.11 P(SET-*co*-NH₂(8)-*co*-G)



P(AGE₁₂-*co*-G) (1.00 g, 200 μ mol) was dissolved in 50 mL EtOH and the mixture was degassed for 30 min with Ar. After adding DMPA (160 mg, 0.624 mmol), EtSH (750 μ L, 10.1 mmol) and cysteamine hydrochloride (250 mg, 2.20 mmol), the solution was stirred at room temperature under UV irradiation for 2 h. The solvent was removed under vacuum, further the polymer was dissolved in 100 mL deionised water and dialysed (MW cut-off 3500 Da) against a mixture of deionised water and EtOH (100:1) for 2 d and against deionised water for 2 d. Afterwards the polymer was freeze-dried and received as a light yellow oil.

¹H-NMR (300 MHz, D₂O): δ = 3.90-3.50 (m, 334 H, **2-12**), 3.24 (t, 14 H, **20**), 2.99-2.82 (m, 14 H, **18**), 2.76-2.55 (m, 34 H, **15-17**), 2.00-1.85 (m, 23 H, **13, 14**), 1.49-1.14 (m, 25 H, CH₂-CH₃, **1, 19**) ppm.

FT-IR (ATR): $\tilde{\nu}$ = 3500-3100 (-O-H, -NH₂), 2900-2850 (-CH, -CH₂), 1600 (-NH₂), 1460 (-C-O-C-) cm⁻¹.

TNBSA assay (OD: 335 nm, 10-20 μ M): 0.19-0.30 a.u.

SEC (RI, Water): M_w: 750 Da, M_n: 1200 Da, \bar{D} : 1.54.

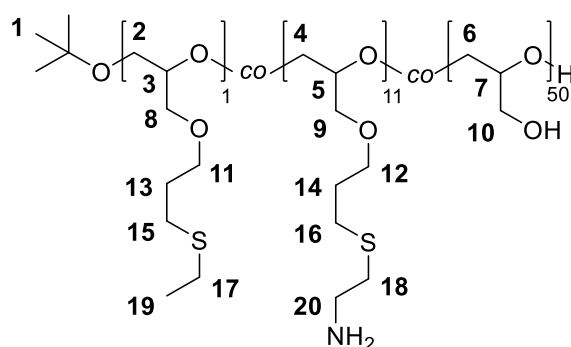
5.2.11.1 AuNP@P(SEt-co-NH₂₍₈₎-co-G)

FT-IR (ATR): $\tilde{\nu}$ = 3500-3100 (-O-H, -NH₂), 2900-2850 (-CH, -CH₂), 1600 (-NH₂), 1460 (-C-O-C-) cm⁻¹.

DLS, UV-vis (Water):

Table 31: *d*, ζ and SPR of 15 nm AuNP@P(SEt-co-NH₂₍₈₎-co-G).

AuNP@P(SEt-co-NH₂₍₈₎-co-G)	15 nm
<i>d</i> (nm)	83 ± 10
ζ (mV)	+23 ± 08
SPR (nm)	525

5.2.12 P(SET-*co*-NH₂(11)-*co*-G)

P(AGE₁₂-*co*-G) (200 mg, 40.0 μmol) was dissolved in a mixture of 4 mL DMF and 4 mL deionised water and degassed for 15 min with Ar. Irgacure (64.0 mg, 285 μmol), EtSH (90.0 μL, 1.21 mmol) and cysteamine hydrochloride (600 mg, 5.28 mmol) were added and the solution was stirred at room temperature under UV irradiation for 2 h. The solvent was removed under vacuum. Afterwards the polymer was dissolved in 50 mL deionised water and dialysed (MW cut-off 3500 Da) against a mixture of deionised water and DMF (100:1) for 2 d and against deionised water for 2 d. The polymer was freeze-dried and received as a light yellow oil.

¹H-NMR (300 MHz, D₂O): δ = 3.95-3.51 (m, 334 H, **2-12**), 3.17 (t, 22 H, **20**), 2.95-2.77 (m, 21 H, **18**), 2.76-2.55 (m, 27 H, **15-17**), 2.00-1.85 (m, 23 H, **13, 14**), 1.49-1.14 (m, 14 H, CH₂-CH₃, **1, 19**) ppm.

FT-IR (ATR): $\tilde{\nu}$ = 3500-3100 (-O-H, -NH₂), 2900-2850 (-CH, -CH₂), 1600 (-NH₂), 1460 (-C-O-C-) cm⁻¹.

TNBSA assay (OD: 335 nm, 5.0-10 μM): 0.16-0.25 a.u.

SEC (RI, Water): M_w: 900 Da, M_n: 600 Da, Đ: 1.44.

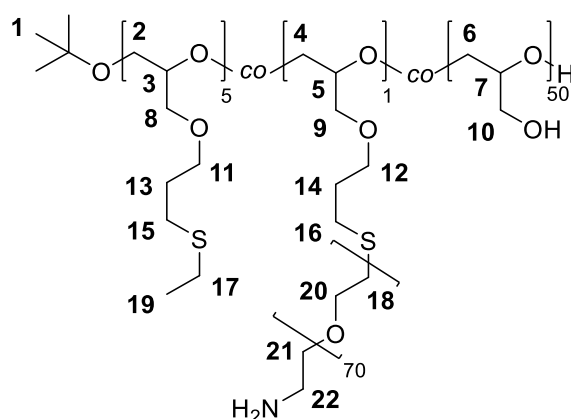
5.2.12.1 AuNP@P(SEt-co-NH₂₍₁₁₎-co-G)

FT-IR (ATR): $\tilde{\nu}$ = 3500-3100 (-O-H, -NH₂), 2900-2850 (-CH, -CH₂), 1600 (-NH₂), 1460 (-C-O-C-) cm⁻¹.

DLS, UV-vis (Water):

Table 32: *d*, ζ and SPR of 15 nm AuNP@P(SEt-co-NH₂₍₁₁₎-co-G).

AuNP@P(SEt-co-NH₂₍₁₁₎-co-G)	15 nm
<i>d</i> (nm)	108 ± 13
ζ (mV)	+33 ± 06
SPR (nm)	526

5.2.13 P(SET-*co*-PEG-NH₂-*co*-G)

P(AGE₆-*co*-G) (250 mg, 52.3 μ mol) was dissolved in a mixture of 15 mL DMF and 1 mL deionised water and degassed for 30 min. After the addition of Irgacure (80.0 mg, 357 μ mol), EtSH (500 μ L, 6.73 mmol) and HS-PEG-NH₂ (175 mg, 52.8 μ mol), the solution was stirred at room temperature under UV irradiation for 2 h. The solvents were removed under reduced pressure and the polymer was dissolved in 50 mL deionised water and dialysed (MW cut-off 3500 Da) against a mixture of deionised water and DMF (100:1) for 3 d and against deionised water for 3 d. The polymer was freeze-dried and obtained as a white solid.

¹H-NMR (300 MHz, D₂O): δ = 4.05-3.52 (m, 565 H, **2-12, 18, 20**), 3.25 (t, 2 H, **22**), 3.03-2.92 (m, 2 H, **21**), 2.76-2.55 (m, 24 H, **15-17**), 2.21-2.01 (m, 11 H, **13, 14**), 1.47-1.23 (m, 26 H, **1, 19**) ppm.

FT-IR (ATR): $\tilde{\nu}$ = 3500-3100 (-O-H, -NH₂), 2900-2850 (-CH, -CH₂), 1600 (-NH₂), 1460 (-C-O-C-) cm⁻¹.

SEC (RI, Water): M_w: 3100 Da, M_n: 1600 Da, \bar{D} : 1.99.

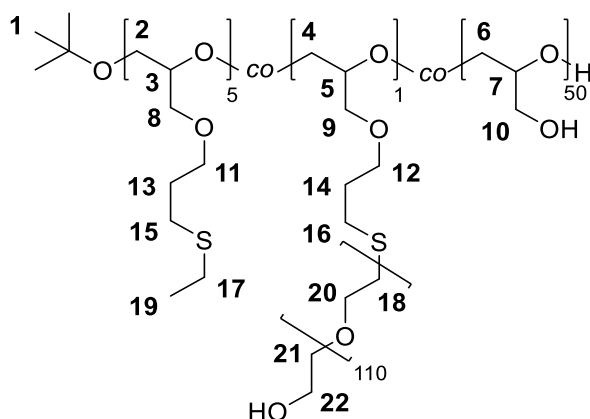
5.2.13.1 AuNP@P(SEt-co-PEG-NH₂-co-G)

FT-IR (ATR): $\tilde{\nu}$ = 3500-3100 (-O-H, -NH₂), 2900-2850 (-CH, -CH₂), 1600 (-NH₂), 1460 (-C-O-C-) cm⁻¹.

DLS, UV-vis (Water):

Table 33: *d*, ζ and SPR of 15 nm AuNP@P(SEt-co-PEG-NH₂-co-G).

AuNP@P(SEt-co-PEG-NH₂-co-G)	15 nm
<i>d</i> (nm)	36 ± 07
ζ (mV)	02 ± 02
SPR (nm)	525

5.2.14 P(SET-*co*-PEG-OH-*co*-G)

P(AGE₆-*co*-G) (25.0 mg, 5.23 μmol) was dissolved in a mixture of 5 mL EtOH and 1 mL deionised water and degassed for 15 min. Subsequently DMPA (9.00 mg, 35.2 μmol), EtSH (50.0 μL , 673 μmol) and HS-PEG-OH (40.0 mg, 8.00 μmol) were added to the solution. After stirring at room temperature under UV irradiation for 2 h, EtOH and deionised water were removed under reduced pressure and the polymer was dissolved in 20 mL deionised water and dialysed (MW cut-off 3500 Da) against a mixture of deionised water and EtOH (100:1) for 2 d and against deionised water for 3 d. The polymer was freeze-dried and received as a white solid.

¹H-NMR (300 MHz, D₂O): δ = 4.01-3.43 (m, 737 H, **2-12, 18, 20-22**), 3.38-2.86 (m, 21 H, **15-17**), 2.21-2.01 (m, 9 H, **13, 14**), 1.47-1.23 (m, 21 H, **1, 19**) ppm.

FT-IR (ATR): $\tilde{\nu}$ = 3500-3100 (-O-H), 2900-2850 (-CH, -CH₂), 1460 (-C-O-C-) cm⁻¹.

Contact angle: θ = 9°.

SEC (RI, Water): M_w: 4000 Da, M_n: 3300 Da, Đ: 1.21.

5.2.14.1 AuNP@P(SEt-co-PEG-OH-co-G)

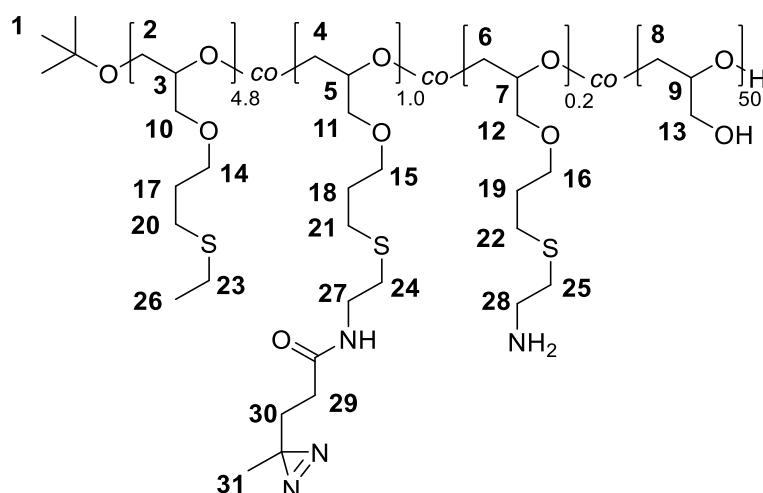
FT-IR (ATR): $\tilde{\nu}$ = 3500-3100 (-O-H), 2900-2850 (-CH, -CH₂), 1460 (-C-O-C-) cm⁻¹.

DLS, UV-vis (Water):

Table 34: *d*, ζ and SPR of 15 nm AuNP@P(SEt-co-PEG-OH-co-G).

<i>AuNP@P(SEt-co-PEG-OH-co-G)</i>	<i>15 nm</i>
<i>d (nm)</i>	32 ± 06
<i>ζ (mV)</i>	-16 ± 04
<i>SPR (nm)</i>	522

5.2.16 P(SEt-co-Diaz-co-G)



P(SET-co-NH₂-co-G) (257 mg, 50.9 μ mol) was dissolved in 10 mL abs. DMF under Ar atmosphere. After the addition of NHS-diazirine (20.0 mg, 88.8 μ mol) the solution was stirred for 5 h at room temperature under the exclusion of light. DMF was removed under vacuum, the polymer was dissolved in 20 mL deionised water and dialysed (MW cut-off 3500 Da) against a mixture of deionised water and DMF (100:1) for 2 d and against deionised water for 3 d under the exclusion of light. Afterwards the polymer was freeze-dried and obtained as a light yellow oil.

¹H-NMR (600 MHz, D₂O): δ = 3.93-3.45 (m, 312 H, **2-16**), 3.40 (t, 2 H, **27**), 3.19 (t, 0.3 H, **28**), 3.12-3.03 (m, 0.3 H, **25**), 3.00-2.13 (m, 22 H, **20-22**, **23**, **24**), 2.02 (t, 2 H, **29**), 1.91-1.80 (m, 9 H, **17-19**), 1.68 (tr, 2 H, **30**), 1.33-1.18 (m, 20 H, **1**, **26**), 1.00 (s, 3 H, **31**) ppm. (see **Figure 59**)

FT-IR (ATR): $\tilde{\nu}$ = 3500-3100 (-O-H), 2900-2850 (-CH, -CH₂), 1650 (-C=O), 1550 (-N-H), 1460 (-C-O-C-) cm⁻¹.

UV-vis (Water): λ_{\max} = 360 nm.

SEC (RI, Water): M_w: 1900 Da, M_n: 1000 Da, Đ: 1.9.

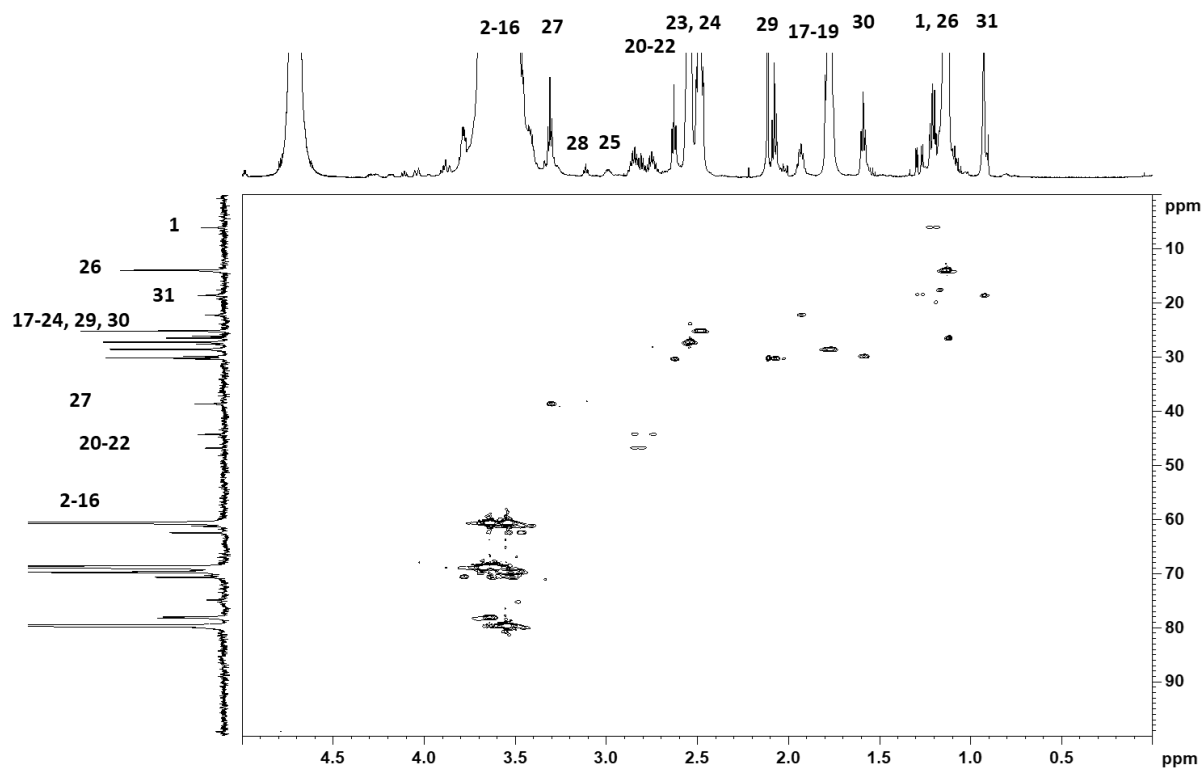


Figure 59: 600 MHz HSQC spectrum of P(SET-co-Diaz-co-G).

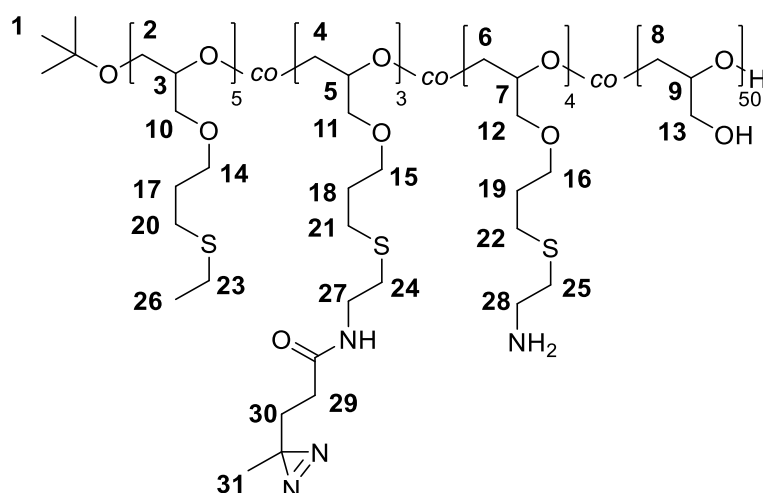
5.2.16.1 AuNP@P(SET-co-Diaz-co-G)

FT-IR (ATR): $\tilde{\nu}$ = 3500-3100 (-O-H), 2900-2850 (-CH, -CH₂), 1650 (-C=O), 1550 (-N-H-), 1460 (-C-O-C-) cm⁻¹.

DLS, UV-vis (Water):

Table 36: *d*, ζ and SPR of 30 nm AuNP@P(SET-co-Diaz-co-G).

AuNP@P(SET-co-Diaz-co-G)	30 nm
<i>d</i> (nm)	33 ± 09
ζ (mV)	-25 ± 08
SPR (nm)	529

5.2.17 P(SEt-co-Diaz₍₃₎-co-G)

P(SET-co-NH₂(8)-co-G) (150 mg, 25.0 μ mol) was dissolved in 10 mL abs. DMF under Ar atmosphere. NHS-diazirine (38.0 mg, 169 μ mol) was added and the solution was stirred for 5 h at room temperature under the exclusion of light. After DMF was removed under vacuum, the polymer was dissolved in 40 mL deionised water and dialysed (MW cut-off 3500 Da) against a mixture of deionised water and DMF (100:1) for 2 d and against deionised water for 2 d under the exclusion of light. Afterwards the polymer was freeze-dried and obtained as a light yellow oil.

¹H-NMR (300 MHz, D₂O): δ = 3.90-3.50 (m, 334 H, **2-16**), 3.44 (t, 6 H, **27**), 3.26 (t, 7 H, **28**), 2.95-2.86 (m, 7 H, **25**), 2.82-2.57 (m, 36 H, **20-22**, **23**, **24**), 2.23 (t, 4 H, **29**), 2.10-1.85 (m, 25 H, **17-19**), 1.68 (tr, 8 H, **30**), 1.46-1.21 (m, 26 H, **1**, **26**), 1.10 (s, 10 H, **31**) ppm.

FT-IR (ATR): $\tilde{\nu}$ = 3500-3100 (-O-H), 2900-2850 (-CH, -CH₂), 1650 (-C=O), 1550 (-N-H), 1460 (-C-O-C-) cm⁻¹.

UV-vis (Water): λ_{\max} = 360 nm.

SEC (RI, Water): M_w: 1700 Da, M_n: 800 Da, Đ: 2.08.

5.2.17.1 AuNP@P(SEt-co-Diaz₍₃₎-co-G)

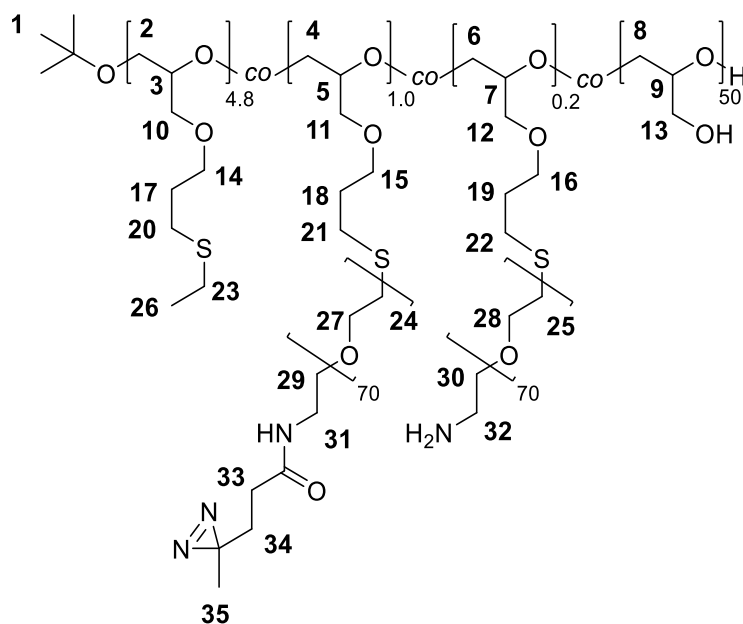
FT-IR (ATR): $\tilde{\nu}$ = 3500-3100 (-O-H), 2900-2850 (-CH, -CH₂), 1650 (-C=O), 1550 (-N-H-), 1460 (-C-O-C-) cm⁻¹.

DLS, UV-vis (Water):

Table 37: *d*, ζ and SPR of 30 nm AuNP@P(SEt-co-Diaz₍₃₎-co-G).

<i>AuNP@P(SEt-co-Diaz₍₃₎-co-G)</i>	30 nm
<i>d (nm)</i>	34 ± 09
<i>ζ (mV)</i>	15 ± 04
<i>SPR (nm)</i>	529

5.2.18 P(SEt-co-PEG-Diaz-co-G)



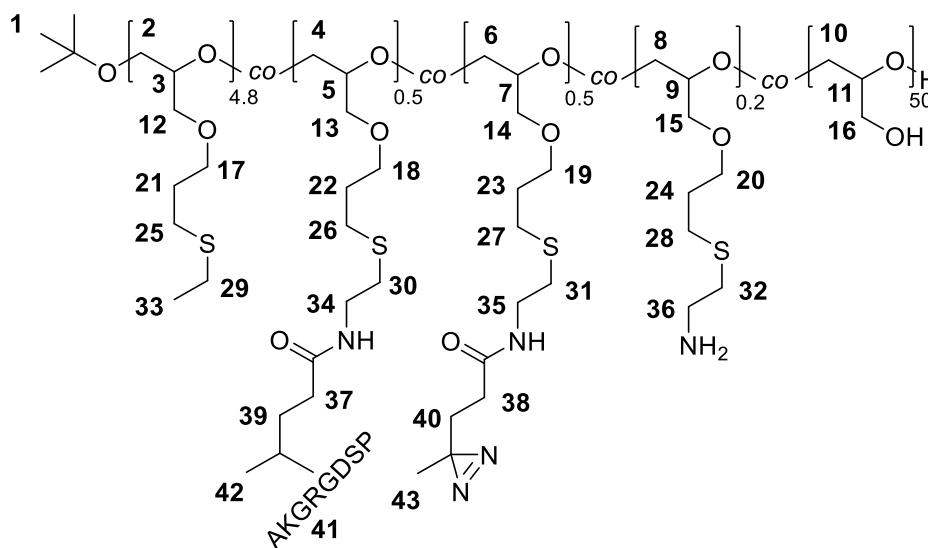
P(SEt-co-PEG-NH₂-co-G) (175 mg, 21.9 μ mol) was dissolved in 10 mL dry DMF under Ar atmosphere. Subsequently NHS-diazirine (10.0 mg, 44.4 μ mol) was added and the solution was stirred at room temperature for 2 h under the exclusion of light. DMF was removed under vacuum, the polymer was dissolved in 20 mL deionised water and dialysed (MW cut-off 3500 Da) against a mixture of deionised water and DMF (100:1) for 2 d and against deionised water for 3 d under the exclusion of light. The polymer was freeze-dried and obtained as a white solid.

¹H-NMR (300 MHz, D₂O): δ = 4.09-3.50 (m, 565 H, **2-16**, **24**, **25**, **27**, **28**), 3.44 (tr, 2 H, **31**), 3.26 (m, 0.5 H, **32**), 2.95-2.86 (m, 1.5 H, **30**), 2.79-2.50 (m, 27 H, **20-23**), 2.28-2.16 (m, 0.5 H, **33**), 1.99-1.83 (m, 13 H, **17-19**), 1.70 (tr, 0.5 H, **34**), 1.45-1.19 (m, 32 H, **1**, **26**), 1.04 (s, 1.5 H, **35**) ppm.

FT-IR (ATR): $\tilde{\nu}$ = 3500-3100 (-O-H), 2900-2850 (-CH, -CH₂), 1650 (-C=O), 1550 (-N-H-), 1460 (-C-O-C-) cm⁻¹.

UV-VIS (Water): λ_{max} = 360 nm.

SEC (RI, Water): M_w: 3100 Da, M_n: 1600 Da, Đ: 1.99.

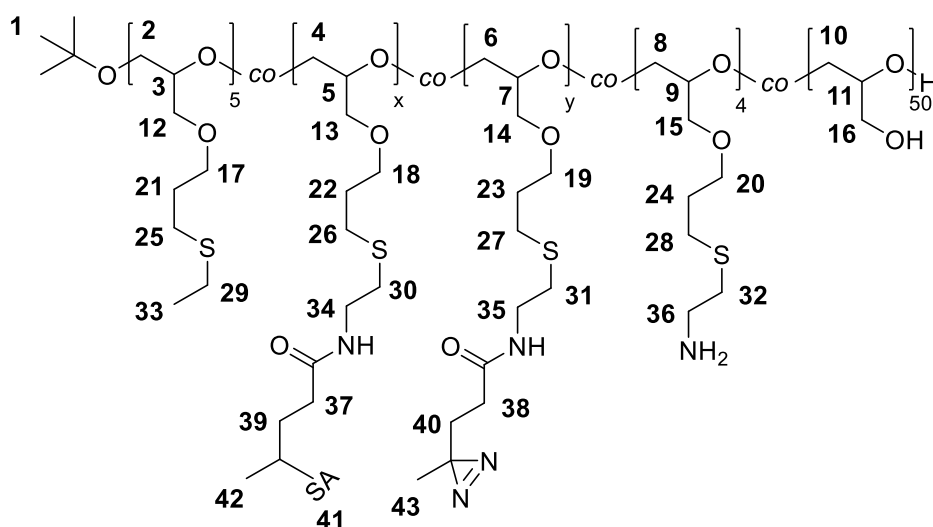
5.2.19 P(SEt-co-peptide-co-G)_{15/3.0}

P(SEt-co-Diaz-co-G) (10.0 mg, 0.146 μmol) was dissolved in 3 mL deionised water. The peptide AKGRGDSP (9.00 mg, 11.9 μmol) was added and the solution was stirred at room temperature. UV irradiation in an open well plate for 30 min was conducted. After dialysis (MW cut-off 3500 Da) against deionised water for 3 d, the polymer was freeze-dried and obtained as a white solid.

¹H-NMR (300 MHz, D₂O): δ = 4.42-4.17 (m, 2 H, **41**), 4.01-3.47 (m, 312 H, **2-20**), 3.44 (t, 3 H, **34, 35**), 3.21 (t, 1 H, **36**), 3.14-3.02 (m, 1 H, **32**), 2.75-2.46 (m, 18 H, **25-31**), 2.38-2.10 (m, 3 H, **37, 38**), 2.07-1.98 (m, 4 H, **41**), 1.91-1.79 (m, 9 H, **21-24**), 1.79-1.56 (m, 3 H, **39, 40**), 1.52-1.39 (m, 1 H, **41**), 1.39-1.09 (m, 20 H, **1, 33**), 1.19-1.13 (m, 1 H, **42**), 1.01 (s, 1 H, **43**) ppm.

FT-IR (ATR): $\tilde{\nu}$ = 3500-3100 (-O-H), 2900-2850 (-CH, -CH₂), 1650 (-C=O), 1550 (-N-H-), 1460 (-C-O-C-) cm⁻¹.

SEC (RI, Water): M_w: 1200 Da, M_n: 800 Da, \bar{D} : 1.49.

5.2.20 P(SEt-co-SA₍₂₎-co-G)

P(SEt-co-Diaz₍₃₎-co-G) (21.0 mg, 291 nmol) was dissolved in 2 mL deionised water. After the addition of SA (1.00 mg, 14.9 nmol) the solution was stirred at room temperature under UV irradiation for 30 min. Subsequently the solution was dialysed (MW cut-off 50000 Da) against deionised water for 3 d and freeze-dried. The product was received as a white solid.

¹H-NMR (600 MHz, D₂O): δ = 3.95-3.47 (m, 334 H, **2-20**), 3.44 (t, 16 H, **34, 35**), 3.29-3.13 (m, 6 H, **36, 41**), 3.12-3.04 (m, 1 H, **32**), 2.75-2.46 (m, 31 H, **25-31, 41**), 2.38-2.05 (m, 8 H, **37, 38**), 1.93-1.81 (m, 22 H, **21-24**), 1.78-1.60 (m, 13 H, **39-41**), 1.39-1.09 (m, 17 H, **1, 33, 41**), 1.17-1.53 (m, 4 H, **42**), 1.02 (s, 4 H, **43**), 0.99-0.54 (m, 3 H, **41**) ppm.

FT-IR (ATR): $\tilde{\nu}$ = 3500-3100 (-O-H), 2900-2850 (-CH, -CH₂), 1650 (-C=O), 1550 (-N-H-), 1460 (-C-O-C-) cm⁻¹.

UV-vis (Water): λ_{\max} = 280 nm.

SEC (RI, Water): M_w: 2000 Da, M_n: 1000 Da, Đ: 2.21.

5.2.20.1 AuNP@P(SET-co-SA₍₂₎-co-G)

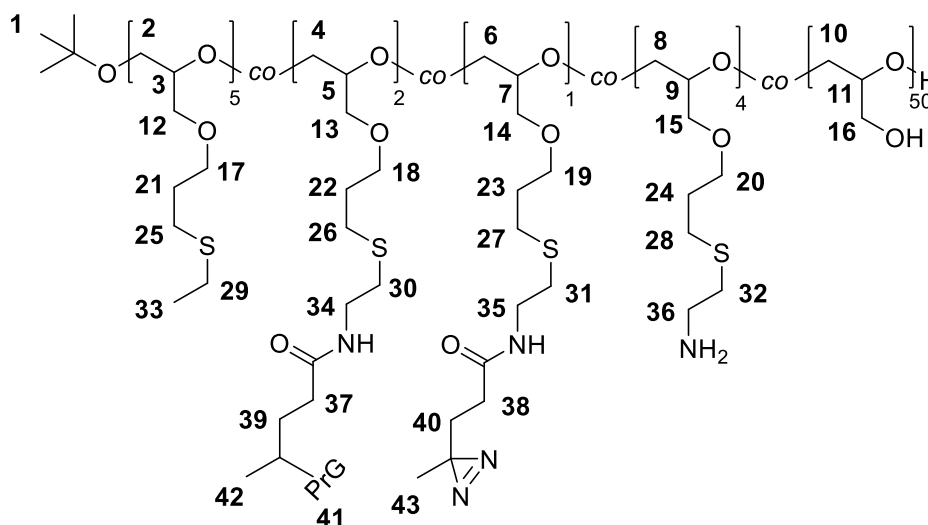
FT-IR (ATR): $\tilde{\nu}$ = 3500-3100 (-O-H), 2900-2850 (-CH, -CH₂), 1650 (-C=O), 1550 (-N-H-), 1460 (-C-O-C-) cm⁻¹.

UV-vis, DLS:

Table 38: *d*, ζ and SPR of 30 nm AuNP@P(SET-co-SA₍₂₎-co-G).

AuNP@P(SET-co-SA₍₂₎-co-G)	30 nm
<i>d</i> (nm)	53 ± 13
ζ (mV)	07 ± 08
SPR (nm)	532

5.2.21 P(SEt-co-PrG-co-G)



P(SEt-co-Diaz₍₃₎-co-G) (21.0 mg, 0.291 μmol) was dissolved in 2 mL PBS (pH 7.0). After the addition of PrG (1.00 mg, 46.3 nmol) the solution was stirred at room temperature under UV irradiation for 30 min. Subsequently the solution was dialysed (MW cut-off 14000 Da) against deionised water for 3 d and freeze-dried. The product was received as a white solid.

¹H-NMR (600 MHz, D₂O): δ = 3.92-3.51 (m, 334 H, **2-20**), 3.49 (t, 16 H, **34, 35**), 3.25-3.18 (m, 6 H, **36**), 3.12-2.79 (m, 1 H, **32, 41**), 2.75-2.50 (m, 31 H, **25-31**), 2.48-2.15 (m, 8 H, **37, 38**), 1.99-1.85 (m, 22 H, **21-24**), 1.78-1.31 (m, 13 H, **39-41**), 1.39-1.09 (m, 20 H, **1, 33, 41**), 1.07-0.66 (s, 12 H, **41-43**) ppm.

FT-IR (ATR): $\tilde{\nu}$ = 3500-3100 (-O-H), 2900-2850 (-CH, -CH₂), 1650 (-C=O), 1550 (-N-H-), 1460 (-C-O-C-) cm⁻¹.

UV-vis (Water): λ_{max} = 280 nm.

SEC (RI, Water): M_w : 1900 Da, M_n : 900 Da, \bar{D} : 2.01.

5.2.21.1 AuNP@P(SEt-co-PrG-co-G)

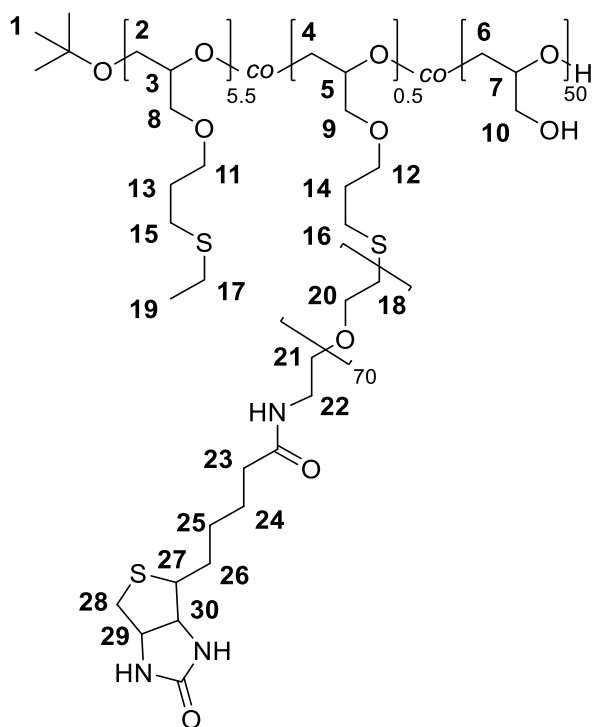
FT-IR (ATR): $\tilde{\nu}$ = 3500-3100 (-O-H), 2900-2850 (-CH, -CH₂), 1650 (-C=O), 1550 (-N-H-), 1460 (-C-O-C-) cm⁻¹.

UV-vis, DLS:

Table 39: d, ζ and SPR of 30 nm AuNP@P(SEt-co-PrG-co-G).

<i>AuNP@P(SEt-co-PrG-co-G)</i>	<i>30 nm</i>
<i>d (nm)</i>	<i>48 ± 06</i>
<i>ζ (mV)</i>	<i>10 ± 09</i>
<i>SPR (nm)</i>	<i>531</i>

5.2.22 P(SET-co-PEG-biotin-co-G)



P(AGE₆-co-G) (25.0 mg, 5.26 μmol) was dissolved in 2 mL deionised water and 2 mL DMF, further the mixture was degassed for 30 min with Ar. After adding Irgacure (4.00 mg, 18.4 μmol), EtSH (750 μL , 673 μmol) and HS-PEG-biotin (15.0 mg, 3.00 μmol), the solution was stirred at room temperature under UV irradiation for 2 h. H₂O and DMF were removed under vacuum, the polymer was dissolved in 20 mL deionised water and dialysed (MW cut-off 3500 Da) against a mixture of deionised water and DMF (100:1) for 2 d and against deionised water for 3 d. Subsequently the polymer was freeze-dried and received as a light yellow oil.

¹H-NMR (300 MHz, D₂O): δ = 4.64-4.59 (m, 0.5 H, **30**), 4.46-4.41 (m, 0.5 H, **29**), 3.90-3.50 (m, 305 H, **2-12**, **18**, **20**, **21**), 3.40 (t, 1 H, **22**), 3.04-2.55 (m, 23 H, **15-17**, **27**, **28**), 2.28 (t, 1 H, **23**), 2.10-1.80 (m, 10 H, **13**, **14**), 1.77-1.46 (m, 2 H, **24-26**), 1.44-1.18 (m, 25 H, **1**, **19**) ppm.

FT-IR (ATR): $\tilde{\nu}$ = 3500-3100 (-O-H), 2900-2850 (-CH, -CH₂), 1700-1640 (-C=O), 1460 (-C-O-C-) cm⁻¹.

SEC (RI, Water): M_w: 3400 Da, M_n: 2900 Da, Đ: 1.17.

5.2.22.1 AuNP@P(SEt-co-PEG-biotin-co-G)

FT-IR (ATR): $\tilde{\nu}$ = 3500-3100 (-O-H), 2900-2850 (-CH, -CH₂), 1700-1640 (-C=O), 1460 (-C-O-C-) cm⁻¹.

UV-vis, DLS:

Table 40: d, ζ and SPR of 30 nm AuNP@P(SEt-co-PEG-biotin-co-G).

<i>AuNP@P(SEt-co-PEG-biotin-co-G)</i>	<i>30 nm</i>
<i>d (nm)</i>	<i>39 ± 11</i>
<i>ζ (mV)</i>	<i>-12 ± 10</i>
<i>SPR (nm)</i>	<i>529</i>

5.3 Studies and applications of functionalised AuNPs

5.3.1 Kinetic study of thiol- and thioether-polymer modified AuNPs

The incubation of 15 nm, 30 nm and 50 nm AuNP@citrate with MeO-PEG-SH, MeO-PEG-SPentyl, P(SH-co-G) and P(SET-co-G) was stopped by taking aliquots of the colloidal solutions after 5 min, 30 min, 2 h, 6 h and 12 h and by successive centrifugation (30 min, 22000 x g, 4 °C). After redispersion in bidistilled water the samples were investigated via UV-vis spectroscopy.

5.3.2 Stability study of thiol- and thioether-polymer modified AuNPs

In order to investigate the colloidal stability 15 nm, 30 nm and 50 nm AuNPs modified with MeO-PEG-SH, MeO-PEG-SPentyl, P(SH-co-G) and P(SET-co-G) were exposed to four successive centrifugation- (30 min, 22000 x g, 4 °C) and resuspensions-cycles in bidistilled water, as well as to 80 °C for 12 h. Further the modified AuNPs were suspended in 5 mM phosphate buffer with distinct pH values (5.4, 7.4, 9.4), in 1 x PBS (0.1 M NaCl), as well as in DMEM cell culture medium and incubated for 12 h. After centrifugation, the AuNPs were once again diluted with the corresponding buffer or medium. Moreover, aliquots of the colloidal solutions were freeze-dried and the lyophilised pellets were resuspended in bidistilled water. After each described treatment of the modified AuNPs, the colloidal stability was investigated by UV-vis absorbance spectroscopy and the colloidal stability in percentage terms was determined. Therefore, the absorbance before (equals 100%) and after the treatment was measured at 530 nm.

5.3.3 Incorporation of amine- and carboxylic-modified AuNPs into hyaluronic acid hydrogels

For the hydrogel formation P(SH-co-G) (18.0 mg, 3.90 μ mol), P(AGE₆-co-G) (27.0 mg, 6.10 μ mol) and Irgacure (150 μ g, 669 nmol) were dissolved in 300 μ L of a colloidal solution containing AuNP@P(SET-co-NH₂-co-G) or AuNP@P(SET-co-COOH-co-G) (136000 ppb) in PBS (pH 7.4). After the addition of hyaluronic acid (10.5 mg, 7.72 nmol), the mixture was filled into silicone molds and irradiated with UV-light. The constructs were removed from the molds and separately stored in 400 μ L PBS. The amount of AuNPs in the supernatant after 1, 5 and 9 d was determined by UV-vis absorbance measurements at 530 nm and ICP-MS investigations.

5.3.4 Complexation of siRNA to amine-modified AuNPs

All following solutions were treated with 0.1% DEPC to ensure RNase-free conditions. The complexation of fluorescently labelled siRNA (13 kDA, GAPDH, Cy5) to 15 nm AuNP@P(SET-co-NH₂-co-G) and 15 nm AuNP@P(SET-co-NH₂₍₈₎-co-G) suspended in bidistilled water and 5 mM phosphate buffer (pH 6.5) respectively was conducted. While 250 μ L of AuNP@P(SET-co-NH₂-co-G) were combined with 2.6 μ L (N/P: 50) and 6.5 μ L (N/P: 20) of siRNA solution (100 μ M), to 250 μ L of AuNP@P(SET-co-NH₂₍₈₎-co-G) 19 μ L (N/P: 50) and 9 μ L (N/P: 100) of siRNA solution (100 μ M) were added. After brief ultrasonication treatment, the solutions were incubated at room temperature for 12 h and subsequently purified by centrifugation (30 min, 22000 x g, 4 °C). Excessive amounts of DTT (3.5 M) were added to the colloidal solution in order to release the siRNA from the particle surface and to determine the amount of siRNA in the supernatant via fluorescence spectroscopy, further termed as positive control. Additionally a negative control was performed by measuring released siRNA due to centrifugation or pipetting steps.

5.3.4.1 AuNP@P(SET-co-NH₂-co-G)@siRNA

FT-IR (ATR): $\tilde{\nu}$ = 3100-2800 (-C-H), 1650 (-C=N, -C=C, -C=O), 1140 (-PO₄⁻) cm⁻¹.

DLS, UV-vis (Water):

Table 41: d, ζ and SPR of 15 nm AuNP@P(SET-co-NH₂₍₈₎-co-G)@siRNA.

AuNP@P(SET-co-NH₂-co-G)@siRNA	15 nm
d (nm)	49 \pm 10
ζ (mV)	-11 \pm 05
SPR (nm)	525
AuNP@P(SET-co-NH₂₍₈₎-co-G)@siRNA	15 nm
d (nm)	57 \pm 11
ζ (mV)	-19 \pm 08
SPR (nm)	526

5.3.6 Photothermal depletion of mouse cancer B cells via streptavidin-modified AuNPs

5 μL of Biotin-CD45R antibody were added to a 45 μL solution of approximately $1 \cdot 10^6$ mouse B cells (LB 27.4) in PBS, mixed thoroughly and incubated at 4 $^\circ\text{C}$ for 10 min. After the addition of 1 mL PBS the cell solution was purified by a successive centrifugation- (10 min, 300 x g, 6 $^\circ\text{C}$) and resuspensions-cycle in 50 μL PBS. 50 μL (OD 1) 30 nm AuNP@P(SEt-co-Diaz₍₃₎-co-G), AuNP@P(SEt-co-SA₍₂₎-co-G) and AuNP@P(SEt-co-SA₍₂₎-co-G)_{-hv} (approximately 6000 AuNPs per cell) were added to the cell solution mixed thoroughly and incubated at 4 $^\circ\text{C}$ for 30 min. The cell solution was diluted with 1 mL of PBS and purified by a successive centrifugation- (10 min, 300 x g, 6 $^\circ\text{C}$) and resuspensions-step in 100 μL PBS. LB 27.4 cells incubated with AuNPs were irradiated with laser as described before (see **Section 5.1.2.13**). Afterwards, cell death and apoptosis were measured by Hoechst33258 and CalceinGreen staining in flow cytometry analyses. All samples were normalised to the untreated control, which was used as a reference.

6 Literature

1. Giljohann, D. A.; Seferos, D. S.; Daniel, W. L.; Massich, M. D.; Patel, P. C.; Mirkin, C. A., Gold Nanoparticles for Biology and Medicine. *Angewandte Chemie (International ed. in English)* **2010**, *49* (19), 3280-3294.
2. Vincenzo, A.; Roberto, P.; Marco, F.; Onofrio, M. M.; Maria Antonia, I., Surface plasmon resonance in gold nanoparticles: a review. *Journal of Physics: Condensed Matter* **2017**, *29* (20), 203002.
3. Daniel, M.-C.; Astruc, D., Gold Nanoparticles: Assembly, Supramolecular Chemistry, Quantum-Size-Related Properties, and Applications toward Biology, Catalysis, and Nanotechnology. *Chemical Reviews* **2004**, *104* (1), 293-346.
4. Gibson, J. D.; Khanal, B. P.; Zubarev, E. R., Paclitaxel-Functionalized Gold Nanoparticles. *Journal of the American Chemical Society* **2007**, *129* (37), 11653-11661.
5. Zhang, X.; Servos, M. R.; Liu, J., Instantaneous and Quantitative Functionalization of Gold Nanoparticles with Thiolated DNA Using a pH-Assisted and Surfactant-Free Route. *Journal of the American Chemical Society* **2012**, *134* (17), 7266-7269.
6. Giljohann, D. A.; Seferos, D. S.; Prigodich, A. E.; Patel, P. C.; Mirkin, C. A., Gene Regulation with Polyvalent siRNA-Nanoparticle Conjugates. *Journal of the American Chemical Society* **2009**, *131* (6), 2072-2073.
7. Xie, X.; Xu, W.; Liu, X., Improving Colorimetric Assays through Protein Enzyme-Assisted Gold Nanoparticle Amplification. *Accounts of Chemical Research* **2012**, *45* (9), 1511-1520.
8. Goodman, A. M.; Hogan, N. J.; Gottheim, S.; Li, C.; Clare, S. E.; Halas, N. J., Understanding Resonant Light-Triggered DNA Release from Plasmonic Nanoparticles. *ACS Nano* **2017**, *11* (1), 171-179.
9. Huschka, R.; Neumann, O.; Barhoumi, A.; Halas, N. J., Visualizing light-triggered release of molecules inside living cells. *Nano Letters* **2010**, *10* (10), 4117-4122.
10. Nitin, N.; Javier, D. J.; Richards-Kortum, R., Oligonucleotide-Coated Metallic Nanoparticles as a Flexible Platform for Molecular Imaging Agents. *Bioconjugate Chemistry* **2007**, *18* (6), 2090-2096.
11. Gref, R.; Minamitake, Y.; Peracchia, M. T.; Trubetskoy, V.; Torchilin, V.; Langer, R., Biodegradable long-circulating polymeric nanospheres. *Science* **1994**, *263* (5153), 1600.
12. Hakkinen, H., The gold-sulfur interface at the nanoscale. *Nat Chem* **2012**, *4* (6), 443-455.
13. Singh, S.; Topuz, F.; Hahn, K.; Albrecht, K.; Groll, J., Einbau aktiver Proteine und lebender Zellen in redoxsensitive Hydrogele und Nanogele durch enzymatische Vernetzung. *Angewandte Chemie* **2013**, *125* (10), 3074-3077.
14. Peterle, T.; Ringler, P.; Mayor, M., Gold Nanoparticles Stabilized by Acetylene-Functionalized Multidentate Thioether Ligands: Building Blocks for Nanoparticle Superstructures. *Advanced Functional Materials* **2009**, *19* (21), 3497-3506.
15. Wan, D.; Fu, Q.; Huang, J., Synthesis of amphiphilic hyperbranched polyglycerol polymers and their application as template for size control of gold nanoparticles. *Journal of Applied Polymer Science* **2006**, *101* (1), 509-514.
16. Sander, F.; Peterle, T.; Ballav, N.; Wrochem, F. v.; Zharnikov, M.; Mayor, M., Loops versus Stems: Benzylic Sulfide Oligomers Forming Carpet Type Monolayers. *The Journal of Physical Chemistry C* **2010**, *114* (9), 4118-4125.
17. Shelley, E. J.; Ryan, D.; Johnson, S. R.; Couillard, M.; Fitzmaurice, D.; Nellist, P. D.; Chen, Y.; Palmer, R. E.; Preece, J. A., Dialkyl Sulfides: Novel Passivating Agents for Gold Nanoparticles. *Langmuir* **2002**, *18* (5), 1791-1795.
18. Wang, Z.; Tan, B.; Hussain, I.; Schaeffer, N.; Wyatt, M. F.; Brust, M.; Cooper, A. I., Design of Polymeric Stabilizers for Size-Controlled Synthesis of Monodisperse Gold Nanoparticles in Water. *Langmuir* **2007**, *23* (2), 885-895.
19. Troughton, E. B.; Bain, C. D.; Whitesides, G. M.; Nuzzo, R. G.; Allara, D. L.; Porter, M. D., Monolayer films prepared by the spontaneous self-assembly of symmetrical and unsymmetrical dialkyl sulfides from solution onto gold substrates: structure, properties, and reactivity of constituent functional groups. *Langmuir* **1988**, *4* (2), 365-385.

20. Jung, C.; Dannenberger, O.; Xu, Y.; Buck, M.; Grunze, M., Self-Assembled Monolayers from Organosulfur Compounds: A Comparison between Sulfides, Disulfides, and Thiols. *Langmuir* **1998**, *14* (5), 1103-1107.
21. Li, X.-M.; Jong, M. R. d.; Inoue, K.; Shinkai, S.; Huskens, J.; Reinhoudt, D. N., Formation of gold colloids using thioether derivatives as stabilizing ligands. *Journal of Materials Chemistry* **2001**, *11* (7), 1919-1923.
22. Hussain, I.; Graham, S.; Wang, Z.; Tan, B.; Sherrington, D. C.; Rannard, S. P.; Cooper, A. I.; Brust, M., Size-Controlled Synthesis of Near-Monodisperse Gold Nanoparticles in the 1–4 nm Range Using Polymeric Stabilizers. *Journal of the American Chemical Society* **2005**, *127* (47), 16398-16399.
23. Sun, Q.; Reddy; Marquez, M.; Jena, P.; Gonzalez, C.; Wang, Q., Theoretical Study on Gold-Coated Iron Oxide Nanostructure: Magnetism and Bioselectivity for Amino Acids. *The Journal of Physical Chemistry C* **2007**, *111* (11), 4159-4163.
24. Hermes, J. P.; Sander, F.; Peterle, T.; Urbani, R.; Pfohl, T.; Thompson, D.; Mayor, M., Gold Nanoparticles Stabilized by Thioether Dendrimers. *Chemistry – A European Journal* **2011**, *17* (48), 13473-13481.
25. Evans, F. A.; Wennerstrm, H., *The colloidal domain: where Physics, Chemistry, Biology and Technology meet*. VCH Publishers: 1994.
26. Hamaker, H. C., The London—van der Waals attraction between spherical particles. *Physica* **1937**, *4* (10), 1058-1072.
27. Chapman, D. L., LI. A contribution to the theory of electrocapillarity. *Philosophical Magazine* **1913**, *25* (148), 475-481.
28. Torrie, G. M.; Kusalik, P. G.; Patey, G. N., Molecular solvent model for an electrical double layer: Reference hypernetted chain results for potassium chloride solutions. *The Journal of Chemical Physics* **1989**, *90* (8), 4513-4527.
29. Zhang, L.; Davis, H. T.; White, H. S., Simulations of solvent effects on confined electrolytes. *The Journal of Chemical Physics* **1993**, *98* (7), 5793-5799.
30. O'Brien, R. W.; Midmore, B. R.; Lamb, A.; Hunter, R. J., Electroacoustic studies of moderately concentrated colloidal suspensions. *Faraday Discussions of the Chemical Society* **1990**, *90* (0), 301-312.
31. Israelachvili, J. N., 6 - Van der Waals Forces. In *Intermolecular and Surface Forces (Third Edition)*, Academic Press: San Diego, 2011; pp 107-132.
32. Louie, S. M.; Tilton, R. D.; Lowry, G. V., Critical review: impacts of macromolecular coatings on critical physicochemical processes controlling environmental fate of nanomaterials. *Environmental Science: Nano* **2016**, *3* (2), 283-310.
33. Napper, D. H., Steric stabilization. *Journal of Colloid and Interface Science* **1977**, *58* (2), 390-407.
34. Wiese, G. R.; Healy, T. W., Effect of particle size on colloid stability. *Transactions of the Faraday Society* **1970**, *66* (0), 490-499.
35. Tømmerraas, K.; Eenschooten, C., Aryl/Alkyl Succinic Anhydride Hyaluronan Derivatives. Google Patents: 2012.
36. Flory, P. J., The Configuration of Real Polymer Chains. *The Journal of Chemical Physics* **1949**, *17* (3), 303-310.
37. De Gennes, P. G., Polymer solutions near an interface. Adsorption and depletion layers. *Macromolecules* **1981**, *14* (6), 1637-1644.
38. Klein, J., Forces between mica surfaces bearing adsorbed macromolecules in liquid media. *Journal of the Chemical Society, Faraday Transactions 1: Physical Chemistry in Condensed Phases* **1983**, *79* (1), 99-118.
39. Israelachvili, J. N., 7 - Repulsive Steric Forces, Total Intermolecular Pair Potentials, and Liquid Structure. In *Intermolecular and Surface Forces (Third Edition)*, Academic Press: San Diego, 2011; pp 133-149.

40. Kegler, K.; Salomo, M.; Kremer, F., Forces of Interaction between DNA-Grafted Colloids: An Optical Tweezer Measurement. *Physical Review Letters* **2007**, *98* (5), 058304.
41. Sofia, S. J.; Premnath, V.; Merrill, E. W., Poly(ethylene oxide) Grafted to Silicon Surfaces: Grafting Density and Protein Adsorption. *Macromolecules* **1998**, *31* (15), 5059-5070.
42. Damodaran, V. B.; Fee, C. J.; Ruckh, T.; Popat, K. C., Conformational Studies of Covalently Grafted Poly(ethylene glycol) on Modified Solid Matrices Using X-ray Photoelectron Spectroscopy. *Langmuir* **2010**, *26* (10), 7299-7306.
43. Perry, J. L.; Reuter, K. G.; Kai, M. P.; Herlihy, K. P.; Jones, S. W.; Luft, J. C.; Napier, M.; Bear, J. E.; DeSimone, J. M., PEGylated PRINT Nanoparticles: The Impact of PEG Density on Protein Binding, Macrophage Association, Biodistribution, and Pharmacokinetics. *Nano Letters* **2012**, *12* (10), 5304-5310.
44. Benoit, D. N.; Zhu, H.; Lillierose, M. H.; Verm, R. A.; Ali, N.; Morrison, A. N.; Fortner, J. D.; Avendano, C.; Colvin, V. L., Measuring the Grafting Density of Nanoparticles in Solution by Analytical Ultracentrifugation and Total Organic Carbon Analysis. *Analytical chemistry* **2012**, *84* (21), 9238-9245.
45. Rahme, K.; Chen, L.; Hobbs, R. G.; Morris, M. A.; O'Driscoll, C.; Holmes, J. D., PEGylated gold nanoparticles: polymer quantification as a function of PEG lengths and nanoparticle dimensions. *RSC Advances* **2013**, *3* (17), 6085-6094.
46. A Monnier, C.; Thévenaz, D.; Balog, S.; L Fiore, G.; Vanhecke, D.; Rothen-Rutishauser, B.; Petri-Fink, A., *A guide to investigating colloidal nanoparticles by cryogenic transmission electron microscopy: Pitfalls and benefits*. 2015; Vol. 2, p 245-258.
47. de Gennes, P. G., Polymers at an interface; a simplified view. *Advances in Colloid and Interface Science* **1987**, *27* (3), 189-209.
48. Alexander, S., Adsorption of chain molecules with a polar head a scaling description. *J. Phys. France* **1977**, *38* (8), 983-987.
49. Kim, S.; Hyun, K.; Moon, J. Y.; Clasen, C.; Ahn, K. H., Depletion Stabilization in Nanoparticle–Polymer Suspensions: Multi-Length-Scale Analysis of Microstructure. *Langmuir* **2015**, *31* (6), 1892-1900.
50. Fler, G. J.; Lyklema, J., Polymer adsorption and its effect on the stability of hydrophobic colloids. II. The flocculation process as studied with the silver iodide-polyvinyl alcohol system. *Journal of Colloid and Interface Science* **1974**, *46* (1), 1-12.
51. Bandulasena, M. V.; Vladislavjević, G. T.; Odunmbaku, O. G.; Benyahia, B., Continuous synthesis of PVP stabilized biocompatible gold nanoparticles with a controlled size using a 3D glass capillary microfluidic device. *Chemical Engineering Science* **2017**, *171*, 233-243.
52. Welch, D.; Lettinga, M. P.; Ripoll, M.; Dogic, Z.; Vliegthart, G. A., Trains, tails and loops of partially adsorbed semi-flexible filaments. *Soft Matter* **2015**, *11* (38), 7507-7514.
53. Jhon, Y. K.; Semler, J. J.; Genzer, J.; Beevers, M.; Gus'kova, O. A.; Khalatur, P. G.; Khokhlov, A. R., Effect of Comonomer Sequence Distribution on the Adsorption of Random Copolymers onto Impenetrable Flat Surfaces. *Macromolecules* **2009**, *42* (7), 2843-2853.
54. Fler, G. J., Polymers at interfaces and in colloidal dispersions. *Advances in Colloid and Interface Science* **2010**, *159* (2), 99-116.
55. Biver, C.; Hariharan, R.; Mays, J.; Russel, W. B., Neutral and Charged Polymer Brushes: A Model Unifying Curvature Effects from Micelles to Flat Surfaces. *Macromolecules* **1997**, *30* (6), 1787-1792.
56. Aubouy, M.; Raphaël, E., Scaling Description of a Colloidal Particle Clothed with Polymers. *Macromolecules* **1998**, *31* (13), 4357-4363.
57. Frens, G., Controlled Nucleation for the Regulation of the Particle Size in Monodisperse Gold Suspensions. *Nature Physical Science* **1973**, *241*, 20.
58. Mie, G., Beiträge zur Optik trüber Medien, speziell kolloidaler Metallösungen. *Annalen der Physik* **1908**, *330* (3), 377-445.
59. Kreibig, U.; Vollmer, M., *Optical properties of metal clusters*. Springer: Berlin; New York, 1995.
60. Jin, R., Quantum sized, thiolate-protected gold nanoclusters. *Nanoscale* **2010**, *2* (3), 343-362.

61. Link, S.; El-Sayed, M. A., OPTICAL PROPERTIES AND ULTRAFast DYNAMICS OF METALLIC NANOCRYSTALS. *Annual Review of Physical Chemistry* **2003**, *54* (1), 331-366.
62. Losquin, A.; Zagonel, L. F.; Myroshnychenko, V.; Rodríguez-González, B.; Tencé, M.; Scarabelli, L.; Förstner, J.; Liz-Marzán, L. M.; García de Abajo, F. J.; Stéphan, O.; Kociak, M., Unveiling Nanometer Scale Extinction and Scattering Phenomena through Combined Electron Energy Loss Spectroscopy and Cathodoluminescence Measurements. *Nano Letters* **2015**, *15* (2), 1229-1237.
63. <https://nanocomposix.eu/pages/gold-nanoparticles-optical-properties>.
64. Scholl, J. A.; Koh, A. L.; Dionne, J. A., Quantum plasmon resonances of individual metallic nanoparticles. *Nature* **2012**, *483* (7390), 421-427.
65. Yeh, Y.-C.; Creran, B.; Rotello, V. M., Gold nanoparticles: preparation, properties, and applications in bionanotechnology. *Nanoscale* **2012**, *4* (6), 1871-1880.
66. Aruda, K. O.; Tagliacuzzi, M.; Sweeney, C. M.; Hannah, D. C.; Schatz, G. C.; Weiss, E. A., Identification of parameters through which surface chemistry determines the lifetimes of hot electrons in small Au nanoparticles. *Proceedings of the National Academy of Sciences* **2013**, *110* (11), 4212-4217.
67. Storhoff, J. J.; Lazarides, A. A.; Mucic, R. C.; Mirkin, C. A.; Letsinger, R. L.; Schatz, G. C., What Controls the Optical Properties of DNA-Linked Gold Nanoparticle Assemblies? *Journal of the American Chemical Society* **2000**, *122* (19), 4640-4650.
68. Eustis, S.; El-Sayed, M. A., Why gold nanoparticles are more precious than pretty gold: Noble metal surface plasmon resonance and its enhancement of the radiative and nonradiative properties of nanocrystals of different shapes. *Chemical Society Reviews* **2006**, *35* (3), 209-217.
69. Poon, L.; Zandberg, W.; Hsiao, D.; Erno, Z.; Sen, D.; Gates, B. D.; Branda, N. R., Photothermal Release of Single-Stranded DNA from the Surface of Gold Nanoparticles Through Controlled Denaturing and Au-S Bond Breaking. *ACS Nano* **2010**, *4* (11), 6395-6403.
70. Guo, S.; Huang, Y.; Jiang, Q.; Sun, Y.; Deng, L.; Liang, Z.; Du, Q.; Xing, J.; Zhao, Y.; Wang, P. C.; Dong, A.; Liang, X.-J., Enhanced Gene Delivery and siRNA Silencing by Gold Nanoparticles Coated with Charge-Reversal Polyelectrolyte. *ACS nano* **2010**, *4* (9), 5505-5511.
71. Rudnitski, F.; Feineis, S.; Rahmzadeh, R.; Endl, E.; Lutz, J.; Groll, J.; Hüttmann, G., siRNA release from gold nanoparticles by nanosecond pulsed laser irradiation and analysis of the involved temperature increase. *Journal of Biophotonics* **2018**, *0* (0), e201700329.
72. Yao, C.; Qu, X.; Zhang, Z.; Hüttmann, G.; Rahmzadeh, R., Influence of laser parameters on nanoparticle-induced membrane permeabilization. *BIOMEDO* **2009**, *14* (5), 054034-054034-7.
73. Lukianova-Hleb, E.; Hu, Y.; Latterini, L.; Tarpani, L.; Lee, S.; Drezek, R. A.; Hafner, J. H.; Lapotko, D. O., Plasmonic Nanobubbles as Transient Vapor Nanobubbles Generated Around Plasmonic Nanoparticles. *ACS nano* **2010**, *4* (4), 2109-2123.
74. Love, J. C.; Estroff, L. A.; Kriebel, J. K.; Nuzzo, R. G.; Whitesides, G. M., Self-Assembled Monolayers of Thiolates on Metals as a Form of Nanotechnology. *Chemical Reviews* **2005**, *105* (4), 1103-1170.
75. Pensa, E.; Cortés, E.; Corthey, G.; Carro, P.; Vericat, C.; Fonticelli, M. H.; Benítez, G.; Rubert, A. A.; Salvarezza, R. C., The Chemistry of the Sulfur-Gold Interface: In Search of a Unified Model. *Accounts of Chemical Research* **2012**, *45* (8), 1183-1192.
76. Lavrich, D. J.; Wetterer, S. M.; Bernasek, S. L.; Scoles, G., Physisorption and Chemisorption of Alkanethiols and Alkyl Sulfides on Au(111). *The Journal of Physical Chemistry B* **1998**, *102* (18), 3456-3465.
77. Reimers, J. R.; Ford, M. J.; Marcuccio, S. M.; Ulstrup, J.; Hush, N. S., Competition of van der Waals and chemical forces on gold-sulfur surfaces and nanoparticles. **2017**, *1*, 0017.
78. Jadzinsky, P. D.; Calero, G.; Ackerson, C. J.; Bushnell, D. A.; Kornberg, R. D., Structure of a Thiol Monolayer-Protected Gold Nanoparticle at 1.1 Å Resolution. *Science* **2007**, *318* (5849), 430.
79. Zhang, P., X-ray Spectroscopy of Gold-Thiolate Nanoclusters. *The Journal of Physical Chemistry C* **2014**, *118* (44), 25291-25299.

80. Burgi, T., Properties of the gold-sulphur interface: from self-assembled monolayers to clusters. *Nanoscale* **2015**, *7* (38), 15553-15567.
81. Vericat, C.; Vela, M. E.; Corthey, G.; Pensa, E.; Cortes, E.; Fonticelli, M. H.; Ibanez, F.; Benitez, G. E.; Carro, P.; Salvarezza, R. C., Self-assembled monolayers of thiolates on metals: a review article on sulfur-metal chemistry and surface structures. *RSC Advances* **2014**, *4* (53), 27730-27754.
82. Reimers, J. R.; Ford, M. J.; Halder, A.; Ulstrup, J.; Hush, N. S., Gold surfaces and nanoparticles are protected by Au(0)-thiyl species and are destroyed when Au(I)-thiolates form. *Proceedings of the National Academy of Sciences* **2016**, *113* (11), E1424-E1433.
83. Cafe, P. F.; Larsen, A. G.; Yang, W.; Bilic, A.; Blake, I. M.; Crossley, M. J.; Zhang, J.; Wackerbarth, H.; Ulstrup, J.; Reimers, J. R., Chemisorbed and Physisorbed Structures for 1,10-Phenanthroline and Dipyrrodo[3,2-a:2',3'-c]phenazine on Au(111). *The Journal of Physical Chemistry C* **2007**, *111* (46), 17285-17296.
84. Chi, Q.; Ford, M. J.; Halder, A.; Hush, N. S.; Reimers, J. R.; Ulstrup, J., Sulfur ligand mediated electrochemistry of gold surfaces and nanoparticles: What, how, and why. *Current Opinion in Electrochemistry* **2017**, *1* (1), 7-15.
85. Noh, J.; Kato, H. S.; Kawai, M.; Hara, M., Surface and Adsorption Structures of Dialkyl Sulfide Self-Assembled Monolayers on Au(111). *The Journal of Physical Chemistry B* **2002**, *106* (51), 13268-13272.
86. Takiguchi, H.; Sato, K.; Ishida, T.; Abe, K.; Yase, K.; Tamada, K., Delicate Surface Reaction of Dialkyl Sulfide Self-Assembled Monolayers on Au(111). *Langmuir* **2000**, *16* (4), 1703-1710.
87. Porter, M. D.; Bright, T. B.; Allara, D. L.; Chidsey, C. E. D., Spontaneously organized molecular assemblies. 4. Structural characterization of n-alkyl thiol monolayers on gold by optical ellipsometry, infrared spectroscopy, and electrochemistry. *Journal of the American Chemical Society* **1987**, *109* (12), 3559-3568.
88. Beulen, M. W. J.; Bügler, J.; Lammerink, B.; Geurts, F. A. J.; Biemond, E. M. E. F.; van Leerdam, K. G. C.; van Veggel, F. C. J. M.; Engbersen, J. F. J.; Reinhoudt, D. N., Self-Assembled Monolayers of Heptapodant β -Cyclodextrins on Gold. *Langmuir* **1998**, *14* (22), 6424-6429.
89. Brust, M.; Walker, M.; Bethell, D.; Schiffrin, D. J.; Whyman, R., Synthesis of thiol-derivatised gold nanoparticles in a two-phase Liquid-Liquid system. *Journal of the Chemical Society, Chemical Communications* **1994**, (7), 801-802.
90. Maye, M. M.; Luo, J.; Lim, I. I. S.; Han, L.; Kariuki, N. N.; Rabinovich, D.; Liu; Zhong, C.-J., Size-Controlled Assembly of Gold Nanoparticles Induced by a Tridentate Thioether Ligand. *Journal of the American Chemical Society* **2003**, *125* (33), 9906-9907.
91. Hermes, J. P.; Sander, F.; Peterle, T.; Mayor, M., Nanoparticles to Hybrid Organic-Inorganic Superstructures. *CHIMIA International Journal for Chemistry* **2011**, *65* (4), 219-222.
92. Huang, H.-M.; Chang, C.-Y.; Liu, I. C.; Tsai, H.-C.; Lai, M.-K.; Tsiang, R. C.-C., Synthesis of gold nanocomposite via chemisorption of gold nanoparticles with poly(p-methylstyrene) containing multiple bonding groups on the chain side. *Journal of Polymer Science Part A: Polymer Chemistry* **2005**, *43* (20), 4710-4720.
93. Taubert, A.; Wiesler, U.-M.; Mullen, K., Dendrimer-controlled one-pot synthesis of gold nanoparticles with a bimodal size distribution and their self-assembly in the solid state. *Journal of Materials Chemistry* **2003**, *13* (5), 1090-1093.
94. D'Aléo, A.; Williams, R. M.; Osswald, F.; Edamana, P.; Hahn, U.; van Heyst, J.; Tichelaar, F. D.; Vögtle, F.; De Cola, L., Oligothia Dendrimers for the Formation of Gold Nanoparticles. *Advanced Functional Materials* **2004**, *14* (12), 1167-1177.
95. Bergamini, G.; Ceroni, P.; Balzani, V.; Gingras, M.; Raimundo, J.-M.; Morandi, V.; Merli, P. G., Synthesis of small gold nanoparticles: Au(i) disproportionation catalyzed by a persulfurated coronene dendrimer. *Chemical Communications* **2007**, (40), 4167-4169.
96. Uehara, N., Polymer-functionalized Gold Nanoparticles as Versatile Sensing Materials. *Analytical Sciences* **2010**, *26* (12), 1219-1228.
97. Szwarc, M., 'Living' Polymers. *Nature* **1956**, *178* (4543), 1168-1169.

98. Szwarc, M.; Levy, M.; Milkovich, R., POLYMERIZATION INITIATED BY ELECTRON TRANSFER TO MONOMER. A NEW METHOD OF FORMATION OF BLOCK POLYMERS¹. *Journal of the American Chemical Society* **1956**, *78* (11), 2656-2657.
99. Thompson, M. S.; Vadala, T. P.; Vadala, M. L.; Lin, Y.; Riffle, J. S., Synthesis and applications of heterobifunctional poly(ethylene oxide) oligomers. *Polymer* **2008**, *49* (2), 345-373.
100. Herzberger, J.; Niederer, K.; Pohlit, H.; Seiwert, J.; Worm, M.; Wurm, F. R.; Frey, H., Polymerization of Ethylene Oxide, Propylene Oxide, and Other Alkylene Oxides: Synthesis, Novel Polymer Architectures, and Bioconjugation. *Chemical Reviews* **2016**, *116* (4), 2170-2243.
101. Knop, K.; Hoogenboom, R.; Fischer, D.; Schubert, U. S., Poly(ethylene glycol) in Drug Delivery: Pros and Cons as Well as Potential Alternatives. *Angewandte Chemie International Edition* **2010**, *49* (36), 6288-6308.
102. Otsuka, H.; Nagasaki, Y.; Kataoka, K., PEGylated nanoparticles for biological and pharmaceutical applications. *Advanced Drug Delivery Reviews* **2003**, *55* (3), 403-419.
103. Kawano, T.; Yamagata, M.; Takahashi, H.; Niidome, Y.; Yamada, S.; Katayama, Y.; Niidome, T., Stabilizing of plasmid DNA in vivo by PEG-modified cationic gold nanoparticles and the gene expression assisted with electrical pulses. *Journal of Controlled Release* **2006**, *111* (3), 382-389.
104. Lee, S. H.; Bae, K. H.; Kim, S. H.; Lee, K. R.; Park, T. G., Amine-functionalized gold nanoparticles as non-cytotoxic and efficient intracellular siRNA delivery carriers. *International Journal of Pharmaceutics* **2008**, *364* (1), 94-101.
105. Oishi, M.; Nakaogami, J.; Ishii, T.; Nagasaki, Y., Smart PEGylated Gold Nanoparticles for the Cytoplasmic Delivery of siRNA to Induce Enhanced Gene Silencing. *Chemistry Letters* **2006**, *35* (9), 1046-1047.
106. Gole, A.; Murphy, C. J., Azide-Derivatized Gold Nanorods: Functional Materials for "Click" Chemistry. *Langmuir* **2008**, *24* (1), 266-272.
107. Oh, E.; Susumu, K.; Blanco-Canosa, J. B.; Medintz, I. L.; Dawson, P. E.; Mattoussi, H., Preparation of Stable Maleimide-Functionalized Au Nanoparticles and Their Use in Counting Surface Ligands. *Small* **2010**, *6* (12), 1273-1278.
108. Bartczak, D.; Kanaras, A. G., Preparation of Peptide-Functionalized Gold Nanoparticles Using One Pot EDC/Sulfo-NHS Coupling. *Langmuir* **2011**, *27* (16), 10119-10123.
109. Agasti, S. S.; Chompoosor, A.; You, C.-C.; Ghosh, P.; Kim, C. K.; Rotello, V. M., Photoregulated Release of Caged Anticancer Drugs from Gold Nanoparticles. *Journal of the American Chemical Society* **2009**, *131* (16), 5728-5729.
110. Dworak, A.; Slomkowski, S.; Basinska, T.; Gosecka, M.; Wałach, W.; Trzebicka, B., *Polyglycidol - how is it synthesized and what is it used for?* 2013; Vol. 58, p 641-649.
111. Schulte, B.; Walther, A.; Keul, H.; Möller, M., Polyglycidol-Based Prepolymers to Tune the Nanostructure of Microgels. *Macromolecules* **2014**, *47* (5), 1633-1645.
112. Stichler, S.; Jungst, T.; Schamel, M.; Zilkowski, I.; Kuhlmann, M.; Böck, T.; Blunk, T.; Teßmar, J.; Groll, J., Thiol-ene Clickable Poly(glycidol) Hydrogels for Biofabrication. *Annals of Biomedical Engineering* **2017**, *45* (1), 273-285.
113. Singh, S.; Zilkowski, I.; Ewald, A.; Maurell-Lopez, T.; Albrecht, K.; Möller, M.; Groll, J., Mild Oxidation of Thiofunctional Polymers to Cytocompatible and Stimuli-Sensitive Hydrogels and Nanogels. *Macromolecular Bioscience* **2013**, *13* (4), 470-482.
114. Mangold, C.; Dingels, C.; Obermeier, B.; Frey, H.; Wurm, F., PEG-based Multifunctional Polyethers with Highly Reactive Vinyl-Ether Side Chains for Click-Type Functionalization. *Macromolecules* **2011**, *44* (16), 6326-6334.
115. Huisgen, R., Kinetics and reaction mechanisms: selected examples from the experience of forty years. In *Pure and Applied Chemistry*, 1989; Vol. 61, p 613.
116. Binder, W. H.; Sachsenhofer, R., 'Click' Chemistry in Polymer and Materials Science. *Macromolecular Rapid Communications* **2007**, *28* (1), 15-54.
117. Lutz, J.-F.; Schlaad, H., Modular chemical tools for advanced macromolecular engineering. *Polymer* **2008**, *49* (4), 817-824.

118. Dondoni, A., The Emergence of Thiol–Ene Coupling as a Click Process for Materials and Bioorganic Chemistry. *Angewandte Chemie International Edition* **2008**, *47* (47), 8995–8997.
119. Hoyle, C. E.; Bowman, C. N., Thiol–Ene Click Chemistry. *Angewandte Chemie International Edition* **2010**, *49* (9), 1540–1573.
120. Lundberg, P.; Lynd, N. A.; Zhang, Y.; Zeng, X.; Krogstad, D. V.; Paffen, T.; Malkoch, M.; Nystrom, A. M.; Hawker, C. J., pH-triggered self-assembly of biocompatible histamine-functionalized triblock copolymers. *Soft Matter* **2013**, *9* (1), 82–89.
121. Imran ul-haq, M.; Lai, B. F. L.; Chapanian, R.; Kizhakkedathu, J. N., Influence of architecture of high molecular weight linear and branched polyglycerols on their biocompatibility and biodistribution. *Biomaterials* **2012**, *33* (35), 9135–9147.
122. Kainthan, R. K.; Janzen, J.; Levin, E.; Devine, D. V.; Brooks, D. E., Biocompatibility Testing of Branched and Linear Polyglycidol. *Biomacromolecules* **2006**, *7* (3), 703–709.
123. Kainthan, R. K.; Zou, Y.; Chiao, M.; Kizhakkedathu, J. N., Self-Assembled Monothiol-Terminated Hyperbranched Polyglycerols on a Gold Surface: A Comparative Study on the Structure, Morphology, and Protein Adsorption Characteristics with Linear Poly(ethylene glycol)s. *Langmuir* **2008**, *24* (9), 4907–4916.
124. Fernandes, E. G. R.; De Queiroz, A. A. A., A bioconjugated polyglycerol dendrimer with glucose sensing properties. *Journal of Materials Science: Materials in Medicine* **2009**, *20* (2), 473–479.
125. Kuhlmann, M.; Reimann, O.; Hackenberger, C. P. R.; Groll, J., Cysteine-Functional Polymers via Thiol-ene Conjugation. *Macromolecular Rapid Communications* **2015**, *36* (5), 472–476.
126. Fitton, A. O.; Hill, J.; Jane, D. E.; Millar, R., Synthesis of Simple Oxetanes Carrying Reactive 2-Substituents. *Synthesis* **1987**, *1987* (12), 1140–1142.
127. Erberich, M.; Keul, H.; Möller, M., Polyglycidols with Two Orthogonal Protective Groups: Preparation, Selective Deprotection, and Functionalization. *Macromolecules* **2007**, *40* (9), 3070–3079.
128. Lunn, G.; Sansone, E. B., *Destruction of hazardous chemicals in the laboratory*. New York, NY (USA); John Wiley and Sons Inc.: United States, 1990.
129. Kelly, K. L.; Coronado, E.; Zhao, L. L.; Schatz, G. C., The Optical Properties of Metal Nanoparticles: The Influence of Size, Shape, and Dielectric Environment. *The Journal of Physical Chemistry B* **2003**, *107* (3), 668–677.
130. Colangelo, E.; Comenge, J.; Paramelle, D.; Volk, M.; Chen, Q.; Lévy, R., Characterizing Self-Assembled Monolayers on Gold Nanoparticles. *Bioconjugate Chemistry* **2017**, *28* (1), 11–22.
131. De Carlo, S.; Harris, J. R., Negative staining and cryo-negative staining of macromolecules and viruses for TEM. *Micron* **2011**, *42* (2), 117–131.
132. Liu, Y.; Shipton, M. K.; Ryan, J.; Kaufman, E. D.; Franzen, S.; Feldheim, D. L., Synthesis, Stability, and Cellular Internalization of Gold Nanoparticles Containing Mixed Peptide–Poly(ethylene glycol) Monolayers. *Analytical Chemistry* **2007**, *79* (6), 2221–2229.
133. Stolnik, S.; Daudali, B.; Arien, A.; Whetstone, J.; Heald, C. R.; Garnett, M. C.; Davis, S. S.; Illum, L., The effect of surface coverage and conformation of poly(ethylene oxide) (PEO) chains of poloxamer 407 on the biological fate of model colloidal drug carriers. *Biochimica et Biophysica Acta (BBA) - Biomembranes* **2001**, *1514* (2), 261–279.
134. Sebby, K. B.; Mansfield, E., Determination of the surface density of polyethylene glycol on gold nanoparticles by use of microscale thermogravimetric analysis. *Analytical and Bioanalytical Chemistry* **2015**, *407* (10), 2913–2922.
135. Smith, A. M.; Johnston, K. A.; Crawford, S. E.; Marbella, L. E.; Millstone, J. E., Ligand density quantification on colloidal inorganic nanoparticles. *Analyst* **2017**, *142* (1), 11–29.
136. Wuelfing, W. P.; Gross, S. M.; Miles, D. T.; Murray, R. W., Nanometer Gold Clusters Protected by Surface-Bound Monolayers of Thiolated Poly(ethylene glycol) Polymer Electrolyte. *J. Am. Chem. Soc.* **1998**, *120*, 12696.
137. Azzam, T.; Eisenberg, A., Monolayer-Protected Gold Nanoparticles by the Self-Assembly of Micellar Poly(ethylene oxide)-b-Poly(ϵ -caprolactone) Block Copolymer. *Langmuir* **2007**, *23* (4), 2126–2132.

138. Gregory, J., *Polymers at interfaces*, by G. J. Fler, M. A. Cohen Stuart, J. M. H. M. Scheutjens, T. Cosgrove and B. Vincent. Chapman and Hall, London, 1993. Pp. xv + 502, price £65.00. ISBN 0-412-58160-4. *Polymer International* **1995**, *36* (1), 102-102.
139. Dunn, A. S., *Polymeric stabilization of colloidal dispersions*. By D. H. Napper, Academic Press, London, 1984. pp. xviii + 428, price £39.50, \$65.00. ISBN 0-12-513980-2. *British Polymer Journal* **1986**, *18* (4), 278-278.
140. Smellie, R. H.; La Mer, V. K., Flocculation, subsidence and filtration of phosphate slimes. *Journal of Colloid Science* **1958**, *13* (6), 589-599.
141. de Gennes, P. G., *Scaling Concepts in Polymer Physics*. Cornell University Press: 1979.
142. Moore, T. L.; Rodriguez-Lorenzo, L.; Hirsch, V.; Balog, S.; Urban, D.; Jud, C.; Rothen-Rutishauser, B.; Lattuada, M.; Petri-Fink, A., Nanoparticle colloidal stability in cell culture media and impact on cellular interactions. *Chemical Society Reviews* **2015**, *44* (17), 6287-6305.
143. Alkilany, A. M.; Bani Yaseen, A. I.; Kailani, M. H., Synthesis of Monodispersed Gold Nanoparticles with Exceptional Colloidal Stability with Grafted Polyethylene Glycol-g-polyvinyl Alcohol. *Journal of Nanomaterials* **2015**, *2015*, 9.
144. Alkilany, A. M.; Abulateefeh, S. R.; Mills, K. K.; Bani Yaseen, A. I.; Hamaly, M. A.; Alkhatib, H. S.; Aiedeh, K. M.; Stone, J. W., Colloidal Stability of Citrate and Mercaptoacetic Acid Capped Gold Nanoparticles upon Lyophilization: Effect of Capping Ligand Attachment and Type of Cryoprotectants. *Langmuir* **2014**, *30* (46), 13799-13808.
145. Abdelwahed, W.; Degobert, G.; Stainmesse, S.; Fessi, H., Freeze-drying of nanoparticles: Formulation, process and storage considerations. *Advanced Drug Delivery Reviews* **2006**, *58* (15), 1688-1713.
146. Schollbach, M.; Zhang, F.; Roosen-Runge, F.; Skoda, M. W. A.; Jacobs, R. M. J.; Schreiber, F., Gold nanoparticles decorated with oligo(ethylene glycol) thiols: Surface charges and interactions with proteins in solution. *Journal of Colloid and Interface Science* **2014**, *426*, 31-38.
147. Dubinsky, L.; Krom, B. P.; Meijler, M. M., Diazirine based photoaffinity labeling. *Bioorganic & Medicinal Chemistry* **2012**, *20* (2), 554-570.
148. Mogal, V.; Papper, V.; Chaurasia, A.; Feng, G.; Marks, R.; Steele, T., Novel On-Demand Bioadhesion to Soft Tissue in Wet Environments. *Macromolecular Bioscience* **2014**, *14* (4), 478-484.
149. Blencowe, A.; Hayes, W., Development and application of diazirines in biological and synthetic macromolecular systems. *Soft Matter* **2005**, *1* (3), 178-205.
150. Green, N. M., Avidin. *Advances in Protein Chemistry* **1975**, *29*, 85-133.
151. Darst, S. A.; Ahlers, M.; Meller, P. H.; Kubalek, E. W.; Blankenburg, R.; Ribi, H. O.; Ringsdorf, H.; Kornberg, R. D., Two-dimensional crystals of streptavidin on biotinylated lipid layers and their interactions with biotinylated macromolecules. *Biophysical Journal* **1991**, *59* (2), 387-396.
152. D'Agata, R.; Palladino, P.; Spoto, G., Streptavidin-coated gold nanoparticles: critical role of oligonucleotides on stability and fractal aggregation. *Beilstein Journal of Nanotechnology* **2017**, *8*, 1-11.
153. Akerström, B.; Björck, L., A physicochemical study of protein G, a molecule with unique immunoglobulin G-binding properties. *Journal of Biological Chemistry* **1986**, *261* (22), 10240-10247.
154. Baumann, B.; Jungst, T.; Stichler, S.; Feineis, S.; Wiltschka, O.; Kuhlmann, M.; Lindén, M.; Groll, J., Control of Nanoparticle Release Kinetics from 3D Printed Hydrogel Scaffolds. *Angewandte Chemie International Edition* **2017**, *56* (16), 4623-4628.
155. Kamoun, E. A.; Kenawy, E.-R. S.; Chen, X., A review on polymeric hydrogel membranes for wound dressing applications: PVA-based hydrogel dressings. *Journal of Advanced Research* **2017**, *8* (3), 217-233.
156. Matthäus, C.; Bird, B.; Miljković, M.; Chernenko, T.; Romeo, M.; Diem, M., Infrared and Raman Microscopy in Cell Biology. *Methods in cell biology* **2008**, *89*, 275-308.

6 Literature

157. Oster, C. G.; Kim, N.; Grode, L.; Barbu-Tudoran, L.; Schaper, A. K.; Kaufmann, S. H. E.; Kissel, T., Cationic microparticles consisting of poly(lactide-co-glycolide) and polyethylenimine as carriers systems for parental DNA vaccination. *Journal of Controlled Release* **2005**, *104* (2), 359-377.
158. Aslan, K.; Luhrs, C. C.; Pérez-Luna, V. H., Controlled and Reversible Aggregation of Biotinylated Gold Nanoparticles with Streptavidin. *The Journal of Physical Chemistry B* **2004**, *108* (40), 15631-15639.
159. Barhoumi, A.; Huschka, R.; Bardhan, R.; Knight, M. W.; Halas, N. J., Light-induced release of DNA from plasmon-resonant nanoparticles: Towards light-controlled gene therapy. *Chemical Physics Letters* **2009**, *482* (4), 171-179.
160. Park, H.; Yang, J.; Seo, S.; Kim, K.; Suh, J.; Kim, D.; Haam, S.; Yoo, K.-H., Multifunctional Nanoparticles for Photothermally Controlled Drug Delivery and Magnetic Resonance Imaging Enhancement. *Small* **2008**, *4* (2), 192-196.
161. Sershen, S. R.; Westcott, S. L.; Halas, N. J.; West, J. L., Temperature-sensitive polymer–nanoshell composites for photothermally modulated drug delivery. *Journal of Biomedical Materials Research* **2000**, *51* (3), 293-298.
162. Tong, L.; Wei, Q.; Wei, A.; Cheng, J.-X., Gold nanorods as contrast agents for biological imaging: optical properties, surface conjugation, and photothermal effects. *Photochemistry and photobiology* **2009**, *85* (1), 21.
163. Hüttmann, G.; Radt, B.; Serbin, J.; Lange, B. I.; Birngruber, R., High Precision Cell Surgery with Nanoparticles? *Medical Laser Application* **2002**, *17* (1), 9-14.

Danksagung

In Liebe und Dankbarkeit an meine Familie & Maxi

„12:34“

...und an euch, für unvergessliche Mittagspausen 😊